Plant fiber mechanical characterization with high precision micro-mechatronic means : investigation of single fiber transverse behavior and inter-fiber adhesion

Jason Govilas

Jason Govilas. Plant fiber mechanical characterization with high precision micro-mechatronic means : investigation of single fiber transverse behavior and inter-fiber adhesion. Matériaux composites et construction. Université Bourgogne Franche-Comté, 2023. English. ⟨NNT : 2023UBFCD007⟩. ⟨tel-04472025⟩

HAL Id: tel-04472025
https://theses.hal.science/tel-04472025v1

Submitted on 22 Feb 2024

THESE DE DOCTORAT DE L'ETABLISSEMENT UNIVERSITE BOURGOGNE FRANCHE-COMTE

PREPAREE A l'UNIVERSITE DE FRANCHE-COMTE

Ecole doctorale n° 37

Sciences Pour l'Ingénieur et Microtechniques (SPIM)

Doctorat de Sciences pour l'ingénieur

Par

Mr. Jason Govilas

Plant fiber mechanical characterization with high precision micro-mechatronic means: investigation of single fiber transverse behavior and inter fiber adhesion

Caractérisation mécanique des fibres végétales à l'aide de moyens micro-mécatroniques de haute précision : étude du comportement transversal de fibres élémentaires et de l'adhésion inter-fibres

Thèse présentée et soutenue à Besançon, le 21 février 2023

Composition du Jury :

Lamine BOUBAKAR	PR, Université Franche-Comté	Président du jury
Laurent ORGEAS	DR, CNRS, 3SR Lab	Rapporteur
Sébastien JOANNES	CR, CNRS, Mines Paris	Rapporteur
Véronique MICHAUD	Professeure associée, EPFL	Examinatrice
Pasi KALLIO	PR, Université de Tampere	Examinateur
Johnny BEAUGRAND	DR, INRAE, BIA Nantes	Codirecteur de thèse
Cédric CLEVY	PR, Université de Franche-Comté	Codirecteur de thèse
Vincent PLACET	IR, Université de Franche-Comté	Directeur de thèse
Violaine GUICHERET-RETEL	MCF, SUPMICROTECH-ENSMM	Invité
Fabien AMIOT	CR, CNRS, FEMTO-ST Institute	Invité

ACKNOWLEDGMENTS

As I set out to write the long awaited acknowledgment section of this thesis, I want to start by sharing the first verse of a poem I studied in high school:

> *As you set out for Ithaka*
> *hope your road is a long one,*
> *full of adventures, full of discovery.*

While as a teenager this verse didn't particularly resonate with me, it often came to mind during my PhD. Indeed, the road towards this thesis was a long one, full of adventures, discoveries and new experiences which would not have been possible without many wonderful people, that I would like to thank and acknowledge.

First of all, I would like to thank my supervisors who guided and helped me in this journey: Johnny Beaugrand, Cédric Clévy and Vincent Placet. I truly believe that it is incredibility difficult to match the combination of your scientific and human qualities, which make for an amazing environment to pursue a PhD in. Johnny, thank you for your constant encouragement and your positive attitude, Cédric, thank you for your light-hearted stand, your pragmatism and your focus and finally, Vincent, thank you for your empathy, your calm and your vision. Thank you all, for being so available despite your loaded schedules, it is through your guidance that I discovered a passion for scientific research.

I would also like to thank the members of my PhD defense committee for taking the time to examine this manuscript and for the enriching discussions that took place during the defence: the president, Lamine Boubakar, the reviewers, Laurent Orgéas and Sébastien Joannès and the examiners, Véronique Michaud and Pasi Kallio. I would also like to acknowledge Emeline Sadoulet and Gael Chevallier, for all their teachings during my master's degree and for making me discover the field of research through my master's internship. I thank them for helping me develop the skills and the confidence to pursue my research work further.

A special thanks also, to all the people I had the chance to collaborate with, on different parts of this thesis work. First, the students who I collaborated with during their internships: Thomas, Anouk, Guillaume et Wajih. I was truly lucky to have such quality contributions from you, in addition to your great attitude and personalities. Thank you to Violaine and Fabien who I collaborated on the question of platen parallelism. Working with you brought me new perspectives and I was proud of the results we were able to obtain. Many thanks also, to all the people that made the experimental part of this thesis possible: Patrick Rougeot, Pierre Roux and Vincent Tissot for the fabrication and equipment aspect, Antoine André, Patrick Sandoz and Guillaume Laurent for their work on HP codes and finally Joël Agnus for the clean room fabrication. A special mention to Patrick R. and Joël for their patience and guidance during my discovery phase of their respective fields. A thank you also to all the unsung heroes of a research laboratory:

IT, HR and maintenance, whose work and support make research endeavors possible. I wish also, to thank all of the people I had the chance to meet within the two research departments I was part of, for creating such an unique and pleasant work environment.

During this thesis work I was also very fortunate, to call many of my colleagues, my friends. Alban, Alex A., Arthur, Etienne, Flora, Guillem, Kevin, Liam, Margaux, Martin, Manu, Nicolas, Quentin, Rafael R., Rafael T., Robin, Shakiba, Simon, Solène, Steph, Svenja, Thibault, Tom, Vincent and more... Whether during a coffee break, our shared lunches, our pétanque matches or numerous nights at the Delta, Madigan's or the lab, it has been a great pleasure to share this journey with you, with so much laughter and great discussions. A special mention as well to the great team I've shared the 45H office (the best office) with: Aflah, Anouk, Benjamin, Guilherme, Taiqu, Tiguida and Wajih. Thank you for making everyday at work so fun, even through tougher periods. A few words for those that I have shared the office the longest with: Aflah I will always remember your resonating laugh, rhino approach to life and chess skills. Wajih, I think your calm and wit are an excellent addition to this office, I regret not sharing it with you longer but I'm happy knowing my desk will be in good hands. Anouk thank you (or not), for all you bad (good) jokes. I was really happy to see you turn from a shy intern to a PhD student with such potential. Keep going. Guilherme, your arrival to the office was like a ray of bright and exotic sun. I appreciate you a lot as a person, thank you for all the great memories and for the Portuguese lessons. Last but definitely not least, Benjamin, I am so glad we shared two years of our PhD journey together, with countless inside jokes and impersonations, hilarious and serious discussions, songs and nerf fights. I am certain you will continue to be great both as a friend, a scientist but also now, a dad.

A very special mention to two of my greatest friends with whom I had the privilege to go through the adventure of the master's and the doctoral degree together, Alex and Kejun. I sincerely doubt that I would have reached this point without you. Our endless discussions, laughs, hard work and sense of brotherhood will be memories that I will keep fondly for the rest of my life. We came a long way already and I cannot wait to see the great things the future holds for you two, who I truly admire.

Finally, a thank you to all the people I did not get to see as much as I wanted during these three years. My childhood friends Anthi and Vasilis. My parents and three sisters: Eléonore, Louise and Elsa, who have always supported me and believed in me. My grandmother. And to Christina, who surmounted all obstacles to be by side in the toughest challenges of these years. Who always believed in me and who helped me, with love and care, to try and be the best version of myself.

Ithaka gave you the marvelous journey.
Without her you wouldn't have set out.
She has nothing left to give you now.

And if you find her poor, Ithaka won't have fooled you.
Wise as you will have become, so full of experience,
you'll have understood by then what Ithakas mean.

Constatinos Cavafis 1911

Dedicated to my grandparents *Λάζαρος*, *Χρυσαυγή* and *Jean-Marie* who I did not get the chance to share this with.

Acronyms

AFM Atomic Force Microscopy.

BU Breaking Unit.

CSA Cross Sectional Area.

CT Compliant Translation.

DMA Dynamic Mechanical Analysis.

DOF Degrees Of Freedom.

EIPHI Engineering and Innovation through Physical Sciences, High-technologies, and cross-dIsciplinary research.

FDAS Fiber Dimensional Analysis System.

FEA Finite Element Analysis.

FEM Finite Element Model.

HM Hammer Mill.

HP High Precision.

HSB Hochschule Bremen.

IFBT Impregnated Fiber Bundle Test.

IFSS InterFacial Shear Strength.

IQR InterQuartile Range.

K29 Kevlar 29.

LVDT Linear Variable Differential Transformers.

MEMS MicroElectro-Mechanical System.

MFA MicroFibrilar Angle.

MSE Mean Squared Error.

NEMS NanoElectro-Mechanical System.

PA11 Polyamide 11.

PFC Plant Fiber Composites.

RH Relative Humidity.

ROM Rule Of Mixtures.

SEM Scanning Electron Microscope.

SFC Synthetic Fiber Composites.

SFTCT Single Fiber Transverse Compression Test.

SFTCTs Single Fiber Transverse Compression Tests.

TRL Technological Readiness Level.

Contents

General introduction

Contents

Academic and funding context

This doctoral thesis was carried out in an unique context, as part of the European *NETFIB* project and the doctoral program of the *EIPHI* graduate school, which co-funded this research work. A short description of each of them is given below:

NETFIB project - In the wider effort to limit the environmental impact of human activity and combat climate change, plant fiber composites have gained popularity as an environmentally friendly alternative to conventional composites materials. Wide scale use of plant fibers however, would require an important increase in land area dedicated to fiber crops. Given the scarcity of land suited for agriculture, such an increase could lead to conflicts between fiber and food crops. It is in this general context that the European Union backed *NETFIB* project is positioned. The project explores a plant fiber production alternative, by using lands that have been marginalized by industrial contamination, making them unsuitable for food production. In addition to fiber production, such an approach also promotes soil rehabilitation and limits contaminant mitigation. The use of native, spontaneously appearing plants is favored in order to promote the renewal of the natural ecosystem. Nettle is the most suited candidate for this purpose in Europe.

The *NETFIB* project regroups 7 academic institutions and 1 industrial partner, from 5 countries, to conduct research on this subject. Various aspects related to fiber production are investigated, from the agronomy stage and post harvest processes, to soil rehabilitation, nettle clone variety development, study of amendments or life cycle and sustainability assessments. A final research axis lies in the mechanical characterization of the harvested fibers and the production and testing of composite materials. It is in this final axis that this PhD work contributes actively in the field of fiber mechanical characterization.

EIPHI-BFC
GRADUATE SCHOOL
CROSS DISCIPLINARY SCIENCE
AND TECHNOLOGY

EIPHI - The Engineering and Innovation through Physical Sciences, High-technologies, and cross-dIsciplinary research (EIPHI) graduate school, is an international integrated Master's and Doctoral degree program of the University of Bourgogne Franche-Comté. Doctoral theses funded by this program are characterized by two main attributes: (i) an inter-disciplinary nature, covering domains such physics and mathematics, material and computer science or smart systems and structures; (ii) a focus on mentoring and supervising undergraduate students through academic projects and research internships. The interdisciplinary nature of this doctoral thesis will become apparent throughout this manuscript and the contributions of student collaborations will be presented.

Scientific context and main research axes

Ever since the start of the industrial revolution, humanity has witnessed an unprecedented economic and scientific growth, that has improved the standards of living of billions of people worldwide. In the recent decades however, it has become apparent that this growth took place in a largely unsustainable way and with a huge environmental impact, undermining the future of new generations. The use of petroleum-based materials has been at the forefront of these changes, offering a plethora of cheap, mass produced goods at the expanse of green-house gas emissions [Shen 20] and wide-scale pollution [MacLeod 21].

Modern composites, generally make use of such materials in their matrices or their fiber reinforcements. Using plant fibers as an alternative reinforcement, is gaining popularity as a sustainable and environmentally friendly alternative. Indeed, plant fibers are a renewable resource, capture carbon dioxide from the air during their growth and are biodegradable. They thus contribute in the fight against climate change while also minimizing pollution. Plant fibers also present some unique advantages, notably in terms of stiffness and lightness or damping properties. In Europe, plant fiber species such as flax, hemp and nettle are favored due to climate suitability and industrial history.

Knowledge of fiber mechanical properties is crucial in the prediction of the properties of the composite materials that integrate them. However mechanical characterization at the fiber scale presents a series of challenges. First, plants fibers are small objects, comparable, albeit generally smaller, to human hair. Consequently, in addition to typical material science and mechanics approaches, the use of tools found in the fields of micro-mechatronics and micro-robotics are also necessary. Indeed, many advances in the field of manipulation [Zhang 19], actuation [Ouyang 08] and force-sensing [Wei 15] have made possible the study of various microscopic objects, whether biological (cell, micro-organisms) or man made (MEMS, micro-parts) in nature. Furthermore, plant fibers present large variations in morphology, structure and biochemical composition, resulting from millions of years of evolution and an active adaptation of the plant to its ever-changing environment [Bourmaud 18]. As a result, their properties can show important variability. In order to approach this mutlidisciplinary project and overcome its inherent challenges, this thesis is a product of the collaboration between two departments of the *FEMTO-ST* institute (applied mechanics, automation micro-mechatronics) for the mechanics and micro-mechatronics aspect, but also of the French national agronomical institute (INRAE), for the plant biology aspect.

Despite the high potential of plant fibers and the means that have become available to test them, their size along with their morphological and material complexity remain significant scientific challenges in terms of manipulation and measurement while also producing complex mechanical behavior. For this reason, the number of different mechanical characterizations performed at the fiber scale is limited. Single fiber tensile testing and fiber-matrix pullout tests are the most common tests found in the literature to characterize longitudinal properties and intra-composite adhesion respectively. In this thesis, plant fiber characterization is expanded through the synergy of analytical, numerical and experimental developments. The problem of plant fiber characterization is approached in 3 main steps by:

1. identifying key fiber properties that can have a major impact on fiber quality or composite behavior, but are essentially unknown.
2. using analytical models or Finite Element Analysis (FEA), for the purpose of shedding light on the complex behavior of plant fibers.
3. developing and employing micro-mechatronic experimental setups to perform tests at the single fiber scale and characterize their mechanical properties.

This work will be presented through 4 chapters:

- Chapter 1: through a literature review, the single fiber transverse properties and inter-fiber adhesion are identified as unknown properties that are key in the future development of plant fiber composites. The most suitable approaches to perform their characterization are also presented.
- Chapter 2: FEA is used to study the influence of fiber morphology and material behavior on the results of a Single Fiber Transverse Compression Test (SFTCT). The ability to identify the plant fiber's transverse elastic modulus E_T with the use of existing analytical models is evaluated.
- Chapter 3: an innovative micro-mechatronic platform is developed and validated for SFTCTs. The transverse behavior of plant fibers under compression is studied and their transverse elastic modulus is identified for the first time.
- Chapter 4: a micromechatronic platform is designed and developed to perform fiber peeling. Inter-fiber adhesion is measured for the first time and new decohesion mechanisms are observed.

Scientific publications and communications

A large number of the approaches, methodologies and results that are presented in this work, have been shared with the wider scientific community through journal article publications and presentations in national and international conferences. A number of works are still in the preparation or reviewing stage. A list of the scientific production related to this doctoral thesis is given below:

Publications

- **J. Govilas**, V. Guicheret-Retel, F. Amiot, J. Beaugrand, V. Placet, C. Clévy. *Platen parallelism significance and control in single fiber transverse compression tests.* Composites Part A: Applied Science and Manufacturing, vol. 159, 2022

- A. André, O. Lehmann, **J. Govilas** (equivalent first authors), G. Laurent, H. Saadana, P. Sandoz, V. Gauthier, A. Lefèvre, A. Bolopion, J. Agnus, V. Placet, C. Clévy. *Automating Robotic Micro-Assembly of Fluidic Chips and Single Fiber Compression Tests Based-on* $XY\Theta$ *Visual Measurement With High-Precision Fiducial Markers*, IEEE Transactions on Automation Science and Engineering, 2022

- **J. Govilas**, J. Beaugrand, C. Clévy, V. Placet. *Plant fiber transverse compression: determining the influence of fiber morphology with finite element analysis*, (in preparation).

- **J. Govilas**, V. Guicheret-Retel, C. Clévy, V. Placet, F. Amiot. *Introducing compression platens parallelism error in single fiber transverse compression model*, (in preparation).

- A. Chevallier, **J. Govilas**, J. Beaugrand, C. Clévy, V. Placet, *Plant fiber transverse compressive properties characterization using micro-mechatronics*, (in preparation).

- C. Viotti, K. Albrecht, S. Amaducci, P. Bardos, C. Bertheau, D. Blaudez, L. Bothe, D. Cazaux, A errarini, **J. Govilas**, H-J Gusovius, T. Jeannin, C. Lühr, J. Müssig, M. Pilla, V. Placet, M. Puschenreiter, A. Tognacchini, L. Yung, M. Chalot. *Nettle, a Long-Known Fiber Plant with New Perspectives.* Materials, vol. 15, 2022

- E. Richelly, A. Zarei, A. Melelli, D. K. Rajan, **Jason Govilas**, X. Gabrion, C. Clévy, D. Legland, J. Perez, S. Guessasma, V. Placet, P. Kallio, J. Beaugrand. *Current trend towards microfibril angle measurement within plant fibres: comparison between X-ray diffraction, second harmonic generation and transmission ellipsometry microscopies*, Composites Part C. (submitted)

Presentations

International conferences

- **J. Govilas**, A. Chevallier, J. Beaugrand, C. Clévy, V. Placet, *Characterization of plant fiber transverse mechanical behavior using a micro-mechanical setup*, 5th International Conference on Natural Fibers, online, 17-19 May 2021.

- **J. Govilas**, T. Guibaud, J. Beaugrand, C. Clévy, V. Placet, *Investigation of the mechanics of interface between individual plant fibers using micro-mechatronics*, 1st European Summer School on Bio-Based Composites, Online, 6-8 July 2021.

- **J. Govilas**, T. Guibaud, J. Beaugrand, C. Clévy, V. Placet, *Studying plant fiber interface toughness and fracture mechanisms using micro-mechatronics*, 7th International Polysaccharide, Nantes - France, 11-15 October 2021.

- **J. Govilas**, A. Chevallier, V. Guicheret-Retel, F. Amiot, J. Beaugrand, C. Clévy, V. Placet, *Sinle plant fiber transverse compression - Investigation of influential parameters and identification of mechanical properties*, The Fiber Society 2022 Spring Conference, Leuven - Belgium, 30 May - 1 June 2022.

National conferences

- **J. Govilas**, V. Guicheret-Retel, F. Amiot, J. Beaugrand, C. Clévy, V. Placet, *Identification des propriétés élastiques transverses de fibres élémentaires : influence des défauts de parallélisme entre plateaux de compression* , JNC 22 - Journées Nationales sur les Composites, Online, 28-30 June 2021.

Mentoring and supervising

During this thesis work, four different six-month internships were co-supervised on various research aspects related to fiber characterization. Two of these internships turned into short-term engineer contracts and later PhD positions, focusing on subjects related to this thesis. These fruitful collaborations contribute in a major way in the number and diversity of the subjects addressed in this work. The detailed contribution of each of these collaborators will be given in the respective chapter/section, however a brief summary is given below:

- **Thomas Guibaud**, 6-month internship (2020): *Design and development of micro-peeling mechatronic experimental platform.*
- **Anouk Chevallier**, 6-month internship (2021), engineering position (2021-2022): PhD thesis (2022-2025): *Plant fiber experimental characterization.*
- **Guillaume Pluvinage**, 6-month internship (2021): *Design and development of single fiber transverse compression micro-fabricated device.*
- **Wajih Akleh**, 6-month internship (2022), engineering position (2023), PhD thesis (2023-2026): *Plant fiber peeling experimental characterization.*

1

LITERATURE REVIEW: PLANT FIBER CHARACTERIZATION - IDENTIFYING NEW CHARACTERIZATION NEEDS

Contents

1.1 Introduction

Despite the large environmental benefits of Plant Fiber Composites (PFC), their wide scale adoption also requires an accurate knowledge of their mechanical properties. In this first chapter, plant fiber mechanical properties, that are critical to ensure or predict composite performance but have never been characterized, are identified. To do so, a literature review is performed covering various domains and scales. Plant fibers will be presented from their microstructure to their integration in composite materials. The methods and approaches that can be used to characterize them will also be discussed. Throughout this review, the overall context, basic principles and state of the art of these different subjects are also presented, providing a general overview of the subject of plant fiber characterization.

This literature analysis will be separated in three parts that will treat the following subjects:

- Section 1 - overview of plant fibers and their composites: history, environmental benefits, microstructure, life cycle.
- Section 2 - plant fiber characterization state of the art: relevant scales, direct and indirect methods, common tests, identifying limitations.
- Section 3 - needs in plant fiber characterization and selected approaches : need for transverse properties and adhesion characterization, relevance of micro-mechatronic experimental platforms and finite element analysis.

1.2 Plant fibers and their composites

1.2.1 History and environmental benefits

Humankind has made use of plant fibers for over 30.000 years, to produce textile materials for a variety of applications [Kvavadze 09]. Since antiquity, several civilizations also realized the mechanical advantages of materials resulting from the combination of multiple constituents, *i.e* composite materials. Plant fibers were incorporated as reinforcements in the first example of composites materials, mud bricks reinforced with straw, found in Egypt and Mesopotamia and dating to 1500 B.C [Nagavally 17, El-hady 12]. The Mongols later used a mixture of animal sinew and glue in their composite bows, who remained “the most powerful projectile weapon until the invention of gunpowder” [Nagavally 17, Bergman 97].

The development of plastics in the early 1900s, revolutionized the field of composite materials since they allowed the production of synthetic resins that far exceeded the properties of natural ones. The development of new types of fibers in particular glass, carbon, aramid (notably Kevlar®) and various other polymeric fibers offered exceptional mechanical properties in addition to being lightweight. The production of these fibers is however very energy intensive and relies, with the exception of glass fibers, on petroleum sourced materials, a non-renewable resource [Nyambuu 14]. Furthermore, the use of plastic materials largely contributes to green-house gas emissions [Shen 20] and wide scale pollution [MacLeod 21]. Numerous recycling approaches can be used to extract the composite components or repurpose the composite itself [Witik 13, Asmatulu 14], reducing the overall environmental impact of these materials. However, numerous challenges remain concerning recycling cost, product quality and commercialization [Yang 12].

In response to these environmental concerns, development of composite materials that integrate natural, renewable resources, called bio-composites, have gained popularity once again. Among these resources, plant fibers are a typical reinforcement choice. Figure 1.1 illustrates the rising trend in scientific publications on the topic of plant fiber reinforced composites. Indeed, combining modern composite manufacturing techniques with the plant fibers that have been used for millennia, can produce materials that are comparable to those using synthetic fiber reinforcements, in terms of cost and material properties [Pickering 16]. When compared to their synthetic counterparts, plant fibers have the benefit of being renewable, easier to recycle and biodegradable. During their growth, the plants that provide the fibers also capture carbon dioxide from the atmosphere. Finally, plant fibers typically have a lower density than the widely used glass fibers, leading to weight reductions when used in composites. When used in the transport industry, this can lead to considerable fuel savings [Gurunathan 15]. Overall, the environmental impact of Plant Fiber Composites (PFC) over their life-cycle, is significantly less important than conventional composites [Mansor 19].

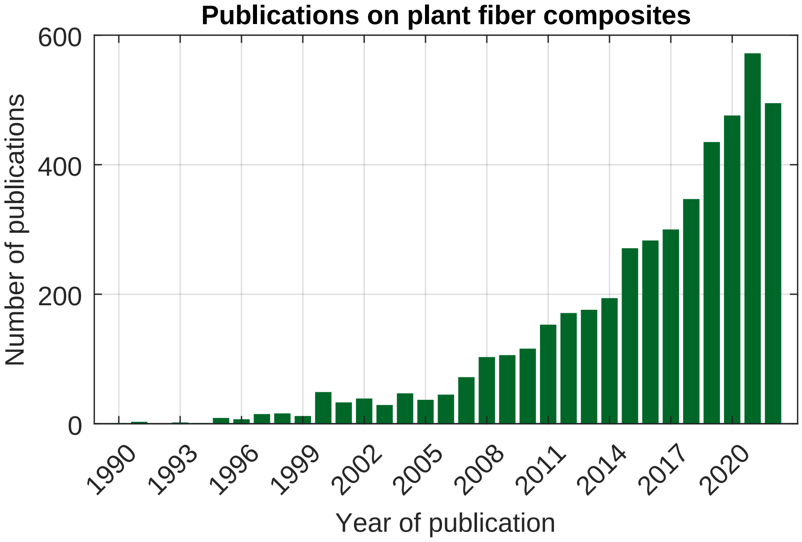

Figure 1.1: Number of topic occurrences in scientific publications (appearance in title, abstracts and author keywords) for plant-fiber (or with english speeling ”fibre”) composites per year of publication. Data included herein are derived from Clarivate Web of Science©. Copyright Clarivate 202. All rights reserved .

1.2.2 Plant fiber diversity - best suited fibers for composite applications

In order to produce environmentally friendly composites with plant fiber reinforcements, two main criteria should guide the choice of fiber: its mechanical properties and its local availability. Indeed, fiber mechanical properties must be adapted to the given composite application, while locally growing and processing fibers that are adapted to their ecosystem, contributes to its healthy functioning, guarantees sustainability and limits emissions related to the transportation of the material.

The mechanical properties of plant fibers, are strongly correlated to the role they play inside their parent plant. Indeed, the number of plants that have evolved fibers in order to perform different functions is astonishing. Figure 1.2 gives an overview of some the plant fibers that can be found in nature, while Figure 1.3 presents the diversity that can be found in fiber morphology and structure across many different species. Some of these fibers are characterized by low mechanical performance. Cotton or kapok fiber for example, grow around the seeds with the goal of being picked up by the wind to disseminate the plant. Lightness and length are thus critical in contrast to mechanical properties. Fibers found in leaves, mainly contribute in the distribution of nutrients in the plant while offering moderate structural stability. Consequently, they present mechanical properties that are higher than dissemination fibers, albeit moderate. Some plants grow fibers for protective purposes. Coconuts for example are surrounded by fibers (coir) that can protect them in the case of a fall. Coir fibers thus present important impact absorption capabilities.

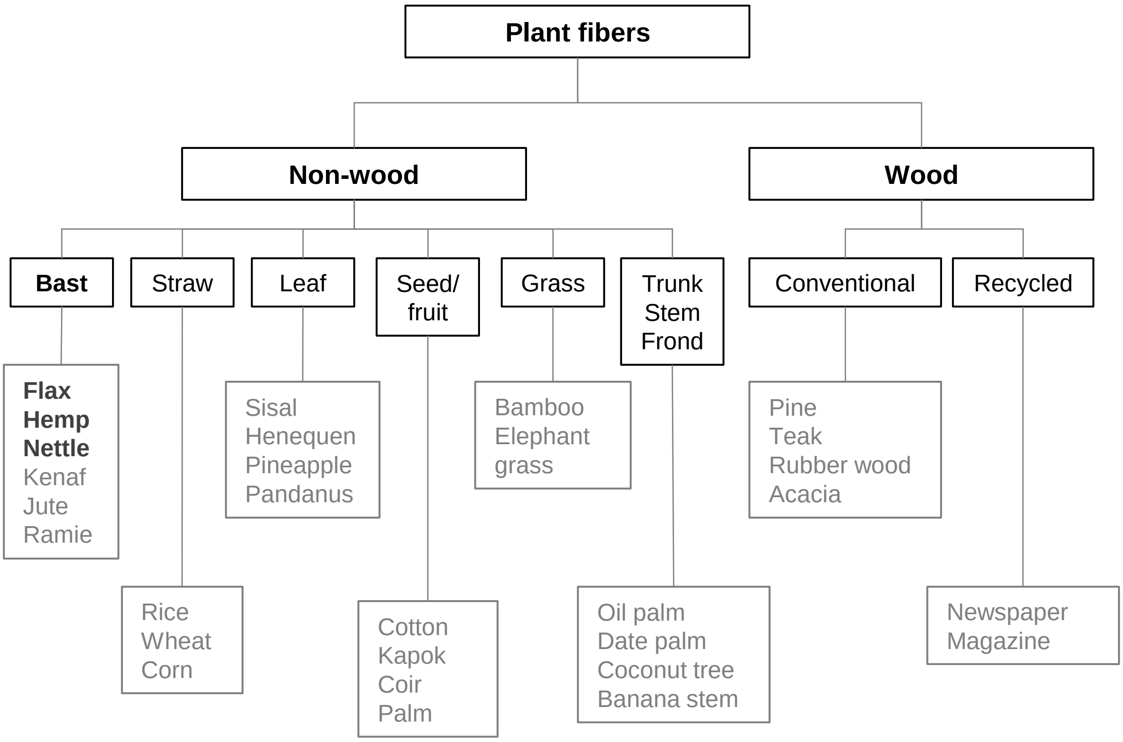

Figure 1.2: Plant fiber classification based on [Jawaid 11, Bourmaud 18]. This thesis will mainly focus on three bast fibers: flax, hemp and nettle.

Nevertheless, the highest fiber mechanical performance can be found in those that have a structural role, supporting the plant during its growth and offering stability against external forces such as wind. Wood fibers play such a role, their small length however is not always ideal for composites. Bast fibers on the other hand, found in plants such flax, hemp, jute and others, are longer fibers growing on the perimeter of the plant's stem offering stability [Zimniewska 11, Sadrmanesh 19]. By consequence, they present high mechanical properties that are comparable to their synthetic counterparts, making them great for composite applications.

Among the large variety of bast fibers that can be found globally, only a few of them have been grown in Europe. Nettle is the only one of them that is both native and spontaneously occurring in this region [Viotti 22]. Flax has been cultivated for centuries for its textile applications, with large quantities being currently produced in Western France [Melelli 21a]. Hemp has also been produced in Europe for centuries. Being a

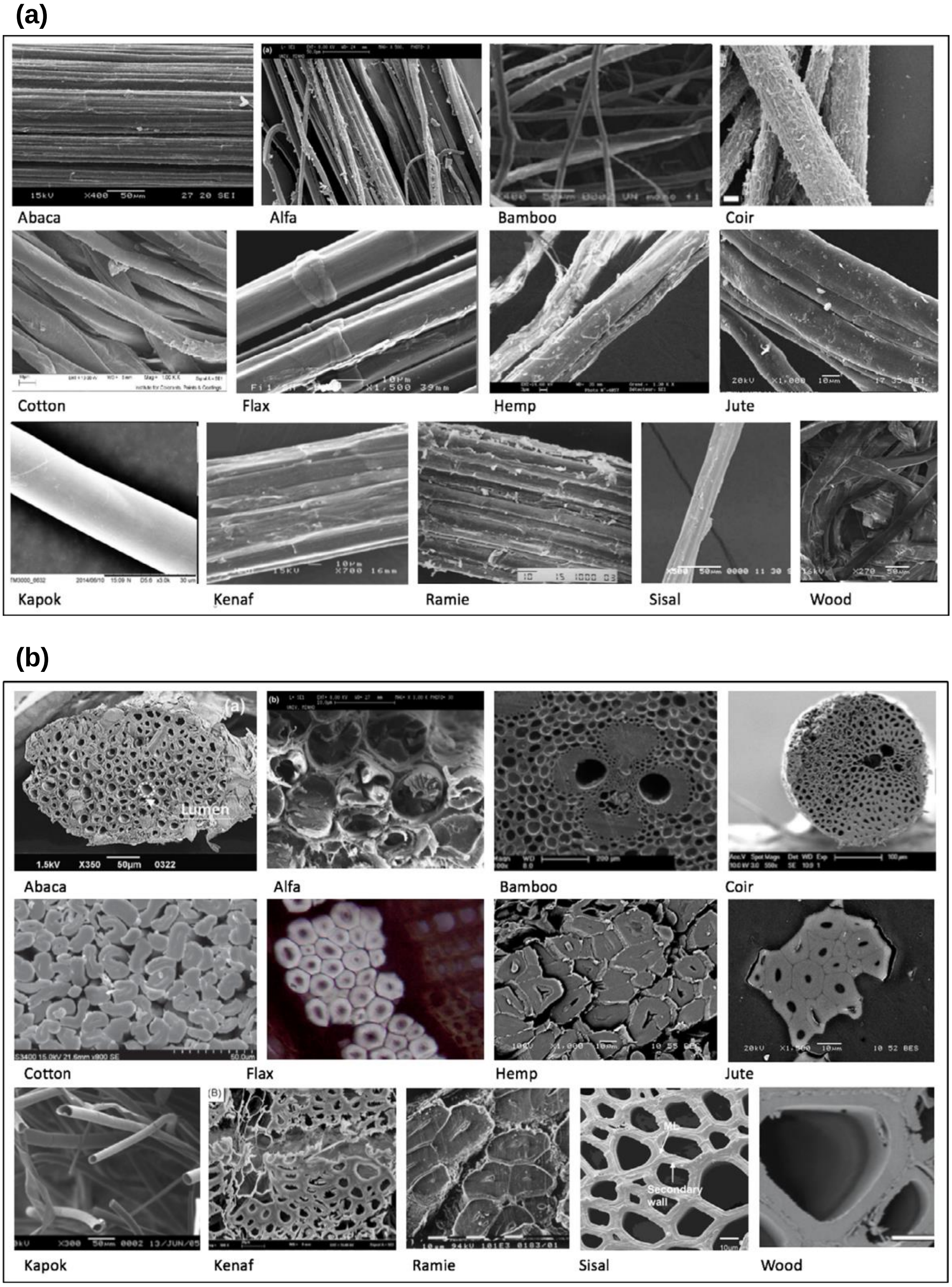

Figure 1.3: SEM images of plant fibers along: (a) the fiber length, (b) the fiber cross section [Bourmaud 18].

member of the cannabis family, its popularity fell in the 20th century, however cultivation of the plant is greatly rising once again [Shahzad 12].

Consequently, given their mechanical advantages and availability, the european PFC sector mainly favors the established flax crop, while hemp is rising in popularity. The adoption of nettle is not as widespread, however interest in the plant is also growing [Viotti 22]. This PhD work will focus on these three fibers, the approaches and methodologies that will be used to study them however, are applicable for most fibers.

1.2.3 Plant fiber structure - from plant stem to microfibril

In order to better understand the source and mechanisms behind plant fiber mechanical performance, the internal structure and organization of the plant itself must be approached. Fiber structure is a result of millions of years of evolution. To ensure their survival in a complex and actively changing environment, plants have evolved a complex, hierarchical, structural organization. Indeed, plants can be equated to composite materials with a fractal design, comprising of multiple levels of reinforcing and cohesion elements. Such elements can be found at the macro-scale, in the plant's stem, at the micro-scale in the plant's elementary fibers and even down at the nanoscale in the polymer chains that make up fiber's building block. Adding to this overall complexity, this organization can be different depending on plant species and environmental conditions [Sadrmanesh 19, Bourmaud 18].

The subject of plant structure has been, and remains, a large research topic in the field of biology. In the case of bast fibers, literature discussing the organization and composition of their plants in the context of their mechanical performance, at all scales, is quite extensive has been presented in many doctoral theses [Richely 21a, Melelli 21a, Viotti 22, Del Masto 18, Bourmaud 18, Sadrmanesh 19, Charlet 08]. For the purpose of this thesis, a synthetic overview of the typical bast fiber structure, covering the macro, meso, micro and nanoscale, will be presented in this section. A representation of the fiber structure across multiple scale is given in Figure 1.4

Plant stem

Plant stems are cylidrical in nature, with a diameter of a few *mm* and a length that can grow to several *dm* depending on plant variety. They can be divided into two main parts: the phloem and the xylem [Carlsbecker 05] (see Figure 1.4.a). The xylem can be found at the center of the stem around a central hollow space. Its role lies in the transportation of water and minerals from the roots to the aerial parts of the fiber. The phloem surrounds the xylem and allows the translocation of nutrients from the plant's leaves to its growing parts. It is within the phloem that bundles of fibers can be found. A bark/skin makes up the exterior of the phloem offering protection from the outside environment and moderate mechanical support [Sadrmanesh 19].

Fiber bundle

Within the phloem, multiple elementary fibers are joined to form fiber bundles of a few *cm* in length. Fiber bundle size can vary quite drastically, even within the same stem, with anywhere from 3 or 4 up to a dozen fibers coalescing into bundles (see Figure 1.4.b). They are generally however, a few hundreds of μm in width. The connection between

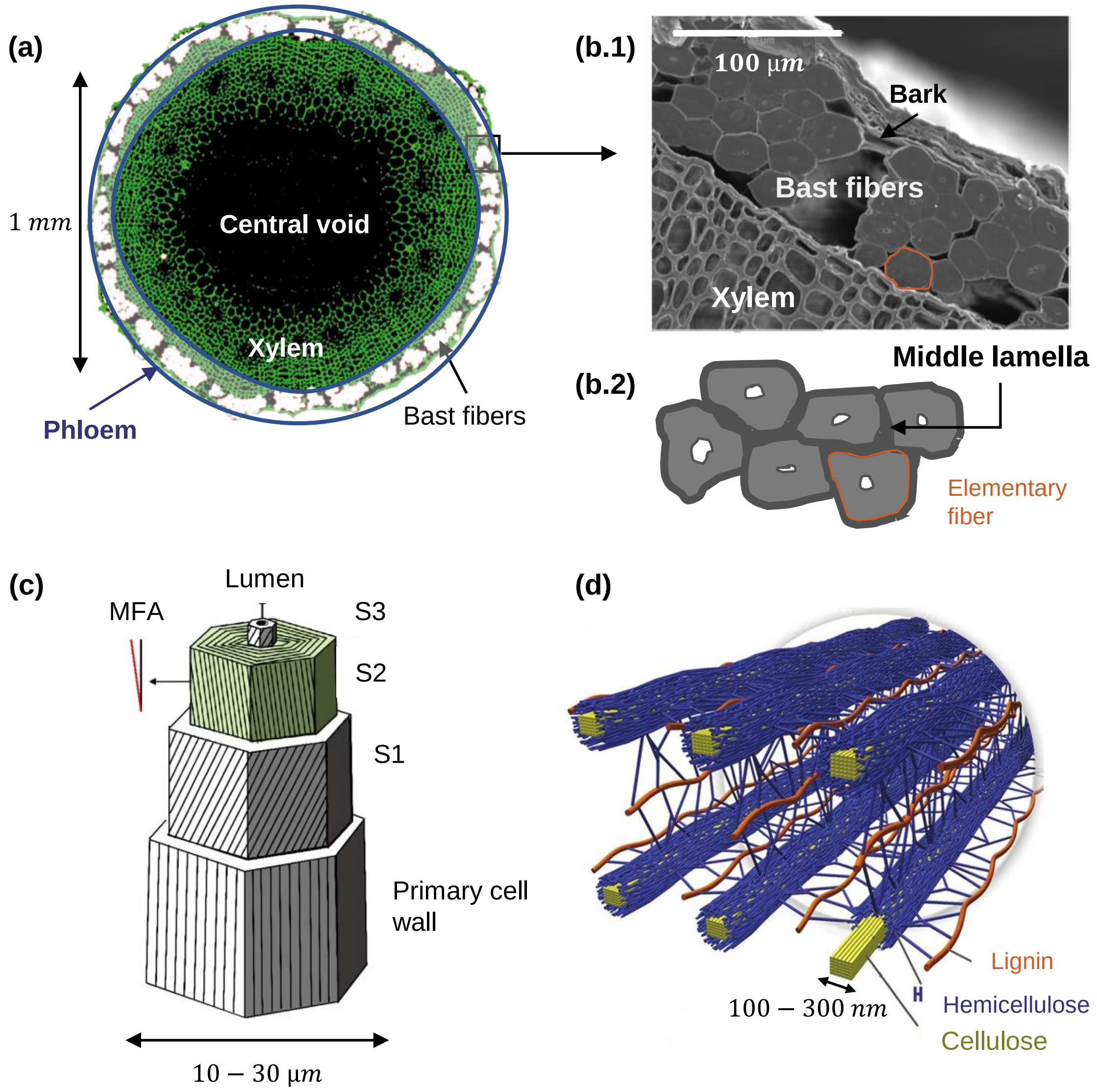

Figure 1.4: Plant fiber structure: (a) Flax stem microtomography [Zeng 15], (b.1) flax stem edge SEM with visible fiber bundles [Zeng 15], (b.2) fiber bundle representation, (c) elementary fiber microstructure representation [Melelli 20b], (d) representation of cellulosic micro-mesofiber in hemicellulose and lignin matrix [Brandt 13].

elementary fibers is made through the middle lamella, a complex pectin network that “glues” the fibers together [Sadrmanesh 19].

Elementary fiber

The elementary fiber is a complex structure, comprised of multiple layers with different compositions and characteristics (see Figure 1.4.c). It is generally a few mm in length with diameters in the tens of μm. In a similar way to the stem, the fiber can be divided into two main parts, the primary and secondary cell wall. These walls surround a central cavity, called the lumen. In this work elementary fibers will be often referred to as single fibers or just fibers.

During plant life, the area of the lumen is full of cytoplasm and organelles but gets emptied after the plant's death [Charlet 10a]. The size and shape of the lumen can change drastically between different fiber species [Bourmaud 18, Richely 21b]. For the studied bast fibers, it is in the range of approximately 5 % for flax and 15 % for hemp [Richely 21a]. In our experience with nettle, lumen size was larger in the range of $20 - 30\,\%$.

The primary cell wall is a 200 to 500 nm thick layer that bounds the exterior of the fiber along its whole length [Bourmaud 18]. The secondary cell wall is comprised of three layers named S1, S2 and S3. The intermediate S2 layer represents the most of the fiber's volume and thus it has the largest part in the fiber's mechanical properties [Baley 02, Bourmaud 18].

Contrary to their synthetic counterparts, plants fibers are commonly characterized by a morphologicaly complex transverse cross section (see Figure 1.3.b). Inside the plant's stem, plant fibers grow together in a limited amount of space. A circular cross section is thus sub-optimal since it would leave a large amount of empty space between fibers. As a result plant fibers have elliptical cross sections with some parts becoming flat due to a contact with neighboring fibers. In other cases, fibers grow into a polygonal geometry. During their transformation from plant supportive tissue to composite reinforcement plant fibers are also exposed to numerous external stimuli that can deform and damage them. Natural parameters such as wind and dried soils or the retting and extraction processes (presened in the next subsection) are the main sources [Bourmaud 18]. These damaged zones can take many different forms and appear clearly along the fiber [Melelli 21b, Richely 22c], as seen in Figure 1.5. They tend to decrease the mechanical properties of the fibers and are often a weak point where fractures start to occur [Richely 22c, Müssig 10]. The terms kink bands, defects, dislocations, knees and more are all used to describe such zones [Nyholm 01]. The term kink bands will be used in this work. Overall, the central lumen, complex cross section and the presence of kink bands make elementary plant fibers a very complex structure.

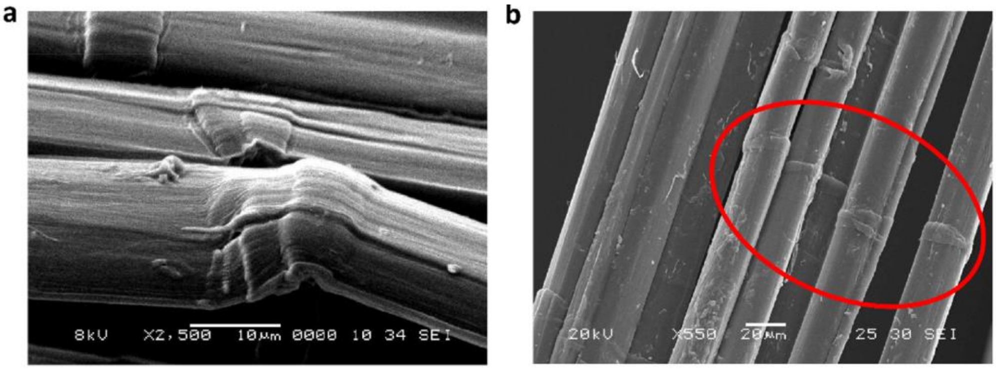

Figure 1.5: SEM kink band observation [Melelli 21b].

Elementary fiber composition

Biochemical composition. Following the fractal nature of plant architecture, elementary fibers can be assimilated to a composite material with cellulose, hemicellulose and lignin making up its basic units. Cellulose is a long polymer comprised of glucose units [Heinze 15]. Interactions between cellulose chains (few nm in diameter) leads to the formation of cellulose fibrils, the prefix micro or meso can be used for these them depending on their size (tens to hundreds of *nm* in diameter). Cellulose fibrils represent the basic reinforcement unit of the elementary fiber and provide it with most of its strength and stiffness [Bourmaud 18].

The cellulose microfibrils are contained within a hemicellulose and lignin matrix (see Figure 1.4.d). Hemicellulose is a complex polysaccharide that coats the cellulose fibrils [Lee 14]. It has poor mechanical properties and is more susceptible to degradation [Bourmaud 18, Sadrmanesh 19]. As the fiber grows and reaches maturity, empty spots in the cellulosic network are progressively filled by lignin, a complex amorphous polyphenolic compound [Lee 14]. The presence of lignin greatly contributes to the fiber rigidity and fiber bundle cohesion while also acting as a protective barrier [Lee 14, Komuraiah 14]. An overview of the fiber structure from stem to cellulose microfibril is given in Figure 1.6.

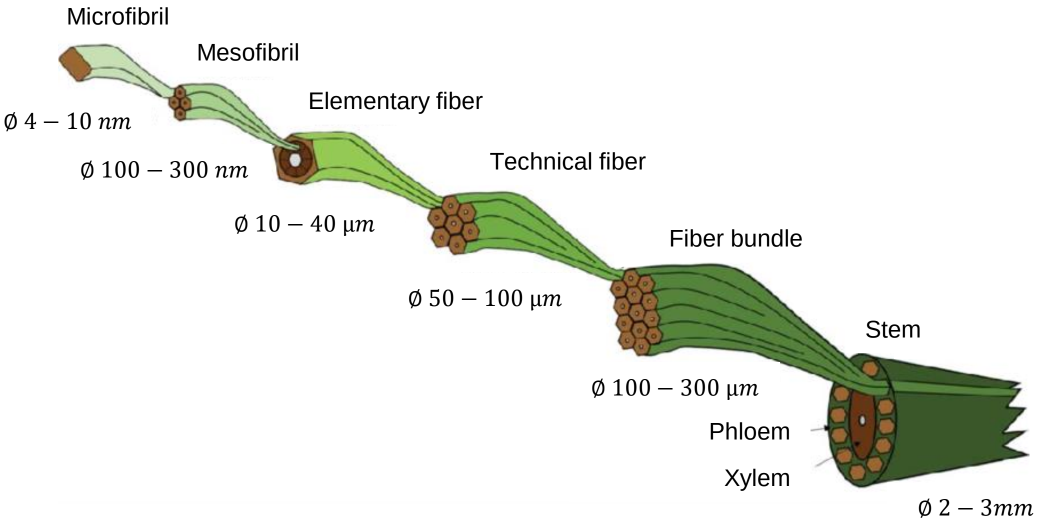

Figure 1.6: Overview of bast fibers from stem to cellulose fibrils [Güven 16]

Microfibril orientation. Within the different layers of the elementary fiber, cellulose microfibrils can take different orientations compared to the main fiber axis (see Figure 1.4.c). The angle between the elementary fiber main axis and the direction of its microfibrils is called MicroFibrilar Angle (MFA). At the primary cell wall, the cellulose fibrils follow the growing direction of the fiber leading to very low values of MFA. For the secondary wall, each layer can have a different MFA. The value of the MFA can have a significant impact on the properties of the fiber, especially in the longitudinal direction where lower MFAs lead to higher stiffness [Baley 02, Bourmaud 13b, Nuez 22, Reiterer 01, Keckes 03, Burgert 06]. Along the fiber's length, the presence of kink bands leads to changes in MFA [Melelli 21b].

While each cell wall layer does have a preferential MFA value, changes in angle between cell wall layers does not occur abruptly. Roland et al. [Roland 95] observed though polarized microscopy, changes in cellulose fibril orientation at the interface between cell wall layers, as seen in Figure 1.7. At these interfaces, fibrils of different layers can be seen coalescing and aligning into denser regions through a progressive change of MFA. It is thus possible that some fibrils are bridging the interface between different cell wall layers. Literature on the subject is quite scarce, further investigations should be performed to shed light on the complex nature of the cell wall interfaces.

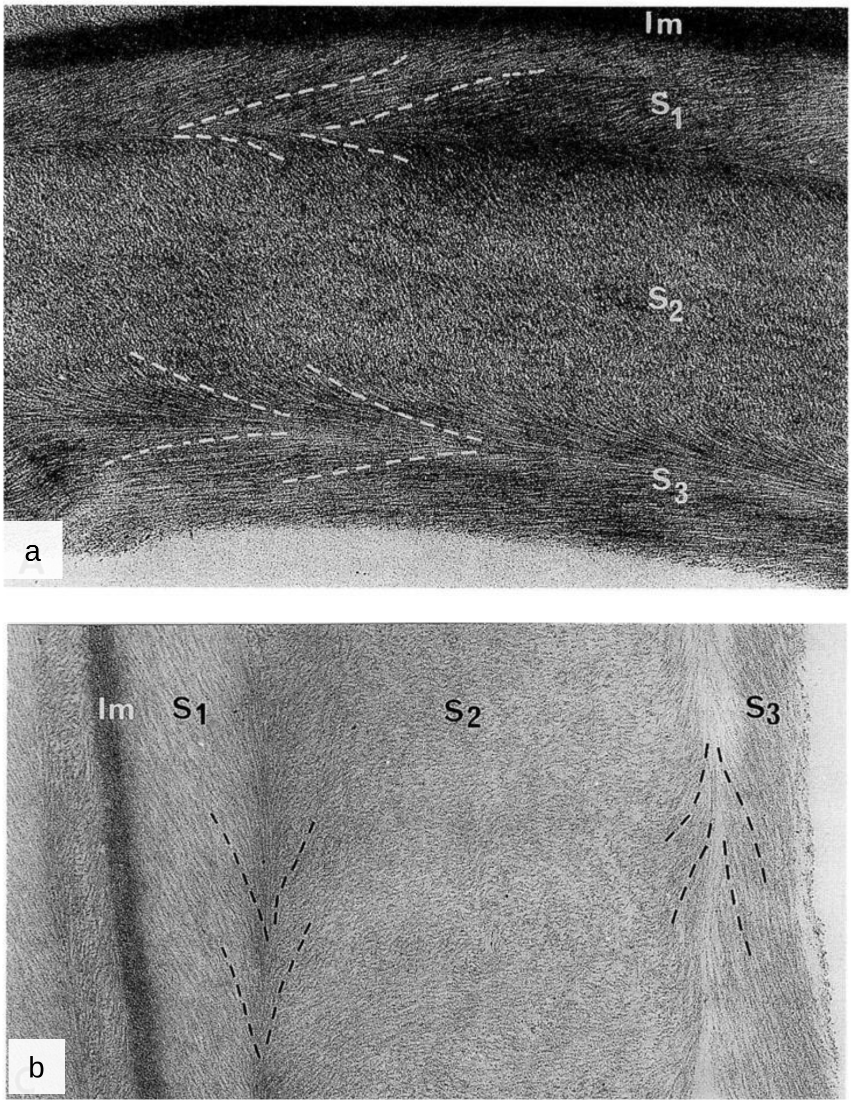

Figure 1.7: Polarized microscopy images of fiber microstructure [Roland 95]. Changes in cellulose fibril orientation can be seen between the cell wall layers.

1.2.4 From the field to the final product - Composite life-cycle and applications

This section presents the life-cycle of a PFCs while focusing on their plant fiber reinforcements. The characteristics of plant fibers can vary significantly between species or varieties, environmental conditions during growth and transformation processes. Transforming them from a natural material which actively adapts to small changes in its environment, to a reliable reinforcement for composite applications, requires a significant amount of transformation techniques and expertise. The most common processes from the production and extraction of plant fibers to the manufacturing and applications of the composites they reinforce are presented here, followed by the end of life of these products.

Plant fiber composite lifecycle

Figure 1.8 illustrates the different stages taking place during this life-cycle. A brief description of each stage is given below.

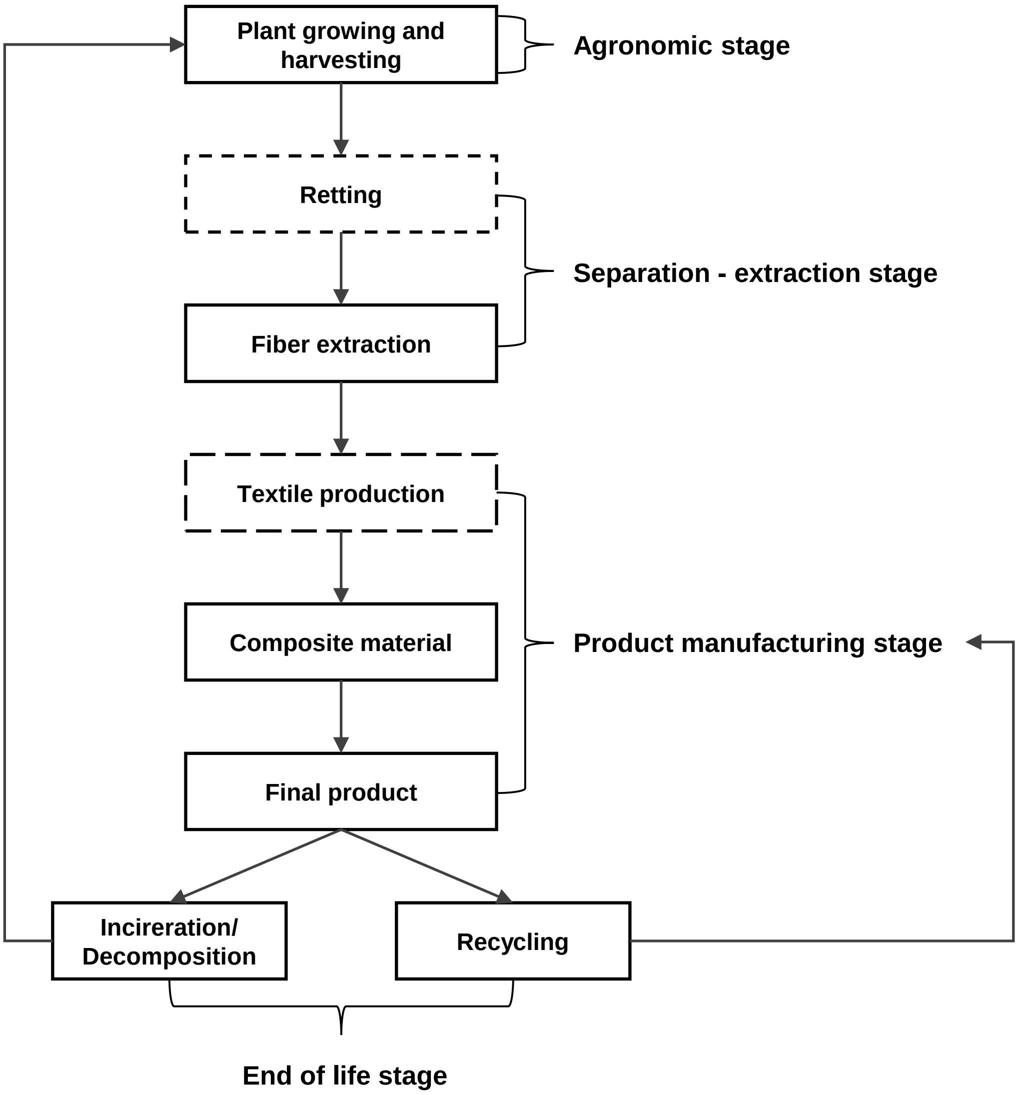

Figure 1.8: Life cycle of plant fibers used as reinforcements in composite materials. Dotted lines represent optional steps.

Agronomic stage. During this first stage, the plants have to be sowed or planted[1], grown and harvested. A great number of parameters concerning the choice of plant variety, soil amendment, irrigation, method and time of harvest, pest control, and more, have to be controlled and optimized to maximize yield and produce fibers of high quality for composite applications. During growth, environmental parameters such as temperature, wind, water availability and more will have a strong influence on the final fiber mechanical properties.

---

[1] depending on the crop, sowing or planting might not be required every year.

Separation/Extraction stage. As presented in the previous section, the plant stem is made up of various different elements. In order to set apart the fiber bundles from the rest of the plant and separate them into elementary fibers, an extraction stage is necessary. This stage is typically performed mechanically and is preceded by a retting step (depending on plant species and environmental conditions).

Retting. Retting consists in a controlled degradation of the plant's tissues [Bourmaud 18], typically performed through natural mechanisms. Fungi and bacteria colonize the plant and secrete enzymes that promote the degradation of inter-fiber plant tissue. The xylem and the pectins of the middle lamella degrade separating the fibers from the rest of the plant and the elementary fibers between themselves [Akin 01, Bourmaud 19]. Different levels of retting can be seen in Figure 1.9 in the case of flax. Overall, the fiber separation that results from the retting process significantly facilitates later fiber extraction. However, over-retting leads to the secretion of enzymes that attack cellulose, leading to significant decreases in mechanical properties [Bourmaud 18]. A balance should thus be struck between a good separation level without damaging the fiber's cellulose.

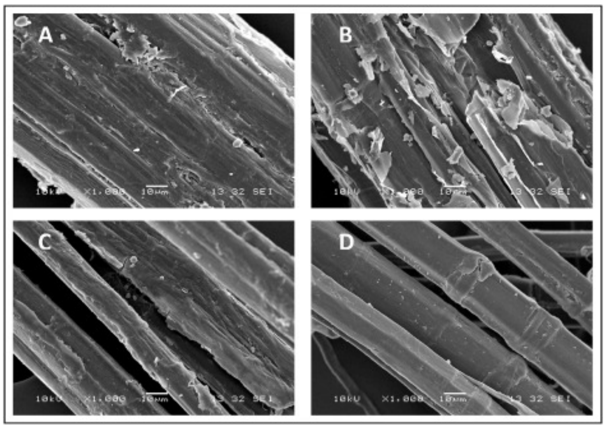

Figure 1.9: SEM images of flax fiber bundles with increasing levels of retting [Bourmaud 19]. After 1 day of retting (A) inter-fiber tissue is present and starts degrading after 9 days of retting (B). After 14 (C) and 19 (D) days of retting fibers are well separated and no inter-fiber tissue remains.

Mild temperatures and wet conditions favor the development of the micro-organisms that are responsible for retting. For this reason retting in bodies of water, man-made or naturally occurring, has been a common approach. Indeed, in a stable aqueous environment degradation will occur in an uniform way, ultimately leading to good fiber quality [Placet 17]. However, many fermentation products are released, polluting the water [Rosemberg 65]. For this reason, this practice has been abandoned in Europe, in favor of dew retting. Plant stems are cut and left in the field, where the presence of dew will promote the growth of the necessary micro-organisms. However, fibers are exposed to the elements, leading to less uniform retting and overall retting times that can vary from one to several weeks [Bleuze 18]. Figure 1.10 shows examples of dew and water retting. Alternative methods that do not rely on spontaneous natural processes also exist, notably chemical and enzymatic retting [Sharma 88, Akin 01], steam explosion [Kessler 98] and ultrasonic and microwave treatments [Nair 14]. However, these processes can also lead to pollution issues or are energy intensive and are therefore used to a lesser extent.

Figure 1.10: **a)** Dew retting of flax in Normandy, France (By Stanzilla - Own work, CC BY-SA 3.0, https://commons.wikimedia.org/w/index.php?curid=20540015), **b)** Jute water retting in Bangladesh (By Nahid Hossain, CC BY-SA 2.0, https://commons.wikimedia.org/w/index.php?curid=61669134).

Mechanical extraction. With the retting procedure being performed, the fibers can be extracted from the plant. A great number of different mechanical processes can be used, depending on the plant type, cultural practices, available means and final applications [Bourmaud 18]. Both machine and hand separated fibers can still be found. Figure 1.11 presents an overview of the large range of different mechanical extractions used just in the case of nettle. Globally, these processes aim at breaking apart the stems, isolating fiber bundles from the rest of the plant tissues (bark, xylem) and eventually refining these bundles through further separation, aligning and untangling.

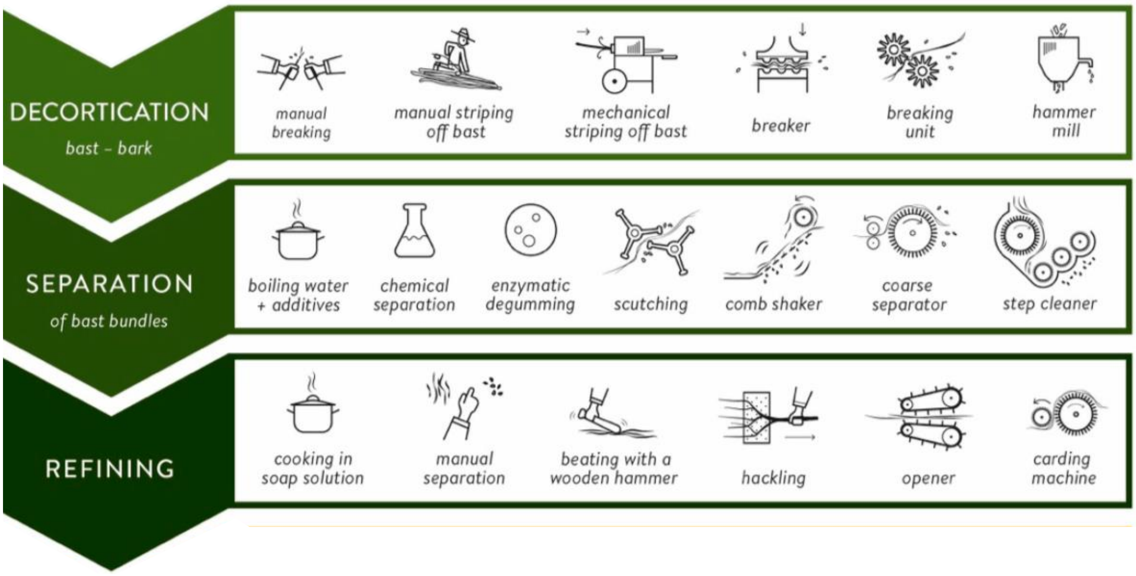

Figure 1.11: Overview of nettle fiber mechanical extraction processes taken from [Viotti 22].

Despite the large variety of existing extraction processes, they can generally be divided into two main categories. First, more aggressive processes, such as hammer and roller mills, that separate the fibers well but lead to damaged and shorter fiber in the end.

Second, the process of scutching followed by hackling leads to longer fibers of higher quality [Bourmaud 18]. Scutching consists of separating the fiber from the straw by passing the plant stems through a series of rollers of different sizes and rotation speeds. Hackling consists in separating and aligning the resulting fiber bundles by passing them through a series of progressively finer combs. Scutching and hackling were originally developed for flax and its textile applications [Müssig 15, Bourmaud 18] but have also been adapted for hemp [Grégoire 21] and nettle [Bacci 11, Viotti 22]. A graphical representation of a scutching and hackling line is given in Figure 1.12.

Figure 1.12: Scutching and hackling procedure for hemp fibers. Figure taken from [Grégoire 21] rearranged from [Müssig 15].

Product manufacturing stage. With the fibers being separated, the manufacturing of composite materials that use them as reinforcements can be performed. A preliminary, yet optional step to this manufacturing lies in the production of a textile product that can later be used in the composite. These products can vary from non-woven mats of parallel-unidirectional fiber, to combinations of different orientations or weaved patterns. The choice between these options depends on the aimed composite properties for a given application. Fibers can be also added to a composite without a particular orientation leading to composite properties that are more isotropic. Figure 1.13 represents these different fiber configurations.

Regarding the composite manufacturing, conventional petrosourced composite matrices are often used, however, ecofriendly and bio-sourced matrices have also been developed [Yi 18, Pourchet 19, Ruiz 20]. Compression or injection molding can be used depending on the application. The resulting composite material can then be integrated into further assemblies and ultimately into a final product.

End of life stage. Once the composite reaches the end of its life-cycle, a few different options are available [Witik 13]. The first consists in recycling and repurposing the material. Through chemical recycling, the matrix can be dissoluted and the fibers recovered [Bensadoun 16]. However, the used chemicals, equipment and overall processing time have a negative environmental impact making it a non-attractive choice. Mechanical recycling can be performed instead. The composite is shredded into flakes that can be used in new

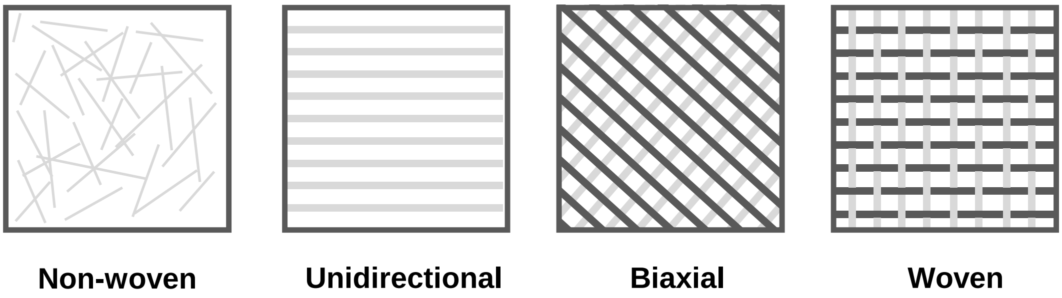

Figure 1.13: Typical fiber configurations within a composite material. Representation inspired by [Bourmaud 18].

composites. Optionally, these flakes can be turned into pellets to produce a more homogeneous product. Nonetheless, the new composites produced by these material present low mechanical properties compared to the initial, long fiber composite [Bensadoun 16]. For this reason, their use is restricted to non or semi-structural applications.

An alternative to recycling consists in the incineration of the PFCs [Mansor 19]. The energy produced by this incineration can then be exploited for other applications. Indeed, natural fibers have high calorific value and consequently their incineration results in higher energy recoveries compared to synthetic fibers. Overall, this process can have a positive environmental impact [Bensadoun 16]. A final alternative consists in a decomposition of the composite in a landfill, which can lead to some advantages compared to incineration, especially by limiting respiratory inorganics [Alves 10]. It leads however to greenhouse gas emissions due to anaerobic degradation [Mansor 19].

Depending on the initial composite material and the available means for its end of life processing, one of the presented approaches can be the best suited. To guarantee the sustainability and environmental benefits of the PFC however, its end of life processing must be planned in advance before manufacturing starts.

Applications

With the life-cycle of a PFC summarized, its potential application can be presented. To understand however, the scale of their current adoption, it is useful to compare them with their conventional, synthetic fiber counterparts.

In terms of mechanical characteristics, PFCs are generally comparable to SFCs in terms of stiffness, they are however weaker in terms of tensile and impact strength [Faruk 12, Pickering 16]. Water absorption and changes due to humidity in general are also a larger concern for PFCs [Ramesh 17, Mahmud 21]. On the other hand, the damping properties of PFCs are much higher than the ones of SFCs [Liu 21], leading to notable reduction in vibrations and noise.

These mechanical characteristics, along with the aforementioned environmental benefits have lead to the use of PFCs in a large panel of diverse sectors (automotive, construction, sports, packaging and more). Weight and noise reductions made them particularly attractive in the transport industry. The automotive industry was an early adopter of PFCs, using them for non structural applications, notably interior paneling [Mohammed 15, Adekomaya 20, Markarian 07]. Many applications in panel construction for buildings and furniture can be also be found, but also for packaging and bio-medical purposes [Mohammed 15, Mahmud 21]. The damping properties of SFCs are also used to good advantage in the fields of acoustics, with their integration in loudspeakers. It has been a common misconception that PFCs should be restricted in such non-structural or indoor applications. New applications have emerged that challenge these views. Bridges and racing boat hulls have been developed, showing that plant fiber materials can be used in challenging environments where their mechanical performance are critical [Smits 16, Collotta 16]. A panel of different PFC applications is given in Figure 1.14.

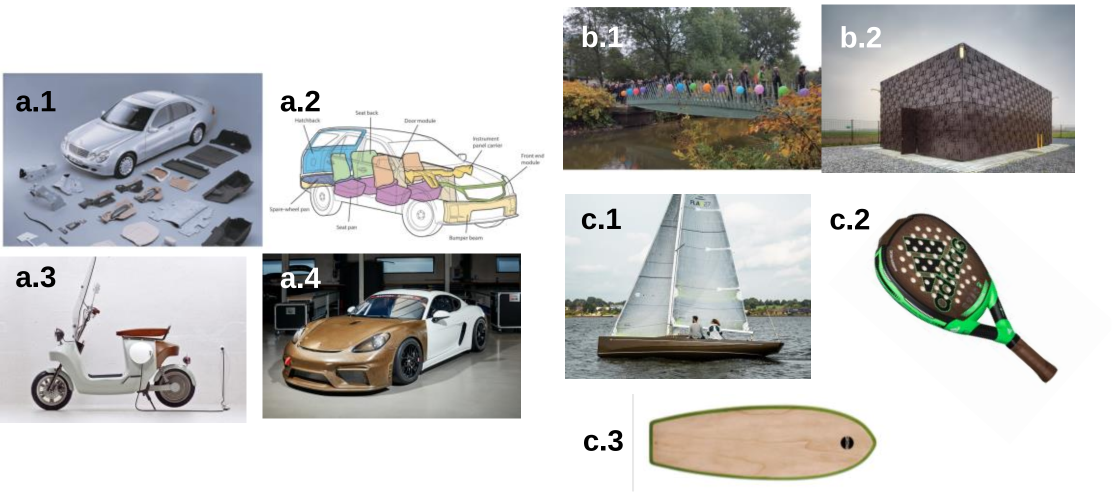

Figure 1.14: Examples of plant fiber composite use: **a)** Transportation industry, a.1, a.2 automobile components [Mohammed 15] [Markarian 07], a.3 electric scooter load-bearing structure (*NPSP*,Netherlands), a.4 sports car flax bodywork (*BCOMP*, Switzerland), **b)** Structural applications, b.1 flax composite bridge in Eindhoven [Smits 16], b.2 bio-composite facade (*NPSP*, Netherlands) **c)** Sports equipment with reinforcements from *BCOMP* (Switzerland), c.1 sailing boat (*green-boats*, Germany) , c.2 padel racket (Adidas, Germany), c.3 sustainable surfboard (*ERTHA*, Spain)

1.3 Plant fiber mechanical characterization

1.3.1 Composite characterization - the need for plant fiber properties

While plant fiber composites have found their way in various products, covering a large range of applications, their adoption is recent (15-20 years) compared to conventional fiber reinforced composites [2]. Furthermore, plant fibers show great diversity in morphology and mechanical characteristics. This diversity is a product of different parameters, notably: species, fiber-role in the plant, environmental stimuli and fiber extraction [Bourmaud 18]. For these reasons, great efforts have been made in recent years, to characterize a plethora of different PFC properties. Literature on the subject is extensive with research topics covering a wide range of mechanical, thermal, humidity and other characterizations. A summary of the properties that have been characterized, as reported in numerous reviews on PFCs is given in Table 1.1 [Ku 11, Dittenber 12, Faruk 12, Koronis 13, CW Nguong

---

[2] With the exception of some efforts during the second world war [Baley 21].

S Debnath 13, Faruk 14, Mohammed 15, Pickering 16, Ramesh 17, Sanjay 18, Gholampour 20, Chaudhary 20, Mahmud 21, Liu 21].

Test domain	**Characterization**
Mechanical	Tensile Compressive Flexural Impact Fiber/matrix adhesion Nanoindentation
Durability	Fatigue Fracture-damage Wear-tribology
Time dependent	Creep Shrinkage
Damping	Dynamic mechanical analysis (DMA) Modal analysis High frequency characterization
Thermal	Fire resistance Thermal conductivity Thermal analysis
Humidity-water absorption	Change in mechanical properties Swelling
Physical	Weight and density Porosity
Morphology	Optical microscopy Scanning electron microscopy X-ray microtomography Atomic force microscopy
Spectography	Fourier transform infrared spectroscopy

Table 1.1: Plant fiber composite characterization, overview of different tests found in the literature.

This extensive testing offers great insight into PFC behavior and quantifies their performance under different environmental and mechanical stimuli. However, when performing tests at the composite scale, the characterized properties are a result of complex interactions between a great number of parameters. The composite's matrix and reinforcements, their interactions but also the impact of environmental and manufacturing parameters, will all influence the composite's final properties. The convolution of all these parameters, represent a significant challenge in the design of PFCs and the modeling of their mechanical behavior. In order to face this complexity and better understand and predict composite behavior, characterizing the properties or studying the influence of each of these elements separately is important. Compared to tests on composites where a great number of parameters can influence the results, direct characterization of separate elements can also significantly reduce measurement uncertainties on a given property.

A first step in this characterization process, lies in the separate study of the composite's constituents: the matrix and the fibers. The mechanical properties of the fiber reinforcements are particularly crucial, since they carry the structural loads and are thus mainly responsible for the composite's stiffness and strength [Pereira 14]. For this reason, the characterization of plant fiber mechanical properties is of major importance. Knowledge of fiber properties under different type of solicitation can feed models that predict the final composite properties. Characterization at the fiber scale can also significantly contribute in the optimization of the plant fiber production chain. Comparison between plant species and varieties, retting and extraction procedures, and more can be made to identify the best practices to obtain high quality fibers.

1.3.2 Plant fiber properties characterization - overview and multiscale aspect

The characterization of plant fiber properties can be performed with different approaches, direct or indirect, using tests at different scales. This section presents an overview of these approaches. While less extensive than work on PFC characterization, many methods have been developed and many characterization efforts have been made. They can generally be divided into two main categories: tests on composites and tests on plant tissues.

Composite tests. Performing tests at the composite scale is a common approach to estimate the properties of the plant fiber reinforcements by inverse method through the so called "back-calculation" [Baley 06, Madsen 09, Shah 12, Shah 13, Pisupati 19, Prapavesis 20, Gabrion 22]. The Rule Of Mixtures (ROM) is used for this purpose: a weighted mean formulation used to predict the properties of a composite material from the properties of their matrix and reinforcements. This method has the advantage of employing experimental procedures that are typical in material characterization and rather easy to implement for composites while offering fiber material properties that are averaged over a large number of fibers, contained within the composite. Nevertheless, it also presents a series of limitations that become more important in the case of plant fibers, as thoroughly discussed by [Shah 16]. Notably, fibers are considered as uniformally distributed, perfectly separated and aligned, with the identical cross sections and areas. Furthermore, adhesion with the matrix is considered to be perfect and fibers are considered to only deform elastically. This leads to important difference between back-calculated and direct measurements [Oksman 02, Virk 12, Charlet 10c, Shah 16].

Plant tissue tests. Performing tests on plant tissues is a more direct approach to characterize plant fiber properties. Due to the multilevel structure of plants, these tests can be performed at different scales, notably at the plant stem, fiber bundle, elementary fiber or cell wall scale. The relevance and state of the art for each of these scales has been extensively covered by [Bourmaud 18]. A brief discussion is proposed here.

Testing plant stems is not widespread, but is generally employed to study plant structure and stability for various species and growing parameters [Schulgasser 92, Jaouen 07, Robertson 15]. These tests can also be used to estimate an average elementary fiber stiffness, calculated over the large number of fibers contained within the stem, providing that the fiber volume fraction is predetermined from morphological analysis [Bourmaud 15, Gibaud 15, Bourmaud 16a]. The larger size of plant stems (many *cm* in length, a few *mm* in diameter) also makes these tests easier. Nevertheless, they only provide an indirect estimation of elementary fiber properties since similarly to the Rule Of Mixtures

(ROM) method at the composite scale, the complexity of the different stem components and their interactions are not considered.

On a very smaller scale, tests at the scale of the cell wall have also been performed. Nanoindentation is the most common approach and allows the characterization of the stiffness and hardness of the fiber cell walls. Tests on flax [Alix 12, Bourmaud 12, Liu 22], hemp [Bourmaud 09], wood [Gindl 04] and bamboo [Zou 09] cell walls have been performed. Atomic Force Microscopy (AFM) has also been used to map the surface of the cell walls but also determine its local elastic properties through the resonance of the cantilever [Rabe 96, Yamanaka 96]. Various plants have been studied this way [Clair 03, Ren 15, Czibula 19, Melelli 20a]. These approaches allow to measure fiber properties very locally, eliminating issues related to the complex shape of elementary fibers, while also bringing to light complex micro-structural related behavior. However, in order to perform these characterizations, the fiber has to be embedded in a thermoset resin, the surface quality of which has a major impact on the results [Eder 13].

While the aforementioned approaches are essential and complementary to better understand the intricacies and structural complexity of plants and their fibers, they only give approximations of the PFC's basic unit: the elementary fiber or the fiber bundle. Indeed, depending on the plant species, retting level and extraction process, fibers are separated to various levels and are present in the form of bundles or elementary fibers in the composite. Characterizing at that scale is thus key in modeling and predicting PFC behavior.

Characterizing at the elementary fiber or fiber bundle scale, does come however with a set of challenges. In particular, their small size along with their complex morphology and composition can make their manipulation and characterization difficult. The state of the art on characterization at the fiber and bundle scale will be presented in the next section along with a detailed discussion regarding characterization challenges.

An overview of the different scales at which plant fiber mechanical properties can be estimated or directly characterized is given in Table 1.2, along with their advantages and disadvantages.

Material	**Testing scale**		**Advantages**	**Disadvantages**
Composite	Full scale - IFBT	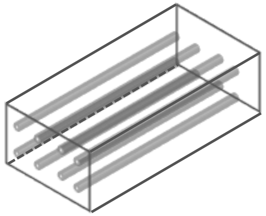	• Common and normalized tests. • Larger object size. • Averaging on large number of fibers.	• ROM simplifying hypotheses. • Measurement uncertainties.
Plant	Stem	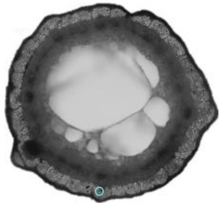	• Plant stability and structure evaluation. • Larger object size. • Averaging on large number of fibers.	• Rough estimation. • Need for fiber volume fraction.
	Bundle	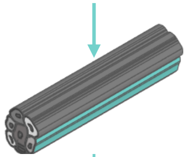	• Present in composite. • Estimation of inter-fiber properties.	• Complex morphology and structure. • Low amount of tested samples.
	Elementary fiber	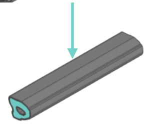	• Composite basic reinforcement unit.	• Small size. • Complex morphology. • Low amount of tested samples.
	Cell wall	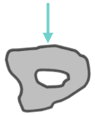	• Limited influence of fiber morphology. • Reveals fiber micro-structural properties.	• Requires resin embedding. • Sensitivity to surface preparation. • Extremely localized measurements. • Not representative of composite reinforcement unit.

Table 1.2: Different approaches used in the determination of plant fiber properties (inspired by [Bourmaud 18]). Stem microscopy image taken from [Bourmaud 16a] (the cross section of a flax stem is represented).

1.3.3 Elementary fiber/fiber bundle characterization - state of the art and challenges

Elementary fiber characterization

Tensile tests. Among the mechanical characterization tests performed at the elementary fiber scale, tensile tests are the most popular. Fibers are generally highly anisotropic materials with their longitudinal stiffness and strength being significantly higher than their transverse counterparts. Through the orientation of the fibers within the composite, this high longitudinal fiber performance can be put to good use. Indeed, the longitudinal stiffness of plant fibers is the main parameter influencing the composite's longitudinal performance [Bourmaud 16b].

To characterize these longitudinal properties, numerous tensile tests have been performed for the bast fibers of main interest in this work: flax [Davies 98, Andersons 05, Aslan 11, Charlet 09, Bos 02, Baley 02, Baley 14, Lefeuvre 14b, Melelli 22, Richely 22b, Nuez 22], hemp [Cisse 15, Duval 11, Guicheret-Retel 15, Pickering 07, Fuentes 19, Placet 12a, Placet 12b, Placet 14] and nettle [Davies 98, Bodros 08, Lanzilao 16, Jeannin 20]. Various other fibers such as wood [Page 71, Burgert 03, Zhang 13] but also bamboo, kenaf, jute and others have been tested as well [Defoirdt 10, Hu 10, Yu 11, Wang 11, Ren 14, Bachtiar 10]. An overview of the range of flax, hemp and nettle tensile properties interest, is given in Table 1.3. A higher variability in the results compared to synthetic fibers can be seen, related to the fiber's natural morphological and composition variability along with the influence of external natural and man-made stimuli.

	Diameter (μm)	Young's modulus (GPa)	Strength at break (MPa)	Strain at break (%)
Flax	12.4-23.9	37-75	595-1510	1.6-3.6
Hemp	10.9-42.0	14-44	285-889	0.9-3.3
Nettle	19.9-35.4	36-79	771-2196	1.3-2.8

Table 1.3: Overview of the range of bast fiber tensile properties. Values taken from: [Bourmaud 18] for flax and hemp, [Jeannin 20] for nettle.

In addition to the characterization of tensile stiffness and strength, many other studies have focused on the influence of additional parameters such as: damage propagation [Beaugrand 15, Beaugrand 17, Guessasma 19], influence of humidity [Davies 98, Placet 12a, Guicheret-Retel 15, Nuez 22], creep behavior [Cisse 15, Guicheret-Retel 15], free fiber rotation [Placet 12a], influence of morphology and defects [Fuentes 19, Richely 21b, Richely 22b, Placet 12b], drought impact [Melelli 22], and more.

Even though the tensile test is a common characterization procedure, its commonly perceived simplicity does not translate to tests at the elementary fiber scale. The complex fiber morphology and microstructure often lead to important non-linear behaviors, that will be discussed later.

Micro-bond test. Another critical parameter in the performance of composite materials is the adhesion between the fiber and the matrix. This adhesion is often tested at the elementary fiber scale through pull-out tests. Through these tests the InterFacial

Shear Strength (IFSS) of the fiber-resin interface can be determined. The pull-out test consists in the extraction of a single fiber from a mass of resin [Teklal 18]. The microbond or microdroplet test is a common variation of the pullout test where droplet of resin is embedded on the fiber [Sockalingam 12]. The fiber is then pulled between two loading blades that come in contact with the droplet, eventually separating it from the fiber. A graphical configuration of these tests is given in Figure 1.15.

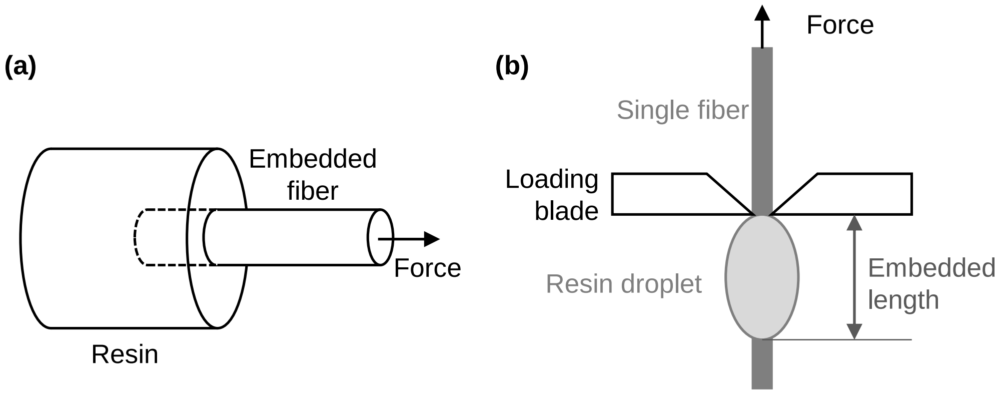

Figure 1.15: Schematic of single fiber/matrix adhesion tests: (a) pullout test, (b) microbond-microdroplet test. Schematic adapted from [Teklal 18, Sockalingam 12].

Such tests have been performed quite extensively on a variety of elementary plant fibers and polymer matrices. The interfacial shear strength of flax [Stamboulis 99, Lee 03, Wong 07, Graupner 14, Kandemir 20] and hemp [Islam 08, Islam 10, Sawpan 10] have notably been studied along with many other fibers such as sisal, kenaf, jute, coir and others [Prasad 83, Graupner 14, Li 17, Ali Zernadji 22].

Other tests. Other methods of mechanical testing on elementary plant fibers are very rare. Bos et al. used an elastic loop test to evaluate the compressive strength of flax, its configuration can be seen in Figure 1.16 [Bos 02]. As the loop gets tightened non-linear deformations are generated and kink bands appear at the top of the loop. It is at this point that a compressive strength is evaluated. While this approach is quite robust for geometrically uniform synthetic fibers, in the case of plant fibers it can be difficult to discern between pre-existing and loop generated kink bands. A more reliable method to characterize the transverse properties of fibers is the Single Fiber Transverse Compression Test (SFTCT), which will be extensively presented and discussed in subsection 1.4.2.

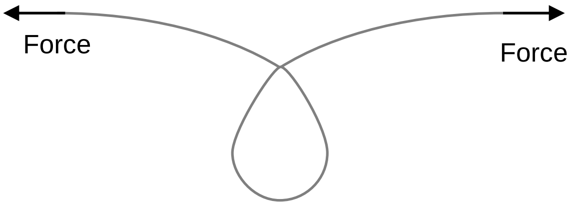

Figure 1.16: Fiber loop test configuration.

Various other characterization on fibers can be found in the literature however, they have only been performed on synthetic fibers. Light diffraction [Wiecek 14], ultrasound spectroscopy [Mounier 14], Brillouin spectroscopy [Elsayad 20] and modal analysis [Perrin 07, Rice 14] have all been used to characterize fiber mechanical properties. Studies on the contact and friction between different fibers can also be found in the literature [Grandgeorge 21, Saketi 14b].

Fiber bundle characterization

Plant fiber characterization at the bundle scale is a common practice in the industry to evaluate the fiber quality after the extraction process [Bourmaud 18]. Bundle properties are a product of the properties of the individual elementary fibers that comprise them and those of the lamellae that connect them. Therefore, they do not represent a direct way to evaluate the properties of the elementary fibers. Tests on fiber bundles provide however, an indirect method to them that is easier to employ, due to their larger size of fiber bundles.

Similarly to elementary fiber characterization, many characterization works can be found, they are however primarily focused on tensile testing. The doctoral thesis of Komlavi Gogoli is a major contribution to the characterization of flax bundles, studying their viscoelastic properties and strength through tensile and relaxation tests [Gogoli 22]. A large focus on the measurement of the bundle's cross sectional area is also found in this work. Romhany et al. identified the main failure mechanisms of a bundle consisting of axial splitting between elementary fibers, followed by transverse cracking of the bundle and progressive failure of the elementary fibers [Romhány 03]. Acoustic emission and X-ray microtomography have also been used to further investigate these failure mechanisms [Barbulée 14, Beaugrand 17], while Xue et al. investigated the influence of the temperature and loading rate [Xue 09]. Finally, Haag and Mussig showed the major influence of the cross sectional area measurements on the determined tensile properties of fiber bundles [Haag 16].

The work of Charlet and Béakou represent an original approach [Charlet 11a]. Through the tensile test of a particular two elementary fiber configuration, illustrated in Figure 1.17, the interfacial strength of the middle lamella was characterized. The interfacial strength between elementary fibers within a bundle was shown to be significantly lower, than the one between an elementary fiber and a typical thermoplastic matrix [Charlet 11a].

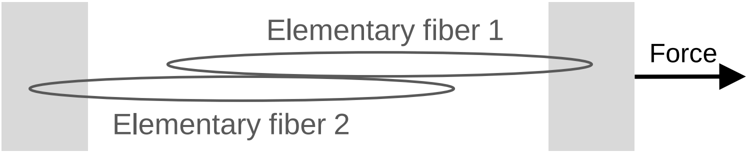

Figure 1.17: Tensile test configuration to determine the interface shearing between elementary plant fibers. Adapted from [Charlet 11b].

Characterization challenges

While many fiber-scale characterization efforts have been performed, many challenges can make the testing, or the post-treatment of the results, difficult compared to conventional materials.

Fiber structure As discussed in subsection 1.3.2 plant fibers are complex, multi-layered, composite structures. This structural complexity is reflected in their material behavior. This is well illustrated by the tensile behavior of plant fibers. Figure 1.18 shows different stress-strain responses obtained on tests on elementary hemp fibers. While fiber typical linear-elastic behavior can be obtained (type 1), significant non-linearity is often observed. This non-linearity can be a result of inelastic behavior (type 2) or more complex phenomena leading to softening and stiffening mechanisms (type 3). In the case of tensile tests, cellulose microfibril reorientation, strain induced crystallization, slip-slick mechanisms and the presence of defects all have a potential influence of fiber behavior [Placet 14, Trivaudey 15, Nuez 22, Richely 22b]. To conclude, elementary plant fiber behavior is often complex, knowledge of the intricacies of their structure and composition is thus critical in designing experiments and correctly analyzing their results.

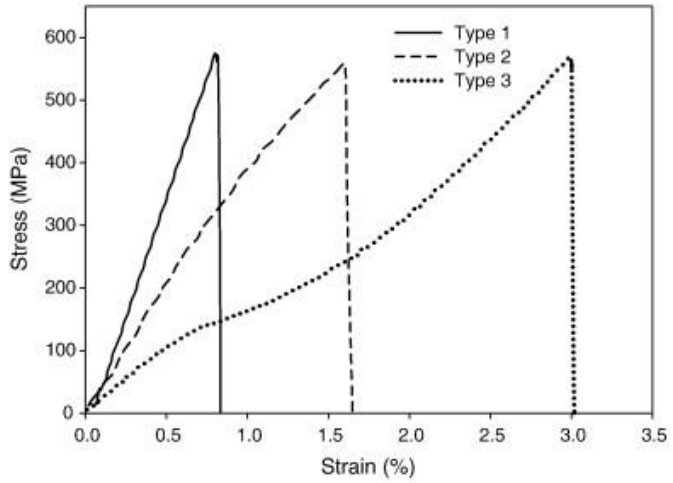

Figure 1.18: Hemp elementary fiber tensile test - types of observed behavior [Duval 11].

Fiber morphology Material characterization often requires geometric considerations such as length, diameter and cross section. The measurement of these geometric properties can have an important impact on the final characterization results [Placet 12b, Lefeuvre 14a, Haag 16]. For instance, measurement of the fiber's Cross Sectional Area (CSA) in particular, is of critical importance in tensile testing.

Many methods exist to characterize fiber morphological characteristics. These methods can be divided into three main categories: (i) fiber transverse cross section measurements, (ii) fiber longitudinal cross section measurements, (iii) volume measurement through microtomography. Their main advantages and disadvantages are given in Table 1.4. Some morphological characterization approaches are also shown in Figure 1.19.

Transverse cross section measurements are usually made on stem cross sections allowing the measurement of multiple fibers at once. Surface preparations and careful

Fiber observation	**Method**	**Advantages**	**Disadvantages**
Transverse section	Optical microscopy, SEM coupled with image processing	Accurate measurements	Single position along fiber length, surface preparation
Longitudinal section	Optical microscopy, Fraunhofer diffraction, shadowgraphy	Multiple measurements along length and perimeter	Apparent diameter
Volume	Microtomography	Accurate, complete fiber reconstruction	Expensive, time consuming

Table 1.4: Overview of fiber morphological characterization methods.

microscope configuration is needed to obtain good quality results. Authors can then use the available tools of microscopy software [Thomason 11, Marrot 13] or custom methods [Nitta 13, Mattrand 14, Del Masto 17] to calculate the surface area of a fiber or bundle. Fiber complexity can be characterized through various geometric indicators such as circularity, convexity, tortuosity or the ratio of area to perimeter [Legland 13, Mattrand 14, Marrot 13]. The fiber geometry can also be assimilated to simpler, circular elliptical or polygonal geometries [Nitta 13]. While these methods can give very accurate measurements at a given point along the fiber length, fiber cell wall and lumen geometry can change significantly along the fiber's length [Charlet 07, Charlet 10b]. Errors can thus occur if these local measurements are extrapolated to characterize the fiber length in its entirety.

Longitudinal cross section measurements rely on measuring the apparent diameter at a given position. The fiber can be rotated to obtain multiple measurements of apparent diameter. Depending on the the geometric assumptions made on the fiber's transverse cross section (circular, elliptical, polygonal) these diameters measurements can be averaged differently. To obtain, these measurements, multiple methods can be used. such as conventional microscopic observations [Charlet 07, Ilczyszyn 12]. Fiber diameter can also be measured by projecting a laser onto it and measuring the width of the diffraction pattern [Gogoli 21] or the width of the fiber's projected shadow [Bourmaud 17, Garat 18, Garat 20]. These methods allow to make multiple measurement along the fiber's length, however concave regions or lumen size cannot be measured leading to potential errors.

Microtomography allows a complete characterization of the fiber's geometry. The lumen and complex contour can be reconstructed with sub micrometer accuracy over a length that typically stays under a centimeter [Richely 22b]. Longer lengths can lead to movements of the fiber's edge during measurements. While microtomography results are unmatched in terms of accuracy they represent an expensive and time consuming method of morphology characterization. Its wide-scale in experimental campaign is thus difficult.

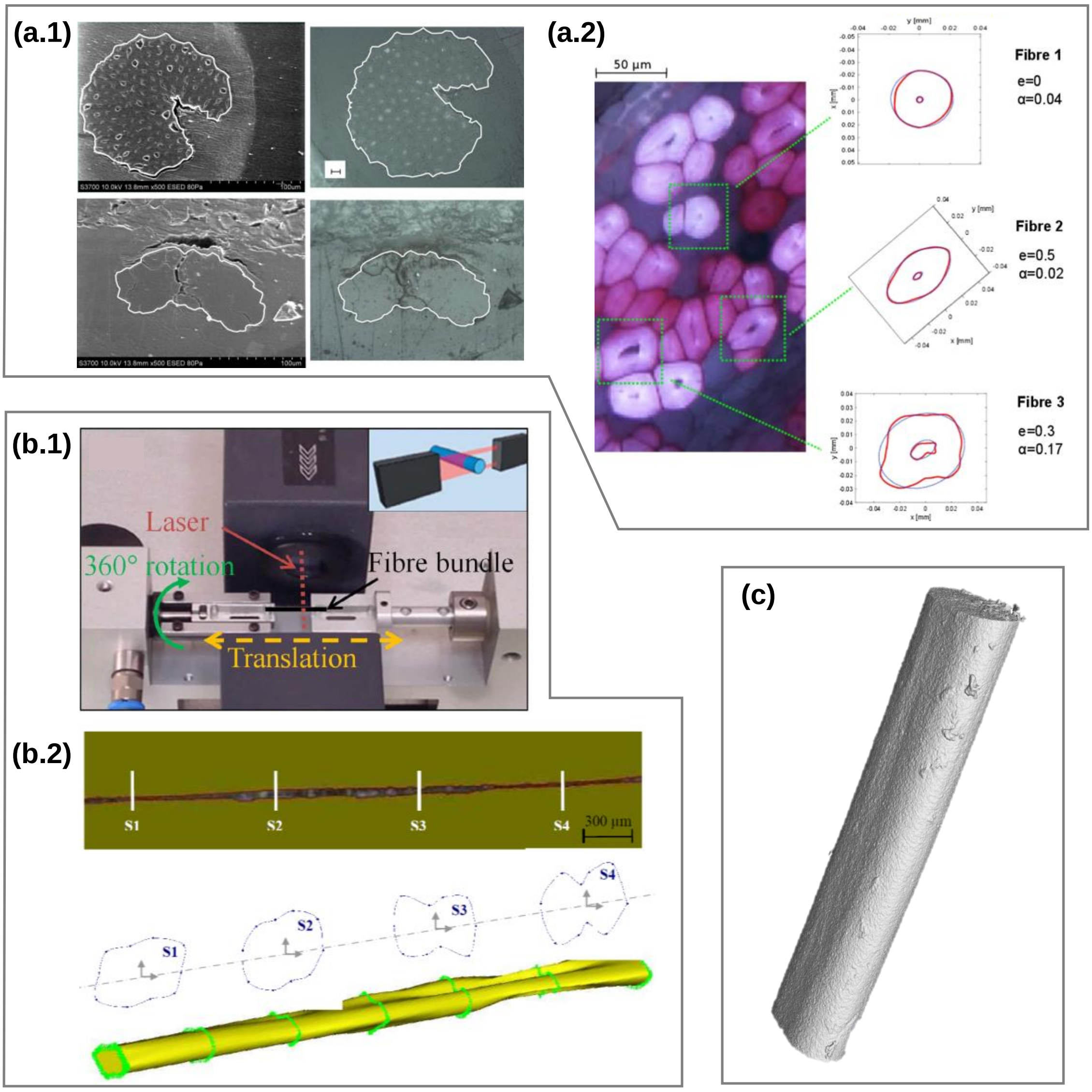

Figure 1.19: Examples of plant fiber morphological characterization: **(a)** Transverse section measurements: (a.1) fiber bundles [Thomason 11],(a.2) elementary fibers [Del Masto 17]. **(b)** longitudinal section measurements: (b.1) shadowgraphy measurement device [Garat 18], (b.2) fiber geometry reconstruction from microscopy images [Ilczyszyn 12]. **c** reconstructed geometry of horse hair from microtomography measurements (performed at *FEMTO-ST-MYPHISTO*).

Fiber size. The small size of elementary fibers or fiber bundles also represents a significant challenge in their characterization. Elementary bast fibers have diameters that typically vary between 10 and 40 μm, while their length does not exceed a few cm. Their length is thus significantly larger than their diameter, while micrometric or submicrometric details such as the lumen and the MicroFibrilar Angle (MFA) are also present. This large difference in scale between the various plant fibers morphological features adds, to their characterization complexity. Bundles size can vary significantly according to the number of fibers they contain, but they are generally a few hundreds of μm in diameter a few cm in length. Accurate measurement and actuation tools are required to perform tests at this scale. However, while the physical quantities measured at this scale can be many order of magnitude higher than the ones measured at the cell wall scale, through nanoindentation or AFM, few standardized equipments exist to measure them.

An additional challenge lies in fiber and bundle preparation and manipulation. Samples must be separated and prepared individually, a time consuming and delicate operation. For this reason, only a limited number of samples is tested at that scale. Furthermore, the small size of fibers means that they can be damaged more easily when manipulated in preparation for testing. Such defects can have an important impact on the measured properties, for this reason special attention and delicate manipulation is needed. Additionally, more fragile fibers that might be visibly damaged during preparation might be discarded and not tested, adding a survival bias to the properties of more robust fibers that make it through testing.

Preloading stage. During mechanical testing, a preloading stage typically occurs where the object gradually gets in the desired loading regime. Examples of preloading can be found in the tension of previously slacked fiber or in the rotation and sliding of a fiber when compressed. The irregular geometry of plant fibers can increase the magnitude of these motions while their small size can make the determination of the end of the preloading stage through visual observation or sensor measurements difficult. Furthermore, plant fiber testing lacks the normalization that can found for other types of tests, meaning that each researcher might adopt different approaches to treat this preloading stage.

System compliance. System compliance is a typical problem in mechanical testing. During testing the experimental setup itself might respond to the applied loads, affecting measurements. For this reason, system compliance is typically characterized separately and subtracted from the measurements performed on the object of interest. Minimizing it however, to a few orders of magnitude lower than the one of the tested object is always preferred. Considering the small size of plant fibers however, achieving this can be very challenging.

Environmental conditions. Plant fibers are known to be sensitive to the environmental conditions and especially to the Relative Humidity (RH). Variations in RH results in changes both in fiber geometry, through hygroscopic swelling [Garat 20, le Duigou 17], and in fiber material properties [Kersavage 73, Stamboulis 01, Sala 22]. Controlling the relative humidity in which fiber testing is performed is thus an additional challenge in their characterization.

Property variability. The biological nature of plant fibers along with their actively changing environment and the various steps required in their extraction, leads to a greater variability in their properties compared to their synthetic counterparts. For this reason, a large amount of tested fibers is necessary in order for their measured properties to be statistically representative [Joannès 20]. This large amount of tests comes at the expanse of increased manual labor or the need for an automation of the testing procedure, a difficult endeavor considering all the aforementioned challenges.

1.4 Plant fiber characterization - new horizons

The previous sections highlighted the benefits of PFCs and the need for the characterization of their basic reinforcement unit, the elementary fiber and the fiber bundle. However, while characterization at the composite scale has been extensive, the same cannot be said for the direct characterization of these objects, where few types of tests, mainly tensile, have been performed due to a series of inherent challenges. Several research directions could be followed to better understand plant fiber behavior and quantify their mechanical properties. Nevertheless, in order to accelerate the adoption of these environmentally friendly materialsW, the fiber properties that are critical to the design and performance of the composites should be identified and characterized first. New approaches and testing methods are highly relevant in these characterization efforts.

1.4.1 Finite element analysis - insights into natural complexity

The intrinsic complex structure and morphology of plant fibers can induce responses under mechanical loading, that are not accounted for in conventional analytical models. Observing and studying *in situ* the mechanisms that are responsible for this complex behavior is not always an option given the small size of plant fibers and wide scale of morphological features, or the volume of the platforms used to test them. For this reason Finite Element Analysis (FEA) can be used in addition to experimental approaches, to reveal and quantify the influence of these complex mechanisms on fiber behavior. Through FEA, the influence of a single parameter can be isolated and its influence can be studied independently. Numerous parameters can also be modeled together, in order to reproduce experimental behavior and help identify fiber material properties.

A significant amount of FEA studies on plant fibers can be found in the literature, mainly on flax and hemp. In their doctoral thesis Del Masto and Richely have performed an extensive overview of the literature on the subject [Del Masto 18, Richely 21a]. Based on these works, an updated table with plant fiber finite element models is given in Table 1.5. A brief overview is also given below.

Elementary fibers are primarily studied with work on bundles being less common [Beakou 13]. Fibers are usually modeled as purely elastic, however viscoelastic [Del Masto 17, Del Masto 19], elastoplastic [Nilsson 07] and damage models [Beaugrand 15, Guessasma 19] can also be found. Regarding fiber morphology, monolayer tubes are the most common modeling choice, with the modeling of numerous layers with different properties (to simulate the different cell wall layers) being rare [Gassan 01, Thuault 14]. Fiber cross sections are generally approximated to circular, nevertheless, elliptical [Gassan 01, Del Masto 17] or hexagonal [Beakou 13] approximations have also been used. Complete fiber geometry reconstructions from microtomography have also been used in finite element models [Beaugrand 15, Guessasma 19, Richely 22a]. Finally, regarding microstructural elements, the influence of the lumen size [Richely 22b] and the MFA [Thuault 14, Del Masto 17, Richely 22b] has been studied numerically.

Reference	**Fiber type**	**Fiber scale**	**Behavior**	**Geometry**	**Parameters**
[Gassan 01]	Plant	Elementary	Elastic	Laminated structure or thick elliptical tube	MFA, cellulose content, ellipticity, lumen
[Nilsson 07]	Flax-hemp	Elementary	Elastoplastic	Monolayer tube	Dislocations
[Roudier 12]	Flax	Elementary	Elastic	Monolayer tube	Relative humidity
[Beakou 13]	Flax	Bundle	Elastic, bilinear cohesive zone	Hexagonal fibers with no lumen, staggered arrangement into bundle	Middle lamella, gauge length
[Thuault 14]	Flax	Elementary	Elastic	Multilayer tube	MFA, cell width and composition
[Beaugrand 15]	Hemp	Elementary-bundle	Elastic-damage	Optical microscopy and microtomography reconstruction	Notch shape
[Del Masto 17]	Hemp	Elementary	Viscoelastic	Monolayer tube	Degree of ellipticity, MFA
[Del Masto 19]	Flax-hemp	Elementary	Viscoelastic-failure	Monolayer tube	26 parameters (ultrastructural, morphological…)
[Guessasma 19]	Hemp	Elementary-bundle	Damage	Microtomography reconstruction	Notch shape, stress criteria
[Richely 22b]	Flax	Elementary	Elastic	Monolayer tube	Lumen, MFA, fibril realignment
[Richely 22a]	Flax	Elementary	Elastic	Microtomography reconstruction	Porosity, irregularities

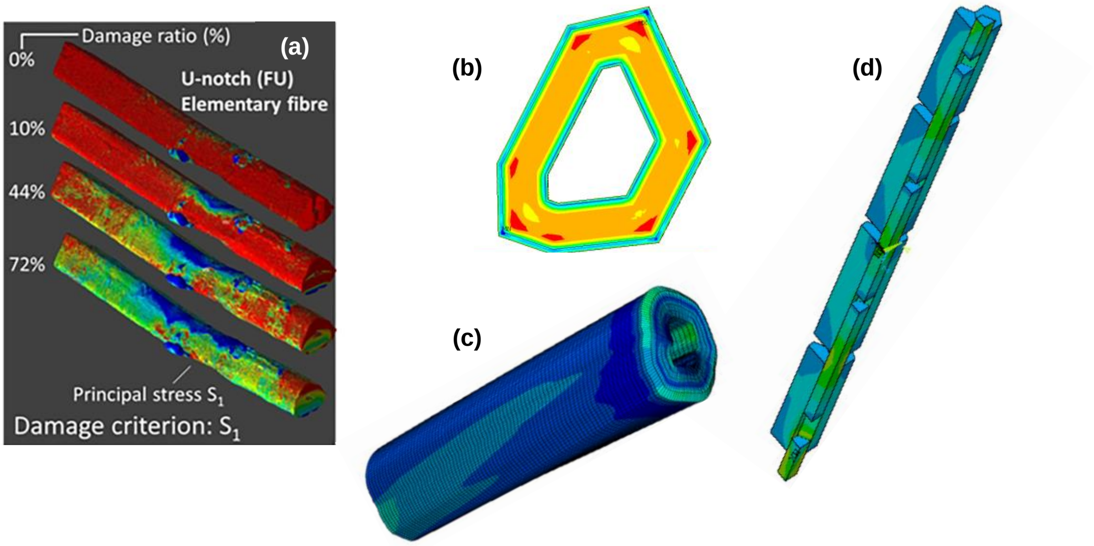

Table 1.5: Overview of finite element analysis studies on plant fibers. Table adapted and expanded based on [Del Masto 18, Richely 21a]. (a) damage simulation on reconstructed 3D geometry [Guessasma 19], (b) multilayered simplified geometry simulation [Roudier 12], (c) complex 3D geometry simulation [Del Masto 17], (d) fiber bundle simulation (hexagonal fibers with symmetry conditions) [Beakou 13].

The presented studies all focus on tensile testing. In order to reproduce and study the complexity of plant fiber tensile behavior (see Figure 1.18), many modeling challenges were overcome, complex multilayered geometries, plant fiber microstructure and different behavior laws were used. The boundary conditions of tensile testing remain however, relatively simple. Modeling tests that include contact or adhesion between surfaces, such as compression and microbond testing, coupled with plant fiber complexity, represent a significant modeling challenge. For this reason literature on other types of tests is scarce. Therefore, in a similar way to experimental research, new mechanical tests should be modeled to expand knowledge on plant fiber behavior and properties.

1.4.2 Elementary fiber transverse properties - single fiber transverse compression test

Elementary fiber transverse properties

While the fiber tensile properties play a major role in the composite's final properties, the fiber's transverse properties can have a major impact on composite performance. Indeed the composite's fiber reinforcements can experience stresses during multiple steps in their lifecycle.

During fiber extraction, stems are fed through multiple rollers. Important compression forces can thus be applied during this step. During composite manufacturing, injection or compression, the fibers also experience important compression stresses in their transverse direction. Finally, during the composite's use, transverse stresses will generally occur. Bending is a typical example where part of the fibers will be compressed. For composites under transverse compression or for tensile tests perpendicular to the direction of the fiber, the fiber transverse properties will be the main element that dictate composite behavior.

Characterizing plant fiber transverse behavior is thus critical to predict and evaluate composite behavior. Plant fiber transverse properties have been characterized before, albeit indirectly, showing a high anisotropic nature. Baley et al. back calculated the transverse properties of flax through tests on composites, while other authors performed nanoindentation on fibers embedded in resin [Gindl 08, Bourmaud 09, Khaldi 16]. Transverse loop tests were also used in the case of flax to evaluate its compressive strength [Bos 02]. Transverse compression however (also called diametral compression) allows a direct characterization of fiber transverse properties, which is expected to be more reliable.

Single Fiber Transverse Compression Test (SFTCT)

The test's basic principle lies in the compression of an object between two rigid and parallel platens across its transverse cross section. General applications and the Single Fiber Transverse Compression Test (SFTCT) are discussed next.

Transverse compression - a wide scale matter Transverse compression tests have been performed across a wide range of objects of different scales. One of its earliest iterations can be found in the "Brazilian test". The test was first developed to indirectly determine the tensile strength of concrete by compressing large disks of the material [Carneiro 43, Azakawa 43]. The test has also been used to study the compressive behavior of ceramics [Shetty 86] and mechanical components such as rollers and bearings [Foppl 07, Lundberg 49]. The compressive strength of geometrically complex objects has also been performed on objects such as rocks [Andreev 91, Li 13], bones [Womack 08] or different fruits and vegetables such a as corn [Sherif 76, Anazodo 81, Rabelo 01, Solomon 02]. Compression at much smaller scales has also been performed, with rice [Kamst 99] or gravel [Cavarretta 12] or even micrometric [Kozhar 15] or submicrometric [Yoshida 05, Mook 07] particles by adapting nanoindendation machines. Finally the transverse compression of fibers has also been studied through the Single Fiber Transverse Compression Test (SFTCT).

SFTCT history and overview The Single Fiber Transverse Compression Test (SFTCT) is the established method to study the transverse material behavior of a fiber, with a main focus being made on the identification of its transverse elastic properties. In its typical configuration the fiber is positioned on a fixed platen. A mobile platen gets in contact with the fiber and starts compressing it as illustrated in Figure 1.20.

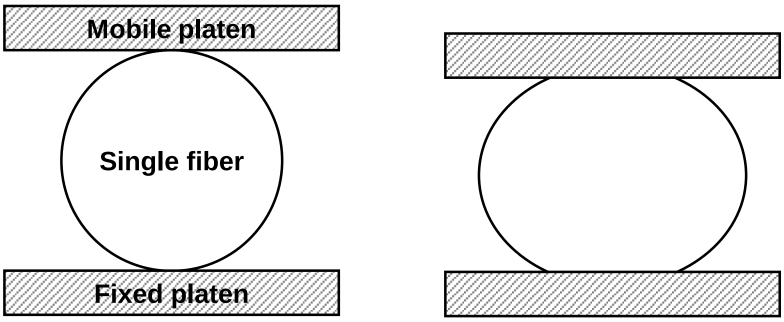

Figure 1.20: SFTCT basic principle with the fiber in an undeformed and deformed state.

Despite its simple principle, SFTCTs can be challenging tests for a variety of reasons. First, even for a purely elastic material, a non-linear stress-strain (or force-displacement) fiber response is produced during compression, due to the progressive increase in contact surface during the test. This means that direct measurements of the transverse elastic modulus E_T are not possible, contrary to the measurement of the longitudinal modulus E_L in tensile tests through stress-strain measurements. Instead, analytical models are used that predict the behavior of the fiber, by assimilating it to a purely elastic cylinder under compression. Through these models, E_T can then be identified by inverse method. Furthermore, the response of the fiber is very sensitive to the contact area, meaning that changes in the test's geometry, caused by changes in fiber and platen morphology or alignment can have a major impact on experimental results. Finally, great measurement accuracy is needed to obtain exploitable results. Compressing a plant fiber of 10 to 40 μm in diameter, in its elastic regime in order to identify E_T generally leads to very small values of displacement ($\leq 1\,\mu m$) and force ($\leq 100\,mN$).

An overview of the literature on the SFTCT, its history and major breakthroughs is given in Table 1.6. A more detailed discussion is given below.

The beginning of SFTCTs can be traced back to the 1960's and 70's. Many analytical models were also developed during that time, based on Hertzian contact formulations [Hertz 96]. A detailed analysis of these analytical models will be made in Chapter 2. Experimentally, during this period the first tests were performed on polymer fibers such as nylon and polyethylene. Generally, weights were used to compress the fibers and microscopes to observe their displacement. Hadley and Pinnock were the first to perform

Year	References	Year	References
1965	[Hadley 65]	2000	[Singletary 00a, Singletary 00b]
1966	[Pinnock 66]	2004	[Cheng 04, Cheng 05]
1968	[Morris 68]	2007	[Stamoulis 07]
1974	[Phoenix 74]	2010	[Lim 10]
1978	[Jawad 78]	2013	[Mikczinski 13]
1990	[Kawabata 90]	2016	a. [Wollbrett-Blitz 16], b. [Sockalingam 16], c. [Guo 16]
1994	[Kotani 94]	2017	a. [Naito 17], b. [McDaniel 17]
1997	[Jones 97]		

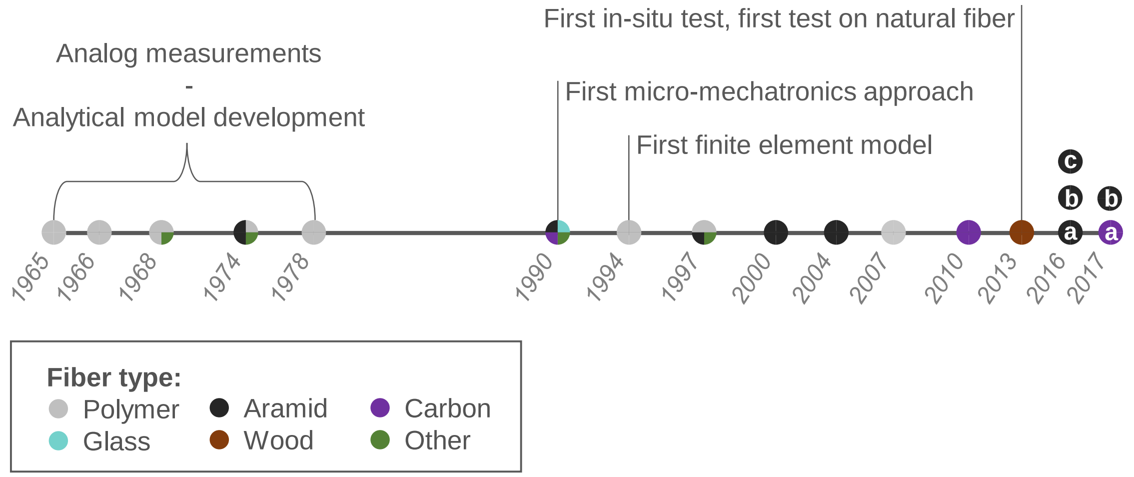

Table 1.6: SFTCT history overview and main milestones.

these tests [Hadley 65, Pinnock 66]. Phoenix et al. were the first to test the stiffer Kevlar® fibers, a challenging material due to smaller displacements of the fiber during testing compared to the more compliant polymer fibers [Phoenix 74]. The improvement of actuators and sensors brought upon micro-mechatronic approaches, with Kawabata being the earliest example [Kawabata 90]. Measurement precision increased significantly, making the testing of very stiff fibers such as carbon possible. Tests on Kevlar® and other aramid fibers became more wide-spread for their ballistic applications. An overview of the experimental methods used to performs SFTCTs is presented in Chapter 3.

In addition to determining the transverse elastic modulus of various fibers, these studies also highlighted or investigated complex structural and material behaviors. Regarding structural effects, the influence of a skin-core structure [Singletary 00b, Wollbrett-Blitz 16] or fiber microstructure [McDaniel 17, Naito 17] have been studied. Fiber inelastic phenomena have also been shown for various fibers through repeated or progressive loading-unloading cycles [Kawabata 90, Cheng 04, Mikczinski 13, Lim 10, Wollbrett-Blitz 16, Sockalingam 16, McDaniel 17]. A few authors have also identified fiber transverse yield and strength [Phoenix 74, Kawabata 90, Jones 97, Singletary 00a, Wollbrett-Blitz 16, Naito 17]. Finite element models of the test have also been created to better understand fiber plastic behavior or to identify plastic parameters by comparing simulation results to experimental ones [Kotani 94, Singletary 00b, Guo 16, Wollbrett-Blitz 16, Sockalingam 14, Sockalingam 16, McDaniel 17]. Finally, time dependent phenomena have also been studied through the influence on loading rate on fiber behavior [Cheng 04, Stamoulis 07, Guo 16] or through stress relaxation tests [Stamoulis 07].

Despite these various studies performed on synthetic fibers, to the authors knowledge, only a single occurrence of plant fiber SFTCTs can be found in the literature [Mikczinski 13]. An added breakthrough in this work, lies in the fact that it was performed in the chamber of SEM allowing for great sample observation during testing. Nevertheless, an important risk of damaging the fiber or altering its behavior due the vacuum inside the SEM or the electron beam, is present. Wood fiber issued from spruce and pine were tested and their compressive behavior was discussed. The focus of this study was centered on the change in cell wall properties under repeated loading, no transverse elastic modulus was identified.

Overall, literature on SFTCTs is rather limited, at least compared to the works treating fiber tensile testing. In the case of plant fibers, only the compression of a few wood fibers has been studied. Indeed, the complex morphology and composition of plant fibers presents a great challenge in the study of their transverse properties. Plant fiber morphology is far from the cylindrical hypothesis made by analytical model and lead to complex contact interactions, while their composition can lead to behaviors that cannot be described by pure elasticity. Furthermore, experimental equipments with the necessary measurement accuracy are not widely available.

1.4.3 Inter-fiber adhesion - peeling test

Fiber separation - the lack of quantitative data

The separation of plant fiber bundles into individual elementary fibers is critical for the performance of PFCs. Indeed, Charlet and Béakou showed that the interfacial strength between elementary fibers withing a bundle is significantly lower, than the one between an elementary fiber and a typical thermoplastic matrix [Charlet 11a]. By consequence, if the resin does not penetrate within the fiber bundle, the interface between elementary fibers could be a weak-spot in plant fiber composites, where fractures initiate. Mechanical testing at the composite scale have shown this to be true [Bourmaud 13a]. On the other hand, fiber separation must not come at the expense of fiber mechanical performance. Over-retting can lead to the degradation of the fiber's cellulose, significantly decreasing stiffness [Placet 17]. Excessive scutching and hackling can also lead to damaged fibers [Keller 01]. In conclusion, a fine control of the retting, scutching and hackling procedure is needed, to guarantee an optimal fiber separation while maintaining mechanical performance.

Numerous challenges however, make this endeavor difficult. Indeed, during dew retting, the fibers are exposed to the external environment. Farmers must thus closely and continuously assess the retting level through organoleptic and subjective evaluations. The color of the fibers, their uniformity, their divisibility and resistance during manual manipulations, are all means of evaluating retting level [Bourmaud 18]. Farmers might also bring a few samples to nearby scutching lines to evaluate fiber separation at a given time. These, scutching lines on the other hand, must also adjust their extraction settings to adapt to the different plant materials that are brought in. Finally, fiber variety and maturity level can also have an impact on fiber separation. The presence of lignin in particular, which varies between species and varieties and increases as the plant reaches maturity, makes fiber separation more difficult [Sharma 99, Keller 01, Bourmaud 18].

The influence of retting and scutching on the mechanical, physical, chemical and thermal properties has been investigated [Sharma 99, Keller 01, Placet 17]. Fiber separation and quality is indirectly estimated through these studies. However, no direct measurement of inter-fiber adhesion has been made at the fiber scale. Such measurements, would allow to closely study the mechanisms that take place during fiber separation and provide data to compare between different fiber species and varieties, maturity levels, retting levels and decortication parameters. In this way, subjective assessments would give place to quantitative data, greatly contributing in the optimization of the fiber extraction chain.

Peeling test

The peeling test represents a common mechanical test to characterize the adhesion strength between surfaces. The test is usually performed with one of two typical configurations as seen in Figure 1.21. The single arm configuration consists in the separation of a layer from a rigid substrate through the action of a force F applied at an angle θ. The T-peeling configuration consists in separating two layers by applying a peeling force on each layer.

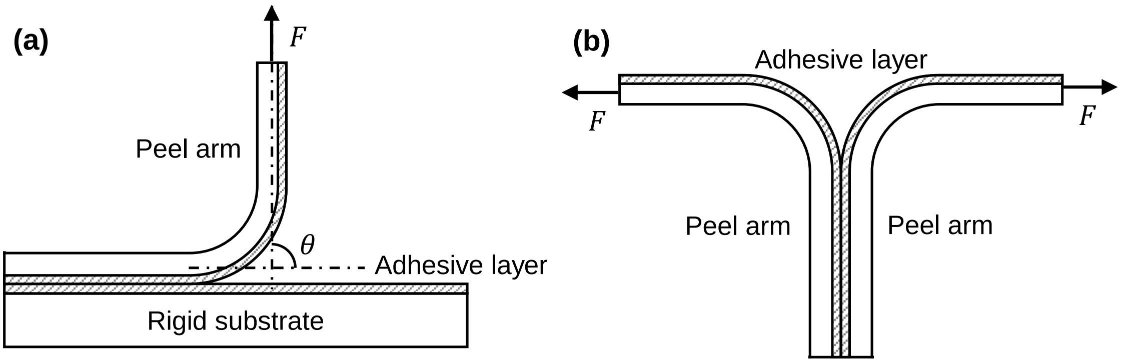

Figure 1.21: (a) Single arm peeling test, (b) T-peeling test. Representation adapted from [Hadavinia 06].

Peeling tests have been used to study the strength of adhesives or bonding of numerous materials such as metals, polymers or composites [Kim 88, Awalekar 18]. Adhesion mechanisms found in nature, such as the ones found in gecko feet, frogs or silks, have also been of particular research interest [Bhushan 11, Wanasingha 21]. In order to better understand these natural mechanisms and replicate them artificially, peeling tests and models to study their adhesive properties have been developed [Gu 16]. Peeling tests have also been performed at the nano-scale through the peeling of nanowires [Mead 18, Mead 20]. The adhesion of NanoElectro-Mechanical System (NEMS) to surrounding surfaces during manufacturing and operation can thus be better understood. Peeling of 2D graphene surfaces and opening of DNA chains have also been performed [Xue 21, Bockelmann 02].

In order to evaluate the adhesive strength of the tested materials numerous analytical models have been developed. These models grew progressively in complexity adding parameters such as the peeling angle, peeling velocity, friction, pre-tension, surface pattern and more [Gu 16]. The peeled materials have been commonly modeled as elastic or elasto-plastic with few visco-elastic models [Kim 88, Chen 13]. For elasto-plastic models, finite element analysis has been used to differentiate between the energy that is stored as plastic deformation and the one that actually contributes to the separation of the peeled layer [Crocombe 82, Hadavinia 06].

Most peeling tests rely on the measurement of the peeling force to later calculate the energy required to separate the two objects. An alternative lies in using beam theory to estimate interfacial adhesion energy through the deformed shape of the peeled arm [Mead 18].

Regarding plant peeling, to the authors knowledge, tests have only been performed at the plant stem scale [Réquilé 18]. In these tests separation occurred between the phloem containing the fibers and the xylem of hemp. A conventional universal tensile machine with a 2 Newton range force sensor, was adapted for this purpose. An important decrease in fracture energy was observed with the increase in retting time, offering valuable informations for plant stem decortication processes. Figure 1.22 presents an overview of theses studies.

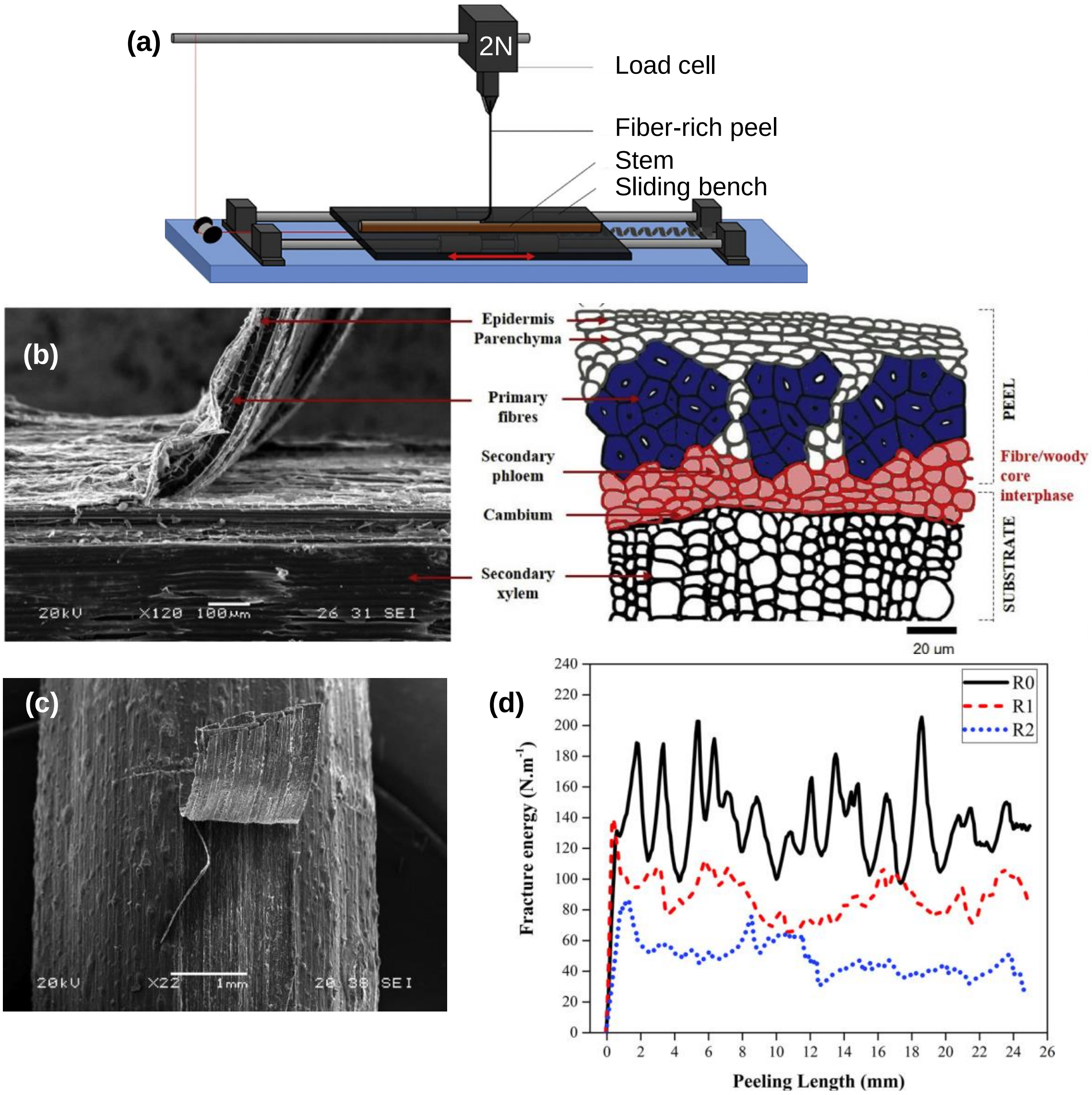

Figure 1.22: Hemp stem peeling by [Réquilé 18]. (a) peeling apparatus, (b)(c) peeled surface SEM images and stem microstructure, (d) fracture energy as a function of peeling length for different retting levels.

Despite these tests at the stem scale, the separation of fibers bundles into elementary fibers has never been investigated. This peeling test at the much smaller fiber scale, requires more precise means in terms of force sensing and actuation. The boundary conditions of the test (fiber fixing and grasping) are also more challenging due to the smaller scale.

1.4.4 Micro-mechatronics - towards innovative fiber characterization

Relevance of micro-mechatronics for plant fiber characterization

Performing mechanical characterization at the elementary fiber and bundle scale, such as Single Fiber Transverse Compression Tests (SFTCTs) and fiber peeling, requires high precision measurement and actuation means. In this way, small mechanical stimuli can be be applied on the fibers and physical measurements can be made to characterize their properties.

For this purpose, some commercially available mechanical testing machines, suitable for small microscale objects are available. Tensile stages are among the most popular ones, ranging from conventional designs (*LABTHINK Instruments Ltd.*, *KLA corporation*,United States) (see Figure 1.23.a), to machines adapted for in-situ measurements in limited spaces, such as SEMs, AFMs or microtomographers (*DEBEN UK Ltd.*) (see Figure 1.23.b). These machines are generally equipped with force sensors with a full scale of several hundreds to thousands of Newtons, or with more precise force sensors that are proprietary to the machine. Their specific purpose and non-modular design means that adapting such machines to different types of tests can be very challenging. Compact nanoindenters can also be found, offering very high measurement precision and very small generated displacements (*FemtoTools Switzerland,*, *Alemnis, Switzerland*, *KLA corporation*,United States) (see Figure 1.23.c and d). As discussed in subsection 1.3.2 however, nanoindendation comes with a series of disadvantages regarding plant fiber characterization while the available tools are once again difficult to adapt to new types of tests.

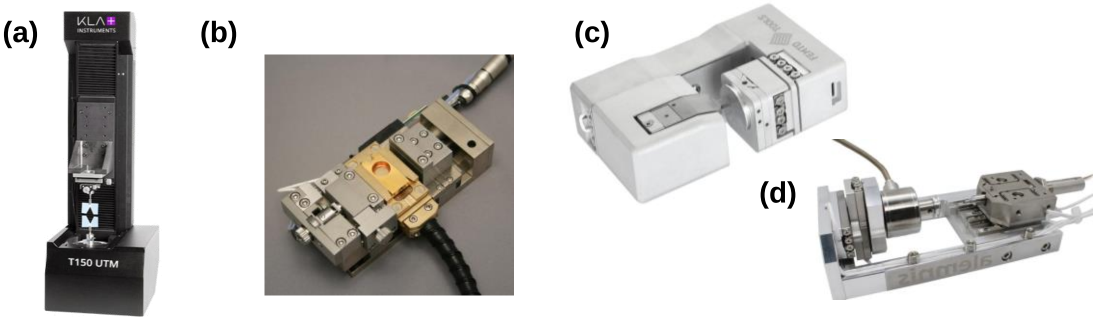

Figure 1.23: Commercially available micromechanical testing devices: (a) T150 tensile tester (*KLA corporation*), (b) 200 N *in situ* uniaxial tester (*DEBEN UK Ltd.*), *in situ* nanoindenters: (c) *FemtoTools Switzerland,* (d) *Alemnis, Switzerland.*

For all these reasons, developing new experimental setups for a specific type of test is investigated. The mechanical aspect of the test along with actuation, sensing, control and related electronics must be considered. The domain of mechatronics is at the interface between these different disciplines [Harashima 96]. To adapt to the small size of plant fibers in particular, micro-mechatronic approaches are needed more specifically. While still an active area of research, pushing the boundaries of actuation and measurement precision further and further, the field of micro-mechatronics offers both actuation and force measurement means:

- **Micromotion devices.** Various physical principles can be exploited to generate motion [Ouyang 08]. Piezoelectric or shape memory alloy actuators, direct current and ultrasonic motors are only some of the available choices, each with its own advantages and disadvantages. The generated displacements can be transmitted by compliant mechanisms: monolithic structures that transmit movements by their deformation [Chaillet 13]. Such mechanisms replace conventional bearings, eliminating problems related to friction. Using the feedback of a sensor, these actuators can be controlled in a closed-loop system, which actively regulates the generated displacement. The synergy between all these elements allows the creation of micromotion devices with nanometric precision and a millimetric range of motion [Tan 15b, Bettahar 22, Andre 20].

- **Force measurements.** Forces are never a direct measurement, they rely on the use of a compliant passive structure, associated with a measurement device. Once a load is applied changes in resistance, strain, position or other are detected by the measurement device and used to calculate the related force. Several technical and physical limitations can make the force measurement procedure challenging [Clévy 11], still, many different types of force sensors can be found: strain gauge based, piezoresistive, capacitive, vision based and more, which can reach sub μN precision [Wei 15, Tiwari 21, Yang 22].

Micro-mechatronic approaches are thus key to the mechanical characterization of plant fibers, providing the necessary precision to apply small loads and measure fiber responses precisely. Furthermore, they can offer various manipulation tools [Zhang 19], such as microgrippers, allowing delicate and repeatable manipulation of the fibers, which is not always feasible with manual approaches. Finally, micromechatronic platforms provide excellent bases for the development of automated testing. A larger number of tests can thus be performed, which is specifically important for the characterization of plant fibers, since their properties can vary significantly between plant variety, growing conditions or extraction processes.

Micromechatronics for small object characterization

Various custom micromechatronic setups have been developed for the characterization of microscale objects. The nature of theses setups can vary with some offering more general capabilities while others are tailored to a specific application. An overview of some such setups are given in Figure 1.24 and dicussed below.

Komati et al. developed a microgripper with integrated force sensing and a position estimation of its end effectors [Komati 16] (see Figure 1.24.b). Using this gripper microscale objects can be grasped and their stiffness can be estimated. The domain of cell characterization has also led to innovative developments. For example, the elasticity of plant cell walls (pollen) have been characterized with custom micromechatronic setup using commercially available sensors and actuators [Burri 19, Läubli 21]. A custom MEMS device allowing an automated characterization of cells has also developed [Sakuma 19] see Figure 1.24.a.

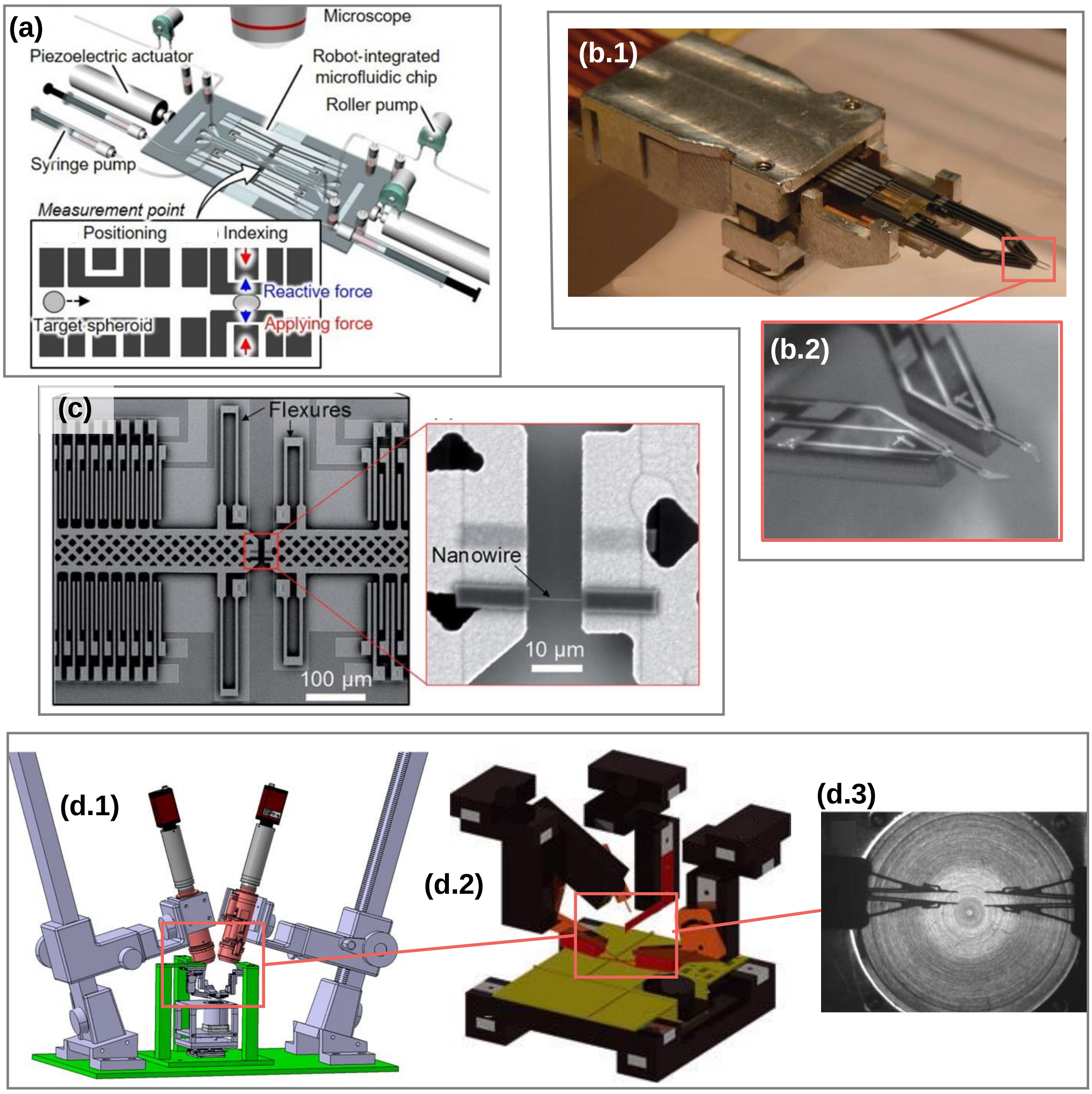

Figure 1.24: Micromechatronic setups for characterization of microscale objects. (a) MEMS device for cell characterization [Sakuma 19]. (b.1) microgripper with sensorized end effectors (b.2) [Komati 16]. (c) MEMS device for nanowire tensile testing [Ladner 19]. (d.2) microrobotic platform for fiber manipulation and characterization [Saketi 12], (d.1) added cameras for 3D geometry reconstruction [Hirvonen 16], (d.3) close-up view on microgrippers and fiber rotary stage [Hirvonen 14a].

The characterization of single fibers has also been investigated with micro-mechatronic means. MEMS devices have been developed to perform tensile test on synthetic nanofibers and plant tissues [Beese 13, Ramachandramoorthy 18, Ladner 19, Zamil 14, Espinosa 12] (see Figure 1.24.c). The most versatile approach however, can be found in the flexible microrobotic platform developed by Hirvonen, Saketi and Kallio [Hirvonen 11] (see Figure 1.24.d). This platform offers capabilities to perform fiber characterization from sample preparation and morphological characterization to various mechanical tests. Most studies focused on pulp fiber, used in the paper industry. Fibers are first placed on an illuminated rotary stage [Hirvonen 14a]. Two microgrippers allow the fibers to be grasped with each gripper handling one end of the fiber. Through an overhead camera the graspability of the fibers is evaluated [Hirvonen 11, Hirvonen 15a]. Through the synchronous control of multiple actuators fibers can be grasped and moved to a testing zone [von Essen 14, Hirvonen 15b]. Using different tools various characterizations could then be performed. Fiber geometry and microstructure were studied through 3D fiber reconstruction [Hirvonen 16] and MFA measurements [Hirvonen 14b]. Regarding mechanical testing pulp fiber bonds [Latifi 15] and droplet contact angle [Saketi 14a, Hirvonen 17] along flexibility, DMA and tensile tests [Grigoray 15] were all studied.

Overall, given the actuation, measurement and manipulations capabilities micro-mechatronic approaches can offer, many innovative platforms have been developed with the purpose of material characterization of microscale objects. Creating such micro-mechatronic platform for SFTCT and peeling applications could allow the characterization of plant fiber transverse properties and inter-fiber adhesion for the first time. However many challenges still remain. Very few commercially available force sensors are adapted to the measurement of force in the range of a mN to a few hundred mN [Andre 22b], values which as we will see in this doctoral thesis represent typical SFTCT and peeling related loads. While actuation can be very precise, measurement of fiber displacements, close to the fiber itself remain rare. Questions of actuator and sensor repeatability and drift must also be adressed before experimental campaigns, through calibration processes. Finally, fine movements and alignment between different setup components to assure no off-axis mechanical stimuli and measurements occur, remain particularly challenging.

1.5 Conclusions

In this chapter, the key role of plant fibers as an environmentally friendly composite reinforcement material was presented. Flax, hemp and nettle fibers were identified as the most highly promising candidates for such developments in Europe. Their rich hierarchical structure along with their life-cycle as a composite reinforcement were presented. The mechanical characterization of plant fibers was shown to be key for designing high-performance composites. Direct characterization at the scale of the elementary fiber or the fiber bundle was determined to be critical to understand fiber behavior and to measure their properties as reinforcing elements. For this reason, this doctoral thesis treats mechanical characterizations at these scales.

Characterizations at the scale of the elementary plant fibers are numerous but heavily focused on tensile behavior and fiber-matrix adhesion. The characterization of transverse properties is required to complement these studies and improve the prediction of Plant Fiber Composites (PFC) behavior. This characterization can be performed through SFTCTs, a test that has already been performed on various synthetic fibers. To the authors knowledge however, with the exception of wood fibers [Mikczinski 13], no such characterization has been made on plant fibers. In this work, the transverse behavior of flax, hemp and nettle are studied through SFTCTs.

In the process of extracting fibers from the plant stem, a lack of quantitative data was identified. Indeed the retting, scutching and hackling procedures mainly rely on subjective criteria to evaluate the separation between fibers. Bad fiber separation or excessive processing however, can become a weak point of composite materials. For this reason, measuring inter-fiber adhesion was identified as a critical characterization need to provide accurate measurements that allow the evaluation of retting and extraction processes. Peeling tests at the scale of the bundle were shown to be a suitable way to measure this adhesion and are performed in this work.

Plant fiber characterization presents several challenges, mainly related to their small size and complex morphology/structure. The use of micro-mechatonics to design unique platforms, capable of carrying out mechanical testing and perform accurate measurements on small objects such as fibers, was shown to be a valuable option. For this reason, in this doctoral thesis micro-mechatronic platforms are developed to perform the transverse compression and peeling tests on plant fibers. Furthermore, the advantages of FEA to gain insights on the significant influence of fiber morphology, structure and composition on plant fiber behavior were discussed. In this work, FEA will be used to complement the transverse compression experiments by reproducing and analyzing complex behaviors that take place during plant fiber SFTCTs.

2

INSIGHTS ON PLANT FIBER COMPRESSION COMPLEXITY THROUGH ANALYTICAL AND FINITE ELEMENT MODELING

Contents

2.1 Introduction

The principle of the Single Fiber Transverse Compression Test (SFTCT) was presented in subsection 1.4.2. In short, the test consists in the compression of a single fiber between a fixed and a mobile platen. The contact between the fiber and the platens induces a non-linearity in the fiber's transverse response. Analytical models are needed to model this behavior, and to identify the fiber's transverse properties by inverse method.

Existing SFTCT models make a series of hypotheses on the test's configuration and the nature of its components. The fiber is considered as a purely elastic, right circular cylinder between parallel platens. An alternative lies in the use of finite element analysis, which allow a much more flexible description of geometry, boundary conditions and material behavior. Depending on the model's complexity however, such models can be computationally expensive or lack the generalization ability required to use them for many types of fibers.

As seen in Chapter 1 plant fibers are complex objects in terms of morphology, microstructure and biochemical composition. Given this complexity, a fundamental question can be asked: to what extent can analytical models, and their ideal representation of SFTCTs, be used in the inverse identification of a plant fiber's transverse elastic modulus? Furthermore, given that plant fibers are complex structures, what does this identified modulus represent? This chapter tries to answer this question through the following steps:

- The state of the art on SFTCT analytical models will be presented and the choice of model will be discussed.
- A finite element model of the test will be developed and validated.
- The influence of fiber morphology and material behavior on the analytical model's identification ability will be evaluated through finite element analysis. Ideal geometric representation of main plant fiber geometric features are studied first to independently assess their influence on fiber behavior. The transverse compression of complex geometries issued from microscopy images is simulate after, allowing the study of complex morphological interactions. Finally, the impact of inelastic material behavior in SFTCTs is evaluated with viscoelastic and plastic models.

2.2 SFTCT analytical models

This section establishes the state of the art on single fiber transverse compression analytical models and chooses the analytical model that will be used for the inverse identification of E_T in the rest of this work.

2.2.1 Common model hypotheses

The source of all SFTCT analytical models can be traced back to the work of Hertz [Hertz 96] on the contact between semi-infinite, isotropic-elastic solids, as seen in Figure 2.1 in the case of two spheres. The contact is a result of a concentrated force per unit length F_L at $x = y = 0$. Contact pressure distribution is assumed to be elliptical. The functions of the stress fields σ_{xx} and σ_{yy} can be calculated close to contact zone, if a series of conditions are met. In the contact zone, where $-b < x < b$, with b the contact half-width, the vertical contraction of the cylinder must be of the linear form $U = ax + b$ to avoid interpenetration of the solids. Additionally, no shear stress should occur ($\sigma_{xy} = 0$) and F_L must be equal to:

$$F_L = -\int_{-b}^{b} \sigma_{yy}\, dx \tag{2.1}$$

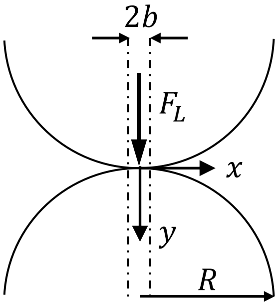

Figure 2.1: Typical representation of contact between semi-infinite solids.

M'Ewen provided functions for the σ_{xx} and σ_{yy} stresses and expanded upon Hertz by modeling the contact with friction by considering tangential forces [M'Ewen 49]. Timoshenko and Goodier made the transition to finite solids, leading to a description of the stress fields on the entire cylinder cross section [Timoshenko 70]. This approach required the addition of a uniform tensile stress $F_L/\pi R$ to the cylinder surface, with R being its radius.

Despite some differences, these analytical descriptions make a series of common hypotheses:

- The problem is treated in plane strain conditions, assuming that cylinder length L is significantly larger than the radius R. Models are thus two-dimensional (2D).
- $b \ll R$, the cylinder radius R is significantly larger than the contact half-width b.
- Material behavior is considered purely linear elastic.
- Solids in contact are uniform.
- An infinitesimal strain approach is adopted.

Hadley et al., based on M'Ewen's work, were the first to create an analytical model, in the case of SFTCTs [Hadley 65]. The test presented a few differences compared to the previous theoretical work. Fibers are not isotropic since stiffness along their longitudinal axis is typically much higher than the transverse one. Compression platens had to be added as well. Material such as glass or sapphire, that are much stiffer than the fiber, were used for these platens. For this reason three fundamental modeling choices were added:

- The fiber is considered transversely isotropic, with the longitudinal axis being the axis of symmetry.

- The platens are considered as flat and rigid.
- The platens are perfectly parallel between each other.

In all the following formulations, the axis of symmetry of the transverse isotropic formulation (x axis) is noted L, while the transverse directions (y and z axes) are noted with T. Given the material model of the fiber its constitutive law is:

$$\underline{\varepsilon} = \underline{\underline{S}} : \underline{\sigma} \tag{2.2}$$

where ε the strain, σ the stress and S the compliance matrix, which can be written as follows, where the x, y and z axes are denoted with the indices 11, 22 and 33 respectively:

$$\begin{bmatrix} S_{11} & S_{12} & S_{13} & 0 & 0 & 0 \\ S_{21} & S_{22} & S_{23} & 0 & 0 & 0 \\ S_{31} & S_{32} & S_{33} & 0 & 0 & 0 \\ 0 & 0 & 0 & S_{44} & 0 & 0 \\ 0 & 0 & 0 & 0 & S_{55} & 0 \\ 0 & 0 & 0 & 0 & 0 & S_{66} \end{bmatrix} = \begin{bmatrix} \frac{1}{E_T} & -\frac{\nu_{TT}}{E_T} & -\frac{\nu_{LT}}{E_L} & 0 & 0 & 0 \\ -\frac{\nu_{TT}}{E_T} & \frac{1}{E_T} & -\frac{\nu_{LT}}{E_L} & 0 & 0 & 0 \\ -\frac{\nu_{LT}}{E_L} & -\frac{\nu_{LT}}{E_L} & \frac{1}{E_L} & 0 & 0 & 0 \\ 0 & 0 & 0 & \frac{1}{G_{LT}} & 0 & 0 \\ 0 & 0 & 0 & 0 & \frac{1}{G_{LT}} & 0 \\ 0 & 0 & 0 & 0 & 0 & \frac{1}{G_{TT}} \end{bmatrix} \tag{2.3}$$

with: E_L, E_T the elastic modulii in the longitudinal and transverse direction respectively, ν_{LT}, ν_{TT} the Poisson ratios in the longitudinal and transverse plane and similarly, G_{LT}, G_{TT} the shear modulii where $G_{TT} = \frac{E_T}{2(1-\nu_{TT})}$. Plane strain compliance terms can be defined as :

$$\tilde{s}_{11} := S_{11} - \frac{S_{13}^2}{S_{33}} = \frac{1}{E_T} - \frac{\nu_{LT}^2}{E_L}, \tag{2.4}$$

$$\tilde{s}_{12} := S_{12} - \frac{S_{13}^2}{S_{33}} = -\frac{\nu_{TT}}{E_T} - \frac{\nu_{LT}^2}{E_L} \tag{2.5}$$

With theses series of additional hypotheses being made, Hadley offered an equation to calculate the contact half-width b, between the fiber and the rigid platens. This formulation was used by the large majority of authors that are cited in this work:

$$b = \sqrt{\frac{4F_L R}{\pi}\tilde{s}_{11}} \tag{2.6}$$

2.2.2 Model overview and common simplifications

Model overview and comparison

Figure 2.2 illustrates a 2D representation of a SFTCT test. A movement of the upper compression platen produces the compression of the fiber through the contact of width $2b$, causing a vertical contraction U, equal to the platen displacement, and an horizontal expansion U_D. The term “fiber displacement” is commonly used to describe the vertical contraction U.

SFTCT analytical models can be constructed to relate fiber contraction or expansion to the applied force, as a function of the fiber's material and geometric parameters. To do so, fiber strain can be calculated through the stress functions and the constitutive relation described in the previous section:

$$\varepsilon_{xx} = S_{11}\,\sigma_{xx} + S_{12}\,\sigma_{yy} + S_{13}\,\sigma_{zz} \tag{2.7}$$

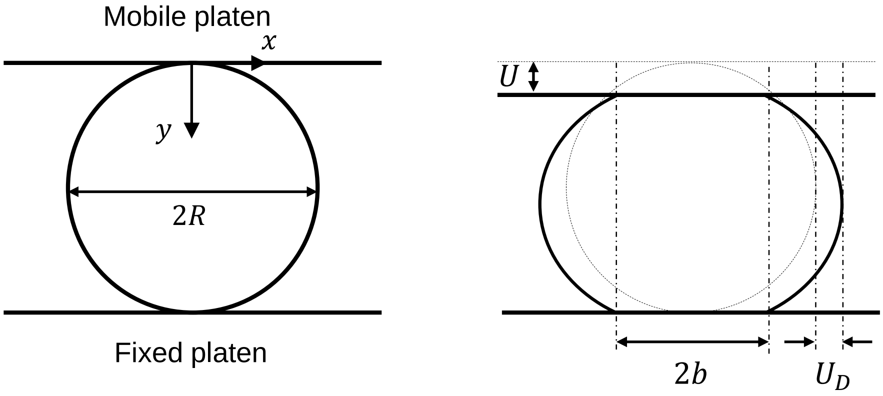

Figure 2.2: 2D representation of single fiber transverse compression test in an undeformed and deformed configuration.

$$\varepsilon_{yy} = S_{12}\,\sigma_{xx} + S_{22}\,\sigma_{yy} + S_{13}\,\sigma_{zz} \tag{2.8}$$

with, given plane strain conditions:

$$\sigma_{zz} = -\frac{S_{12}}{S_{11}}\left(\sigma_{xx} + \sigma_{yy}\right) \tag{2.9}$$

By integrating these strains along the fiber diameter, the radial displacement of the fiber, in its vertical or horizontal direction (x and y axis respectively) can be calculated:

$$U = 2\int_0^R \varepsilon_{yy}\,dy \tag{2.10}$$

$$U_D = 2\int_0^R \varepsilon_{xx}\,dx \tag{2.11}$$

Based on this approach the following models can be found in the literature. The majority of them offer an equation to calculate the vertical displacement U. [Morris 68] and [Cheng 04] proposed an analytical expression for U based on the stress function given by M'Ewen. [Phoenix 74] along with [Jawad 78] adopted Timoshenko's approach for finite solids. Additionally, these authors did not consider the typical concentrated loads at $x = 0$. Jawad considered a distributed load on the contact with upper-mobile platen, while Phoenix used a distributed load on both the upper and the lower contact zones.

Similar models of transverse compression have also been developed independently in other contexts, such as cylindrical rollers and bearings [Foppl 07, Lundberg 49] or for the compression of cylindrical biological materials such as carrots [Sherif 76] and corn [Anazodo 81, Anazodo 83]. McCallion derived a general equation based on Timoshenko's work [McCallion 82]. Its originality lies into a parameter named β which controls the form of the pressure distribution. For an elliptical distribution ($\beta = 0.5$) the resulting equation is identical to the one formulated by [Lundberg 49]. Sherif et al. [Sherif 76] arrived to a similar equation based on the work of [Poritsky 50]. For a parabolic distribution ($\beta = 1$) the resulting equation corresponds to the one derived by [Foppl 07]. All of these models are expressed for isotropic elastic materials. Transitioning to transverse isotropy can be achieved by converting the term $(1-\nu^2)/E$ to $\tilde{s}_{11}$ as seen in [Jawad 78] and [Hillbrick 19].

Table 2.1 summarizes the equations of these models along with their modeling hypotheses. Figure 2.3 shows the force per unit length F_L as a function of the fiber's vertical displacement for all models. The force level is chosen based on our experimental capabilities (see subsection 3.3.2) and the rest of the input parameters are identical to the numerical studies performed in sections 2.3 to 2.6 . The equations by Lundberg, Phoenix and Jawad produce very similar results with Föppl being close by slightly less stiff. All these models use Timoshenko's stress functions that consider the entire cylinder cross section. Models that rely on local stress function produce varied results. Morris and Cheng lead to a stiffer response while Sherif produces a lower slope. These results are in agreement with the comparison made by [Hillbrick 19] with different input parameters.

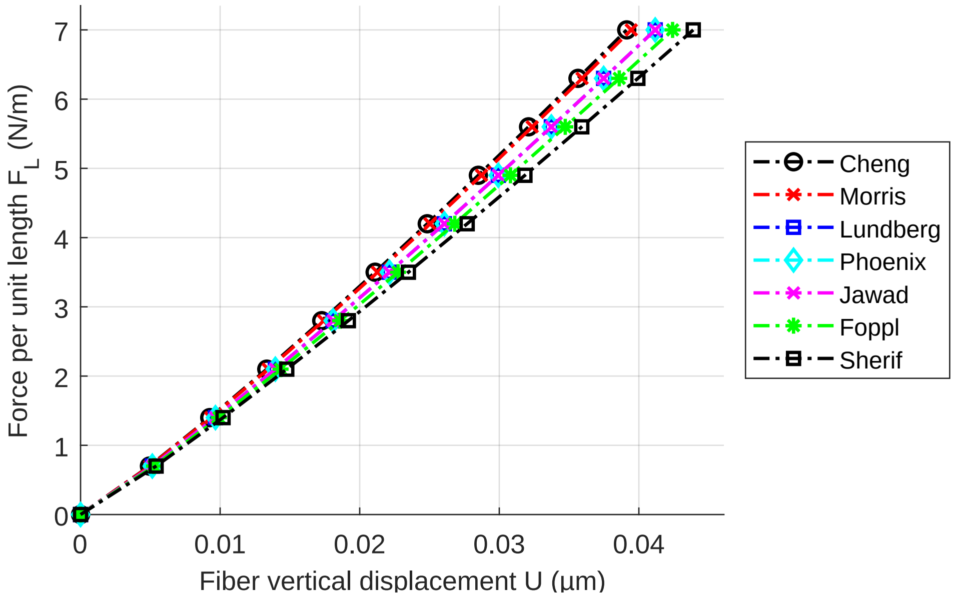

Figure 2.3: Comparison of SFTCT analytical models with input values of $R = 16\,\mu m$, $E_T = 1\,GPa$, $E_L = 50\,GPa$, $\nu_{LT} = 0.4$, $\nu_{TT} = 0.07$. The force per unit length F_L is chosen based on our experimental capabilities (a maximum of $350 mN$ applied on a length of $300\,\mu m$)

	Equation of vertical displacement	**2D representation**
[Morris 68]	$U = \frac{4F_L}{\pi}\, \tilde{s}_{11}\, sinh^{-1}(R/b)$ (2.12)	
[Sherif 76]	$U = \frac{4F_L}{\pi}\, \tilde{s}_{11} \Big(ln(4R/b) + 1/2\Big)$ (2.13)	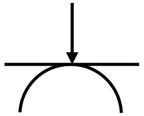
[Cheng 04]	$U = \frac{4F_L}{\pi b^2}\left[\tilde{s}_{11}\, b^2\, ln\left(\frac{\sqrt{b^2+R^2}+R}{b}\right) + \tilde{s}_{12}\, R\left(\sqrt{b^2+R^2}-R\right)\right]$ (2.14)	
[Foppl 07]	$U = \frac{4F_L}{\pi}\, \tilde{s}_{11} \Big(ln(2R/b) + 1/3\Big)$ (2.15)	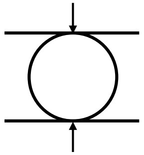
[Lundberg 49]	$U = \frac{4F_L}{\pi}\, \tilde{s}_{11} \Big(ln(4R/b) - 1/2\Big)$ (2.16)	
[Phoenix 74]	$U = \frac{4F_L}{\pi}\left[\tilde{s}_{11}\, sinh^{-1}(2R/b) - \frac{1}{2}(\tilde{s}_{11}+\tilde{s}_{12}) + \tilde{s}_{12}\frac{2R}{b}\left(\sqrt{1+(2R/b)^2} - 2R/b\right)\right]$ (2.17)	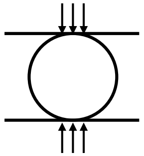
[Jawad 78]	$U = \frac{4F_L}{\pi}\left[\tilde{s}_{11}\left(sinh^{-1}(R/b)+ln(2)\right) - \frac{1}{2}(\tilde{s}_{11}+\tilde{s}_{12}) + \tilde{s}_{12}\frac{R}{b}\left(\sqrt{1+(R/b)^2} - R/b\right)\right]$ (2.18)	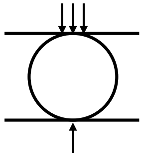

Table 2.1: Analytical models of fiber vertical displacement U in SFTCTs . A single arrow represents a concentrated load, multiple arrows represent a load distribution. When the whole fiber section is represented Timoshenko stresses are used, half-sections correspond to M'Ewen stresses.

While the aforementioned models present many similarities, in terms of both approach and results, some authors offer more distinct approaches. Pinnock et al. derived an equation for the horizontal expansion U_D, assuming a finite solid and concentrated loads [Pinnock 66].

$$U_D = F_L\left[\left(\frac{4}{\pi}-1\right)\tilde{s}_{11}+\tilde{s}_{12}\right] \tag{2.19}$$

A unique approach compared to the previous models was used by [Anazodo 81]. Based on the work of [Muskhelishvili 77] and [Loo 58], they accounted for the curvature of the compressed cylinder in the contact zone, under a purely elastic and isotropic assumption and concentrated loads. A contact arc length $2s$ is thus used, instead of the flat contact width $2b$. Equations were derived for both the vertical and horizontal displacements in both small [Anazodo 83] and large strain configurations [Chikwendu 84]. Contrary to all previous models however, the vertical displacement U is not calculated directly. Instead, the contact arc s is calculated with the help of U/R data. Formulas to calculate the Young's modulus E are then given. Considering a small strain assumption the equations are:

$$\frac{U}{R} = \frac{ln(4R/s)-1/2}{2(R/s)^2-1} \tag{2.20}$$

$$E = \frac{4F_L}{\pi R}\left(1-\nu^2\right)\left(2(R/s)^2-1\right) \tag{2.21}$$

Finally, [Olesiak 75] derived a model using the contact half angle α as well as complex parameters employing the Bessel function. This model is very rarely mentioned in the open literature. Given its complexity and the work being written in its original language (Polish) further analysis of this model is not performed in this work.

Common simplifications

This subsection provides typical simplifications used by authors to simplify the equations that describe fiber behavior under SFTCTs.

Contact width simplification. The Hertz contact model is formulated for a contact strip that is much smaller than the radius of the objects in contact ($b \ll R$). Considering this condition, the terms multiplied by $\tilde{s}_{12}$ in equations (2.14), (2.17) and (2.18) can be neglected ($\sqrt{b^2+R^2}-R \simeq \sqrt{R^2}-R$). Jawad proposed this simplification for his model while Phoenix and Cheng did not. The simplified equations are given in Table 2.2. Jawad simplified his model further by neglecting the remaining $\tilde{s}_{12}$ term. Doing so eliminates the Poisson ratio in the transverse plane, ν_{TT}, from the models. Many authors chose to use this simplified model [Kawabata 90, Kotani 94, Jones 97, Singletary 00a, Sockalingam 16, McDaniel 17, Guo 16, Naito 17].

	Equations of vertical displacement with $b \ll R$	
[Phoenix 74]	$U = \frac{4F_L}{\pi}\left[\tilde{s}_{11}\left(sinh^{-1}(2R/b) - 1/2\right) - \frac{1}{2}\tilde{s}_{12}\right]$	(2.22)
[Jawad 78]	$U = \frac{4F_L}{\pi}\left[\tilde{s}_{11}\left(sinh^{-1}(R/b) + ln(2) - 1/2\right) - \frac{1}{2}\tilde{s}_{12}\right]$	(2.23)
[Cheng 04]	$U = \frac{4F_L}{\pi}\tilde{s}_{11}\, ln\left(\frac{\sqrt{b^2+R^2}+R}{b}\right)$	(2.24)

Table 2.2: SFTCT analytical models considering that the contact half-width is significantly smaller than the fiber radius ($b \ll R$) .

High anisotropy simplification. Fibers can be highly anisotropic materials with stiffnesses in the longitudinal direction highly exceeding the transverse one ($E_L \gg E_T$). PAN-based carbon fibers are a typical example with $E_L = 291\,GPa$ and $E_T = 8.94\,GPa$ [Naito 07, Naito 17]. The following simplifications can thus be made:

$$\tilde{s}_{11} = \frac{1}{E_T} - \frac{\nu_{LT}^2}{E_L} \approx \frac{1}{E_T} \tag{2.25}$$

$$\tilde{s}_{12} = -\frac{\nu_{TT}^2}{E_T} - \frac{\nu_{LT}^2}{E_L} \approx -\frac{\nu_{TT}^2}{E_T} \tag{2.26}$$

The plane strain compliance terms $\tilde{s}_{11}$ and $\tilde{s}_{12}$ are thus equal to the compliance terms S_{11} and S_{12} respectively. Many works on the SFTCT make this simplification, especially when high anisotropy fibers such as carbon or Kevlar® fibers are tested [Morris 68, Phoenix 74, Jones 97, Singletary 00a, Guo 16, Naito 17].

2.2.3 Choice and study of analytical model

With an overview of SFTCT analytical models being performed, this section focuses on choosing an analytical model for the rest of this research work along with establishing a better understanding of its most influential parameters.

Choice of model

Jawad's analytical model constitutes by far the most popular model in the SFTCT literature [Kawabata 90, Kotani 94, Jones 97, Singletary 00a, Sockalingam 16, McDaniel 17, Guo 16, Naito 17], with only a few authors using Phoenix's model [Stamoulis 07] or Cheng's [Lim 10]. To verify this popular choice, analytical model predictions are compared to those of a 2D, small strain finite element model. Details on this model can be found in section 2.3. The details of this comparison can be found in appendix A.1 .

Jawad's model produces the closest results to the predictions of the 2D Finite Element Model (FEM). Lundberg's and Phoenix's models are also quite close. The rest of the presented models however, shows significant differences with the FEM. On this basis they will not be used in this work. While any of the models of Lundberg, Phoenix and Jawad could be used without any major differences in the identification of E_T, the model developed by Jawad [Jawad 78] produces the results that are the closest to the Finite Element Model (FEM) making it our analytical model of choice.

In their comparisons Hillbrick et al. also recommended these three models [Hillbrick 19]. They noted however that the model developed by Morris produced the best experimental predictions, however experimental uncertainties might influence this result.

In the case of plant fibers the contact width hypothesis ($b \ll R$) will not be used since fiber morphology can lead to contact width's that are larger than the one predicted for cylinders. The anisotropy ratio of plant fibers will be shown to be high (see Table 3.8 in subsection 3.4.4), for this reason the anisotropy simplification $E_L \gg E_T$ will be used. Further justification and analysis on the domain of validity of these hypotheses can be found in appendix A.2.

Sensitivity analysis

Using Jawad's analytical model, E_T can be identified by inverse method through a least-square regression analysis. Force F and fiber displacement U data are measured experimentally during compression while the fibers' geometrical and material properties: radius R, longitudinal elastic modulus E_L and Poisson's ratios ν_{LT}, ν_{TT} are measured separately. To quantify which of these input parameters has the largest influence on the identified transverse elastic modulus, a sensitivity analysis is performed using Sobol's variance based analysis [Sobol 01]. This method has the advantage of considering not only the influence of a single parameter but also parameter interaction.

For this study, the nominal values of the input parameters are chosen based on the properties of Polyamide 11 (PA11) fiber that will be studied experimentally in Chapter 3 ($E_L = 2155\,MPa$, $E_T = 706\,MPa$, $\nu_{LT} = 0.4$, $\nu_{LT} = 0.07$, $R = 17.55\,\mu m$). The value of the force is taken from a simulated compression of this fiber at a displacement of $1\,\mu m$. For this analysis, $10,000$ samples are used. A variation of 10% is allowed on all parameters, as opposed to variations related to measurement uncertainties, in order to study the models intrinsic sensitivity to its parameters.

The results of the sensitivity analysis are given in Table 2.3. The total effect indicator is given which accounts for the interactions between parameters. The fiber radius R results in the largest Sobol index. The transverse elastic modulus E_T is thus the most sensitive to R. The Poisson ratio in the longitudinal plane, ν_{LT}, has a smaller but still important influence followed by the longitudinal modulus E_L whose effect is limited. Finally, the Poisson ratio in the transverse plane, ν_{TT}, has a negligible effect on the identification of E_T. Similar results for different input parameters are reported by Wollbret-Blitz [Wollbrett-Blitz 16] who performed a sensitivity analysis with different model parameter values and the fiber displacement as the output.

Model parameter	R	ν_{LT}	E_L	ν_{TT}
Sobol total effect indicator	0.77	0.18	0.04	$3.7 \cdot 10^{-8}$

Table 2.3: Sobol total effect indicator for each analytical model input parameter.

Plant fibers have a higher anisotropy ratio than PA11, for this reason, E_L and ν_{LT}

are often neglected through the high anisotropy hypothesis. We can thus except the sensitivity to the radius parameter R, to be even higher in the case of plant fibers.

In conclusion, at a given force and displacement level the fiber radius, sole geometric parameter of Jawad's model, is the most influential input in the identification of E_T. Accurate knowledge of fiber dimensions is thus critical. In addition, any morphological deviation from the model's representation of the test (a cylinder between parallel flat platens) might cause significant differences with the predictions of the analytical model.

2.3 SFTCT finite element model - creation and validation

This section focuses on the creation and validation of finite element models that will constitute the bases for the studies of fiber morphology and material behavior. The use of geometric symmetries, mesh element type and refinement will be discussed.

2.3.1 Finite element model and methods

Finite element fundamental modeling choices

The bases of the Finite Element Model (FEM), used to simulate the SFTCT are presented in this section. In order to verify a series of modeling choices, the results of Finite Element Analysis (FEA) will be compared with the ones of Jawad's analytical model. For this reason, a number of modeling hypotheses made for the analytical models will be used:

- The fiber is modeled as a right circular cylinder of radius R.
- Compression platens are parallel and rigid.
- A small strain formulation is used.

Figure 2.4 offers a geometric representation of the model along with its boundary conditions. The model's boundary conditions are defined as follows:

Displacements. The upper compression platen is mobile with a displacement towards the fiber along the y axis of $u_y = 1\,\mu m$ with 20 loading increments of $0.05\mu m$. Displacement along the two other axes is not allowed ($u_x = u_z = 0$). The lower compression platen is fixed with all of its displacements being blocked ($u_x = u_y = u_z = 0$).

Contact. An augmented Lagrangian contact formulation is used to define the contact between the fiber and the platens. The platens, being stiffer, are the masters in the contact pairs with the fiber being the slave. The contact is defined in a limited zone corresponding to an arc of $\pi/3$ on the fiber perimeter, as seen in Figure 2.5. By limiting the area in which the contact search will occur, significant computation time is saved. The contact half width b does not exceed this zone. To better fit the circular geometry of the fiber a quadratic element shape function is employed.

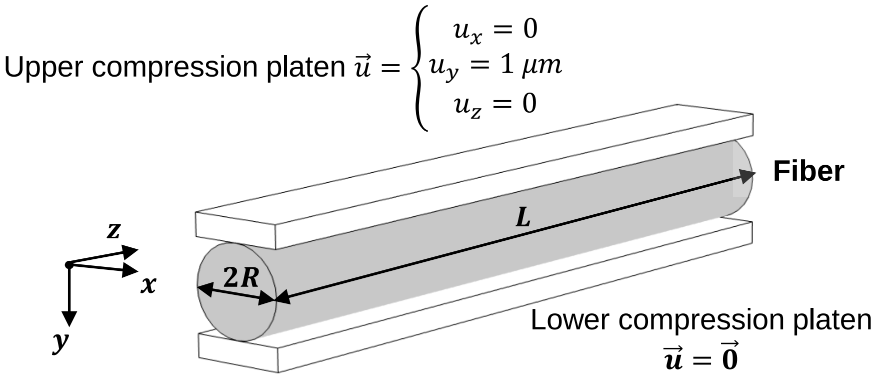

Figure 2.4: Representation of SFTCT with compression platen boundary conditions.

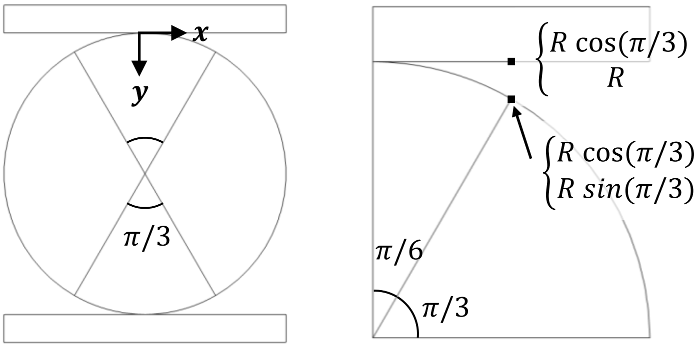

Figure 2.5: Potential contact zone of arc length $\pi/3$ (left) with the coordinates of the contact limits (right).

2D-3D. Depending on the needs of the study, 3D or 2D models (representing the xy cross section) are used. When a 3D model is used, the longitudinal displacement (u_z) of one of the fiber's edge faces is blocked to eliminate rigid body motions. This configuration, also better corresponds to the one used in our experimental studies (free-clamped configuration, see Chapter 3). In the case of a 2D model a plane strain formulation is used, just like the analytical model.

Solver. For purely elastic or elastoplactic behaviors, a time-independent, stationary solver is used. In the case of viscoelasticity, a time dependent solver is employed.

Mesh. The mesh used across all models remains simple. On the fiber's xy cross section, triangular elements with sides of $R/26$ are used. A mesh convergence study that justifies this choice will be presented (see subsection 2.3.3). In the case of 3D models this mesh is then extruded along the fiber's length, resulting in prismatic elements. 60 prisms are used along a fiber length of $300\mu m$.

Nominal geometric and material parameters

The fiber's nominal geometric and materials parameters, that will be used throughout the analyses, are presented in Table 2.4. The chosen radius R is representative of most single plant fibers, while the fiber length L is chosen as equal to the experimentally compressed length in our SFTCT setup (see Chapter 3). Later experimental studies will show that plant fibers exhibit a high anisotropy ratio (E_L/E_T) (see Table 3.8), with the transverse modulus being in the order of the GPa. For this reason, E_T was chosen as $1\,GPa$ while the longitudinal modulus was set at $50\,GPa$ based on results from plant fiber tensile tests (see Table 1.3). Values for the Poisson's ratios are set arbitrarily at the values of PA11 fibers [Placet 20]. While these values might not be perfectly representative of plant fibers, the analytical model's sensitivity to these parameters were shown to be low in subsection 2.2.3. When it comes to the compression platens they are represented as rigid rectangular blocks of a width equal to the fiber's diameter, a height of $R/5$ and a length equal to the fiber's length.

Parameter	Values	Description
R	16 (μm)	Radius
L	300 (μm)	Length
E_L	50 (GPa)	Longitudinal Young's modulus
E_T	1 (GPa)	Transverse Young's modulus
ν_{LT}	0.4	Longitudinal plane Poisson's ratio
ν_{TT}	0.07	Transverse plane Poisson's ratio

Table 2.4: Nominal fiber geometric and material properties in numerical analysis.

These parameters are nominal values and are subject to change depending on the study. Every change in value will be noted and explained in its respective study.

Transverse elastic modulus identification

In order to perform inverse identification from simulation data with an analytical model, the fiber's vertical displacement U and compression force per unit length F_L need to be extracted from the finite element model. To obtain the force data from the simulation, the vertical component of the contact pressure T_{n_y} is integrated along the defined contact zone between the fiber and the upper compression platen. In the case of a 2D model this results in a force per unit length. When a 3D model is used, T_{n_y} is integrated along the defined contact surface, resulting in a force (in Newtons). Dividing it by the fiber length results in a force per unit length. A validation of this integration is presented in appendix A.3. When it comes to displacement, the fiber's radial displacement will be identical to the imposed platen displacement. This displacement and the associated calculated force per unit length can thus be directly given to the analytical model, along with the rest of the fiber's geometric and material parameters, to feed the inverse identification procedure and identify E_T.

Throughout this analysis the difference between the analytical and finite element models will often be investigated and quantified to verify modeling choices or to highlight analytical model limitations. More precisely, with the use of finite element analysis data, a transverse elastic modulus $E_{T_{id}}$ will be identified through the analytical models by inverse identification, using a least-squares method. This identified modulus will then be compared to the transverse elastic modulus that was defined in the Finite Element Model (FEM), that we will name $E_{T_{sim}}$. The relative difference between the two, ΔE_T, can then be calculated with:

$$\Delta E_T = \frac{E_{T_{id}} - E_{T_{sim}}}{E_{T_{sim}}} \tag{2.27}$$

The average residual of the least-squares identification procedure will also be used to quantify how close the fiber response produced by the analytical model is to the simulated fiber response. It is calculated as follows :

$$\rho = \frac{1}{N}\sqrt{\sum_{i=1}^{N}(U_{i_{sim}} - U_{i_{model}})^2} \tag{2.28}$$

with: N the number of data points, $U_{i_{sim}}$ the fiber displacement given by the simulation and $U_{i_{model}}$ the displacement predicted by the analytical model.

Through these metrics, two main insights can be obtained. Through the residual, the analytical model's ability to reproduce the fiber behavior is estimated. If the residual is small, the response obtained through simulation and the one produced by the analytical model are close. ΔE_T on the other hand, allows to see if the analytical model accurately identifies the transverse elastic modulus of the fiber material. Positive values indicate that the identified transverse elastic modulus is overestimated, a negative value on the other hand signifies an underestimation. It should be noted that these two metrics are independent. The analytical model might be able to accurately reproduce the fiber response, leading to a small ρ values, by over or underestimating E_T, leading to large ΔE_T values. Inversely, the identified E_T value might be close to the one imposed in the simulation for fiber responses that can be quite different, leading to high ρ values. The analytical model's prediction ability is thus not defined by a single of these metrics but is rather estimated through the parallel study of both of them.

2.3.2 Modeling choice validation

In this section a series of studies are presented, to validate a number of modeling choices that aim at making the model as simple as possible while remaining accurate. More precisely, the inherent symmetries of the test will be studied followed by mesh construction and convergence.

SFTCT symmetries

In its typical right circular cylinder representation, the simple geometric nature of the SFTCT offers 3 symmetry planes, as represented in Figure 2.6. These symmetries can be used in order to greatly reduce the size of the created FEM. The yz symmetry allows to model only half of the fiber length, while the xy symmetry allows to model the compression model in a two-dimensional plane. Even though the xz symmetry would further reduce the size of the model to a quarter of the fiber, some caution is needed when considering it. The upper and lower platens perform different functions, the former moving along the y direction, compressing the fiber while the latter remains stationary. Platen movement is thus not symmetric with respect to the xz plane. A movement of the lower platen along the $-y$ direction would allow however to use the said symmetry plane. An equivalence between these mobile-fixed and mobile-mobile platen configurations can be drawn. For a displacement dy of the upper platen in the mobile-fixed configuration a displacement $dy/2$ of the upper platen and $-dy/2$ of the lower platen should provide an equivalent fiber response.

In order to validate the choice in fiber symmetries, two separate studies are performed. First, the xy symmetry is considered and the results of a full section (no further symmetry), half section (yz symmetry) and quarter section (yz and xz symmetry) are compared. Then, the xy symmetry is studied, resulting in a comparison between a 2D and 3D model.

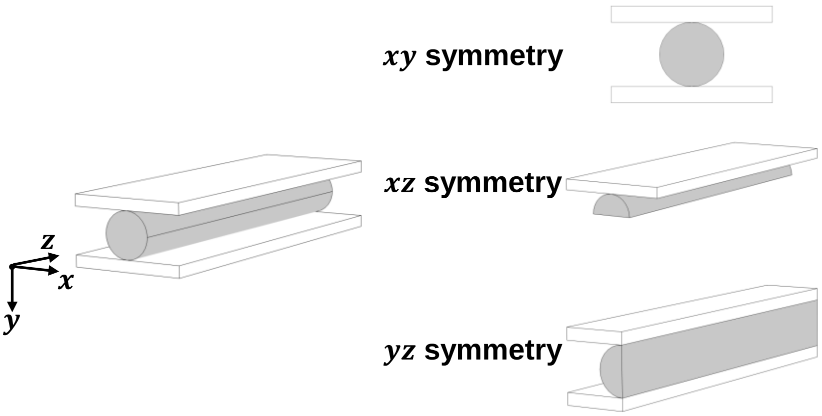

Figure 2.6: The 3 symmetry planes of a single fiber transverse compression test.

2D model - Full, half and quarter sections

Representing the single fiber transverse compression problem in a 2D plane offers many advantages in terms of model size and simplicity. The elongated nature of fibers allows the use of a plane strain formulation, thus eliminating the $\varepsilon_{zz}, \varepsilon_{xz}$ and ε_{yz} strain components. Consequently, the equations for the compression stresses can be formulated as follows :

$$\begin{cases} \sigma_{xx} = \frac{E_T}{1-\nu_{TT}^2-2\nu_{LT}^2\frac{E_T}{E_L}(1-\nu_{TT})}\left(\left(1-\frac{E_T}{E_L}\nu_{LT}^2\right)\varepsilon_{xx}+\left(\nu_{TT}+\frac{E_T}{E_L}\nu_{LT}^2\right)\varepsilon_{yy}\right) \\ \sigma_{yy} = \frac{E_T}{1-\nu_{TT}^2-2\nu_{LT}^2\frac{E_T}{E_L}(1-\nu_{TT})}\left(\left(\nu_{TT}+\frac{E_T}{E_L}\nu_{LT}^2\right)\varepsilon_{xx}+\left(1-\frac{E_T}{E_L}\nu_{LT}^2\right)\varepsilon_{yy}\right) \\ \sigma_{zz} = \nu_{LT}(\sigma_{xx}+\sigma_{yy}) \end{cases} \tag{2.29}$$

Despite this apparent simplicity however, 2D modeling of SFTCT can prove challenging. When modeling highly anisotropic fibers, where the ratio E_T/E_L becomes small, numerical locking can occur due to a disproportionately large out of plane stress [Suri 96]. Consequently, no convergence can be obtained. To represent this, the out of plane to total stress ratio r_σ can be calculated (shear stresses are omitted):

$$r_\sigma = \sqrt{\frac{\sigma_z^2}{\sigma_x^2+\sigma_y^2+\sigma_z^2}} \tag{2.30}$$

Figure 2.7 shows r_σ for three anisotropy ratios for a quarter fiber model for an upper platen displacement of $0.5\,\mu m$ (equivalent to $1\,\mu m$ in mobile-fixed platen configuration).

The anisotropy ratios are changed by keeping E_T at $1GPa$ and increasing E_L. As E_L increases, the ratio of out of plane to total stress becomes greater and greater. For $E_T/E_L = 1/6$ the simulation does not converge anymore.

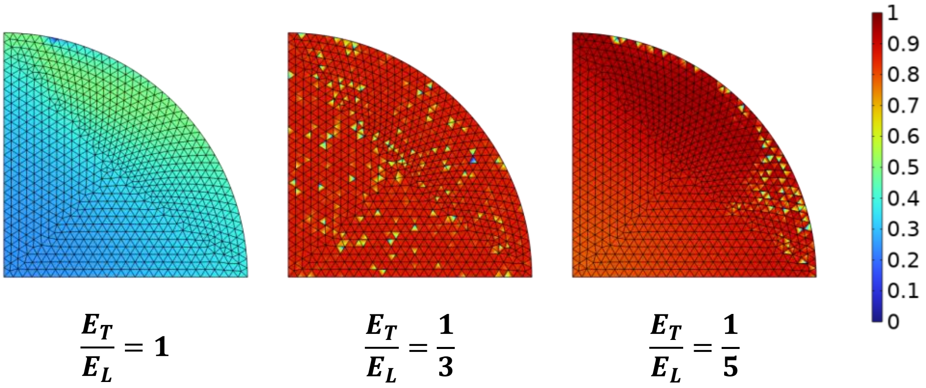

Figure 2.7: Out of plane stress ratio r_σ for different anisotropy ratios.

Defining $\nu_{LT} = 0$ solves this problem by resulting in $\sigma_{zz} = 0$, thus decoupling the in and out of plane fiber behavior. This definition has no major influence on the in-plane stresses σ_{xx} and σ_{yy} since ν_{LT} is always a product of E_T/E_L which becomes negligible for highly anisotropic fibers. The resulting stress equations are thus:

$$\begin{cases} \sigma_{xx} = \frac{E_T}{1-\nu_{TT}^2}(\varepsilon_{xx} + \nu_{TT}\varepsilon_{yy}) \\ \sigma_{yy} = \frac{E_T}{1-\nu_{TT}^2}(\nu_{TT}\varepsilon_{xx} + \varepsilon_{yy}) \\ \sigma_{zz} = 0 \end{cases} \tag{2.31}$$

By fixing $\nu_{LT} = 0$ Jawad's model for SFTCT takes the form obtained with the $E_L \gg E_T$ hypothesis which can be written:

$$U = \frac{4F_L}{\pi}\Bigg[S_{11}\Big(sinh^{-1}(R/b) + ln(2)\Big) - \frac{1}{2}(S_{11} + S_{12}) + S_{12}\frac{R}{b}\Big(\sqrt{1+(R/b)^2} - R/b\Big)\Bigg] \tag{2.32}$$

with b the half-contact width:

$$b = \sqrt{\frac{4FR}{\pi E_T}} \tag{2.33}$$

Using this assumption on ν_{LT}, the full, half and quarter cross sections can be simulated. For the half fiber model, the symmetry condition $u_x = 0$ is used on the y axis. The symmetry condition $u_y = 0$ is added along the x axis for the quarter fiber model. While these symmetry conditions block any potential fiber rigid body movement, this is not the case for the full fiber section, which is free to move along the x axis. For this reason, the horizontal translation of the lowest fiber point, which is the first to be in contact with the lower compression platen is blocked ($u_x = 0$).

The resulting force and displacement results are essentially identical for all models, as can be seen in Figure 2.8. To correctly compare between models, the force per unit length has to be multiplied by 2 when the yz symmetry and xz symmetry are used. The upper platen displacement has also to be multiplied by 2 when the xz symmetry is used.

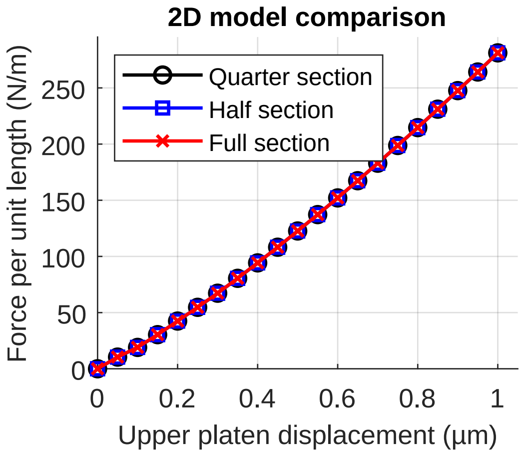

Figure 2.8: Comparison of 2D SFTCT models.

Table 2.5 compares the computation time along with ΔE_T and least-squares residual values between models. While differences remain small, the quarter and half model result in the lowest values of both the ΔE_T and the residual while offering a significantly faster computation time. The quarter fiber model can thus accurately model fiber behavior in addition to lowering computation time and leading to a good prediction of E_T by the analytical model. Its only limitation lies in the study of displacement fields. The quarter fiber model will, due to its boundary conditions, produce no vertical displacement on the center of the fiber. The displacement field will thus be different then in a mobile-fixed platen configuration. Therefore, if fields studies are necessary the half model should be used instead of the quarter one.

2D Model	**CPU time**	$\boldsymbol{\Delta E_T}$**(%)**	**Residual (nm)**
Quarter	13 s	$-3 \cdot 10^{-4}$	0.4334
Half	19 s	$-3 \cdot 10^{-4}$	0.4344
Full	44 s	0.02	0.4388

Table 2.5: Comparison of analytical model identification ability and computation time for 2D finite element models with different symmetries.

2D and 3D model comparison

With the benefits of the xz and yz symmetries being demonstrated, this section focuses on the comparison between models where the xy symmetry is considered or not. A 2D and 3D quarter fiber model are thus compared. The resulting force per unit length and displacement data can be seen in Figure 2.9. Once again, using symmetries has no major influence on simulated fiber behavior. The computation time along with ΔE_T and residual values for each model, are given in Table 2.6. The difference in computation time is major, going from 10 seconds for the 2D model to over 3 hours for the 3D model. When compared to the 2D model, the 3D model does produce a lower residual value, the fiber behavior is thus closer to the one described by the analytical model, it comes however with a significant increase in the value of ΔE_T.

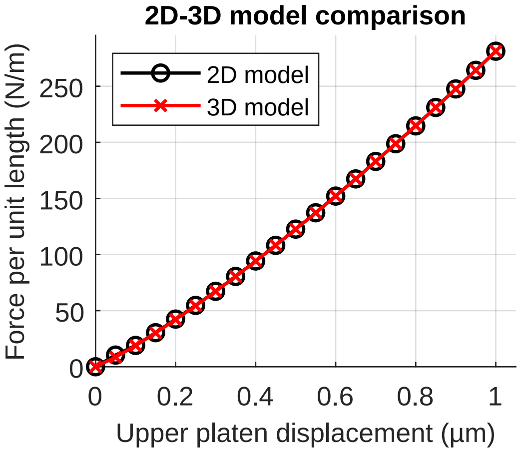

Figure 2.9: Comparison of analytical model identification ability and computation time for 2D and 3D quarter fiber finite element models.

Model	**CPU time**	$\boldsymbol{\Delta E_T}$**(%)**	**Residual (nm)**
2D	10 s	$-3 \cdot 10^{-4}$	0.43
3D	3h 43min	-0.34	0.05

Table 2.6: 2D-3D model comparison.

These differences between the 2D and 3D model results can be explained analytically: for the analytical model, fiber behavior is a function of the fiber's material properties $(E_L, E_T, \nu_{LT}, \nu_{TT})$, its radius R, its radial displacement U and of the compression force per unit length F_L. The FEM shares all of these parameters with the only exception being the compression force which is calculated with:

$$F_L = \int_{-b}^{b} \sigma_{yy} dx \cong \int_{-Rcos(\pi/3)}^{Rcos(\pi/3)} T_{n_y} dx \tag{2.34}$$

For a transversly isotropic material σ_{yy} takes the form :

$$\sigma_{yy} = \frac{E_T}{1 - \nu_{TT}^2 - 2\nu_{LT}^2 \frac{E_T}{E_L}(1 - \nu_{TT})} \left(\left(\nu_{TT} + \frac{E_T}{E_L}\nu_{LT}^2\right)\varepsilon_{xx} + \left(1 - \frac{E_T}{E_L}\nu_{LT}^2\right)\varepsilon_{yy} + \left(\nu_{LT} + \frac{E_T}{E_L}\nu_{LT}^2\right)\varepsilon_{zz} \right) \tag{2.35}$$

In our 2D, plane strain model, $\varepsilon_{zz} = 0$ and $\nu_{LT} = 0$. Thus :

$$\sigma_{yy} = \frac{E_T}{1 - \nu_{TT}^2}(\nu_{TT}\varepsilon_{xx} + \varepsilon_{yy}) \tag{2.36}$$

In the case of the 3D model, the fiber is highly anisotropic, therefore $E_L >> E_T$. The term E_T/E_L can thus be omitted, which simplifies the equation to:

$$\sigma_{yy} = \frac{E_T}{1-\nu_{TT}^2}\left(\nu_{TT}\varepsilon_{xx} + \varepsilon_{yy} + \nu_{LT}\varepsilon_{zz}\right) \tag{2.37}$$

The main difference between the two models is thus the presence of the longitudinal strain ε_{zz}. This term along with border effects on the 3D geometry lead to minor differences with the 2D plane strain model, thus resulting in a higher value of ΔE_T. Nevertheless, these values remain small as long as the anisotropy ratio E_L/E_T remains large, since it results in minor values of ε_{zz}. If the anisotropy ratio is however lower, then ε_{zz} is not negligible and plane strain conditions are not respected. Differences between the 2D planes strain and 3D model become more important as a result. This correlation between anisotropy ratio, ε_{zz} and ΔE_T is shown on Figure 2.10. For anisotropy ratios over 20, longitudinal strain values remain very small and ΔE_T values stabilize to near zero. For lower anisotropy ratios however ε_{zz} increases leading to ΔE_T values of up to 15% for an isotropic case.

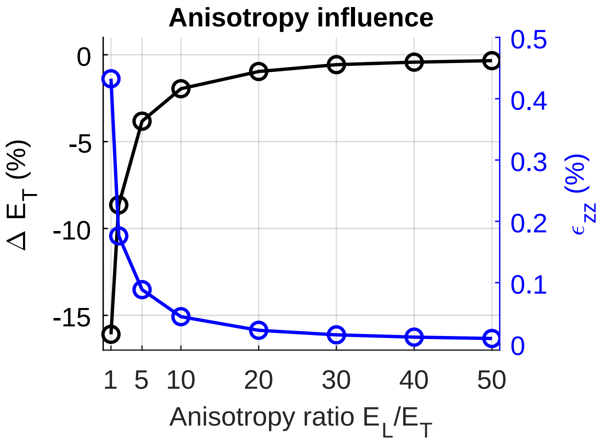

Figure 2.10: ΔE_T as a function of fiber anisotropy.

To conclude, the use of a 2D model, analytical or finite element, is better suited to cases of high E_L/E_T ratios, where ε_{zz} values are low and plane strain conditions are thus applicable. If this condition is respected, a great gain in computation time can be achieved with a 2D simulation and the fiber's transverse elastic modulus is correctly identified. For fibers with lower anisotropy ratios, caution should be used as plane strain conditions will not be fully respected. Errors will therefore be made on the identification of their transverse elastic modulus when a 2D plane strain model is used.

2.3.3 Mesh optimization

Selecting the right mesh for a given problem is a key part of every Finite Element Analysis (FEA). The accuracy of the solution must be guaranteed while also keeping the memory requirements at a minimum and convergence as easy as possible. To do so, a compromise in terms of the number of mesh elements (or degrees of freedom) and solution accuracy should be found. Mesh skewness should also be kept at a minimum along with the aspect ratio of the elements [Wollblad 18a, Wollblad 18b]. The mesh should also be smooth, abrupt changes in element size should be avoided. In this section a mesh element type is chosen and a mesh convergence study is performed. When it comes to the platen mesh, the same approach will be used in all studies. Being a rectangle, the platen will be meshed with mapped, structured quadrilateral elements, which seamlessly fit its geometry. Being the master in the contact pair, the platen can be meshed more coarsely than the fiber. For this reason, elements twice the size of the fiber elements are used in all studies.

Choice of mesh element type

Given the mainly two-dimensional nature of the studied problem two types of mesh elements are available: triangular and quadrilateral. Triangular elements are the default meshing choice. They represent a simplex, meaning any 2D surface can be meshed with triangles, regardless of shape or topology. Triangles are avoided when linear shape functions are used, since they lead to constant strain inside the element. For the quadratic shape functions used in our studies however, they represent a valid choice. Quadrilateral elements typically lead to higher accuracy, but do not adapt as easily to all geometries. Elements with higher aspect ratios or higher skewness can occur when trying to mesh complex shapes. This is especially true for structured meshes, where the connectivity between elements is regular. Using free quadrilateral elements can combat this issue, since it allows for irregular connectivity between elements. They can lead however to a worse convergence or lower accuracy [Frei 13].

In this work, complex geometries will be studied through FEA in order to study the influence of plant fiber morphology on the identification ability of analytical models. For this reason triangular elements will be used in all studies since they represent the best compromise in terms of solution accuracy and ability to create good quality meshes regardless of morphology. A detailed study of mesh quality and accuracy for different mesh elements is presented in appendix A.4.

Mesh convergence study

With the choice of model symmetry and element type being made the question of mesh convergence can now be approached. The element size will be kept the same on the whole fiber section. The maximum size of on an edge of the triangular element will be equal to R/N where R the fiber radius and N a scalar with values from 2 to 40. By keeping an uniform mesh across the whole fiber section, its refinement can be controlled through the variation of a single parameter, N. Figure 2.11 illustrates five different levels of mesh refinement.

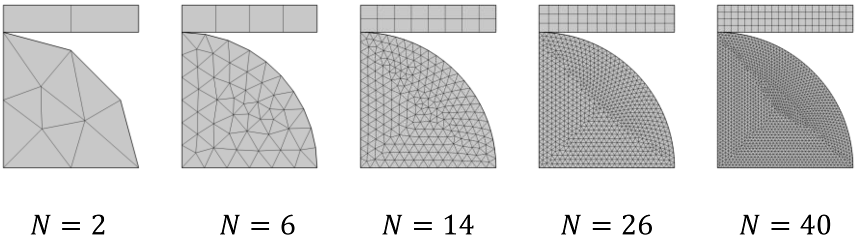

Figure 2.11: Five levels of mesh refinement of the finite element model mesh convergence study.

To evaluate the convergence of the finite element model, ΔE_T and the least-squares residual is used. If the values of these parameter converge, the analytical model closely describes the simulated fiber behavior for the same identified value of E_T. The simulated fiber behavior is thus stabilized and the solution given by the finite element model has converged. Consequently, a reference is established for what an accurate finite element solution to this SFTCT problem is.

If establishing a low value of ΔE_T was the only goal, a common approach would be to manually refine the mesh in the contact zone, in order to have the maximum precision in the integration of the contact pressure T_{n_y}, while having a coarser mesh for the rest of the fiber in order to reduce the size of the model. The resulting ΔE_T and residual would then be compared to the one of the uniform mesh to verify model accuracy. This manual mesh readjusting and case by case convergence study is however not realistic in our case, where a great number of fiber geometries will be simulated. Instead, given the fast computation time of the 2D models, an element size that produces satisfying values of both ΔE_T and residual, will be chosen and used throughout all the simulations of different geometries. This should keep solutions accurate even for complex geometries without manual adjustments and separate convergence studies at the the expense of some computation time.

The evolution of ΔE_T and the residual as a function of the radius subdivision N can be seen in Figure 2.12. ΔE_T starts stabilizing at $N = 10$ and remains steadily under $0.5\,\%$, from $N = 14$ and onward, reaching its minimum value at $N = 26$. Variations after this point are extremely minor. It can be observed however that the value of the residual stabilizes later at around $N = 35$ and reaches its minimum at $N = 48$. This can be explained by the precision of T_{n_y} for very small displacements. In these cases, very few elements are in contact with the platen resulting in some error in its integration. Figure 2.13 illustrates this phenomenon. For displacements of $0.05\,\mu m$ a difference in force can be seen between three mesh refinements levels. For greater displacements however forces are essentially identical. This very local error does not justify the switch from $N = 26$, which produces the lowest ΔE_T, to $N = 48$, which produces the lowest residual. Eliminating this small error would require an increase in computation time, if the mesh is to be kept uniform, or a local refinement of the mesh, which as explained previously is not in the best interest of this study. By choosing $N = 26$, a converged value of ΔE_T is used at the expanse of a small error on the force estimation at the lowest displacement level.

2.3.4 Conclusions

In this section, the construction and validation of a SFTCT finite element model was presented. Model symmetries were shown to be crucial in order to reduce the size of the model. If no displacement field analysis is needed, modeling a quarter of the fiber is the best option. The importance of the anisotropy ratio E_L/E_T was also shown. This highlights an important limitation of the analytical models, since they identify with less precision the transverse elastic modulus in these cases. If the anisotropy ratio is higher however, a 2D model can be used, leading to huge gains in computation time with the analytical model identifying E_T more accurately in parallel. When it comes to meshing the use of triangular element is the most adapted for a fiber under transverse compression. After a mesh convergence study, the element size resulting in the lowest value of ΔE_T is chosen.

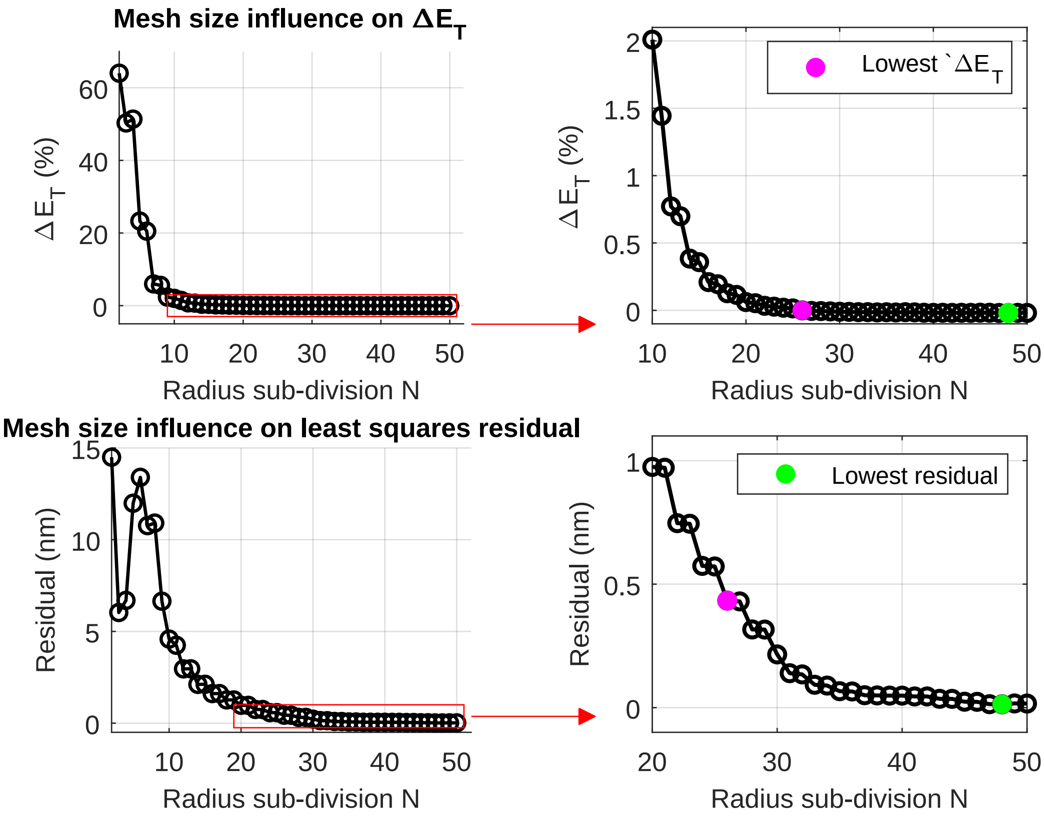

Figure 2.12: Mesh convergence study through the evolution of ΔE_T. The graphs on the right represent the values inside the right rectangles on the left graphs.

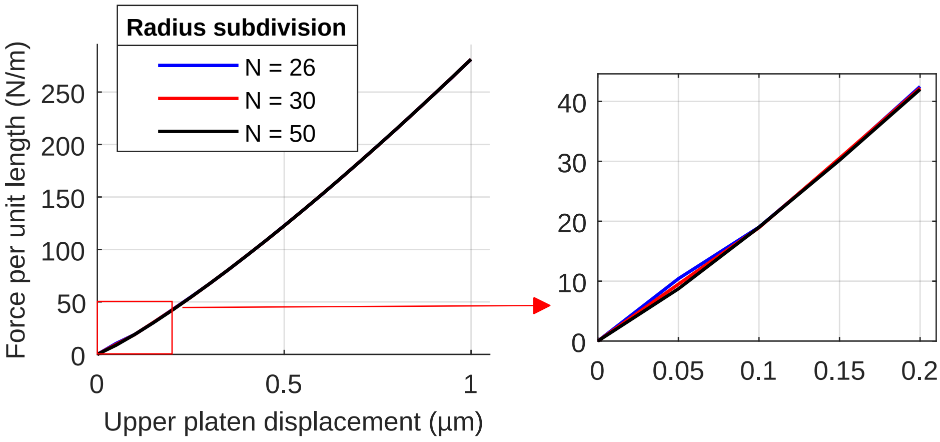

Figure 2.13: Force-displacement data for three different mesh refinement levels. The graph on the right represents the values inside the right rectangle on the left graph.

2.4 Identification error caused by main plant fiber geometric characteristics

While all analytical models represent the fiber as a right circular cylinder, many variations in fiber geometry can occur. This is especially true for plant fibers. With the finite element model of SFTCTs being developed and validated, it is used to simulate the transverse compression of plant fibers with ideal representations of their most common geometric characteristics. These studies aim at providing a basic understanding of the impact of these characteristics on fiber behavior and by consequence on the identification of their transverse elastic modulus E_T. The ability of the analytical model to identify E_T, despite this added geometric complexity is quantified through the ΔE_T metric and the residual of the least squares fitting. Similar studies have been performed for tensile testing (see subsection 1.4.1), but to the author's knowledge, no such work exists for SFTCTs.

2.4.1 Choice of studied parameters

As discussed in Chapter 1, plant fibers show significant morphological complexity. Along their cross section plant fiber posses the central porosity of their lumen, while limited space inside the stem during growth, leads to flattened elliptical or polygonal geometries. The SEM observations shown in Figure 2.14 illustrate such geometries.

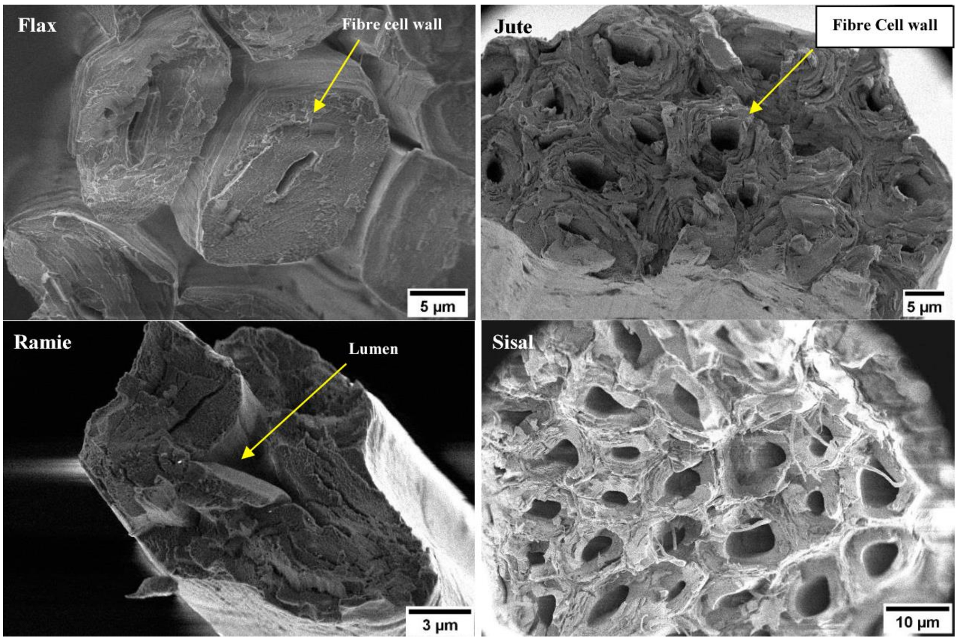

Figure 2.14: Scanning electron microscope observations of plant fiber cross sections [Hamad 17]. A single fiber is shown in the case of ramie (bottom left) with the rest being fiber bundles

Plant fiber morphology is also complex along their length, where important variations in cross section can be observed [Charlet 07, Charlet 10b]. The fiber can also be twisted along its longitudinal axis, or present kink bands. This length-wise geometric variability is very difficult to predict. Accurately, reconstructing the 3D geometries of the fibers requires costly and time consuming means, such as microtomography. Simulation of the mechanical loading of these 3D geometries can then be performed, as was done for tensile tests [Richely 22a, Guessasma 19, Beaugrand 15], it is however computationally expensive. While never performed, this would especially the case in the simulation of SFTCTs where contact between the fiber and the platens must be modeled.

During mechanical testing, tensile preloading can significantly reduce fiber twist while transverse compression preloading can force the fiber's major ellipse axis to realign and become parallel with the compression platens. The influence of longitudinal variations on fiber behavior is thus reduced.

For these reasons, as a first step in the study of the influence of plant fiber morphology in the context of SFTCTs, the fiber's cross section will be considered unchanged along its length. The influence of lumen size, ellipse flatness and contact zone flatness will be evaluated through finite element analysis. Each geometric parameter will be studied independently and using an idealized geometric representation. Following the results of the studies in the previous section, a 2D finite element model considering all three symmetries will be used as the basis to model these geometries. The fiber cell wall will be modeled as a single layer.

2.4.2 Lumen

The lumen is a common characteristic of plant fibers. To simulate this central void, the fiber is considered as perfectly circular with a radius R. A concentric circle of radius R_L is subtracted from the original circle to create the lumen, as seen in Figure 2.15. To study its influence, the ratio R_L/R is varied from 0 to 0.9 with a step of 0.05, covering all type of different lumen sizes. The resulting force-displacement data can be seen in Figure 2.16. For a given displacement value, the resulting force per unit length decreases with an increase in the lumen size. This can be explained by the structural response of the fiber. When the fiber is full, *i.e* $R_L/R = 0$, it deforms locally close to the contact zones, resulting in high stress concentrations in these areas. However, the presence of the lumen renders the fiber more compliant, with the central void of the lumen reducing in size as the fiber is compressed by the platen. We can talk in this case of an added structural displacement generated by the presence of the lumen. As a result, stresses are lower and appear in zones of the fiber that are not close to the contact zone, such as the edge of the lumen. The resulting contact force is thus lower for a given displacement. Figure 2.17 illustrates this change in stress magnitude and concentration.

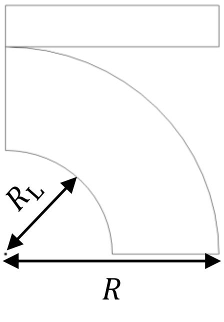

Figure 2.15: Quarter fiber cross section of radius R and central void of radius R_L.

This decrease in force has also repercussions in ΔE_T. Jawad's model, not accounting for the presence of a central void, underestimates E_T in order to fit on the simulation data resulting in decreasing, negative values of ΔE_T, as can be seen in Figure 2.18. A

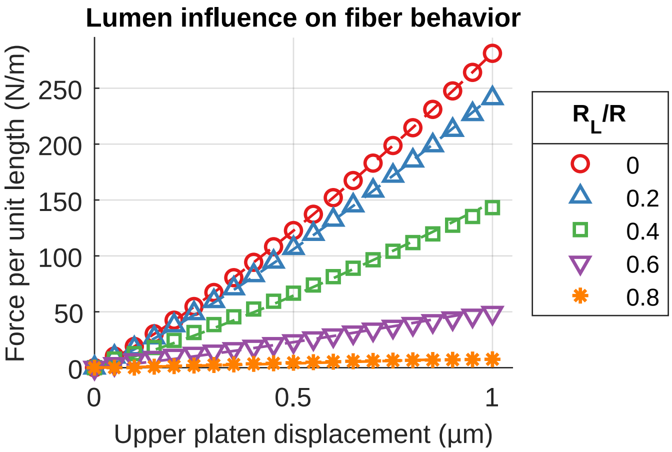

Figure 2.16: Force-displacement results for varying lumen radii R_L. The data from the simulation is represented by markers with the fitted analytical model represented with dotted lines.

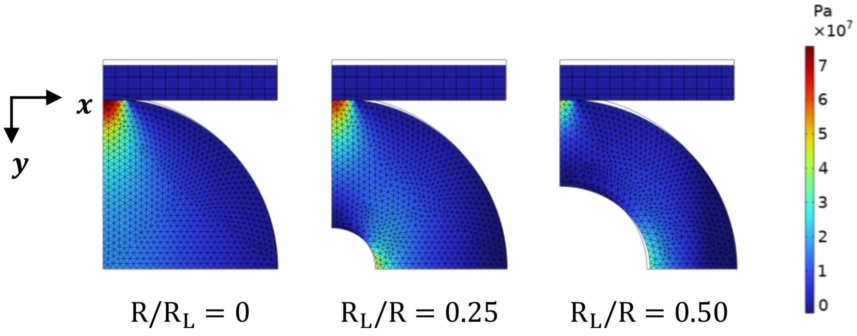

Figure 2.17: σ_{yy} field for various lumen sizes. As the lumen radius increases, stress become less important and expands on the lower part of the lumen. The fiber is shown in its deformed state with black continuous lines representing its initial position.

similar underestimation related to the lumen has be found in tensile tests [Placet 12b]. It is important to note however, that an apparent transverse elastic modulus is identified, that represents both the material and structural response of the fiber under compression. The change in lumen size also produces a slight change in the non-linearity of the force-displacement data, with an increase in lumen size resulting in an increase in the linear nature of the curve. This change leads to a change in the least square residual, as seen in Figure 2.18. The increase in lumen size leads to an increase in the residual, the analytical model's ability to reproduce the simulation data is thus decreased. However, the value of the residuals remains low for $R_L \leq 0.6R$, its influence on fitting quality is thus limited. The analytical model is therefore capable of producing fiber responses that are typical of fibers with lumens. As a consequence, ΔE_T should be approached with caution. It represents the difference between an apparent modulus identified by the analytical model, which represents both the material and structural response, and the modulus of the fiber's cell wall defined in the FEM. Depending on the context of characterization, one measure might be of interest over the other.

In any case, ΔE_T changes in a major way as a function of the lumen size. Lumen size, on the other hand, can change significantly as a function of plant species, growing conditions and maturity level [Bourmaud 18]. Figure 2.19, shows the lumen area as a

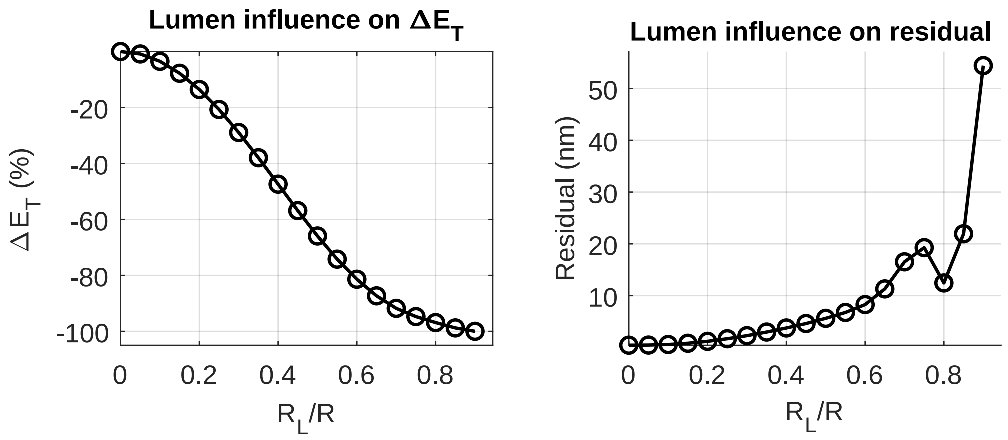

Figure 2.18: Evolution of ΔE_T (left) and least squares residual (right) as a function of lumen radius.

percentage of the total fiber area for various fiber varieties. When focusing on the bast fiber of interest in this study, flax fibers have lumens that are generally under 10% of the fiber surface ΔE_T is thus very minor, staying under 10%. Hemp fibers have a larger lumen ranging around 12% to 16%, which leads to ΔE_T under 20%. Nettles fiber E_T underestimations are potentially up to 30%, since based on our experience, they posses the largest lumen among the bast fibers of interest at 20% to 30%. Most plant fibers have lumen of similar sizes as flax, hemp or nettle. Abaca, kenaf and kapok are unique in terms of lumen size since they it can reach 45%, 60% or 90% respectively leading to major ΔE_T values that can reach up to 100%. It is important to note however that both the fiber and the lumen are perfectly circular in our studies. When fiber geometry is different its interaction with the lumen could lead to different ΔE_T values that can be more or less important. Results point however to moderate underestimations of the identified modulus when $R_L \leq 0.3R$, which can be found at good plant maturity for the most popular plant species. Identifying E_T with an analytical model that considers the fiber as a uniform cylinder is thus a viable option for these fibers.

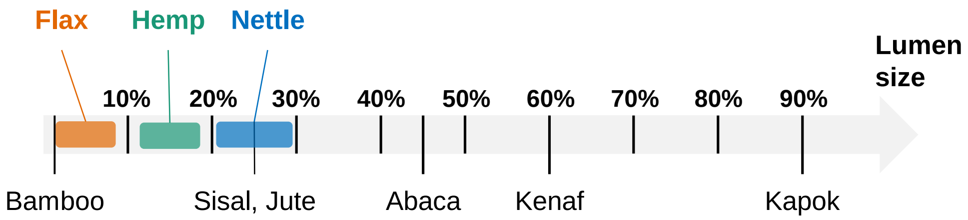

Figure 2.19: Lumen size (lumen area/ total surface area) for different plant species. Figure adapted from [Richely 21b] with added data from [Bourmaud 18]. Nettle lumen size is based on our own observations.

A few further conclusions on plant fiber SFTCTs can be drawn from these studies. The ability of the fiber to recover to its initial structure after the lumen compresses is not guaranteed. This means that if a second compression takes place, the structural displacement of the fiber due to the lumen collapsing could be less important. In this case the fiber's walls themselves will compress more. The decrease in structural displacement and increase in material deformation will lead to a higher identified transverse elastic modulus. In other words, the fiber's identified modulus could stay low, as long as the lumen is able to recover after compression, and increase once a certain threshold has been passed and the lumen irreversibly collapses. The lumen's likelihood of permanent collapse would be a function of the lumen's size and geometry, compared to the fiber's, along with the material properties of the fiber wall. In conclusion, it is important when performing plant fiber characterization to interpret its behavior as one of a structure instead of just a material and analyze results accordingly.

Creating analytical models that model central porosities could improve the prediction of plant fiber behavior. Analytical work on such models can be found in the context of the semi-ring test [Markides 18] or the compression of hollow bones [Womack 08].

2.4.3 Elliptical geometry

The majority of plant fiber cross sections are closer to an ellipse than a circle, due to the restricted space during growth inside the plant stem. Simulating the influence of cross section ellipticity on fiber behavior is thus important to understand plant fiber behavior. Such studies have been performed in the case of tensile test simulations [Del Masto 17]. The procedure used to simulate ellipticity in the case of SFTCT is explained below.

In order to simulate an elliptical geometry, the fiber's cross section is modeled as an ellipse, with its major radius being noted R and its minor radius being noted r, as seen in Figure 2.20. A plant fiber's major axis is typically in the range of our R parameter ($16\mu m$) with the minor radius being smaller. To study the influence of the fiber's elliptical geometry on ΔE_T the ellipse's flattening factor $f = 1 - r/R$ is changed from 0.05 to 1 with a step of 0.05, by modifying r. The higher the fiber's flattening factor, the more elliptical its shape is, with a factor of zero representing a perfect circle. The elliptical form of the fiber increases the contact zone with the platen, adapting the potential contact zone in the finite element model is thus important. As seen in Figure 2.5, when the yz symmetry is used, the contact zone represents an arc of $\pi/6$ with its limits at $Rcos(\pi/3)$ on the x axis and $Rsin(\pi/3)$ on the y axis. To adapt the contact zone according to the fiber's aspect ratio, the limits of the contact zone are defined as $Rcos(\frac{r}{R}\pi/3)$ and $Rsin(\frac{r}{R}\pi/3)$ for the x and y axis respectively. With this definition the potential contact zone increases proportianally as the fiber gets more elliptical. To adapt to the change in fiber size the mesh element size is set as $R_{mean}/26$ with $R_{mean} = (R + r)/2$.

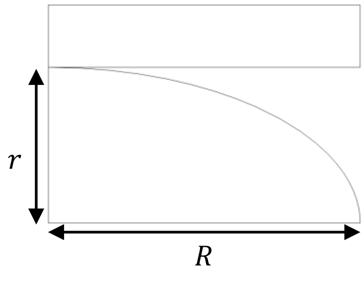

Figure 2.20: Quarter elliptical fiber cross section of of major radius R and minor radius r.

The force-displacement data for different ellipse flattening factors can be seen on Figure 2.21. Increased elliptical shapes (higher f values) lead to a larger half contact width b and larger stress concentrations close to the contact zone, resulting in an important increase in the force per unit length for a given platen displacement. By consequence, analytical models will significantly overestimate E_T since they do not take the elliptical geometry into consideration.

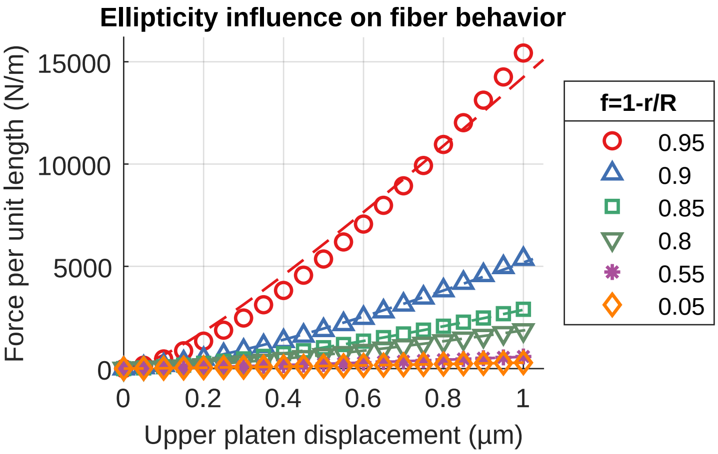

Figure 2.21: Force-displacement results for different ellipse flattening factors. The data from the FE simulation is represented by markers with the fitted elliptical analytical model (presented hereafter) represented with dotted lines.

This limitation becomes apparent when ΔE_T is considered. To evaluate it, three different methods are compared. The first consists of using the major ellipse radius R as a model input in the inverse identification procedure with the second one using the minor radius r. The third methods uses both R and r in different parts of the analytical model. When single fiber transverse compression occurs, rigid body movements and rotations usually result in the fiber aligning its major radius to the compression platens. The contact half width b is thus majorly influenced by R. For this reason, in the analytical calculation of b, the major fiber radius is used.

$$b = \sqrt{\frac{4FR}{\pi E_T}} \tag{2.38}$$

On the other hand, the effective compressed fiber radius corresponds more closely to the minor fiber radius r, it is thus used in the rest of the analytical model. Figure 2.22 helps illustrate the aforementioned modeling choices. This new simple model that accounts for the fiber elliptical geometry can be written as follows:

$$U = \frac{4F_L}{\pi}\left[S_{11}\left(sinh^{-1}(r/b) + ln(2)\right) - \frac{1}{2}(S_{11} + S_{12}) \right.$$
$$\left. + S_{12}\frac{R}{b}\left(\sqrt{1 + (r/b)^2} - r/b\right)\right] \tag{2.39}$$

The evolution of ΔE_T as a function of the ellipse flattening factor can be seen on Figure 2.23. The elliptical geometry has a major influence on the identified E_T with higher flattening factors resulting in very high values of ΔE_T. The choice of the geometric parameter input in the analytical model is also very influential. Providing the major radius

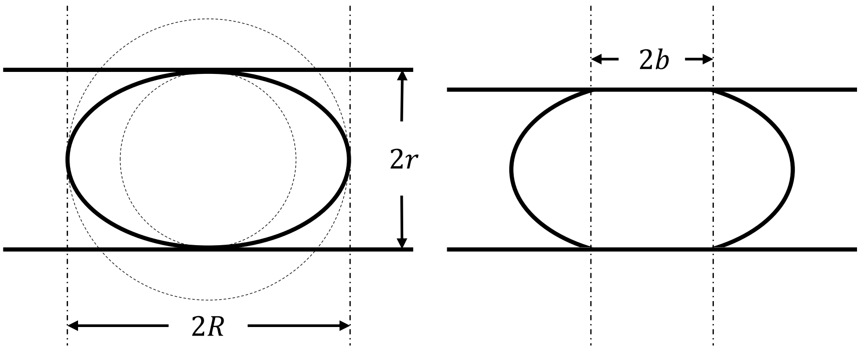

Figure 2.22: Representation of compression of elliptical fiber. The contact width $2b$ is mainly influenced by the major radius R while the compressed radius corresponds to the minor radius r.

R as an input leads to the highest values of ΔE_T. The minor radius r significantly reduces the identification error. If only one geometric parameter is used it is thus preferable to use the effective compressed radius of the fiber. However, using the simple proposed elliptical model leads consistently to the smallest ΔE_T values. The same trends are also observed in the least squares residual with the elliptical model producing the lowest residual. Similarly to the lumen study, residual values remain low attesting to good fit quality regardless of the fiber ellipticity except for the largest flattening ratios.

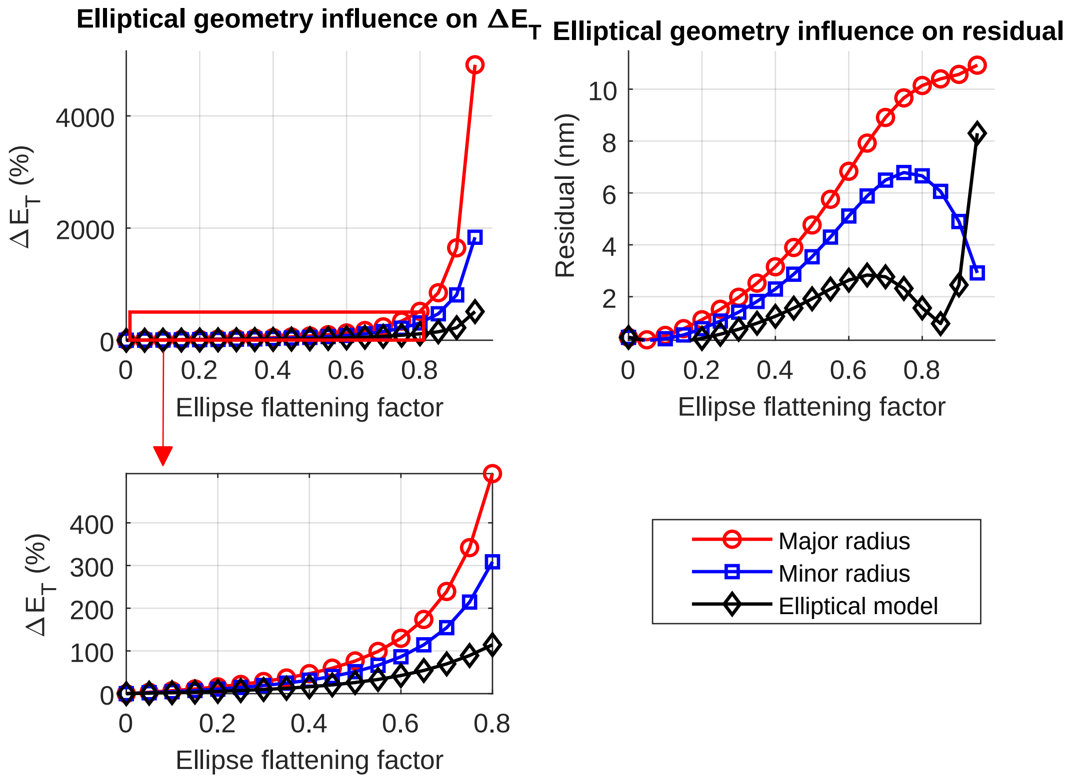

Figure 2.23: Evolution of ΔE_T (left) and least squares residual (right) as a function of the ellipse flattening factor for three different inputs in the analytical model. The bottom figure gives a closer look to data inside the red rectangles.

Once again, plant fiber ellipticity strongly depends on a number of parameters from plant species to growing and extraction conditions. Bibliography on the elliptical nature of plant fibers is scarce, however some data can be found. On their study on flax fiber morphology Mattrand et al. [Mattrand 14] reported an average flattening factor of 0.25 by considering Feret diameters. Also on flax, Aslan et al. [Aslan 11] measured flattening factors of 0.1 to 0.57. Measurements performed in the context of this doctoral thesis on flax, hemp and nettle found their average flattening ratios to be 0.4 for flax and hemp, and 0.7 for nettle (see Table 3.6). For flax and hemp this would lead to a ΔE_T of 16%, if the elliptical analytical model is used. For nettle fibers however the ΔE_T value would be at 70%, a significant overestimation.

In conclusion, measuring a major and minor radius of a fiber is crucial when performing SFTCTs. These measurements along with the proposed analytical model that accounts for both major and minor radii lead to low values of ΔE_T for the most plant fibers. Nevertheless, the exponential increase of ΔE_T as function of the flattening factor means that overestimations can easily become major for slightly more elliptical geometries. Developing a new analytical model for elliptical geometries or performing inverse identification through a finite element model seems to be the best choice for these more extreme cases of ellipticity.

2.4.4 Flatness

In addition to elliptical cross sections, the reduced space inside the plant stem can also result in a flatter outer surface of the fiber. The flat section typically occurs along the longer side of the fiber (in the direction of the major radius) where the contact surface with neighboring fibers is the largest. In order to model this flatter region, the fiber cross section is constructed in 2 sections. First, a quarter of a circular cross section of a radius R is constructed. A rectangle of height equal to R and of a variable width w is then added to simulate the flat section as can be seen on Figure 2.24. The width of the contact zone is kept at arc of $\pi/6$ along the circular part of the geometry. The influence of this flat section will be evaluated by modifying the ratio w/R from to 0 to 1 with a step of 0.05, by modifying w. Similarly to the elliptical geometry study, ΔE_T will be evaluated through different methods by providing: a major radius of $R + w$ or a minor radius of R to Jawad's model. The ΔE_T resulting from the use of the elliptical model will also be evaluated.

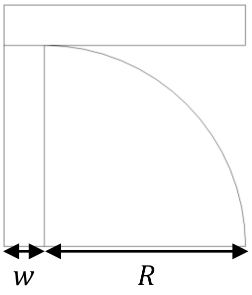

Figure 2.24: Quarter fiber cross section with a flat section of width w.

Figure 2.25 illustrates the force per unit length as a function of upper platen displacement for different values of w/R. The added flat section causes an increase in the contact zone between the fiber and the platen resulting in a higher force for a given displacement.

The flat section also causes the fiber response to become more linear. As the flat section becomes more important the fiber's geometry gets closer to a rectangle which, since the material is purely elastic, would produce a linear response.

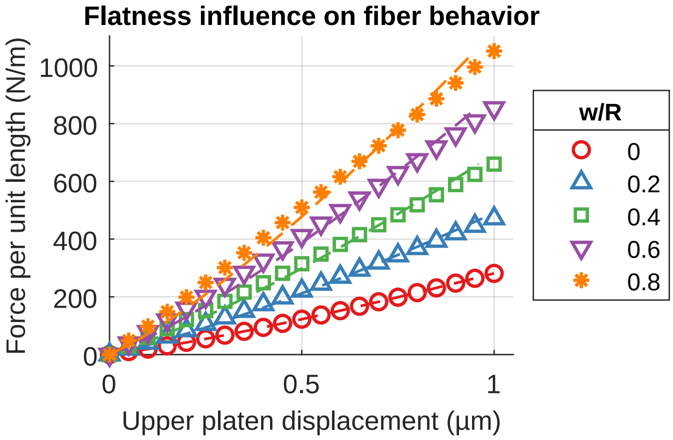

Figure 2.25: Force-displacement results for different aspect ratios w/R. The data from the simulation is represented by markers with the fitted elliptical analytical model represented with dotted lines.

The influence of the flat fiber section on the force per unit length is passed on to ΔE_T. As seen in Figure 2.26, the increase in contact force for a given displacement results in an overestimation of the fiber's transverse elastic modulus by the analytical model. Contrary to the elliptical geometry that led to an exponential increase of ΔE_T, the increase for flat sections is linear. Even small flat sections can thus lead to an important error in the identification of E_T. The elliptical analytical model still results in the lowest error in its E_T prediction. Interestingly, it produces however the higher least-squares residual, which remains nevertheless in the range of all previously studied residuals. The analytical model is thus able to reproduce the response of flat fibers rather well.

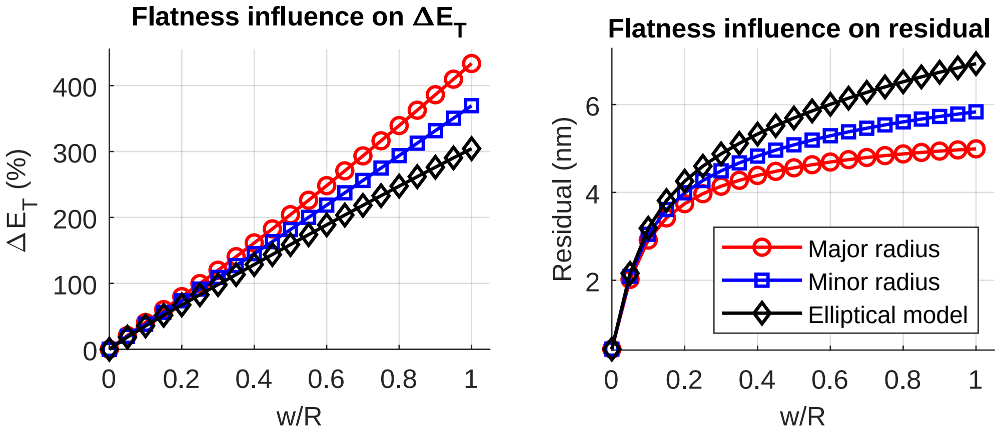

Figure 2.26: Evolution of ΔE_T (left) and least squares residual (right) as a function of the aspect ratio r/R for three different inputs in the analytical model.

Predicting the width of flat fiber sections as function of plant species, growth etc. proves to be more difficult than estimating lumen size and ellipticity. To the authors knowledge, no direct quantification of this morphological parameter exists in the literature. Legland and Beaugrand [Legland 13] quantified the rectangularity of lignocellulosic fibers by computing the ratio between the fiber surfaces and the Feret orientated rectangle. While this can help estimate fiber flatness it does not provide direct quantifiacations. Given the uncertainty on this parameter and its important influence even for minor values, special attention should be given to fiber flatness. For that reason, when studying the compression of flatter fibers it should be noted that the identified transverse elastic modulus of the fiber is more than likely overestimated. It is however safe to assume that the flat section width is typically inferior to 30% of the fiber radius, which would place the highest value of ΔE_T at around 100%. Similarly to the conclusion drawn for elliptical geometries however, an adapted analytical model or finite element model should be used for the identification of E_T for the more extreme cases of fiber flatness in order to avoid severely overestimating the fiber modulus.

2.4.5 Comparing main geometric parameters

The influence of each of the studied geometric parameters on the identified fiber transverse elastic modulus was shown along with the underlying mechanical phenomena that lead to fiber behavior variations. Each parameter however was studied independently and in an ideal case (circular lumen and fiber, perfect ellipse, perfectly flat sections). Nevertheless, comparing the influence of these parameters on ΔE_T can still provide valuable insight into the behavior of fibers that are far from these ideal geometric approximations without performing complex simulations. The evolution of ΔE_T as a function of lumen size, ellipse flattening factor and flat contact zone width is shown in Figure 2.27.

We can separate the geometric parameters into two groups: the lumen, which causes an underestimation of ΔE_T and the elliptical geometry and flat section that lead to an overestimation. These groups generate antagonist behaviors, since they can cancel each other out to some extent if the fiber has both a lumen and an elliptical-flat section. When these geometric parameters are combined, low values of ΔE_T could thus be obtained despite the morphological complexity of the fiber. When considered independently, the contact zone flatness is the most influential parameter, since the quasi-linear increase of ΔE_T means that an important identification error is produced across the whole studied parameter range. Elliptical geometries and lumen size have a limited effect on the identified transverse elastic modulus for low ratios (under 0.3) due to the non linear variation of E_T. If flat sections are excluded, lumen size is more influential than the elliptical geometry, up until ratios of around 0.7. Only for larger ratios, the exponential nature of ΔE_T for elliptical geometries leads to important changes that can exceed the underestimating effect of the lumen. In any case, the complexity of fiber behavior under a transverse compression load is apparent even through these ideal case studies. Fiber morphology should be examined carefully to better predict fiber behavior and to anticipate potential over or under estimation of the transverse elastic modulus.

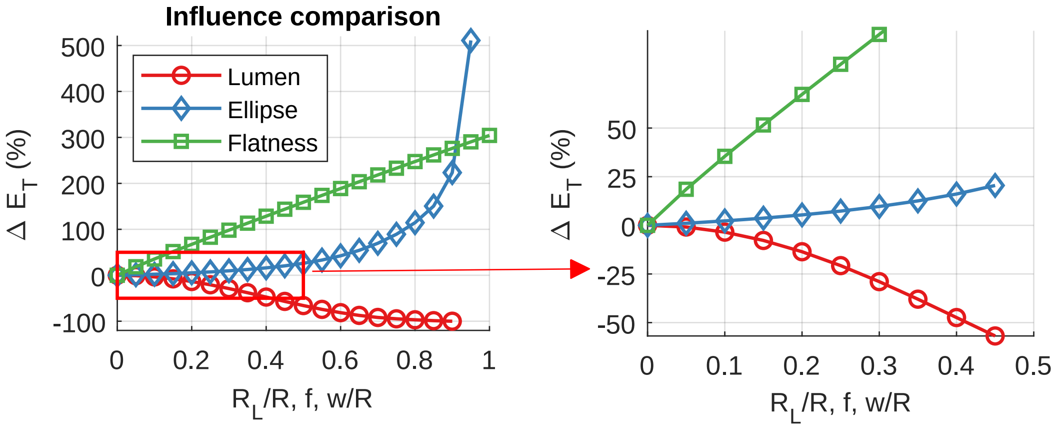

Figure 2.27: Comparison of ΔE_T as a function of different geometric parameters. The right represents a zoom on the parameter space that is the most realistic for bast fibers (flax, hemp, nettle).

2.5 SFTCT simulation of microscopy-extracted fiber geometries

The previous section demonstrated the influence of the most common plant fiber geometric characteristics on the analytical model's ability to identify the transverse elastic modulus of a fiber. Valuable insights were gained in the mechanisms that lead to an over or underestimation of E_T along with the antagonist behavior they can have with each other. While the analytical model exhibited relatively good identification ability for a large range of parameters, the studies were performed on ideal geometric representations. The model's identification ability on realistic fiber geometries remains an open question given the morphological complexity that plant fibers can exhibit. In this section, a method similar to the one presented by [Legland 13, Mattrand 14, Del Masto 17], is used to extract fiber contours from microscopy images and perform morphological measurements. The transverse compression of these contours is then simulated and analytical model identification ability is evaluated through ΔE_T. In order to perform this study a multi-step algorithm is necessary. Starting with an initial microscope image, the algorithm can be divided into 3 main steps:

1. Detecting and extracting the fiber contours from the image.
2. Processing an individual fiber contour. The contour is smoothed to ease the construction of the finite element model. An ellipse is fitted to provide an apparent major and minor radius to the analytical model. The fiber is positioned by the user in a realistic configuration for compression.
3. A finite element model is constructed and the transverse compression of the fiber is simulated. ΔE_T is calculated from simulation data.

A series of geometric indicators is also estimated to search for correlations between them and ΔE_T. While some interdependences can be observed, complex interactions between morphological parameters make it difficult to predict easily the value of ΔE_T for a given fiber geometry. Machine learning techniques however, are shown to perform such predictions with relatively good accuracy, even when trained on a small dataset.

2.5.1 Contour extraction

A microscopic observation of part of the cross section of a hemp stem, seen in Figure 2.28, is used to extract fiber geometries. Turning the image into binary is necessary to perform said extraction. A *MATLAB* implentation of Otsu's thresholding method [Otsu 96] is used for this purpose. The pixel size is found at $0.28\,\mu m$, the size of the extracted fibers can thus be determined. The *MATLAB* function *bwboundaries* is then used to detect the fiber contours. The user can manually choose a fiber of interest to treat independently. For each fiber, the biggest interior contour inside the fiber wall (the lumen) can be kept or not.

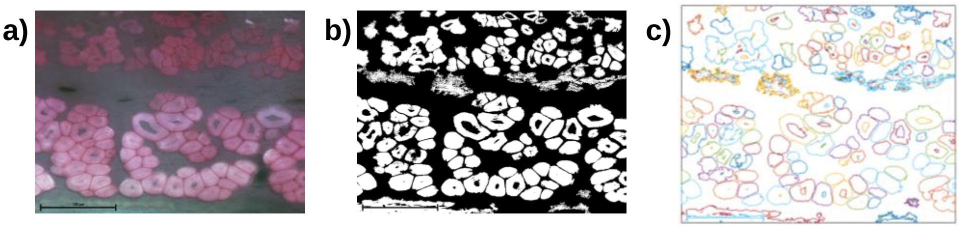

Figure 2.28: Steps for fiber contour detection : a) original hemp stem microscopy image, b) image binarization, c) contour detection with *bwboundaries*. Each independent contour is shown with a different color.

Once a fiber contour is chosen, its raw data presents very fine irregularities that are most likely due to the contour detection algorithm than the fiber geometry itself. In any case, keeping such a level of detail in a finite element model would be problematic, since it would need very fine meshing and could cause very local stress concentrations. For this reason a smoothing algorithm is used to eliminate some of this fine detail while maintaining the overall fiber geometry. Such smoothing algorithms are best suited for a one dimensional signal with unique values for each abscissa. The closed fiber contour in a Cartesian coordinate system is thus not well adapted for smoothing. A conversion to polar coordinates is used instead. However, if the closed lumen or fiber cell wall contour is not centered around the origin of the cartesian coordinate system, data discontinuities can occur when switching to polar. For this reason the contours are centered before conversion with the offsets:

$$dx = \frac{x_{max} - x_{min}}{2}, dy = \frac{y_{max} - y_{min}}{2} \tag{2.40}$$

with dx and dy the offsets along the x and y axis, respectively. The data is also sorted in an ascending order of angles to avoid closed contours. The described process is illustrated in Figure 2.29 with a continuous signal being obtained at the end of the process.

With the contour data now ready, a smoothing spline operation is performed. The smoothed polar data is converted to Cartesian coordinates and the offsets dx, dy are removed so that the contours find their original positions without being centered on the coordinate system origin. Figure 2.30 shows this smoothing procedure on a fiber contour. The general shape of the fiber is well maintained while eliminating very fine details.

The analytical model that was established previously considers the fiber as an ellipse. For this reason, an ellipse is fitted on the smoothed fiber contour in order to provide the best elliptical approximation of the fiber's complex geometry to the analytical model. An open access *MATLAB* script developed by Gal [Gal 22] was used for the ellipse fitting. A major and minor radius along with the ellipse's orientation is identified. During transverse

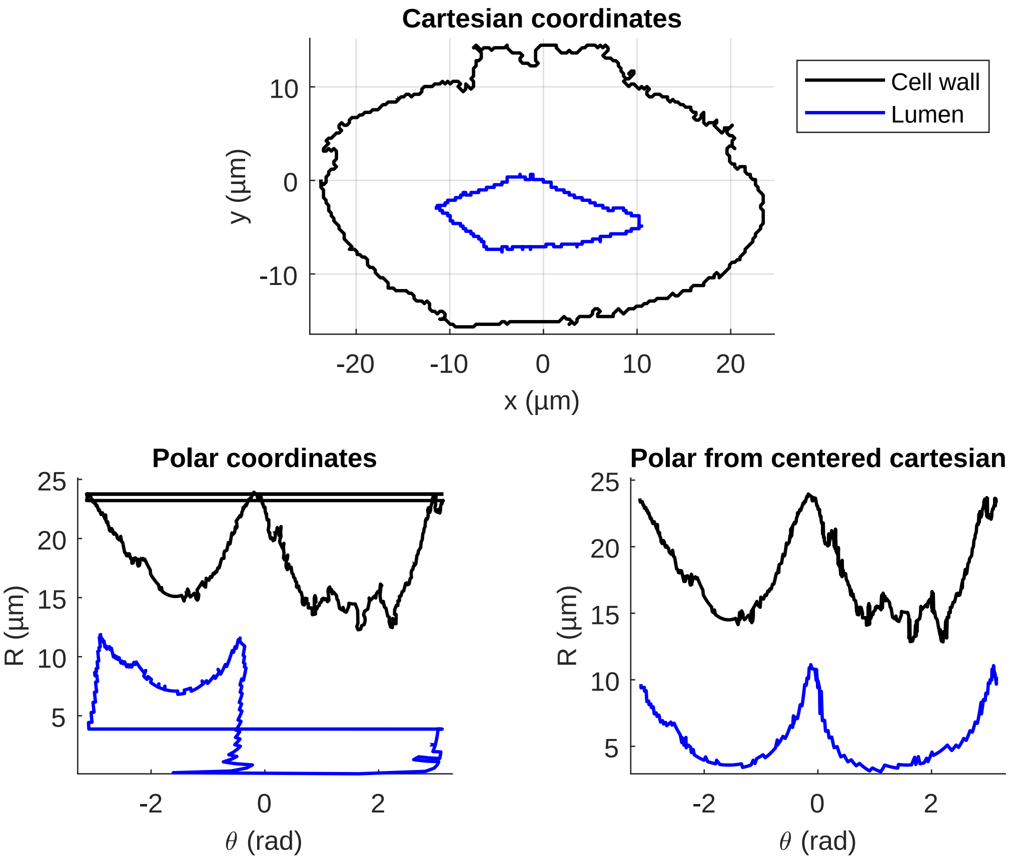

Figure 2.29: Polar conversion to prepare for data smoothing: (top) raw contour data in cartesian coordinates, (left) direct polar conversion, (right) polar conversion with an ascending angle order and from centered cartesian data.

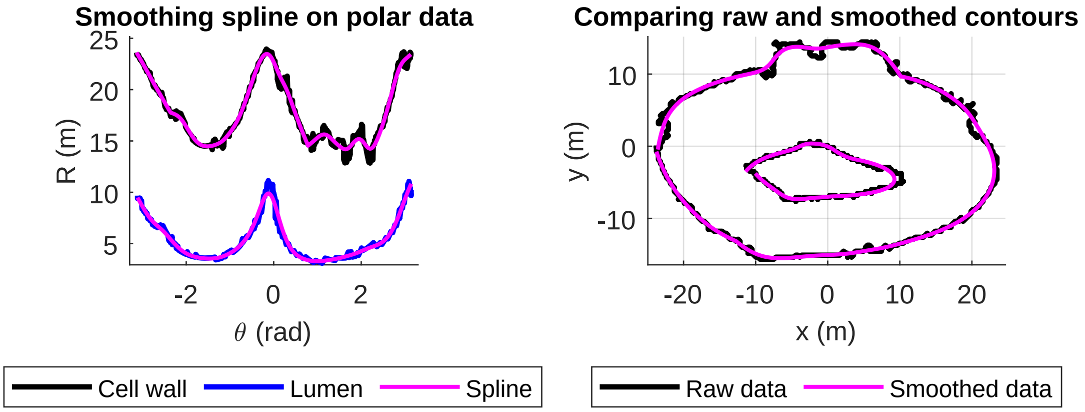

Figure 2.30: Smoothing operation: (left) smoothing spline algorithm operating on polar data, (right) comparison between the initial and smoothed cartesian contours.

compression, the fiber will usually be subject to rotational movements that tend to align its major axis with the compression platens. Thereby, the analytical model considers that the fiber's major axis is horizontal (rotating the fiber to obtain an horizontal minor axis is also possible). The fiber contour and fitted ellipse are rotated to achieve this horizontal configuration. While this placement represents a good initial prediction of a realistic fiber placement, it is not adapted to all geometries. For this reason, the user can rotate the fiber to a realistic compression position, where compression will happen as vertically as possible with the least amount of rotation. If such a user rotation is performed, the major axis of the fiber will not completely horizontal, which leads to some difference with the analytical model. Figure 2.31 shows such an example of ellipse fitting and rotation.

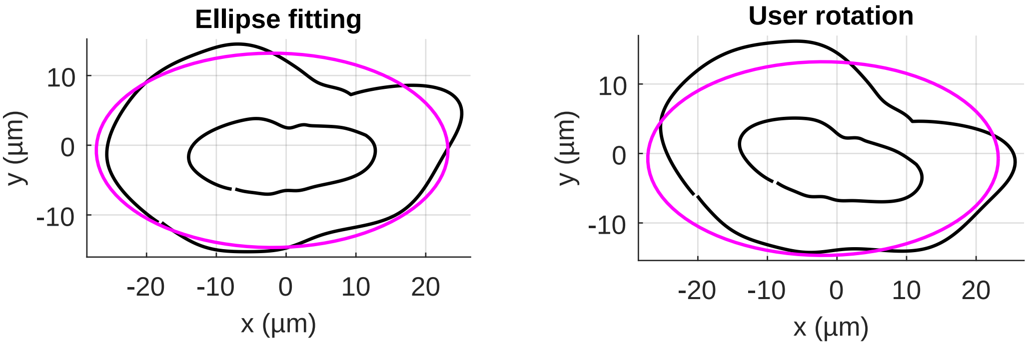

Figure 2.31: Ellipse fitting and rotation: (left) the ellipse in magenta is fitted on the fiber contour and a rotation is performed to position its major axis horizontally, (right) the user rotates the fiber to a position that seems more probable to occur during compression preloading.

At the end of this series of operations realistic yet smooth fiber contours, suitable for FEA, are extracted and positioned in a way that represent a realistic transverse compression scenario. Figure 2.32 shows the fibers that were extracted and simulated in this study. Fiber with varying geometric features were chosen, notably lumen size, aspect ratio and convexity.

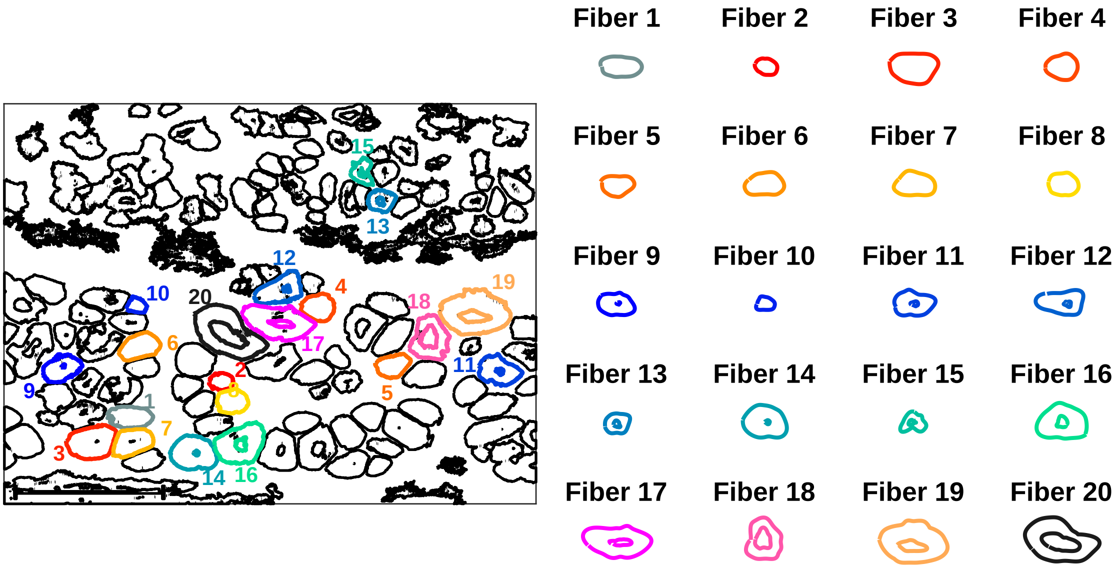

Figure 2.32: Chosen fiber contours on original image (left), fiber contours after smoothing and rotation operations (right). The scale between fibers is respected.

2.5.2 Transverse compression simulation

Finite element model

In order to perform a finite element simulation, a series of steps must be taken to construct the model. First, contact zones must be defined between the fiber and the platens. The limits of these contact zones are defined as the points to the left and the right of the highest and lowest fiber points that have the closest value to 65% of this maximum and minimum. This method allows for a good definition of contact zones for all tested geometries, even when there are multiple convex zones. It also enables the automation of the contact zone definition, greatly accelerating the process. An example of generated contact zones is given in Figure 2.33. The limits of the contact zone on the compression platens are positioned at the same abscissa as the contact zone of the fibers.

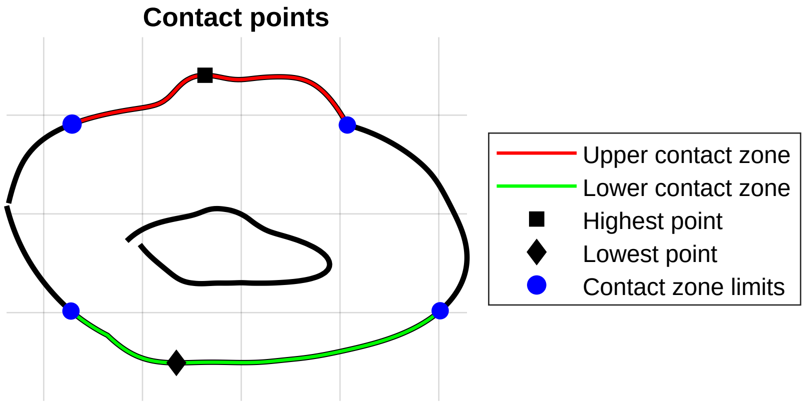

Figure 2.33: Example of contact zone definition on an extracted fiber geometry.

The final step in the construction of the finite element model consists in establishing the boundary conditions and the mesh. Like all previous studies the displacement of the lower platen is blocked while the upper platen moves by $1\mu m$ in order to compress the fiber. Similarly to the 2D full section simulations (see subsection 2.3.2), the horizontal displacement of the lowest fiber point, who gets in contact with the lower compression platen first, is blocked ($u_x = 0$). Thus, the rigid body movement that can occur along the x axis is eliminated while allowing the fiber to compress and rotate freely during compression. For the meshing the same approach is used as for the elliptical geometry simulation with triangular elements with sides of $R_{mean}/26$, where $R_{mean} = (R + r)/2$ where R is the major and r is the minor radius of the fitted ellipse. Figure 2.34 illustrates the presented boundary conditions on a meshed fiber geometry. With the simulation complete, a force per unit length is obtained by integrating the vertical component off the contact pressure T_{n_y} along the defined contact zone.

In some cases some rotational movement can take place during the initial phase of compression resulting in very low force levels. These points are removed and not taken into consideration in the identification of E_T.

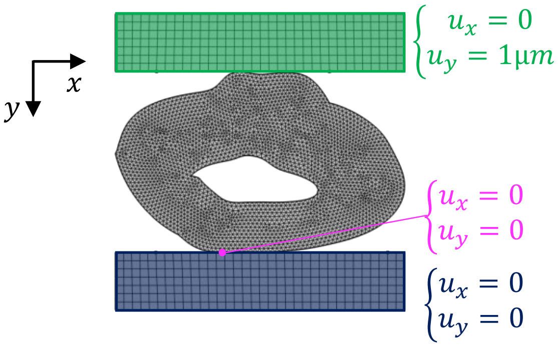

Figure 2.34: Example of fiber geometry mesh with finite element model boundary conditions.

Transverse compression results

The force per unit length as a function of upper platen displacement are shown in Figure 2.35. A variety of force levels for a given displacement are seen. However, one distinction can be made clearly. Fibers with no lumen, represented with color filled markers, lead to higher force levels while fibers with lumens, represented by markers with no filling, lead to lower force levels. This illustrates clearly the influence of structural displacement on the fiber response. This distinction becomes clearer when looking at ΔE_T as seen in Figure 2.36. In accordance with the previous study 2.4.2, all fibers with a lumen result in negative values of ΔE_T. Fibers with no lumen on the other hand, produce positive values of ΔE_T with the exception of fiber 10. Despite the morphological complexity of the studied fibers, the average ΔE_T values are rather low at -7%. The standard deviation is calculated at 33.04%. Such deviations values are in the same order of magnitude with the typical standard deviation found in identified plant fiber parameters such as the tensile modulus and strength [Aslan 11, Jeannin 20, Lefeuvre 14b, Baley 14]. Least-square residual values are also low with an average of $2.5nm$. Therefore, the analytical model fits well to the simulation data.

These results show that the analytical model's ability to reproduce the fiber response under transverse compression is good, despite the geometric complexity of the fibers. Some errors on the identified transverse elastic modulus occur but are within the deviations typically observed for plant fibers. The conclusions drawn from the ideal-case studies are also valid in many cases. It is however demonstrated that the underestimating effect of the lumen-generated structural displacement is typically greater than the overestimating one resulting from elliptical cross sections and flat contact zones, since all tested fibers with lumens produced negative ΔE_T values. It seems thus reasonable to except an underestimation for fibers with lumens and an overestimation in the opposite case. The value of the error however is difficult to predict, since it is a results of complex interactions and antagonist behavior between morphological parameters.

Geometric indicators

In order to better understand the complex interactions between the fiber's geometric parameters and ΔE_T a series of geometric indicators are evaluated. Such, indicators have been constructed before in the works of [Legland 13] and [Mattrand 14], to provide detailed characterization of fiber or bundle cross section morphology. In the present case, these indicators are an analog to the geometric parameters that were studied previously

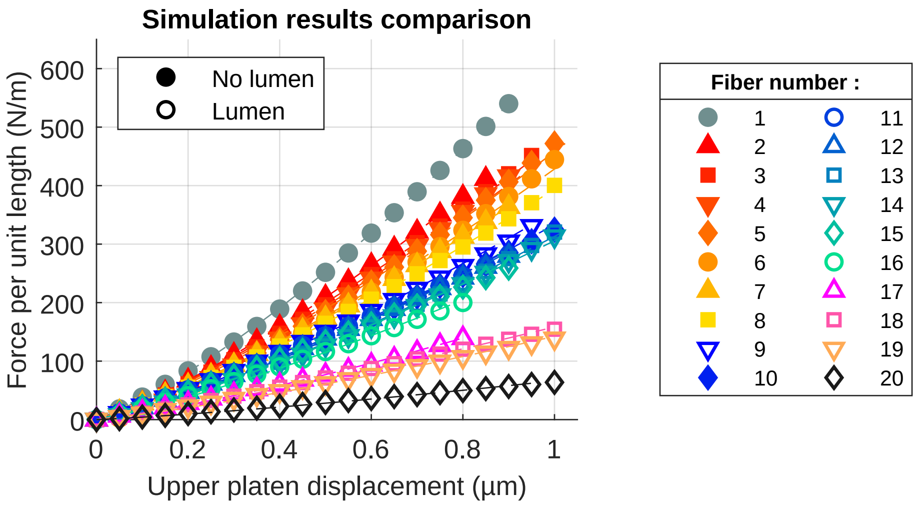

Figure 2.35: Force-displacement results of different fibers. The data from the simulation is represented by markers with the fitted elliptical analytical model represented with dotted lines. Maximum displacement values are not identical for all fibers due to the removal of initial rotational movement for some fibers.

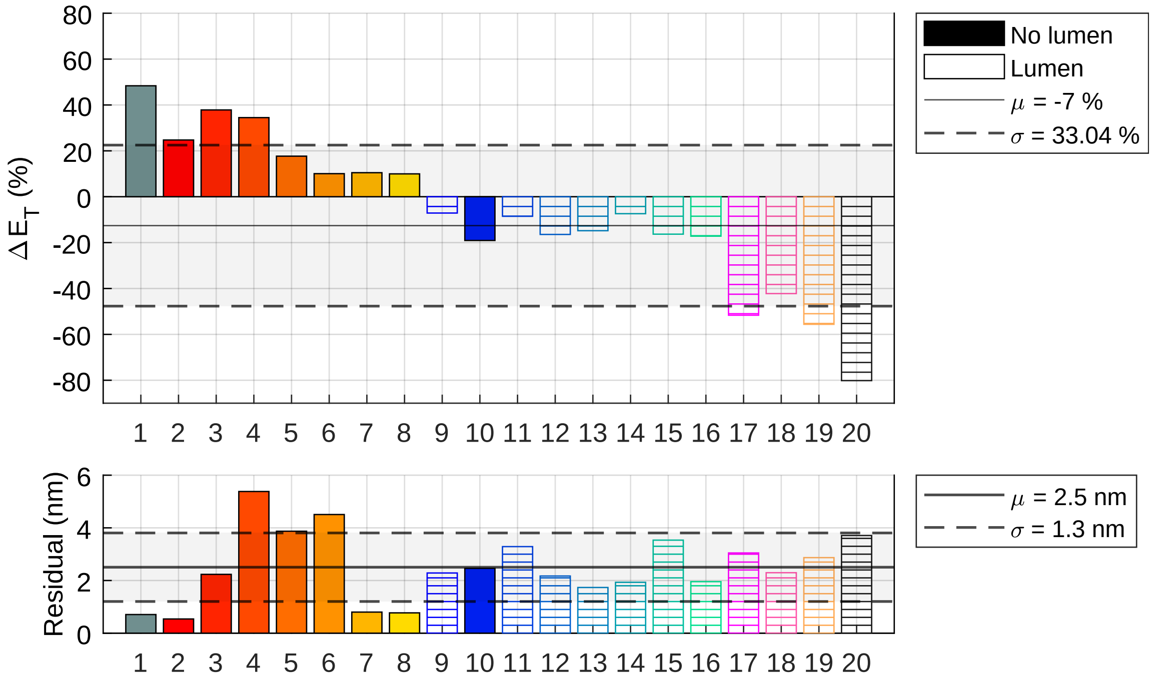

Figure 2.36: ΔE_T and least-squares residual values for all fibers.

in their ideal representations: the lumen, the ellipse flatness and the contact zone flatness. Understanding the impact of these indicators on fiber behavior could subsequently help predict the error made in the identification of E_T by the analytical model. Fibers whose transverse elastic modulus can be identified with confidence and fiber for which this is impossible could be identified.

Surface indicator. The first geometric indicator is the surface of the fiber and of the fitted ellipse. The surface of the lumen is substracted from the surface contained inside the cell wall. The *MATLAB* function *alphashape* is used to first to create a bounding area inside the the cell wall, lumen or ellipse contour. The function *area* is then used to calculate the surface of these bounded areas. In this way, the difference in surface between the fitted ellipse and the fiber can be studied.

Ellipse flattening indicator. The next geometric indicator consists in calculating an ellipse flattening factor. For the fitted ellipse, this consists in calculating the factor in the typical way, using the major and minor radius. For the fiber geometry, the Feret diameters (object height and width at a given orientation) [Mattrand 14] along the horizontal and vertical direction are taken to calculate the factor with the fiber in its final configuration. In this way, the elliptical nature of the geometries can be quantified.

Contact width indicator. Finally, an estimation of contact width ($\boldsymbol{2b}$) is made at the maximum displacement. First, the analytical formula is used to estimate the contact half width b. The major or minus radius of the fitted ellipse is used for the calculation, depending on the direction of compression. In the case of the simulation, the vertical component of the contact pressure T_{n_y} is extracted along the whole defined contact zone. The lengths on which this pressure is non zero are summed in order to give an estimate of contact half width that is produced in the simulated compression. In order to accurately compare between contact widths, the values are divided by the maximum displacement level (u_{max}) for a given fiber.

The values of these indicators, both from analytical calculation and simulation data are shown in Figure 2.37. The color of each data point corresponds to the ΔE_T value of a given fiber. Just like for previous figures, fibers with no lumen are presented with a color-filled marker while fibers with a lumen only have a colored contour. When looking at the surface data, it can be seen that when the fiber presents no lumen, the surface contained in the fitted ellipse and in the fiber cell are very close. However, when lumens are present ellipse surfaces are larger than their fiber counter-parts. Structural displacement is thus added resulting to an underestimation of the transverse elastic modulus. Bigger differences between surfaces (points further away gets from the diagonal line) lead to larger errors. This correlation supports the hypothesis that the effect of the lumen is greater than the one resulting from flat/elliptical geometries. When it comes to the flattening ratios, the ellipse and fiber data is overall relatively close. The biggest flattening ratios do produce some of the largest ΔE_T, negative or positive, however the correlation is not as clear as with the surface data. Finally, the contact width calculations can be studied. The contact width predicted by the analytical model is for most fibers, inferior to the one produced in the simulation. This difference tends to be larger for fibers with no lumen where the lack of structural displacement leads to larger stress concentrations and consequently, larger contact width. The following mechanism takes place: in simulations large contact widths occur, resulting in high force values. The analytical model prediction of the contact width is underestimated. When the model is used for inverse identification, the identified E_T gets overestimated, since its the only way to account for the increase in force. However, big differences in simulation and analytical contact width do not result necessarily to high ΔE_T values.

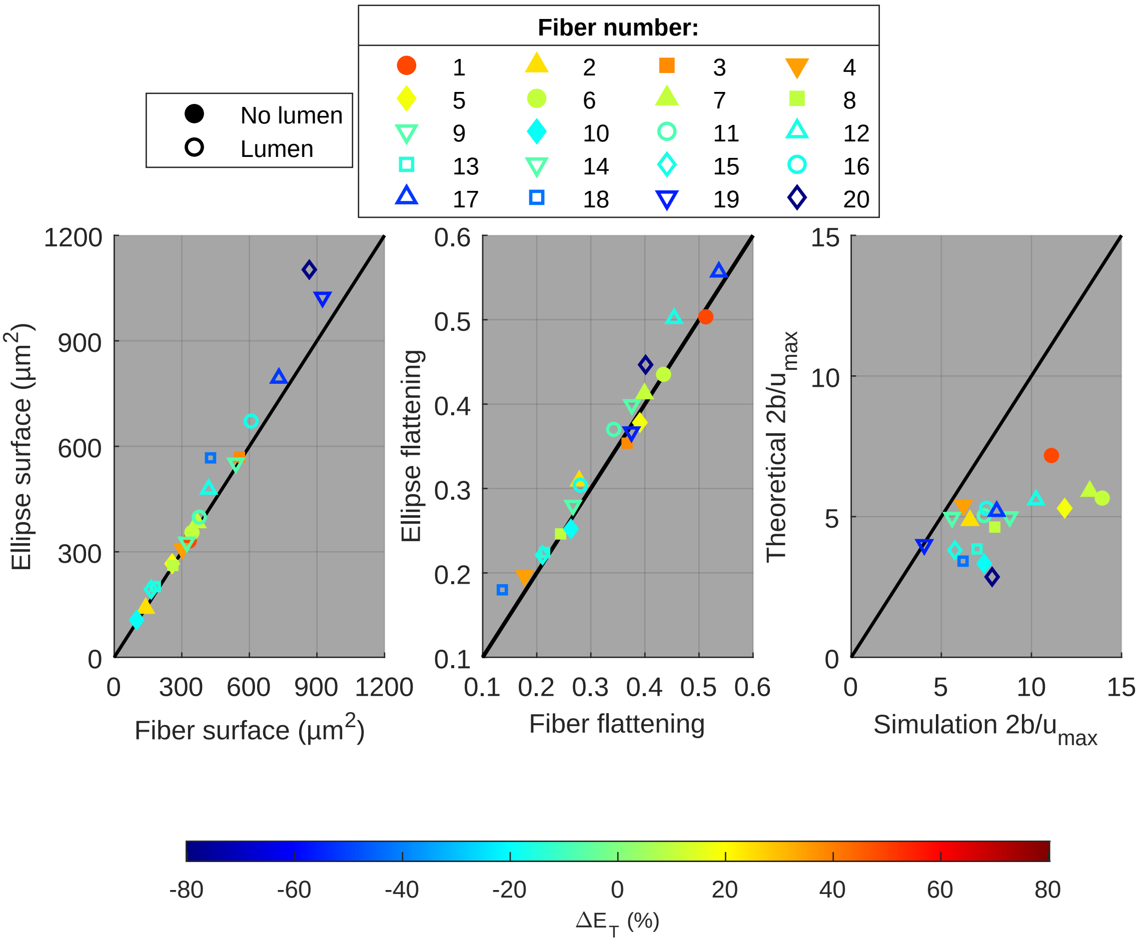

Figure 2.37: Geometric indicators for analytical and simulated compression. $2b$ represents the contact with and u_{max} the maximum displacement level of a given fiber.

This lack of clear correlation between the geometric indicators points to complex correlations and antagonist behaviors between them. Additionally, there are more morphological parameters that can influence ΔE_T. Fibers 6 and 7 for example have the highest differences between analytical and simulated contact width but produce low ΔE_T values. The convex nature of their lower part might be the explanation, generating some structural displacement, reducing the overestimation of E_T resulting from the high contact width. Additional indicators, such as the ones found in the work of [Legland 13] and [Mattrand 14], could help to explain better the analytical model's identification ability. However as the number of parameters increases detecting correlations between them becomes more difficult.

2.5.3 Neural networks for ΔE_T prediction

Introduction

Identifying correlations and understanding interactions between parameters gets more complex as their number increase, however, machine learning techniques present a valuable solution to their study. More specifically, neural networks represent an established method to find correlations between a large number of parameters. The artificial neuron, as developed by McCulloch [McCulloch 43] represents the elementary unit of a neural network. It receives N inputs x and produces an output y in the following way;

$$y = \phi\left(\sum_{i=1}^{N} w_i x_i + b_i\right) \tag{2.41}$$

where: w the weight, allowing to increase or decrease the effect of a given input, b the bias allowing to shift the function value by a constant amount and ϕ the transfer function. Different transfer functions can be used depending on the nature of the problem [Duch 99]. By assembling multiple neurons, a neural network is created. This model can be "trained" on examples where the output is known, called training data. The difference between the network prediction and the actual output is minimized by modifying the weights and biases of the the network using various optimization algorithms, notably the back propagation method [Wythoff 93, Liu 10]. Through the optimization of its parameters, the network is able to give an accurate output estimation for a series of given input parameters. Its performance is validated by evaluating its prediction ability on examples with known outputs that were not used in the training procedure, called testing data.

In our case, a neural network is trained to give a ΔE_T estimation for an input consisting of 6 geometric values: the ellipse's and fiber's surfaces and flattening ratios along with simulated and analytical contact width divided by the maximum displacement level. *MATLAB* is used to create and train the network with the functions *fitnet* and *train* respectively. A simple feed-forward neural network is used composed of an input layer, intermediate hidden layers and output layer. Since the used dataset is small, a Bayesian regularization [MacKay 92] backpropagation algorithm is used to train the network [Dan Foresee 97]. This prevents over-fitting on the training data allowing for better generalization and consequently better prediction ability by the network. To train the network, 75% of the data is used with the 25% remaining being used as testing data. Each time a network is trained weights, biases, training and testing data are chosen randomly.

It is important to note that the network's prediction error that will be presented in the following sections, corresponds to the absolute value of the difference between the network output and the actual ΔE_T values. The error is expressed in % since it is the unit of ΔE_T. For example if for a given fiber, the networks predicts a ΔE_T of 50% with an actual value of 40%, the error will be 10%. This is not to be confused with an error expressed as a percentage of the correct value.

Network construction and validation

In order to construct the best possible network, a few validation procedures are performed. First, three different transfer functions for the neurons of the hidden layer are compared: logistic sigmoid, hyperbolic tangent sigmoid and purely linear. A single hidden layer with 8 neurons is used. The transfer function at the output layer is maintained as purely linear.

For each function, 100 networks are trained and their error on the training and the testing data is averaged. The results are shown in Table 2.7. The hyperbolic tangent sigmoid function produces the lowest error on both the training and testing data it will thus be used in our network.

	Logistic sigmoid	**Hyperbolic tangent sigmoid**	**Purely linear**
Training data	3.74%	2.19%	9.34%
Testing data	9.34%	6.82%	13.88%

Table 2.7: Average error of 100 networks on ΔE_T values for different transfer functions.

Next the influence of the size of the network is studied. The number of hidden layers will be changed from 1 to 5 and the numbers of neurons within them from 1 to 20. The amount of neurons in each layer remains the same. Just like the previous study, 100 networks are trained in each configuration. The results are shown in Figure 2.38. Increasing the number of layers increases the error made by the model. The number of neurons on the other side has no significant influence on the error (with the exception of a single neuron layer). The network's generalization ability is thus low regardless of neuron number.

Given the results of these studies the network is constructed with a single hidden layer of 8 neurons. A schematic representation is given in Figure 2.39

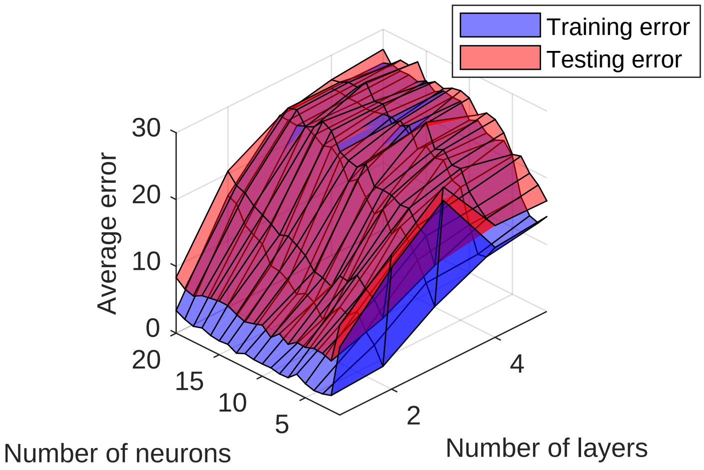

Figure 2.38: Average error of 100 networks on ΔE_T values for different network sizes.

Network prediction ability

With the construction of neural network finalized its overall performance can be approached. Figure 2.40 illustrates the performance of a trained network through the Mean Squared Error (MSE). The MSE value converges quickly after only 25 epochs (optimization iterations). The network regression is also shown. The output of the model is plotted as a function of the target. Predictions from training and testing data are present. Both are overall close to the diagonal line, which represents a perfect prediction. Table 2.8 gives a detailed quantification of the model's performance. The error on training data is low at

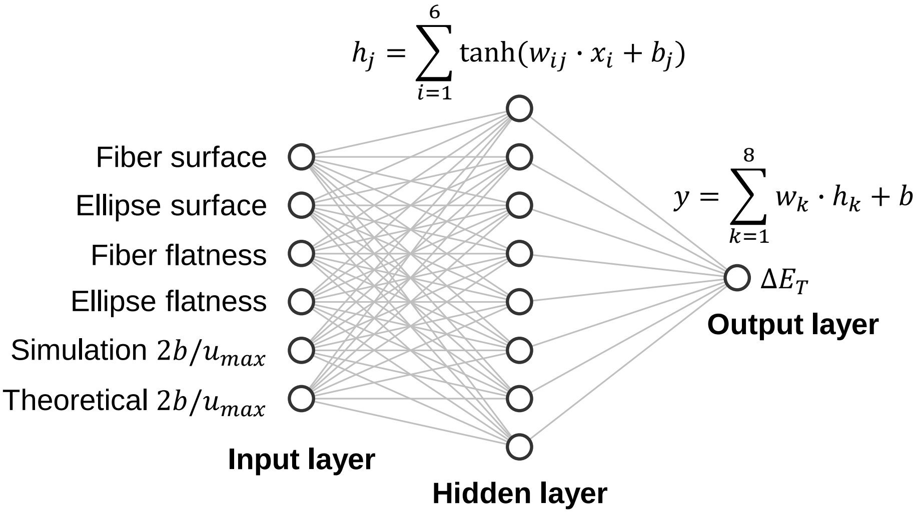

Figure 2.39: Schematic representation of final neural network.

2.42%. Error on training data is slightly higher but close to the training error at 2.99%. No overfitting has thus occurred. Pearson coefficients and coefficients of determination are close to 1 for both data sets. The linear regression is thus of good quality and is close to the perfect prediction line.

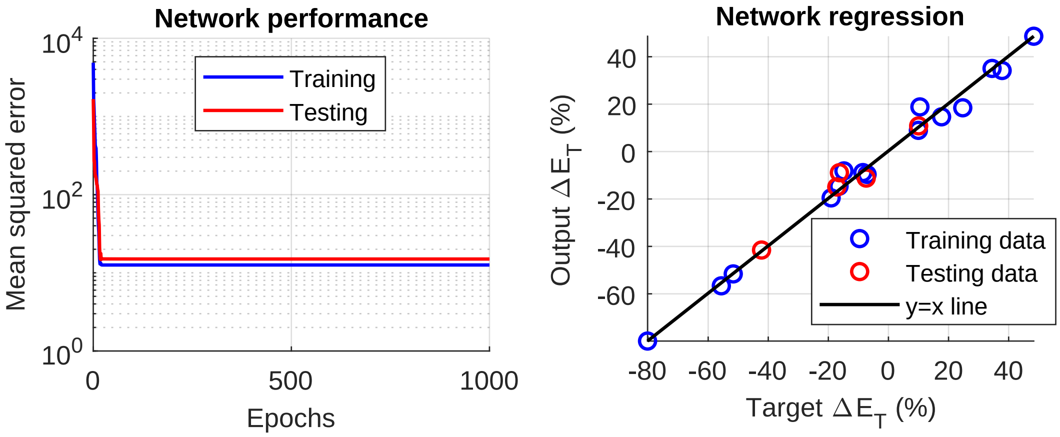

Figure 2.40: Network performance and regression.

These results show that a neural network can be trained, even with a small dataset, to predict the identification error on the fiber's transverse elastic modulus E_T, made from a simple analytical model of the SFTCT. This is made possible by the network's ability to find correlations between the input geometric indicators and ΔE_T. Such models can thus still be used, since through such a network, fiber morphological characteristics can help improve identification accuracy. These characteristics could be measured in practice, for fibers used in SFTCTs experimentally. Training the network on a larger dataset could help it improve its accuracy and become more robust. The process of fiber extraction and simulation has been designed to be easily automated, a large number of microscopy images could therefore be used.

	Error	r	R^2
Training	2.42%	0.995	0.990
Testing	2.99%	0.978	0.947
Global	2.56%	0.994	0.987

Table 2.8: Network performance and regression values, with r the Pearson coefficientof correlation and R^2 the coefficient of determination

2.5.4 Conclusions

In this section, SFTCT simulations of 2D fiber geometries extracted from microscopy images are shown for the first time. Accounting for the morphological complexity of the chosen fibers the analytical model's ability to reproduce the fiber response and identify the transverse elastic modulus is decent, with the average error situated within the typical variations found on plant fiber material parameters. The influence of the main geometric characteristics of plant fibers is shown once again, with the lumen being the most influential. However, the interactions between all geometric parameters of the fiber and the resulting ΔE_T is still difficult to predict. A neural network approach shows that a prediction of ΔE_T with the used geometric indicators as inputs is possible.

2.6 Identification error caused by fiber material behavior

Analytical models of SFTCTs consider the fiber as a purely elastic material. Plant fibers however are complex structures not only from a morphological point of view but also in terms chemical composition and microstructure. For this reason, plant fibers are far from purely elastic materials. The polymeric and heterogenous composition of the fiber cell wall offers it significant viscoelastic behavior. In parallel, high mechanical loads can damage it resulting in irreversible deformation. These properties have made the subject of various characterizations efforts, primarily in tensile testing (see subsection 1.3.3)

Accurately identifying the transverse elastic properties of plant fibers requires an understanding of the impact of inelastic behavior on SFTCTs. This section aims at studying this impact with FEA. While complex material models could be used to simulate the rich material complexity of plant fibers, knowledge of the material parameters of such models is poor to non-existent for plant fibers, especially in the transverse plane. For this reason very simple models are used instead, aiming to illustrate the impact of inelastic behavior on SFTCTs instead of accurately reproducing plant fiber behavior. In this way, signs of inelastic phenomena on the fiber's behavior under SFTCT can be identified and potentially accounted for. The ability of the analytical models to identify the transverse elastic properties of the fiber, despite these inelastic behaviors is also evaluated.

2.6.1 Viscoelasticity influence

Plant fibers are known to exhibit significant viscoelastic behavior, giving them an important advantage in damping properties over some synthetic fibers [Liu 21]. Characterizing the viscous property of a material can be done mainly through two ways: quasi-static tests and dynamic tests. Quasi-static tests, after a rapid initial loading step, apply a constant load to a material. This loading can be controlled in terms of strain (stress relaxation tests) or stress (creep tests). Under this stable load the material can express its viscous properties which can then be characterized with the help of various analytical models. Dynamic tests apply a rapid periodic load to the material. While an elastic material would produce a stress and strain response that would be perfectly in phase, a phase lag occurs for viscoelastic materials which allows for the characterization of their viscous properties.

Typical SFTCTs consist in characterizing the elastic properties of a fiber through a relatively rapid compression (or decompression). Depending on fiber nature however, viscous properties can express themselves in the fiber response if the loading speed is not fast enough. As a result, an "apparent" elastic transverse modulus will be identified through the analytical models that is not the product of a purely elastic response, but a viscoelastic one. The goal of this section is to study the influence of viscous properties on the fiber behavior during a SFTCT and quantify the error made on the identified transverse elastic modulus E_T, through a finite element viscoelastic model. To the author's knowledge, viscoelastic behavior has not been studied by FEA in the context of SFTCTs

Finite element viscoelastic SFTCT model

To study the influence of viscoelastic behavior on the fiber response the two-dimensional quarter fiber model is used. As explained previously, accurately modeling plant fiber viscous behavior in all its complexity is not the goal of this study, a simple visocelastic model with a single spring and damper is thus used. Since the compression is controlled in terms of displacement, the Maxwell model of viscoelasticity is used (spring-damper in series) with a spring constant of $1\,GPa$. Further justifications on the model choice can be found in appendix A.5. The influence of the relaxation time of the damper τ and loading speed v on the fiber behavior will be studied. To simulate viscoelastic behavior, a time-dependent solver replaces the stationary one. The fiber is loaded up to $1\,\mu m$ ($0.5\,\mu m$ platen movement for the quarter fiber model) at a speed v. The study is made through 21 time step increments. The nominal value of the damper's relaxation time is set at $\tau = 10\,s$ while the loading speed is set at $10\,\mu m/s$, the maximum speed achievable with our experimental SFTCT setup. To study the influence of the viscous parameter, the relaxation time will be changed from 10^{-2} to 10^4s. To study the influence of the loading speed it will be varied from 10^{-2} to $10\,\mu m/s$.

Influence of viscous parameter τ

The fiber's response under transverse compression can be seen through the force-displacement data in Figure 2.41. For a purely elastic response ($\tau = 0$) or slow viscous responses $\tau > 1s$, the fiber behavior is basically identical. Only for rapid viscous behaviors $\tau < 1s$ the influence of fiber viscosity can be seen on fiber behavior. As relaxation times get shorter the force for a given upper platen displacement decreases and the non-linearity gets gradually reversed. This is reflected on the values of ΔE_T with short relaxation times resulting in an underestimation of the identified transverse elastic modulus and longer relaxation times having no impact as seen in Figure 2.42. The least-squares residual follows the observed trends. Short relaxation times with their change in non-linearity are far away from the predictions of the analytical model, the fit is thus of bad quality and the residual is high. As the relaxations time get bigger, fiber behavior is extremely close to a pure elastic response, resulting in a good quality fit and low residuals.

Tensile tests have identified relaxation times at a magnitude of $100\,s$ [Cisse 15]. It seems reasonable to assume that in the transverse direction, relaxation times are close or at least within one order of magnitude of these values. This would mean that for the experimentally achieved loading speed the fiber's viscous behavior has no influence on the identified transverse elastic modulus. Considering the fiber as purely elastic during SFTCTs is thus a valid hypothesis for the chosen loading speed.

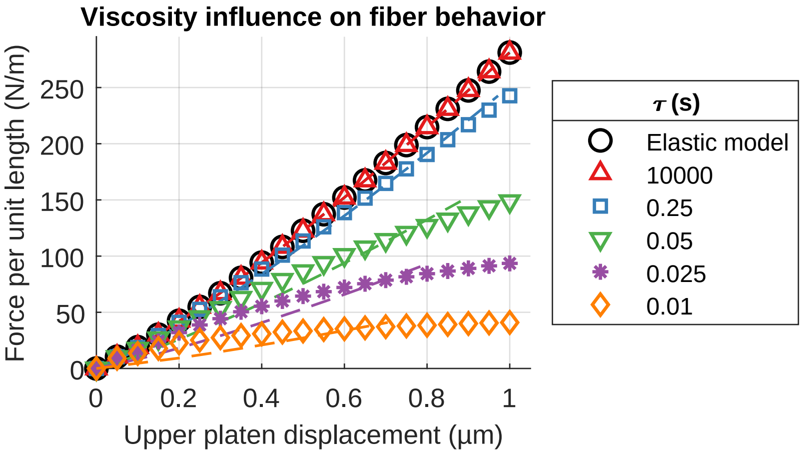

Figure 2.41: Force-displacement results for different relaxation times τ. The data from the simulation is represented by markers with the fitted elliptical analytical model represented with dotted lines.

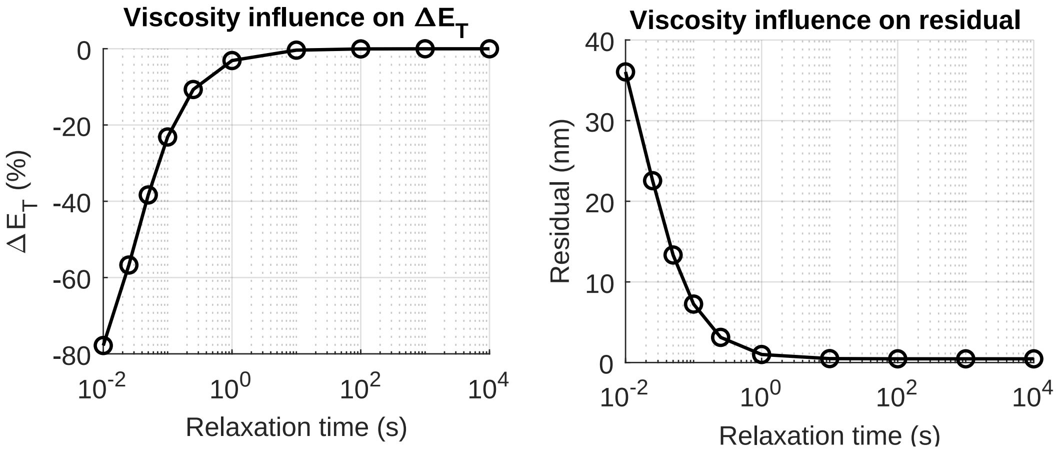

Figure 2.42: Evolution of ΔE_T (left) and least squares residual (right) as a function of the relaxation time τ.

Influence of loading speed v

The fiber's viscous behavior was shown to have no influence on the identified transverse elastic property for loading speeds at $10\,\mu m/s$. This speed is now decreased in order to observe when fiber viscous behavior can become influential. The fiber's relaxation time is set at $\tau = 10\,s$. It represents a "worst case scenario" where the relaxation time in the transverse direction is a order of magnitude lower than the tensile one [Cisse 15]. The force-displacement data resulting from tests at different loading speeds are shown in Figure 2.43. A loading speed of $1\mu m/s$ results in a small decrease of the force for a given upper platen displacement but the fiber behavior remains very close to the one observed at the original speed of $10\mu m/s$. A further decrease by a factor of 10 results in a significant decrease in force. As expected, only with a very slow speed of $0.01\mu m/s$, the fiber's viscous behavior has enough time to fully express itself, resulting in a complete change in fiber behavior. These changes in behavior are reflected on the identified transverse elastic modulus and the least-squares identification residual as seen in Figure 2.44. Only the lowest loading speeds result in a severe underestimation of the transverse elastic modulus and a bad fit of the model, as seen in the high residual values. We can conclude that if the overall loading time is of the same order of magnitude as the relaxation time or shorter, viscous fiber behavior will have no significant influence and the transverse elastic modulus will be correctly identified. Nevertheless, if the loading time is larger than the relaxation time, viscous phenomena will alter fiber behavior resulting in error on transverse elastic property identification.

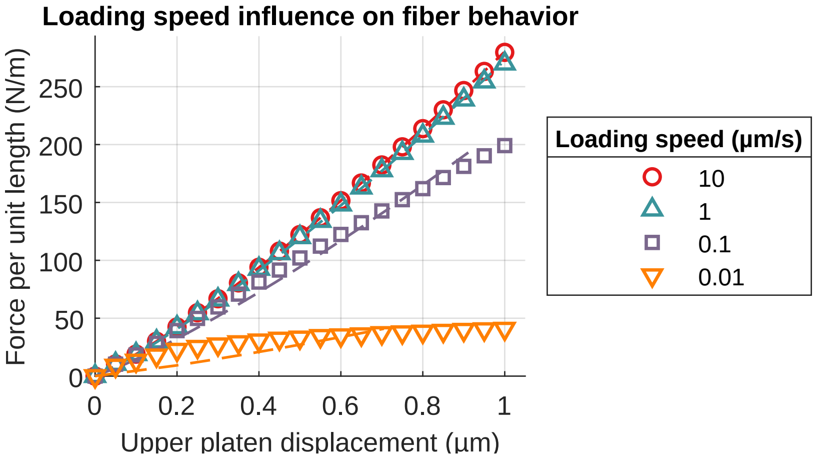

Figure 2.43: Force-displacement results for different loading speeds. The data from the simulation is represented by markers with the fitted elliptical analytical model represented with dotted lines.

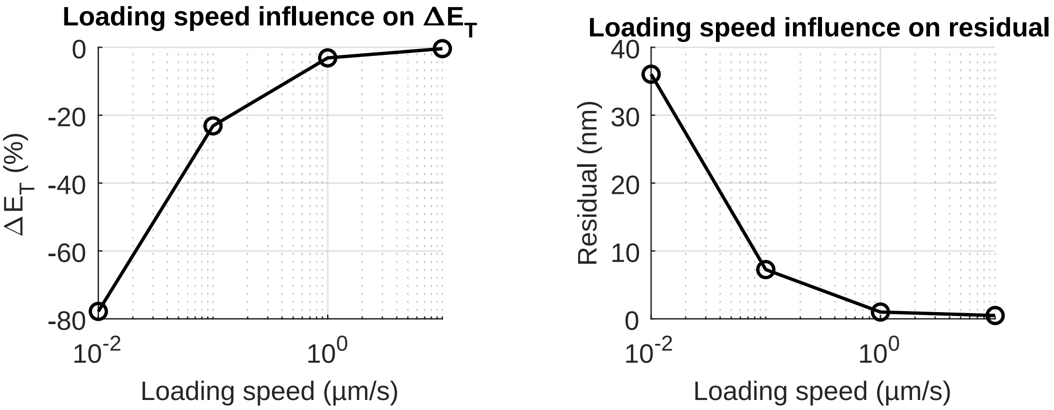

Figure 2.44: Evolution of ΔE_T (left) and least squares residual (right) as a function of loading speed.

2.6.2 Elastoplasticity influence

Introduction-model choice

In addition to purely elastic or viscoelastic behavior, plant fibers can also exhibit inelastic or more generally non-reversible behaviors. Once again, these phenomena are quite complex and can be a result of many underlying mechanisms. The fiber material itself for instance can express inelastic behavior. Structural effects can also influence the response of the fiber under compression. The lumen or micro-scale porosities inside the fiber wall can also collapse irreversibly leading to a change in fiber response. In order to accurately identify the transverse elastic properties of the fiber through SFTCTs it is thus crucial to recognize the effects irreversible behavior can have on the fiber response.

Similarly to the study on the influence of viscosity on the fiber's behavior and its subsequent influence on the identification of the transverse elastic modulus, the goal of this study will not be to accurately model all the complex mechanisms that lead to irreversible phenomena. More complex finite elements models with plastic behavior have been developed to study irreversible behaviors in SFTCTs and to help identify yield stresses in experimental data [Kotani 94, Singletary 00b, Wollbrett-Blitz 16, Sockalingam 14, Sockalingam 16, McDaniel 17]. Instead, the simplest of elastoplastic material models is chosen for the fiber and its transverse compression is simulated with FEA. The fiber material is considered as perfectly plastic (no hardening) and a von Mises yield criterion is used. The two-dimensional quarter fiber model is used with a stationary solver. A single plastic parameter, the yield stress σ_Y will be varied across a large range of values to observe its influence on the fiber response. Thus, a wide range of responses can be studied and their influence on the identification of E_T by the analytical SFTCT is evaluated. The chosen values for σ_Y vary from $1MPa$ to $1GPa$.

Influence of yield stress

The impact of plastic behavior is quite apparent on the force-displacement response of the fiber as seen in Figure 2.45. While for higher yield stress values plastic behavior is not being activated, resulting in an identical response with a purely elastic material, as σ_Y falls under $50MPa$ the non-linearity of the force gets completely inverted. For a given upper platen displacement, the force level also decreases significantly. By reducing the yield stress further, forces tend to reach an asymptotic value. These changes in force lead to an underestimation of the transverse elastic modulus once inverse identification is performed, as seen in Figure 2.46. Values of a similar order of magnitude with the viscoelasticity study are obtained. The effect on the least-squares residual is also large, since the analytical model cannot reproduce the change in non-linearity.

Experimental campaigns can be performed in order to identify a mean yield stress for a particular type of fiber. However, large deviations are to be expected, since the fiber morphology and internal structure can influence σ_Y considerably. Since yield stresses are variable, it can be difficult to perform fiber loading while staying in a pure elastic regime. Repeated loads with incremental increases in compression level can be a solution to this problem. Loads where an inverted non-linearity is detected can be excluded. However if very small displacements are necessary to stay in a purely elastic regime, the fiber might not be yet in a pure compression state where no rotation and sliding occurs Such displacements can also be a challenge to measure. For all these reasons the unloading phase of the compression is the best suited for the identification of the transverse elastic modulus. The irreversible material response is expressed during loading, leaving mostly the instantaneous-reversible elastic part in the unloading. Large compression levels can be attained thus eliminating problems related to measurement accuracy or to sliding and rotation movements.

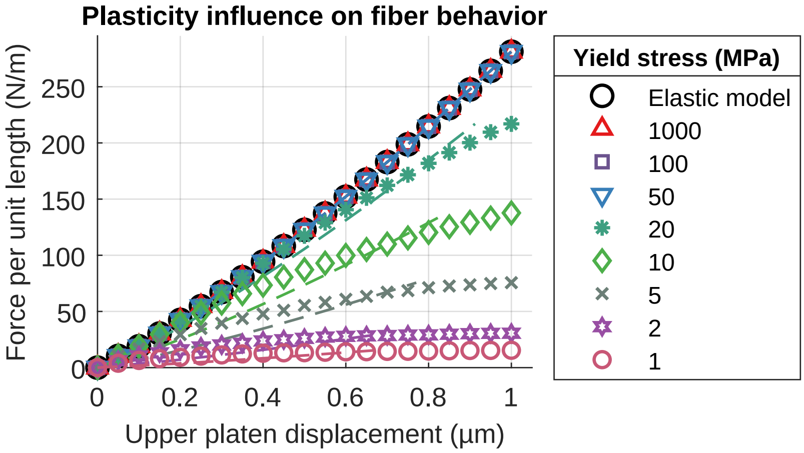

Figure 2.45: Force-displacement results for different yield stresses. The data from the simulation is represented by markers with the fitted elliptical analytical model represented with dotted lines.

2.6.3 Conclusions

In this section, the viscous and plastic behaviors were added to the typical purely elastic representation of a fiber under transverse compression. Both behaviors produced a decrease in force for a given displacement level, leading to under-estimations of the identified transverse elastic modulus. An inversion of non-linearity was observed once the yield stress was reached, in the case of plastic behavior, or for a combination of low relaxation times and slow loading speeds in the case of viscous behavior. Existing analytical models do not account for this type of behaviors resulting in a bad overall fit and high residual values. If an inverted non-linearity is observed experimentally, performing an identification would lead to an apparent transverse elastic modulus resulting from a combination

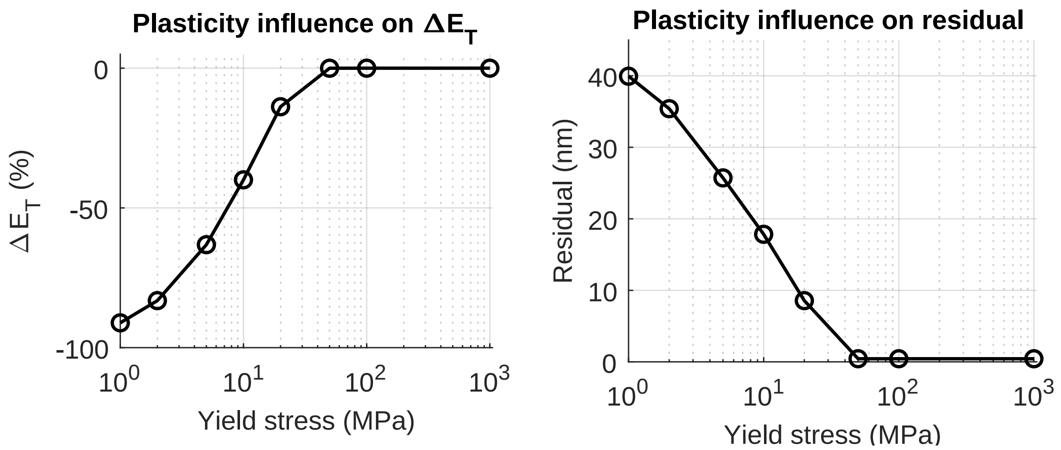

Figure 2.46: Evolution of ΔE_T (left) and least squares residual (right) as a function of yield stress.

of elastic and inelastic behaviors, that would be underestimated compared to the fiber's transverse elastic modulus. The use of existing analytical models is thus not well-suited in such cases. When considering the typical relaxation times of plant fibers and the loading speeds that can be attained experimentally, viscous behavior was shown to be unlikely to express itself. Inelastic-irreversible behaviors are thus the most likely material related mechanisms that can lead to significant deviations between the predictions of typical SFTCT analytical models and experimental data. Performing the identification of the transverse elastic modulus is thus best suited to the unloading part of the compression where mostly reversible material behavior is expressed.

2.7 Conclusions and perspectives

In this chapter finite element analysis was used, to better understand and quantify the influence of fiber morphology and material behavior on SFTCT results. First, a finite element model was created and validated by a series of studies and comparisons. A two-dimensional, quarter fiber model with fine triangular elements was shown to be the most efficient way to model the problem. Using this model the influence of fiber morphology on fiber behavior, assuming a purely elastic material, was shown with ideal case studies (lumen, ellipse, flatness) and with plant fiber sections extracted from microscopy observations. The analytical model's ability to identify the transverse elastic modulus of the fiber was shown to be satisfactory despite the complex geometries that were modeled. The influence of different material behavior were also studied. Viscous behavior was shown to not influence fiber behavior for typical compression speeds. Plastic behavior was shown to be influential, however, methods to isolate a purely elastic response were proposed. In conclusion, when working with bast fibers (flax, hemp, nettle) and with a carefully chosen experimental approach, analytical model that represent the fiber as a purely elastic cylinder, can be used in the inverse identification of the fiber's E_T.

Still, improvements in analytical models can be made. Models that account for larger contact widths, such as those found in elliptical or partially flat sections could be developed. Models for hollow structures [Womack 08, Markides 18] or with variable stress distributions [McCallion 82] could be adapted to plant fiber SFTCTs to account for their morphological complexities. MicroFibrilar Angle (MFA) and cell wall layers could also be added to analytical models in the context of SFTCTs.

Many more studies could be performed to further improve the understanding of plant fiber SFTCTs. This work establishes a framework and methodologies which can be expanded upon. For instance, morphological and material studies can be coupled. Separate cell wall layers could be also be modeled, as can be found in simulations of tensile testing [Thuault 14], offering potential insights on skin/core phenomena in plant fibers [Wollbrett-Blitz 16, Singletary 00b]. For 2D microscopy extracted geometry studies, more geometric indicators can be used to find correlations with ΔE_T. Machine learning techniques could greatly help in this regard as the number of parameters gets bigger and the interactions between them complex. Trained neural networks could indicate a ΔE_T for a given geometry without the need for simulations. While the presented studies aimed to minimize rotational movements by choosing a most likely fiber position, the influence of the fiber's initial position could also be studied. Initial conditions will affect the rotational a fiber can be subjected to, causing significant changes in its behavior. Finally, while numerically demanding, 3D geometries could also be studied highlighting even more complex mechanisms. In that regard, finite element models could also be validated on experimental data. The analytical models, with their inherit limitations could thus be replaced by finite element models or trained networks for a more accurate inverse identification of a fiber's transverse material properties.

3

SINGLE PLANT FIBER TRANSVERSE PROPERTY CHARACTERIZATION WITH HIGH PRECISION MICRO-MECHATRONIC SETUP

Contents

3.1 Introduction

The bases of the single fiber transverse compression test along with valuable insights on a series of influential parameters, were presented in the previous chapter with the use of analytical and finite element models. This chapter focuses on performing Single Fiber Transverse Compression Tests (SFTCTs) experimentally, providing for the first time, results on the transverse behavior of plant fibers. First, a state of the art on the experimental SFTCT is presented, highlighting its inherent challenges, limitations and possible improvements. Then, a new micro-mechatronic setup, developed within the frame of this doctoral thesis is presented, which improves on a lot of these previous limitations, offering fine control over force and displacement measurement, relative humidity, system compliance and sample observation. Furthermore, the major influence of platen parallelism on the identification of the transverse elastic modulus is quantified for the first time. An experimental protocol to assure parallelism with high precision is proposed. The performance of this setup is evaluated and validated, experimentally induced variability is thus greatly reduced. Finally, this experimental setup is used to perform for the first time, single fiber transverse compression tests on plant fibers: flax, hemp and nettle. Their elastic parameters are identified for the first time and mechanisms of inelastic and irreversible behavior are discussed.

This chapter contains numerous contributions from the work of both pre-graduate and post-graduate engineers. Work prior to this doctoral thesis laid the groundwork for future experimental developments. The intership of *Hamdi Saadana* (2017) produced the first version of the custom multisensing device used for force and displacement measurements. *Melissa Blot* (2018-2019) developed the first operational experimental setup for SFTCTs. Two undergraduate internships, related to experimental SFTCT investigations were also carried out and supervised in the context of this PhD work. *Anouk Chevallier* (2021-2022) made major contributions on experimental preparation and protocols, implemented a relative humidity control and performed the first experimental SFTCT campaign on plant fibers, throughout her internship and later engineering work. *Guillaume Pluvinage* (2021) developed a new protype of multisensing devices for compact SFTCT setups.

The presented results were also made possible by multiple collaborations within the *FEMTO-ST* institute. The work of *Antoine André*, *Guillaume Laurent* and *Patrick Sandoz* on the detection of fiducial markers and of *Joël Agnus* on clean room fabrication, made the fabrication and use of the custom sensors possible. Work on platen parallelism was also performed with the collaboration of *Violaine Guicheret-Retel* and *Fabien Amiot*.

The results of this chapter made the subject of three publications treating the use of fiducial markers for an innovative force-displacement sensor [Andre 22b], the importance and control of platen parallelism [Govilas 22] and the identification of plant fiber transverse elastic properties (paper in preparation).

3.2 Experimental SFTCT setups: overview and critical assessment

This section aims at presenting an overview of SFTCT experimental setups from their earliest implementations to their most recent iterations. The design and specifications of each of these setups can be quite unique, adapted for a specific type of fiber and using technology available at the time. For this reason, common approaches are presented and innovations are highlighted, without providing a detailed description of each one. Through this survey, a critical approach is employed, aiming at highlighting potential sources of measurement error, but also identifying and discussing possible improvements.

3.2.1 Overview of SFTCT experimental setups

Studying the transverse compression of a single fiber comes, regardless of its nature, with a series of experimental challenges. Most of them can be attributed to their small size, with diameters typically in the range of 10 to 100 μm. This means that if an elastic regime is studied, in a small fiber deformation range ($1-5\%$), sub-micrometric displacements need to be measured in order to study fiber behavior. Compression forces can vary largely with fiber nature and the studied deformation range, with typical values in the range of a few mN to a few hundred mN for small deformations and several Newtons for larger ones. The size of the fibers also implies that large magnifications are needed in order to observe them during compression. Furthermore, two important considerations are made in the choice of compression platens. The platens have to be rigid compared to the compressed fiber and surface irregularities must be much smaller than the fiber itself, to ensure that the platens do not influence compression results. For this reason, materials such as glass, sapphire, steel and silicon are commonly used for their rigidity and low roughness.

As a result of these experimental requirements, only a few authors chose to perform the test by adapting existing testing machines typically adapted for larger object testing [Phoenix 74, Sockalingam 16, McDaniel 17, Naito 17]. The majority of authors working on SFTCTs choose to develop custom experimental setups specifically for the purpose of the test.

The first SFTCT can be attributed to Hadley et al. [Hadley 65]. The fiber was loaded using weights and glass platens were chosen for their transparency in order to measure the contact width $2b$. Through the applied force and contact width data, the transverse elastic modulus of the fiber E_T was identified. This approach was common in this era with Pinnock and Jawad using the same method [Pinnock 66, Jawad 78]. Morris kept the loading by weights but added a platen displacement measurement through a micrometer instead of measuring the contact width [Morris 68].

With the improvements in actuation and sensing technology most authors adopted Moriss's approach, consisting of measuring displacement. The first modern SFTCT can be attributed to Kawabata who employed an electromagnetic power drive to perform the compression [Kawabata 90]. Since, the most common approach consists in controlling the movement of one of the platens through piezoelectric actuation while the other is fixed. A load cell is used to measure the compression force while the displacement of the platen/fiber is measured through capacitive sensors [Jones 97, Singletary 00a, Lim 10, Guo 16, Naito 17] or Linear Variable Differential Transformers (LVDT) [Kawabata 90, Kotani 94, Stamoulis 05, Cheng 04]. In most setups the upper compression platen is mobile and moving downwards towards the fiber, some setups however, move the lower platen upwards [Stamoulis 05, Wollbrett-Blitz 16].

The work of Mikczinski et al. is a standout among SFTCT experimental work, with an experimental setup developed to operate inside a scanning electron microscope, offering unprecedented observations capabilities [Mikczinski 13]. A force sensor played the role of the mobile platen and compressed allowing for direct measurements on the fiber.

3.2.2 Common limitations and possible improvements

It can be noted that, despite the history of SFTCTs spanning many decades, a relatively small amount of experimental studies have been performed when compared to more conventional tests such as tensile testing (see section 1.3). This means that a certain number of shared limitations and possible improvements can be identified among SFTCT experimental setups. This section aims at identifying said limitations and discusses possible solutions, in the context of plant fiber SFTCTs.

Platen parallelism

As we saw in Chapter 2, all analytical models of SFTCTs consider the fiber as a right circular cylinder between parallel platens. A lack of parallelism will thus cause an error in the identification of E_T if such a model is used.

The importance of platen parallelism has been recognized in the field of compression in general. The "Brazilian test" is a notable example. A standardization of the test proposed in 1978 suggested that compression jaws need to be "parallel within 0.25°" [Bieniawski 78], without quantifying however the induced error nor providing a method to set this parameter. Other compression studies report platen parallelism as well. In his review on uniaxial compression, [Darvell 90] noted that platen parallelism is "essential" though "rarely commented on in the print". In their study of strain rosettes under compression, [Little 05] also identified platen parallelism as "the most predominant of the factors investigated".

When it comes to SFTCTs, only few authors consider platen misalignment and propose means to experimentally adjust it. Yet, descriptions are usually extremely short and can even lack any sort of methodology, hindering reproducibility. No quantification of the tilt angle can be found either. [Hadley 65] manually adjusted parallelism using a screw mechanism, [Jones 97] proposed an apparatus with an aligning sphere, while [Wollbrett-Blitz 16] used three external stepping motors and optical fringes to finely control platen position [Josse 04]. [Sockalingam 16] and [Naito 17] proposed methods using platen preloading. A unique approach was proposed by [Guo 16] who performed a simultaneous compression of two fibers to avoid a rotation of the upper platen around the main fiber axis. Ultimately, even though platen parallelism is recognized as an important parameter and could explain variations in measured transverse properties, no clear and widely adopted solution exists to control it. Furthermore, to the authors knowledge, no direct quantification of the angle between the two compression platens has ever been performed and its influence on measured material properties has never been studied.

Developing a protocol to assure platen parallelism and quantify the error induced by a misalignment angle is therefore key in improving the accuracy of SFTCT experiments.

Low throughput

Another challenge in the experimental study of single fiber transverse properties lies in the time consuming nature of SFTCTs, leading to a low throughput in terms of testing. The small size and delicate nature of single fibers adds to the overall preparation time of the test, from sample observation and dimension measurement to proper positioning and loading. For this reason, the number of tested fibers in the literature is low, with authors usually testing 1 to 5 samples of each fiber type. Only a few authors reported testing a larger amount of fibers ranging from 20 to 40 [Singletary 00b, Stamoulis 07, Wollbrett-Blitz 16, Naito 17].

Literature on the tensile testing of synthetic fibers indicates that large data-sets are required to significantly reduce uncertainty and provide more confidence in experimental results [Joannès 20]. Such data sets can only be achieved realistically through automation. Automated tensile testing has been developed and employed [Mesquita 21], fiber preparation remains however, manually performed. More general microrobotic platforms able to perform both fiber preparation and measurements in addition to various mechanical tests, have been developed [Saketi 12, Hirvonen 15b, Latifi 15, Laurikainen 20] (see section 1.4 for more details), however a modest amount of fibers or filaments was tested.

The question of throughput becomes even more important in the case of plant fibers since their properties are naturally more variable than those of synthetic fibers [Bourmaud 18]. Therefore, testing a larger sample size than for synthetic fibers should be a long-term goal. Developing a setup that reduces the overall testing time, from fiber preparation to data post-treatment is thus essential.

System compliance

In mechanical testing setups, dealing with system compliance is key to assure the accuracy of the obtained result. In SFTCT experimental setups, complex assemblies are often made between actuators, pushing rods, platens and sensors. Small gaps and irregularities between components, or even component deformation, can cause small displacements and changes in force during compression, that need to be subtracted from the fiber compression related measurements. Many authors perform compression tests between platens without a fiber between them in order to characterize this system compliance [Singletary 00a, Sockalingam 16, Guo 16, Naito 17]. Some of them even chose to repeat these measurements before or after each fiber compression [Phoenix 74, Jones 97, Wollbrett-Blitz 16]. While such calibration procedures can reduce compliance-related uncertainty, they cannot eliminate it fully.

Furthermore, compliance characterization procedures increase the overall testing time significantly. For this reason some researchers find ways to avoid this characterization altogether. [Stamoulis 05] compresses in the upward direction to eliminate compliance related to the compression platen weight. [Hillbrick 19] in their cylinder compression studies use a video extensometer to directly measure displacement. This is possible due to the large diameter of cylinders used ($25mm$). Finally, [Mikczinski 13] eliminates numerous compliance issues by replacing the mobile platen by a force sensor. A direct force measurement is thus obtained, eliminating most compliance-related uncertainties.

Developing a setup that limits system compliance can thus reduce both measurement uncertainty and overall testing time, increasing throughput and measurement accuracy.

Force and displacement measurement

The measurement of force is key point in many different mechanical tests. However, force sensing presents a challenge when micro-scale objects such as fibers are tested due to many technical and physical limitations [Clévy 11, Liang 14, Wei 15, Zhang 19]. For this reason only a few commercially available sensors exist, that can measure forces in the range of interest for small deformation SFTCTs (few mN to a few hundred mN), which are the most adapted for the characterization of elastic properties. For this reason, excluding researchers who use weights as a force load reference, many researchers use sensors with a full measurement range of $100-200\,N$ across a single direction [Jones 97, Cheng 04, Sockalingam 16] or even higher [Stamoulis 05]. Typical precision for such sensors is around 0.05 to 0.1% of their full scale measurements, resulting in force measurement precision in the order of the mN. While serviceable, such sensors are not well adapted to study SFTCTs, at least not in a small deformation range. [Mikczinski 13] used a sensor offering great accuracy ($0.4\,\mu N$) (FT- S270, Femtotools, Switzerland), which comes however at the expense of a small measurement range of $2\,mN$. Only very small compression loads could thus be studied. Nevertheless, a few authors do use sensors with better adapted measurement range of $2\,N$ [Naito 17] or $500\,mN$ [Singletary 00b], offering adequate precision while allowing more important compressive loads to be studied. Such force sensors, that combine precision with a larger measurement range, should be preferred in SFTCTs.

In most setups developed since the one from [Kawabata 90], capacitance sensors and LVDTs provide displacement measurements with a precision reported by the authors of tens of nm [Kawabata 90, Kotani 94] down to a few nm [Jones 97, Guo 16] or even sub-nanometric precision [Lim 10]. Such precision is adequate to study fiber transverse compression, even in small deformation ranges where displacements are in the order of a few hundred nm to a few μm. However, these sensors are systematically positioned far from the fiber itself, measuring the displacement of the mobile platen or its pushing rode, adding to the compliance issues discussed previously. Measuring platen displacement closer to the fiber, or measuring fiber displacement directly, should be prioritized.

Fiber observation

Observing the fiber in-situ during compression can offer many advantages. First, it can greatly help in the fiber mounting stage and as a way to monitor the test, ensuring that it is taking place as expected. Sliding or rotating fiber motions, platen misalignments and platen surface conditions, can all be identified and assessed. A view of the fiber along its longitudinal or transverse cross section can also be used to identify the Poisson's ratios in the longitudinal and transverse plane, ν_{LT} and ν_{TT}, respectively.

These observations however, can be challenging. The small size of fibers means that microscopes with large magnifications are needed. However, space in the setups can be limited, making the addition of multiple microscopes to observe the fiber from different angles difficult. Furthermore, the fiber and the mobile or fixed compression platen are typically situated in different planes and can have edges that are not perfectly flat. Obtaining a sharp image can thus prove difficult even with larger depths of field.

Researchers who incorporate vision into their setup typically use vertically mounted microscopes, used for observing and sometimes measuring the contact width through transparent platens [Hadley 65, Jawad 78, Kotani 94, Jones 97, Stamoulis 05, Sockalingam 16]. In contrast, [Kawabata 90] and [Naito 17] use a horizontally mounted microscope to help with fiber positioning and monitoring. It is unclear which fiber cross section is observed. It should be noted that authors do not typically share images from these microscopes in their publications, which attests to the difficulty of obtaining good quality fiber observations during SFTCTs. The use of a setup inside a Scanning Electron Microscope (SEM) as seen in the work of [Mikczinski 13] offers exceptional observation abilities, it does need however a very compact experimental setup and increases overall testing time significantly. The environmental conditions inside a SEM chamber (vacuum, drying, electron beam) can also alter the properties of the tested fiber or damage it.

In conclusion, while challenging the use of high magnification microscopes in SFTCTs can offer great advantages in terms of test preparation and monitoring or even for measuring parameters of interest. For this reason incorporating it in SFTCT setup should be favored.

Relative Humidity (RH) and temperature control

Control of the test environmental conditions is also crucial in experimental measurement repeatability. Both sample behavior and geometry but also sensor measurements can be impacted by changes in the test's environmental conditions.

As already discussed in Chapter 1, plant fibers are particularly vulnerable to changes in Relative Humidity (RH), which can cause swelling or changes in material properties (see subsection 1.3.3). Controlling the experimental environment in terms of relative humidity is thus key. Existing SFTCT studies however, were performed exclusively on synthetic fibers (with the exception of [Mikczinski 13]) where sensitivity to humidity is less important. For this reason no active control of humidity can be found in the open literature and few authors document the relative humidity in which the tests are performed [Kawabata 90, Singletary 00a, Stamoulis 07, Naito 17].

Control of temperature during testing is also important. For one, it can be of interest to test fiber behavior in wide temperature ranges. Heating elements can be used for this purpose [Hadley 65, Kawabata 90]. Furthermore, accurate temperature control limits drifts in sensor measurements. Such changes are larger during an initial transient stage, when all the setup's electronic components are turned on and start heating. This transient behavior generally stabilizes to a stable one after some time [Mauze 20]. If no active temperature control can be established it thus important to ensure that temperatures are stabilized before performing tests, or limit overall testing time.

3.3 Developing and validating an innovative micro-mechatronic SFTCT setup

In the previous section, a critical overview of previous SFTCTs was performed. Good practices and equipment choices were discussed, while possible improvements were proposed. This section presents an innovative experimental setup developed specifically to perform SFTCTs while addressing previous limitations and integrating innovative approaches. A force-displacement sensor, developed for this application is introduced and its operating principle and calibration are detailed. Measurement accuracy and repeatability are evaluated and compared to those found in the literature. Finally, the question of platen parallelism is treated, showing its major influence on E_T identification while also proposing an experimental protocol that minimizes platen misalignment.

3.3.1 Overview of new SFTCT setup

This subsection aims at providing an overview of the SFTCT experimental setup that was developed and used in this work. The experimental setup can be seen in Figure 3.1. The most typical configuration of the test is adopted, with the fiber placed between two compression platens with the lower one being fixed and the upper one being mobile. The test configuration in our case can be summarized as follows:

- The lower-fixed compression platen is a metallic parallelepiped fixed on a stationary aluminum support. It provides a surface of $21 \times 2\,mm$ on which a fiber can be positioned and compressed. Initially an aluminum platen was used, whose stiffness greatly exceeded the fiber's, with a roughness of $S_a = 980\,nm$ (mean arithmetic surface height). Knowing the fibers can have diameters at the scale of a few microns this roughness was not satisfactory. For this reason, this platen was eventually replaced with a tungsten carbide one, providing a roughness of $S_a = 390\,nm$ and an even higher stiffness.

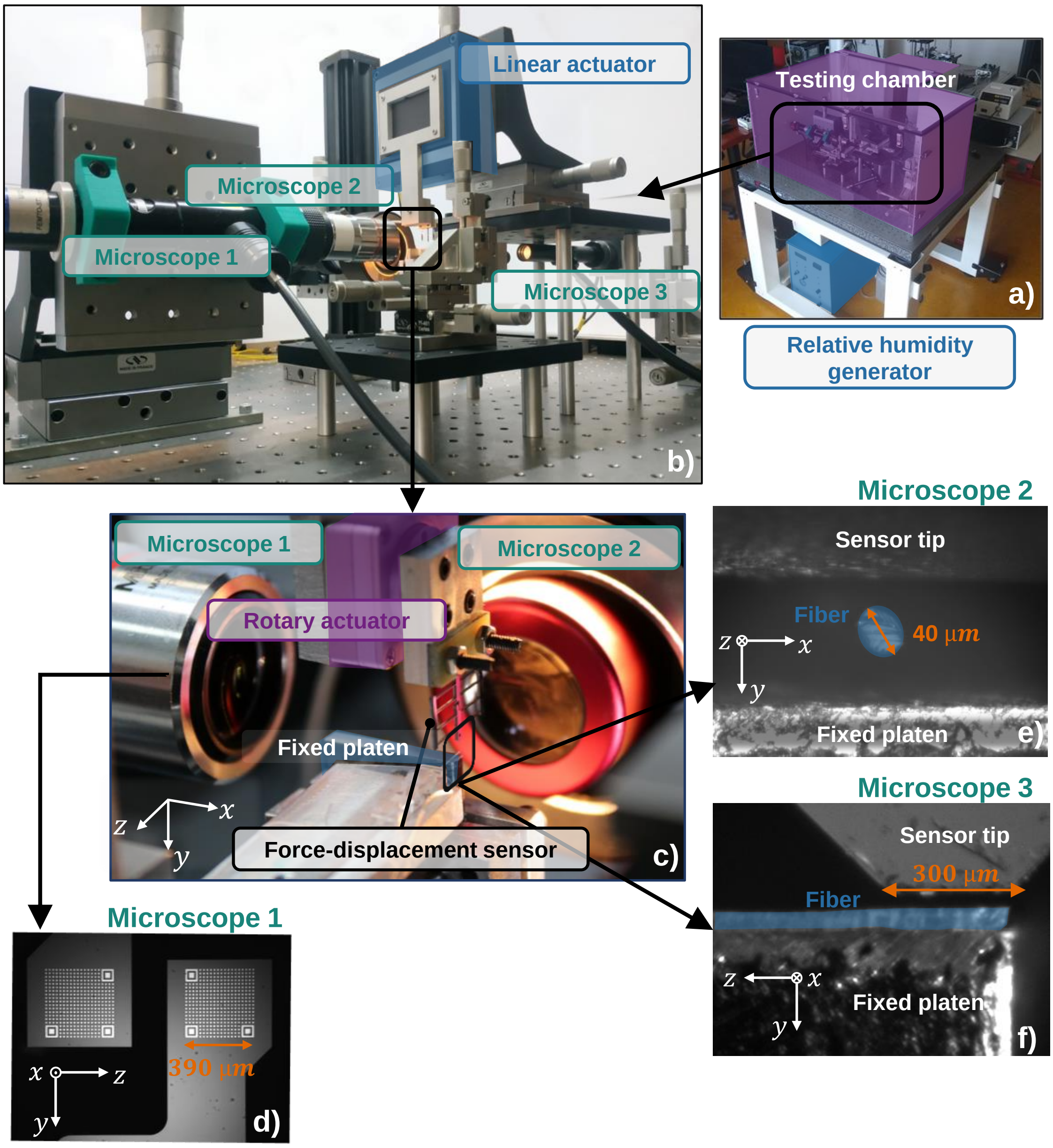

Figure 3.1: SFTCT experimental setup. a) testing chamber on active anti-vibration table and relative humidity generator, b) overview of setup with its three microscopes, linear actuators and micropositioning tables, c) closeup view on rotary actuator, force displacement sensor and fixed platen with views from all three microscopes (d, e, f).

- The tested fiber is positioned in a fixed-free configuration, with its free end resting on the lower compression platen. This configuration allows the observation of the fiber cross transverse section during compression (see Figure 3.1.e). The fixation is made with photo-polymerized glue on a special tab (see subsection 3.4.1). The tab is then mounted on a XYZ manual micropositioning stage (*Newport*) to accurately place the fiber on the lower platen.

- The upper-mobile compression platen is replaced by a custom force-displacement sensor, positioned directly above the fiber (see Figure 3.1.c). The sensor is a compliant structure that allows for vision based measurements through the tracking of fiducial markers (see Figure 3.1.d). A detailed discussion on its functioning will be given in subsection 3.3.2. Its thickness of $500\,\mu m$ covers with ease the entire diameter of all tested fibers along the x axis (see Figure 3.1.e). Contact between the fiber and the sensor tip is established on a length of $300\,\mu m$ along the z axis (see Figure 3.1.f). The use of this sensor allows for direct measurements close to the fiber, limiting the measurement uncertainty of system compliance, along with the time consuming nature of its calibration.

In order to carry out the SFTCTs, actuation is required to move the sensor against the fiber and compress it. Our setup uses two different actuators to accurately and repeatably perform fiber compression:

- A rotary actuator (*SmarAct SR-2013*) to control the angle between the force-displacement sensor and the lower compression platen (see Figure 3.1.c). This system is closed loop controlled, employing a rotary encoder with a resolution of $25\,\mu°$. The sensor is mounted on the actuator through an intermediate aluminum piece. The use of this actuator allows for the control of parallelism between sensor and platen (see subsection 3.3.4).

- A linear piezoelectric nanopositioner (*PI PIHera 629.1*) to move the sensor-rotary actuator assembly towards the fiber and compress it with a resolution of $14\,nm$. The system is closed loop controlled with a capacitive sensor performing a direct position measurement. Its travel range extends to $1.8\,mm$. An intermediate aluminum push rode links the nanopositioner to the rotary actuator (see Figure 3.1.b). A manual XYZ micropositioning stage (*Newport*) is used to position the nanopositioner-actuator-sensor assembly above the fiber.

Vision is also a key parameter in our experimental setup. In order to measure the displacement of the sensor's fiducial markers and observe the fiber during compression, three microscope assemblies are used:

- Microscope 1: Guppy F-046B camera with $5X$ lens (Mitutoyo, Japan), for the force-displacement sensor's fiducial marker observation (yz plane) (see Figure 3.1 b,c and d).

- Microscope 2: uEYe camera with a $20X$ magnification lens (Mitutoyo, Japan), for the fiber diameter observation (xy plane) (see Figure 3.1 b,c and e).

- Microscope 3: uEye camera with $0.8X$ magnification lens (Edmund 62-789), for the fiber length observation (yz plane) (see Figure 3.1 b and f).

Finally, control of the Relative Humidity (RH) during compression is also critical especially in the case of plant fibers. For this reason a custom enclosure was created for the setup, its total volume being around 200 liters. A RH generator (HumiSys HF) was added with a flow of $20\,L/min$ (see Figure 3.1.a). Active regulation is performed with a temperature and relative humidity sensor placed close to the compressed fiber. Based on the measurements of these sensors, the generator adapts an air mixture inside the preparation chamber. This prepared air mixture then gets transmitted inside the testing chamber. No active temperature control is implemented in the setup.

Overall, the approaches used to address the previous discussed SFTCT limitations (see 3.2) are summarized in Table 3.1.

Test domain	**Previous setups**	**Potential problems**	**Implemented improvement**
Platen parallelism	Limited-no control	Errors in E_T identification	Rotary actuator - Misalignment minimization protocol
Low throughput	No automation	Limited number of tested samples	Basis for automation, reduced overall testing times
System compliance	Pre-test calibration	Potential measurement errors, time consuming	Direct force-displacement measurements
Force-displacement measurement	Commercially available sensors	Not adapted to all SFTCTs	Custom multisensing device, improved accuracy, measurement range
Fiber observation	Limited	Limited test monitoring - image based measurements	Multiple microscope integration
Relative humidity	No active control	Reduced repeatability, impacted fiber properties	Active RH control
Temperature	Rare active control	Reduced repeatability, impacted fiber properties	Limited changes resulting from RH control.

Table 3.1: SFTCT experimental setups, overview and proposed improvements.

3.3.2 Custom force-displacement sensor: design, operation and characteristics

Given the questions raised in terms of system compliance and force/displacement measurement (see. section 3.2), a custom sensor was developed, designed to directly compress the fiber and measure both the applied compression force and the fiber's displacement. The term FU sensor will be used to refer to this sensor (F and U to symbolize force and displacement respectively). This section presents the sensor's design, operating principle and dimensioning that results in a sensor suitable for SFTCTs. Analytical and numerical estimations of stiffness are also presented.

Design and operating principle

The proposed force-displacement sensor is a compliant structure that includes 8 bending beams organized along a Compliant Translation (CT) joint [Trease 05]. This architecture is very compliant along a single axis (axis of beam bending) while presenting a high translational and torsional rigidity along the other axes. This allows a highly straight and guided motion along the measurement axis with off axis movements being limited. The use of a compliant sensor to eliminate system compliance might seem paradoxical. As it will be detailed later, when using this sensor, measurements are made by tracking the relative displacement of its different parts. In order to track these movements, their amplitude must be important enough to be detected with a microscope. For this reason high sensor compliance is important. Nevertheless, this compliance is stable, can be accurately measured by calibration (see subsection 3.3.3) and can be changed if needed.

The sensor is a product of clean room fabrication on a silicon wafer (*FEMTO-ST MIMENTO Technology Center*). Being a brittle material [Hull 99], silicon will present no plastic behavior and exhibit a linear elastic behavior until failure. Coupled with the CT joint architecture, a linear sensor behavior during compression is ensured in this way. Silicon also presents high stiffness in the wafer's plane at $E = 169\,GPa$ [Hopcroft 10] which is much higher than the stiffness of the fibers that will be compressed.

The sensor is comprised of three main parts as seen in Figure 3.2: (i) the upper part, connected to the linear actuator; (ii) the lower part, whose tip gets directly in contact with the fiber and (iii) 8 beams connecting the upper and lower parts. The sensor's operating principle can be summarized as follows: the linear actuator moves the sensor vertically downwards (y axis), establishing a direct contact between its lower part and the fiber. Once the contact is established, a compressive load is generated and the sensor's beams start bending through elastic deformations. This allows the upper part of the sensor to continue its imposed downwards movement. The lower part however, moves only as much as the fiber contracts. Since the stiffness of silicon is much higher than the one of the tested fibers and all of the sensor's compliance is expressed through the deformations of its beams, the lower part of the sensor acts as a rigid compression platen. This difference in behavior between the two sensor parts leads to a relative vertical displacement, ΔY, between them.

In order to measure ΔY, fiducial markers, similar to QR codes, are printed by photolithography and metal deposition on two emplacements at the center of the sensor. The term High Precision (HP) code is used to describe them. The left HP code is printed on the sensor's upper part, which is fixed on the push rode of the linear actuator. Its movement is completely dependent on the actuator movement. For this reason this HP code will be referred to as "dependent". The right HP code is printed on the bottom sensor part, that moves independently of the actuator's movement reacting to the movements of the compressed object. For this reason it will be referred to as "independent".

The horizontal (Z) and vertical (Y) position along with the in-plane rotation (ψ) of each HP code, can be tracked and measured [Guelpa 16, Andre 21]. Through the HP code's periodic nature, changes in its position are detected through the use of Fourrier transforms. This method offers sub-pixel accuracy which can be at the nanometer scale [Andre 20]. This offers exceptional measuring capabilities for SFTCTs. Such measurements can also be expanded to off plane Degrees Of Freedom (DOF) [André 22a]. HP codes can thus form the basis for accurate, multi-DOF measurement devices [Andre 22b].

Using HP code tracking the relative vertical displacement between the two sensor parts

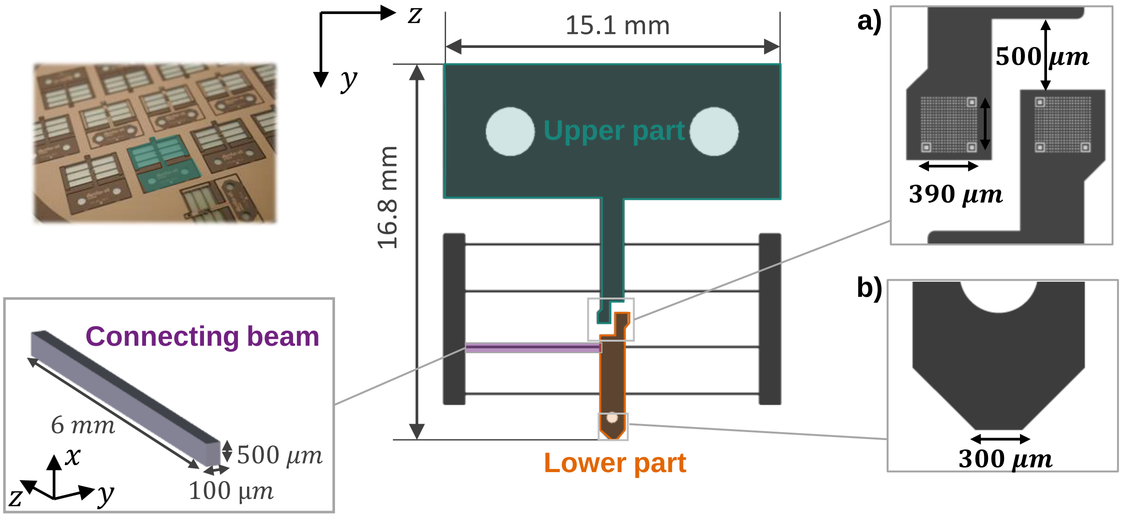

Figure 3.2: *FU* sensor design with close-up view on fiducial markers (a) and sensor tip (b).

can thus be obtained by:

$$\Delta Y = Y_d - Y_i \tag{3.1}$$

where: Y_d and Y_i are the vertical coordinate of the dependent and independent HP codes respectively. Consequently, the applied compressive force can be calculated by:

$$F = k \cdot \Delta Y \tag{3.2}$$

with k being the sensor's stiffness. A calibration procedure to determine k will be presented in 3.3.3.

Since the lower part of the sensor plays the role of a conventional rigid mobile platen, the displacement of the fiber under compression, U, corresponds directly to the displacement of the lower part of the sensor, from the position at which contact is first established. It can be calculated by:

$$U = Y_i - Y_{ic} \tag{3.3}$$

with: Y_i the current coordinate of the independent fiducial marker and Y_{ic} its coordinate when the contact is first established (where Y_d becomes greater than Y_i). A more accurate method to detect the contact point is discussed in appendix B.1. The HP codes at the contact point and at maximum compression as seen, by the microscope, are shown in Figure 3.3. While the measurement along the compression (y axis) are of main interest in SFTCTs, the off-axis measurements can also be used to estimate displacements and forces.

Using a compliant sensor to directly compress the fiber, presents an interesting side effect in the manner the compression is performed. The test is controlled through the nanopositioner that generates displacements following a reference loading protocol. As already detailed, the upper part of the sensor will follow these displacements for many tens or hundreds of μm from the initial loading point, according to the chosen loading level. The lower part however will move only as much as the fiber contracts, generally in the order of a few μm. The vertical displacement of the independent HP code is thus significantly smaller than the displacement of the dependent one ($Y_i \ll Y_d$). The relative displacement between the two is therefore almost equal to the movement of the

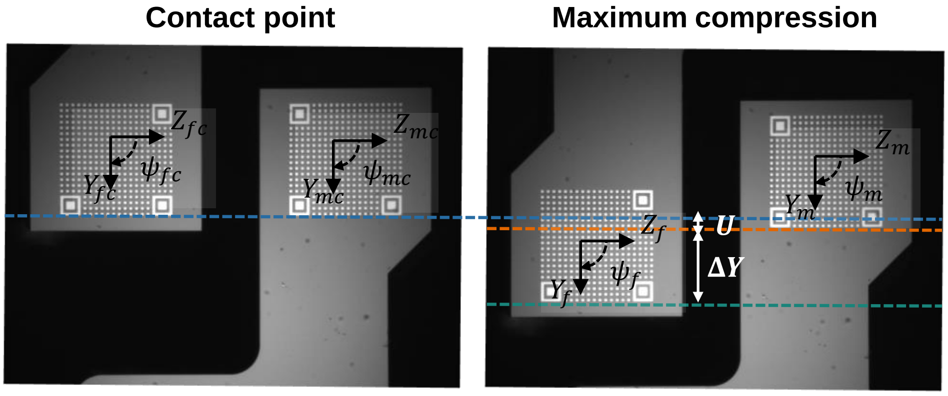

Figure 3.3: Image of sensor HP codes as observed by a microscope at: initial contact point, with the tracked coordinates Y, Z and ψ (left), at maximum fiber compression for a fiber displacement U and relative displacement between HP codes ΔY (right).

sensor's dependent part ($\Delta Y \simeq Y_d$). Since the applied compression force is calculated by: $F = k \cdot \Delta Y$, the compression test in our SFTCT is essentially controlled in terms of load. The following, statement thus stands: using our custom compliant sensor, a test controlled through nanopositioner generated displacement produces a compression controlled in terms of force.

Sensor dimensioning

The overall characteristics of the sensor are depended on multiple parameters. Choosing the dimensions of key sensor parts is the main way to control them. A first main parameter is sensor stiffness, which is mainly dictated by the dimension of the bending beams. Sensors with different stiffnesses can be produced by changing the length l and width w of these beams, or by choosing a wafer of different thickness t. Beam width is the most influential parameter in the final stiffness since it represents the dimension in the direction of the applied force and is therefore cubed in the calculation of the second moment of area:

$$I_y = \frac{tw^3}{12} \tag{3.4}$$

Considering a bending of the beams along the y axis, the sensor's lower and upper parts, with their according beams, can be considered as two sets of 4 parallel springs connected in series. Through this approximation the sensor stiffness can be calculated with:

$$k = 2\frac{tw^3}{l} \tag{3.5}$$

The maximum force that can be applied constitutes another important sensor parameter. It is a function of the sensor's stiffness and maximum possible relative displacement ΔY_{max}. This parameter depends on the spacing between the upper and lower parts of the sensor and by the strength of the beams, where stress concentrations will be the largest and the risk of material failure is the highest.

Finally, the accuracy in the measurement of HP code displacement is dependent on their relative size inside the field of the view of the microscope that observes them. The larger the size the better the accuracy. However, enough space inside this field of view must be present in order to track the HP code in their entire range of motion.

Overall, designing such a force sensor consists in finding an optimum compromise between maximum force and HP code tracking accuracy. If the sensor is very stiff, large forces can be applied at the expense of very small HP code displacement, that can be difficult to track. Sensors that are more compliant, offer less maximum force with HP code displacements that are easier to track.

For the sensor used in all presented experimental studies the chosen dimensioning can be summarized as follows:

- Beam dimensions were chosen as $l = 6\,mm$ and $w = 100\,\mu m$ with a wafer thickness of $t = 500\,\mu m$. The theoretical sensor stiffness, as calculated by equation 3.5 is of $k = 782\,N/m$. With a gap between the upper and lower sensor part of $500\,\mu m$ the theoretical maximum force that can be measured is $F_{max} = 391\,mN$, which is well adapted for the transverse compression of most fibers in a small deformation range.
- The HP code width is chosen as $390\,\mu m$ with a periodic pattern of $10\,\mu m$. This allows to observe the HP codes for the full range of movement of the sensor while offering good accuracy (characterized in subsection 3.3.3).
- The sensor's tip length was set at $300\,\mu m$. Given the average diameter of plant fibers at $20 - 40\,\mu m$, the contact length with the sensor is an order of magnitude greater than fiber diameter.
- The overall footprint of the sensor was chosen such as to maximize the amount of sensors that can fit on a wafer, while allowing easy manipulation and mounting.

Finite element simulations were also used in order to quantify the sensors stiffness in compression and torsion. A detailed description of this finite element analysis can be found in appendix B.2. Torsional rigidity is found to be very high at $k_t = 0.06\,N \cdot m/°$, limiting off-axis movements and attesting to the good design of CT joints. Compressional stiffness on the other hand is found to be low enough, to allow for a linear sensor compression along its vertical axis, with $k = 773.5\,N/m$, which is very close to the analytical prediction.

3.3.3 Setup validation and calibration

Before proceeding to SFTCTs, it is necessary to analyze the behavior of the components of the experimental setup, perform calibrations and evaluate the measurement repeatability in order to validate the experimental procedure and quantify the level of precision. This section focuses on quantifying the repeatability of displacement measurements through HP code tracking, on the calibration of the force-displacement sensor. The subject of thermal drift is also discussed.

Displacement measurement repeatability

In order to examine the sensor's behavior and to quantify the repeatability of HP code measurements, compression tests are performed against the fixed platen, to eliminate the influence of a deformable and potentially geometrically complex object. Given the compliance of the force sensor, the fixed platen can be considered as rigid.

Ten successive tests were performed on the fixed platen in ambient conditions. The parallelism between the force-displacement sensor and the fixed platen was adjusted with the rotary actuator by observing the objects through Microscope 3. The presented results, are thus obtained in sub-optimal experimental conditions compared to the setup capabilities and represent a type of worst-case scenario in terms of repeatability. Using the parallelism setting protocol (see subsection 3.3.4) and controlled environmental conditions should result to even better results.

Figure 3.4 shows the evolution of the three HP code coordinates (Y, Z, ψ) as a function of time. Their evolution over the ten tests is plotted. In the y direction both HP codes follow the same trajectory until contact is established (see Figure 3.4.a). The movement of the independent HP code is then stopped, since it is pushing against the fixed platen. The sensor's beams are bending allowing the dependent code to continue its trajectory. The HP codes follow the same trajectory once again during the unloading phase, once the contact is lost. A similar behavior occurs on the z axis (see Figure 3.4.b), with a much smaller magnitude of displacement at the micrometer scale. Before contact, movements in the z axis can be attributed to a movement of the sensor which is not perfectly aligned with the vertical axis of the camera's frame. Small misalignment angles between the different components and the camera are the main reason. Slight non-linearity in the movement generated by the nanopositioner could also contribute to these changes in the Z coordinate. Once the contact is established, the evolution of the Z coordinates becomes slightly different. Sliding motions due to small parallelism defects between the sensor tip and the fixed platen are the most probable cause. This is why the Z movement of the independent HP code is slightly higher. However, the overall Z movement of the two HP codes is very close, attesting to the sensor's ability to limit off axis motion. Finally, rotation behavior follows a slightly different pattern (see Figure 3.4.c). The dependent HP code rotation can be attributed to a nonlinear displacement of the actuator that does not produce a perfectly straight movement [Tan 15a]. For the independent code, contact with the fixed platen stops the rotation. These rotations however are very small in the order of $0.1°$ pointing to the sensor's ability to limit torsion.

To quantify HP code measurement repeatability, the standard deviation of the Y, Z and ψ quantities is calculated at each time step for the 10 tests. This deviation is then averaged for the entire procedure and for both HP codes, resulting in values of : $41\,nm$ in the y direction, $111\,nm$ in the z direction and $69\,\mu rad$ for the rotation. Contrary to Y and ψ, the deviation in Z is much more important since sliding motions are hardly predictable and repeatable at the microscale.

Overall, these repeatability values are of the same magnitude, or larger, than the precision announced in the literature for SFTCT measurements ($1-50\,nm$, see subsection 3.2.2). However, displacement measurements with this new sensor are much more direct and not dependent on setup assembly compliance. Larger HP codes or higher microscope magnification could be used to improve measurement accuracy, at the expense of some force range (the movement of the HP codes has to stay in the observation frame). A new sensor was also designed and fabricated during the internship of *Guillaume Pluvinage*. A single HP code was placed at the sensor's tip. An observation of the fiber's compression and HP code movement could thus be made in parallel, leading to even more direct measurements. Further details on this work are given in appendix B.3.

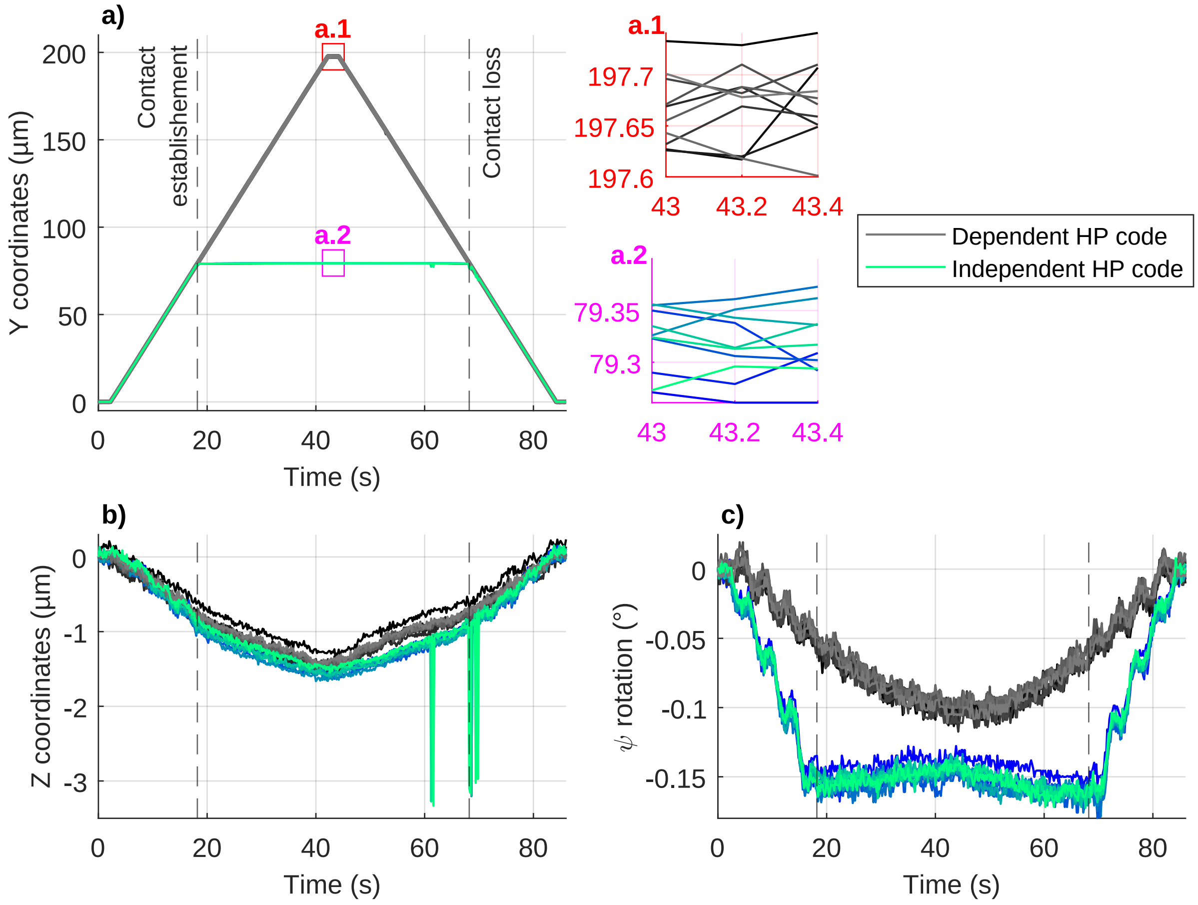

Figure 3.4: HP code measurements over 10 compression tests against the fixed rigid support for: a) Y, b) Z and c) ψ coordinates. Each line represents a different test. In the Y coordinate plot, the dependent HP code coordinate is shown with a thicker line for visibility purposes. a.1 and a.2 show a closeup of the Y position of the dependent and independent code respectively.

Force-displacement sensor calibration

Calibration of our custom FU sensor is made through the compression of a commercially available sensor (TEI FSB 101) that is used as a reference. The reference sensor is calibrated according to the ISO-10012 norm. With the use of the force given by the reference sensor F and the relative displacement between the two HP codes ΔY, the sensor stiffness k can be identified by linear regression.

The reference sensor was chosen for its measurement range of $200\,mN$ which is relatively close to the one of our sensor ($\simeq 350\,mN$). The manufacturer claims a non-linearity of $\pm 0.1\%$ and repeatability of $\pm 0.05\%$, the sensor's accuracy is thus expected to be between 0.1 and $0.2\,mN$. A spherical ruby tip is mounted on the top of the reference sensor. Its spherical nature limits error related to a lack of parallelism between the sensors. The experimental setup's microscopes are used to center the tip of the FU sensor over the ruby tip. To perform the calibration, the mount holding the fixed platen is replaced with a mount holding the reference sensor. Figure 3.5 illustrates this experimental configuration along with a photo of the two centered sensor tips. Every time a new FU sensor is used, this calibration is performed, since small irregularities in the sensor's beam can lead to changes in stiffness between sensors.

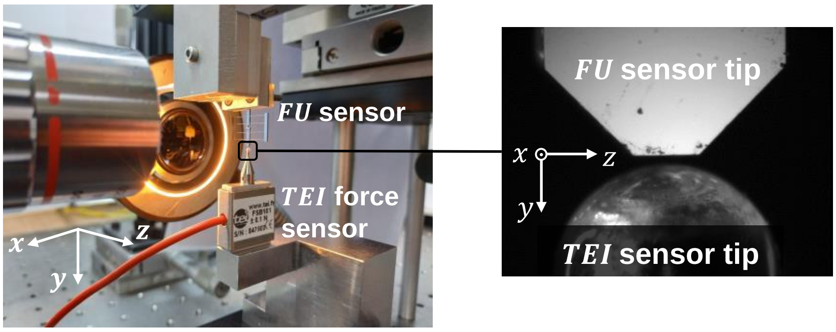

Figure 3.5: SFTCT experimental setup for force sensor calibration. The *FU* sensor tip is centered over the ruby tip of the reference sensor as seen on the microscope image on the right.

Calibration results for three different sensors are presented in Table 3.2. The stiffness was calculated at both the load and the unload phase. Calibrations were repeated 20 successive times. Average sensor stiffness was found to be $k = 666.70\,N/m$. The small value of the standard deviation ($0.95\,N/m$ on average) in the identified stiffness of each sensor, illustrates a great repeatability of the calibration test. Given the gap of $500\,\mu m$ between the upper and lower part of the sensor, the *FU* sensors can measure, on average, a maximum force of $F_{max} = 327.4\,mN$. Pearson's coefficient [Pearson 96] between F and ΔY is calculated at 0.99, with a value of 1 representing a perfectly linear correlation. Sensor response is thus extremely linear throughout the whole calibration process.

Sensor	$\boldsymbol{k\,(N/m)}$	$\boldsymbol{F_{range}(mN)}$	$\boldsymbol{F_{max}\,(mN)}$	$\boldsymbol{r_{Pearson}}$	$\boldsymbol{N_{test}}$
1	689.2 ± 0.4	344.6	130.8	$0.99 \pm 4 \cdot 10^{-6}$	20
2	664.7 ± 1.6	332.3	117.5	$0.99 \pm 3 \cdot 10^{-5}$	20
3	646.2 ± 0.9	323.1	179.9	$0.99 \pm 1 \cdot 10^{-6}$	20

Table 3.2: Results of *FU* sensor calibration with: k the identified sensor stiffness, F_{range} the force measurement range of the *FU* sensor, F_{max} the maximum applied force during the calibration test, as measured by the reference sensor, $r_{Pearson}$ the Pearson correlation coefficient and N_{test} the number of repeated calibration tests.

Caution was used in the maximum displacement of the *FU* sensor to avoid exceeding the maximum force that can be measured by the reference sensor. Since, a real time force measurement numerical feedback was added, which will allow to easily assess when the limit of the reference sensor is reached. A reference force sensor with a measurement range that is equal to the *FU* sensor's range would also allow the study of sensor stiffness and linearity across its whole measurement range. Nevertheless, given the elastic and brittle nature of silicon and the architecture of the CT-joint, no changes in the linearity of the sensor should occur at any force, before reaching its breaking point or the maximum relative displacement allowed by the gap between the upper and lower part of the sensor.

A small difference exists between the stiffness calculated by analytical or finite elements models (782 and $773\,N/m$ respectively) and the one obtained experimentally through calibrations. This can be mainly explained by a difference in beam width resulting from the clean room fabrication. Deep reactive-ion etching [Laermer 20] is used to separate the sensor contour from its wafer. This process creates a "sidewall angle", meaning the sides are not perfectly vertical, due to the different times of exposure to the ion beam. Beam width is thus slightly smaller than the theoretical one, leading to a decrease in sensor stiffness. Other small geometric imperfections and some inaccuracy in the Young's modulus used in the models can add to these differences.

A final point of interest in the calibration tests lies in comparing the force measurements between the sensors. Three types of force related data are calculated across the whole length of the calibration test:

- dF, the difference in measured forces from the two sensors across the whole calibration test.
- δF an estimate of measurement noise for each sensor. It is calculated in a similar way to displacement repeatability measurements (see subsection 3.3.3). The standard deviation in force measurement is calculated at each step, across the 20 tests. These deviations are then averaged to give a mean value of force measurement deviation across the whole test.
- NR, noise to measurement range ratio. The noise estimate δF is divided by the sensor's measurement range.

Table 3.3 summarizes this force data for three calibrated sensors. The average value of dF for the four calibrated sensor is of $0.27\,mN$ or 0.13% of the reference sensor's measurement range. This difference may result by noise, slight misalignment between sensors and slippage at the contact surfaces. It is nevertheless very small compared to the applied forces and in the order of magnitude of the reference sensor's accuracy. Force measurements coming from both sensors are thus consistent. When measurement noise is considered, the reference sensor produces a very repeatable δF of $0.27 \pm 3 \cdot 10^{-4}\,mN$ which represents 0.13 % of its measurement range. The force displacement sensor produces a lower yet slightly less repeatable value of δF of 0.10 ± 0.02 which represents only 0.03 % of its measurement range.

		reference TEI sensor		***FU* sensor**	
Sensor	$\boldsymbol{dF\,(mN)}$	$\boldsymbol{\delta F\,(mN)}$	$\boldsymbol{NR}\,(\%)$	$\boldsymbol{\delta F\,(mN)}$	$\boldsymbol{NR}\,(\%)$
1	0.32	0.27	0.13	0.06	0.02
2	0.22	0.27	0.14	0.11	0.03
3	0.26	0.26	0.13	0.10	0.03
Overall	0.27 ± 0.04	$0.27 \pm 3 \cdot 10^{-4}$	$0.13 \pm 1 \cdot 10^{-3}$	0.10 ± 0.02	$0.03 \pm 7 \cdot 10^{-4}$

Table 3.3: Difference in force measurements between reference and FU sensors during calibration dF, along with noise estimate δF and noise to range ratio NR. Overall data is presented with an average and standard deviation value.

Several conclusions can be drawn from these results. The performed calibration tests are very repeatable as attested by the small values of deviation in measured forces, noise levels and by consequence identified sensor stiffness. The developed force-displacement sensor also produces a lower level of noise compared to the reference one while also offering a larger measurement range. When compared to the force sensors used in the literature for SFTCTs (see subsection 3.3.1) it also offers great performance. The sensor used by [Mikczinski 13] offers greater precision at $0.4\mu N$ it has however only 0.28% of the FU

sensor's measurement range. All other used sensors are adapted for much higher force levels, allowing the study of large deformation regimes, but offering precision that is orders of magnitude lower than the *FU* sensor. Given that small deformation ranges are needed to identify elastic parameter, the use of such sensors makes such studies difficult, while the *FU* sensor is very well adapted.

Thermal drift

Temperature related drifts in position measurement have been observed for HP code measurements [Mauze 20] and typical microrobotic setups [Tan 13]. Changes of $1°C$ were shown to cause drifts at the micrometer scale. Changes in temperature are more important when all experimental components are first turned on. As lighting, electrical circuits etc. are activated a transient increase in temperature occurs, which eventually gives places to temperature changes that are much slower.

While, force measurements should not be severely influenced by a position drift, since they rely on the relative difference in the position of the two HP codes, the measurement of fiber displacement could be impacted since it relies on the position of a single HP code. Since temperature related drifts have not been characterized on our SFTCT setup, tests that are conducted over long periods of time, such as creep of fatigue tests will not be performed. Measurement repeatability however, was demonstrated for shorter testing times (a few minutes). For this reason, SFTCT will performed over such shorter time scales.

3.3.4 Platen parallelism control and influence on SFTCT results

This section focuses on an often acknowledged but rarely treated experimental parameter in SFTCTs: platen parallelism. An experimental protocol to reduce the angle between compression platens is presented. The influence of this angle, that will named "tilt angle", on the identification of the fiber's transverse elastic modulus will also be studied and quantified through finite element analysis and experimental studies.

Introduction

As we saw in Chapter 2, all analytical models of SFTCTs consider the fiber as a right circular cylinder between parallel platens. This allows to model the contact between fiber and platens through Hertzian contact as long as the contact half-width b is significantly smaller than the fiber radius R. It was also shown, through sensitivity analysis (see section 2.2.3), that the identified transverse elastic modulus E_T is very sensitive to R, the only geometric parameter in the model. Consequently, any change in the geometry of the test, that deviates from its typical representation, can cause a significant variation in the identified E_T. This change in geometry can be linked to complex fiber morphology which deviates from the right cylinder hypothesis, as shown in section 2.5. It can also be caused by a lack of parallelism between the platens, which can significantly change the contact surface between fiber and platen.

Figure 3.6 illustrates platen misalignment through two main rotations of the upper platen. A rotation along the fiber's longitudinal axis (z axis), with an angle named θ, and a rotation along the x axis, with an angle named φ. In the case of a θ angle rotation, the whole fiber length remains in contact with the upper platen. Furthermore, the circular nature of the fiber minimizes the change in contact surface resulting from this rotation. The main problem with this rotation lies in the fact that the compression force is not completely vertical, pushing the fiber horizontally (along the x axis) in addition to compressing it. This can lead to deviations from the analytical model predictions and errors in the identification of E_T. For small angles however ($< 1°$), these differences should be limited. When a φ angle rotation takes place however, only part of the fiber is in contact with the upper platen. The contact surface is thus majorly impacted, even for small angle values. For this reason, we choose to study the influence of the φ angle on the identification of E_T. The term "tilt angle" will be used to describe it.

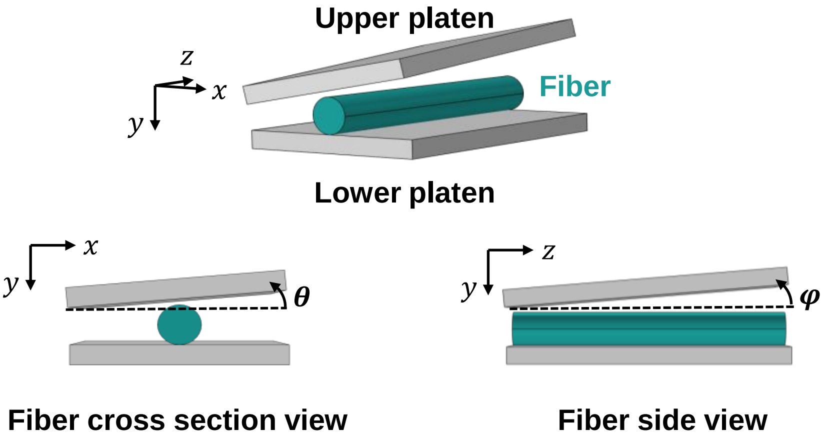

Figure 3.6: Representation of possible misalignment angles between compression platens. The angle φ is defined as "tilt angle".

Platen parallelism control

Analytical model - In order to use the existing SFTCT analytical models the parallelism between compression platens must be assured. In other words, the tilt angles must be experimentally minimized. For this reason, an experimental protocol was developed that allows to place the tip of our force-displacement sensor, parallel to the fixed platen through rotations generated by the rotary actuator.

The basis of this protocol lies in the analytical description of the evolution of the distance between two objects when one of them is fixed and the other is subject to a rotation. In the present case, the objects are the fixed lower platen and the force-displacement sensor, rotating with an angle α given by the rotary actuator. The sensor is modeled as a rectangle of length L and width w, with a distance of Y_0 from the fixed platen when the tip of the sensor is parallel to the fixed platen. The length L also corresponds the distance between the sensor's tip and the rotation center of the rotary actuator. A representation of the sensor-fixed platen configuration for an angle $a > 0°$ is given in Figure 3.7. In this configuration, the distance between the rectangle and the plane, Y_c is given by:

$$Y_c = Y_0 + L\big(1 - cos(\alpha)\big) - \frac{w}{2}\big|sin(\alpha)\big| \tag{3.6}$$

Figure 3.8 shows the distance Y_c as a function of the angle α. Its overall shape is similar to a lower-case omega(ω) with the parallelism between sensor and platen located at the center tip.

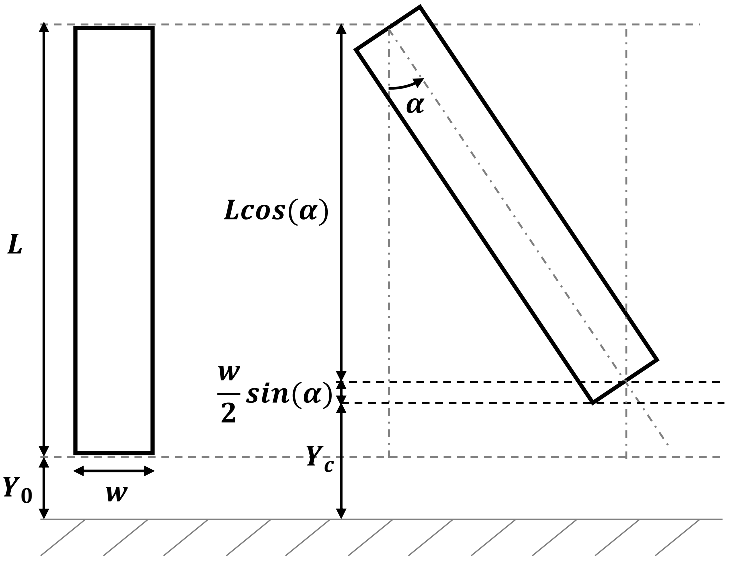

Figure 3.7: Sensor- fixed lower platen simple geometric representation in a parallel state and with an angle α.

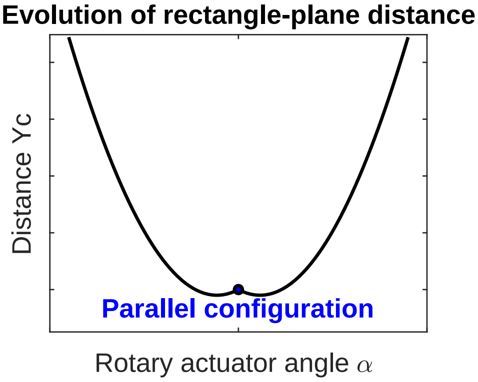

Figure 3.8: Distance between sensor and fixed platen Y_c as a function of the angle given by the rotary actuator α. The parallelism between the object is ensured for the angle at the tip of the ω shape, represented with a blue point.

In practice, different misalignments with respect to the vertical axis of compression occur during the assembly of the different components of the experimental setup (sensor, rotary actuator, nanopositioner etc.). Therefore, the reference position of the rotary actuator ($\alpha = 0°$) does not correspond to a sensor parallel to the lower platen. An angle β is thus introduced to describe the combination of all these misalignments. Consequently, the rotary actuator has to generate a rotation of $\alpha = -\beta$ from its reference position, to ensure parallelism. In order for β to represent all misalignments between the sensor and nanopositionner, L must represent the distance between the sensor's tip and an apparent rotation center point located on the nanopositioner instead of the rotary actuator. The new equation can be written as follows:

$$Y_c = Y_0 + L\big(1 - cos(\alpha)\big) - \frac{w}{2}\big|sin(\alpha + \beta)\big| \tag{3.7}$$

Experimental tilt angle minimization - Using the presented analytical model, the necessary rotation generated by the rotary actuator that ensures the parallelism between the sensor and the lower platen can be identified experimentally. The sensor is approached to fixed platen and pressed against it with different α angles. The distance Y_c corresponds to the distance traveled by the sensor's lower part, until it gets in contact with the fixed platen and stops moving because of the platen's rigidity. This procedure is repeated for multiple α angles in the range of $-4°$ to $4°$. Equation 3.7 is then used to fit the experimental α and Y_c data using a least squares algorithm. The misalignment angle β is thus obtained by inverse identification. The initial distance between the sensor tip and the platen, Y_0, is also identified along with L, since the apparent center of rotation on the nanopositioner assembly cannot be properly defined. A trust region-algorithm is used in the identification, allowing to set realistic bounds for each parameter. The sensor's tip width w is known and equal to $300\,\mu m$

Using the XYZ manual micropositioning stage the nanopositioner-actuator-sensor assembly is mounted on, the same contact zone is approximately kept to minimize the influence of the fixed platen surface on the results.

Table 3.4 shows the result of the parallelism setting procedure for 4 separate tests, performed throughout many days on approximately the same point of the fixed platen. The misalignment angle is identified at $\beta = -0.58° \pm 0.01°$ (mean value and standard deviation). Figure 3.9 shows the results of test number 4. Good correlation can be observed between the analytical model and the experimental data. An apparent omega tip can be observed around 0.57°. The distance L is identified at $L = 70 \pm 0.8mm$ (mean value and standard deviation), which corresponds to a distance between the sensor's tip and a point on the nanopositioner, situated across 2/3 its length. The good fitting of the model, small standard deviation of L along with its value that corresponds to a realistic sensor- nanopositioner distance, altogether validate the approximation that was selected to represent the inherent misalignments in the experimental setup. Taking all this into consideration the proposed experimental protocol ensures a sensor-platen parallelism with an accuracy below 0.1°.

Test n°	**1**	**2**	**3**	**4**	**Average**	**Standard deviation**
$L\,(mm)$	70	71	69	70	70	0.8
$\beta(°)$	-0.60	-0.58	-0.56	-0.57	-0.58	0.01

Table 3.4: Results of tilt angle minimization procedures. Both the misalignment angle β and the distance from the apparent rotation point are identified with a small standard deviation.

Tilt angle influence on the identification of E_T

While an experimental procedure to minimize the tilt angle can now be used, quantifying the influence this angle has on the identified E_T from SFTCTs, is crucial in order to draw conclusions on its importance. To quantify this influence two types of studies are performed. First, a finite element model of a SFTCT with a tilt angle is created and the compression is simulated. This allows to see the influence of the angle in an ideal representation of the problem's geometry, boundary conditions and material behavior.

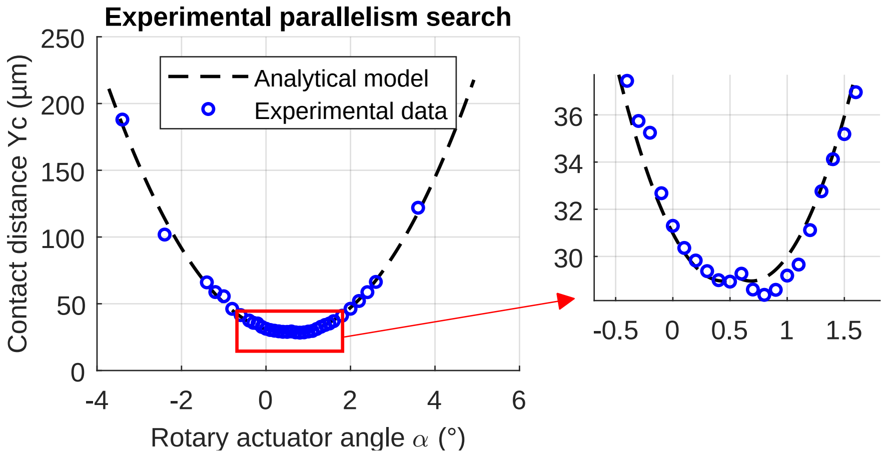

Figure 3.9: Distance between sensor tip and fixed platen as a function of the angle of the rotary actuator. Fitting the analytical model to the experimental data gives the necessary rotation to minimize the tilt angle. The tilt is thus found at its minimum $\varphi = 0°$ when the actuator is rotated at $\alpha = 0.57°$ from its reference position.

The influence of the tilt angle is then studied experimentally by compressing a fiber with different tilt angles.

For the purpose of this study, the tested fiber needs to be as close as possible to the hypotheses in the analytical model of the test. In that way, the tilt angle will be the main parameter which will cause deviations from theoretical predictions. For this reason, a Polyamide 11 (PA11) fiber is chosen for its cylindrical geometry, homogeneous structure and transversely isotropic nature. The fiber's mean diameter was measured at $D = 35.17 \pm 0.02\,\mu m$ (mean value and standard deviation) at 6 cross sections along the fiber length, using the Fiber Dimensional Analysis System (see 3.4.1 for details on fiber morphological characterization). [Placet 20] measured the properties of this fiber lot at $E_L = 2155\,MPa$, for the longitudinal elastic modulus and $\nu_{TT} = 0.07$ for the Poisson's ratio in the transverse plane. The Poisson's ratio in the longitudinal plane is set at $\nu_{LT} = 0.4$ based on data provided by the bulk material provider. These geometric and material parameters are used throughout both the numerical and experimental studies. Their values and source are summarized in Table 3.5.

Parameter	Value	Source
R	$17.55\,(\mu m)$	FDAS measurement
E_L	$2155\,(MPa)$	Determined by [Placet 20]
ν_{LT}	0.4	Given in [Placet 20]
ν_{TT}	0.07	Determined by [Placet 20]
L	$300\,(\mu m)$	Compressed fiber length (sensor tip width)

Table 3.5: PA11 fiber geometric and material parameters.

To quantify the influence of the tilt angle, the same approach as the one presented in 2.3.1 is used, employing ΔE_T and the residual of the least squares identification. Numerical simulations or experimental tests are performed with different tilt angles. Force and displacement data are extracted from these tests, which along with the fiber's geometric and material properties allow for the identification of E_T. The modulus identified for a compression with parallel platens is used as the reference. In the experimental study, the tilt angle is varied between $-1°$ and $-1°$ with a step of $0.1°$. Values from $0°$ to $1°$ are studied in simulations since in its ideal representation the problem is symmetric.

Tilt angle - finite element analysis. The finite element model used to simulate SFTCTs with a tilt angle is based on the 3D model presented in section 2.3. The geometry of the problem presents a single symmetry along the yz plane as seen in Figure 3.6. The tilt angle is modeled with a rotation of the upper platen around the x axis. Compression platens exceed the fiber by $5\,\mu m$ to avoid a point to point contact of the fiber and the upper platen after compression, which would lead artificially high stress concentrations.

Given that, with the exception of platen rotation, the geometry of the problem remains the same, a different approach in terms of meshing is adopted compared to the finite element studies presented in Chapter 2. Fourteen mesh elements are used along the potential contact zone, which corresponds to the number of elements used for the mesh of the previous studies (see section 2.3.3). To ensure numerous elements are in contact even for the smaller platen displacements, elements along the potential contact zone follow an exponential distribution, with a denser concentration of elements close to the initial contact point. To make sure that multiple mesh elements will be compressed for an upper platen displacement of $1\,\mu m$, 4 mesh elements are placed along one micrometer on the fiber's edges that are in contact with the platens at $x = 0$. The rest of the fiber is meshed in a coarser way, since gradients in these zones are less important and no data for the identification of E_T will be extracted there. Sixty mesh elements are placed along the fiber length. Along the fiber's length (z axis), to adapt to the change in tilt angle and keep more elements in the contact zone, a ratio of $|1 - 500 \cdot sin(\varphi)|$ is kept between the size of the first element (inside the contact zone) and the last element (potentially outside the contact zone). The change in size between these two elements is made progressively through an arithmetic progression. In this way, the fiber mesh along its length is uniform when the platens are parallel ($\phi = 0°$), while an active refinement along the contact zone occurs as the tilt angle increases. For compression platens, the same approach as before is used, with elements being twice the size of the fiber, in each respective zone. Figure 3.10 illustrates the mesh and boundary conditions of the finite element model.

Figure 3.11 shows the evolution of the force per unit length as a function of the mobile platen displacement for four different simulated tilt angles. The fitted analytical model is represented with dotted lines. For parallel platens the analytical model follows the simulation data closely. However, with the increase of the tilt angle and resulting decrease in contact surface, the contact force decreases for a given upper platen displacement. The non-linearity of the force displacement curves also changes. The analytical model cannot match this behavior as closely, leading to a worse fit.

These changes are reflected on the identified transverse elastic modulus E_T and least squares residual. Their evolution as a function of the tilt angle are shown in Figure 3.12. The value of E_T gets underestimated with the increase in tilt angle, decreasing rapidly for smaller angles and decelerating towards tilts of $1°$. The influence of the tilt angle on ΔE_T is major, with an angle of $1°$ causing a decrease of $92.53\,\%$ on the identified E_T. This underestimation of E_T is linked to the decrease in compression force resulting from the reduction of the contact surface. The model's ability to predict fiber behavior

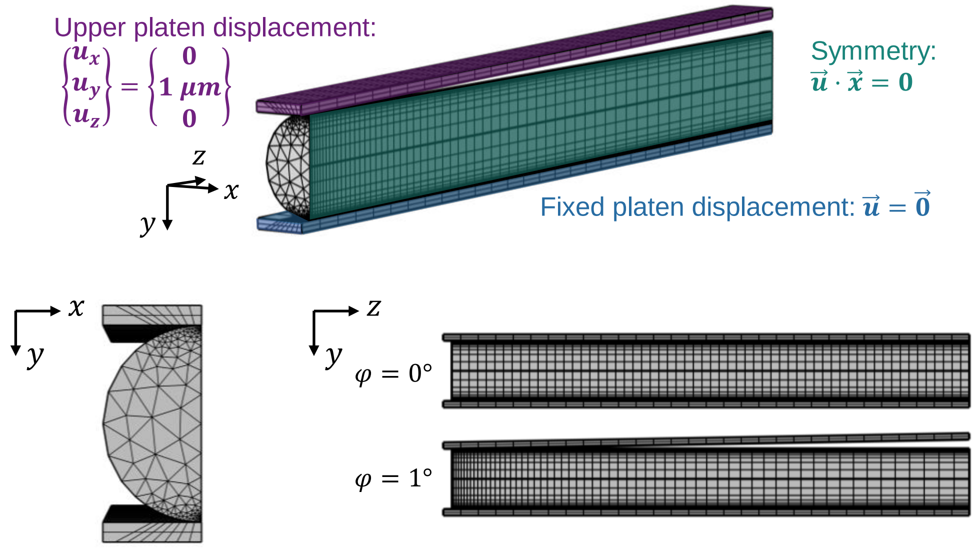

Figure 3.10: Finite element model of SFTCT with an upper platen tilt angle. Boundary conditions are shown on top while the mesh along the xy and yz plane are shown on the bottom. The uniform and tilt-adapted mesh along the yz plane are illustrated for $\varphi = 0°$ and $\varphi = 1°$ respectively.

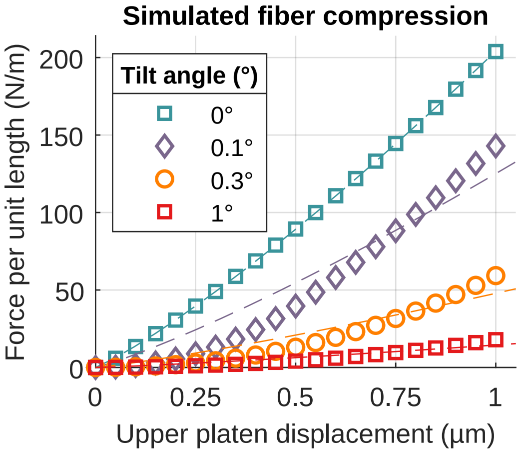

Figure 3.11: Force-displacement results of finite element analysis for different tilt angles. The data from the simulation is represented with markers and the fitted analytical model represented with dotted lines.

also decreases as tilt angles increase. The value of the residual, rises rapidly for smaller tilt angles and stabilizes as the tilt angle approaches 1°. SFTCTs simulations, therefore directly demonstrate the key role of the mobile platen's tilt angle. In order for the analytical model to correctly identify the transverse elastic modulus of the fiber and successfully predict fiber behavior, maintaining the compression platens parallel is critical.

Tilt angle - experimental analysis. In order to study the influence of the tilt angle experimentally, a loading protocol must first be chosen. Every test starts with the sensor at a certain distance from the fiber and its tilt angle is set with the rotary actuator. Then, the sensor descends and compression takes place with a single loading and unloading cycle for each tilt angle. The maximum speed attainable by the actuator of 10 $\mu m/s$ is used to

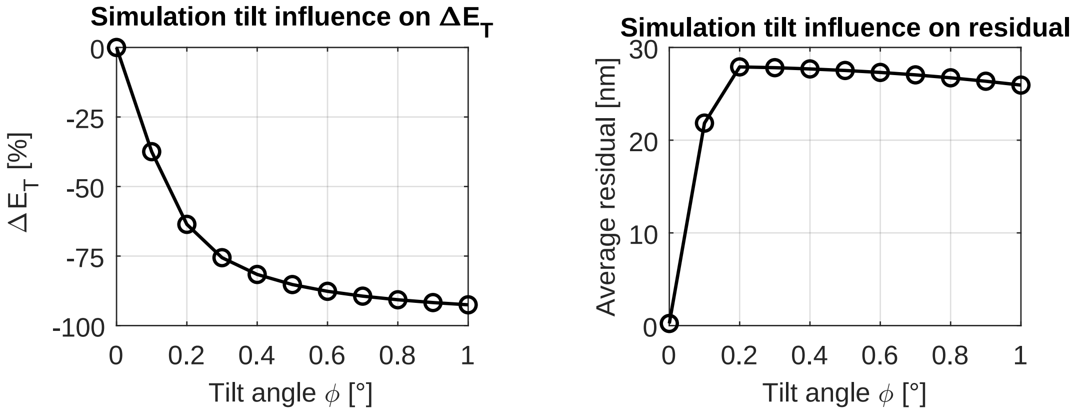

Figure 3.12: Evolution of ΔE_T (left) and least-squares residual as a function of tilt angle.

minimize the influence of fiber viscocity (as seen in subsection 2.6.1). Identical displacements are generated by the linear actuator for all tilt angles. During the loading phase the fiber exhibits some rigid body motions and small rotations before being completely restricted between the sensor's tip and the fixed platen, where it starts compressing (see section 3.4.2 for details on fiber preloading). For this reason, the transverse elastic modulus of the fiber is identified on the unloading phase where the fiber's rigid body motions are less important. The last 12 data points were also eliminated for all tests, to eliminate potential fiber rotation and sliding.

Fibers such as PA11 can exhibit complex material behavior, mainly through viscous and inelastic mechanisms. The identification of E_T is made through Jawad's model (no simplifying hypotheses are used). Given the purely elastic, transverse isotropy hypothesis made by the model, the identified E_T from experimental data represents an apparent elastic modulus. Before studying the influence of the tilt angle, its important to verify that this apparent modulus can be identified repeatably, showing that fiber behavior is not loading history dependent. 10 consecutive loading-unloading cycles were performed on the fiber with a minimized tilt angle configuration ($\varphi = 0\,°$).

The compression protocol along with the force displacement results at the unloading stages are shown in Figure 3.13. Experimental data are shown as markers with the fitted analytical model being represented by dotted lines. No significant change in fiber behavior can be observed after successive loadings. The PA11 fiber's apparent elastic modulus is identified at the unloading stage at $E_T = 706 \pm 32\,MPa$. The standard deviation represents a variation of 4.45% of the mean value. These results point to a good repeatability of fiber behavior, the fiber's inelastic behavior can thus be safely omitted from the study of the tilt angle's influence.

With the fiber behavior repeatability being validated, the influence of the tilt angle can be studied. Figure 3.14 shows the view of microscope 3 for tilt angles of 0 and ±1°. The angle of the sensor's tip is visible, with negative tilt values leading to an initial compression force close to the fiber's edge, while for positive values contact is established away from the edge, which could lead to some local indentation. Figure 3.15 shows the evolution of the force per unit length as a function of fiber displacement for compressions with a tilt equal to zero and ±1°. The decrease in the contact zone surface induced by the tilt angle leads to an importance decrease of compression force for a given fiber

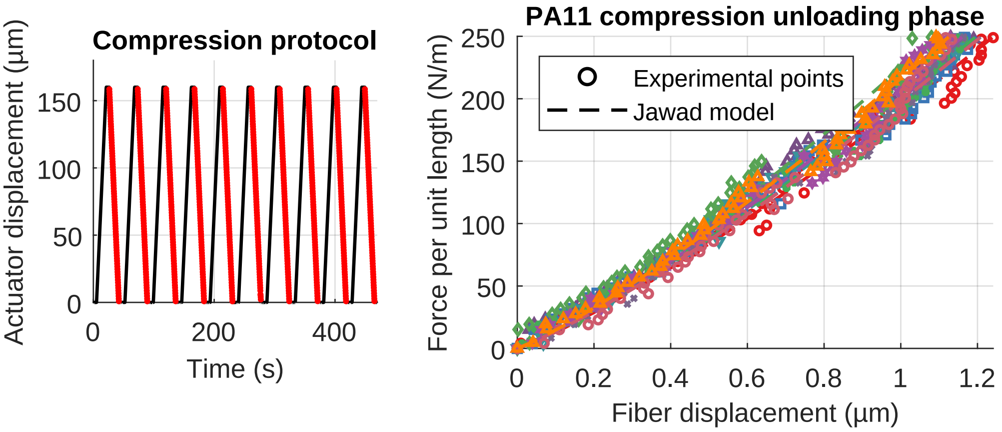

Figure 3.13: PA11 repeated transverse compression results. The compression protocol is shown on the left with the force and displacement data at the unloading stage being shown on the right.

displacement. No significant difference can be observed between positive and negative angles.

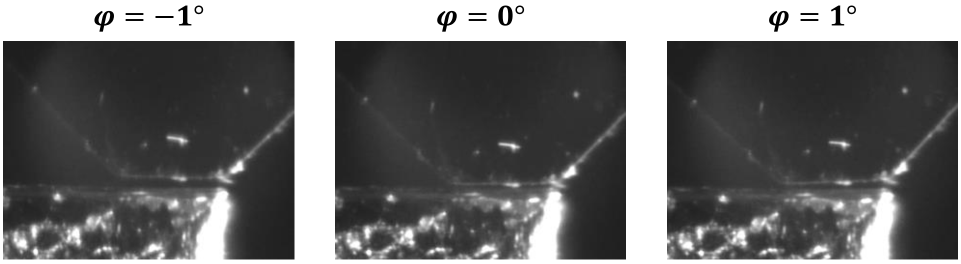

Figure 3.14: View of the sensor tip (top) and fixed compression platen (bottom) for three different tilt angle values.

The decrease in force produced by the tilt angle leads to an underestimation of the fiber's apparent transverse elastic modulus by the analytical model. Figure 3.16 shows the evolution of ΔE_T and the least-squares residual as a function of tilt angle. An angle of ±1° leads to decrease in the identified E_T of up to 35%. This is much higher than the variation of 4.45% observed during the repeated tests with a minimized tilt. These large variations of E_T can thus be attributed to the tilt angle. When looking at the values of the residual no clear trend can be observed. This lack of trend can be attributed to the precision in the measurement of the HP code position, which is in the order of 40 nm as seen in subsection 3.3.3.

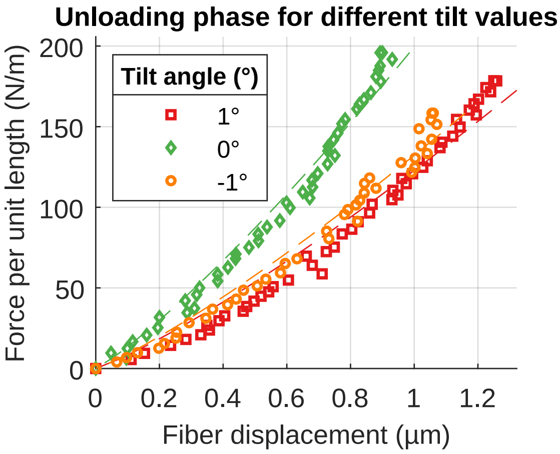

Figure 3.15: Force-displacement results of experimental compression of PA11 fiber for different tilt angles. The data from the simulation is represented with markers whith the fitted analytical model represented with dotted lines.

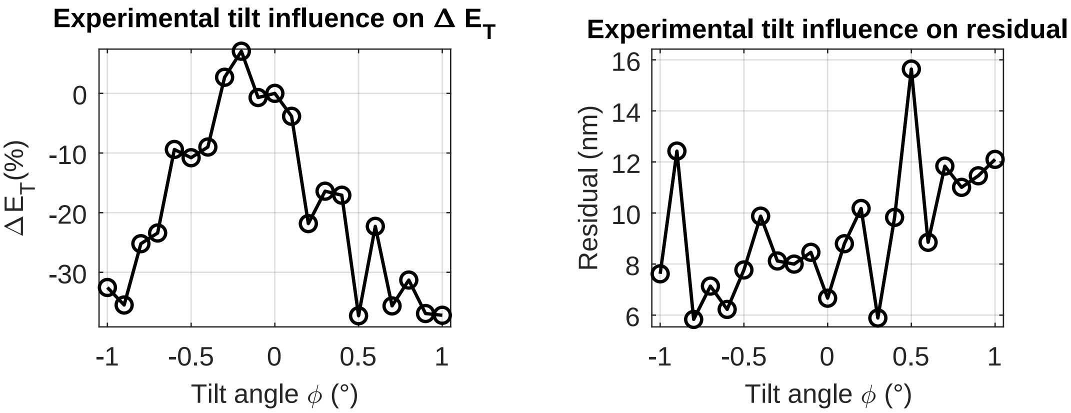

Figure 3.16: Evolution of ΔE_T (left) and least-squares residual as a function of tilt angle.

Finite element - experimental study comparison. When comparing the evolution of ΔE_T between the finite element and experimental studies, the tilt angle's influence is significantly larger in the simulations. This difference also becomes apparent when comparing the force-displacement data directly, as seen in Figure 3.17. In a parallel configuration, simulation and experimental results are very close. For tilt angles of 1° however, experimental results are close to simulation results at 0.1°.

To understand the source of this difference, measurements of HP code position, as seen in Figure 3.18 can be examined. The most distinct values of tilt are used : $-1°$, $-1°$ and $0°$. The vertical position Y of the HP codes follows the expected trend, with the dependent code continuing its movement freely, while the independent code moves as much as the fiber contacts, once contact is established. The angle of the HP codes also follow expected trends. Since the independent code moves very little and is restrained by the contact with the fiber, very small changes in angle inside the camera's frame are observed once contact is established. The dependent HP code on the other hand, experiences an unrestrained motion and shows a smoother change in angle. In either case however, angle values remain very little, no significant rotation thus occurs. Therefore, the

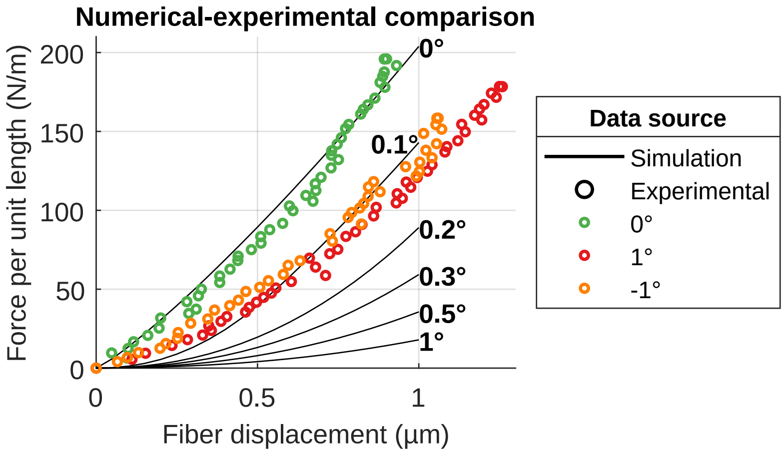

Figure 3.17: Comparison of force-displacement results of a PA11 fiber compression at different tilt angles, from finite element and experimental studies.

sensor experiences no significant torsion even when compressing objects in a non parallel configuration. The high torsional rigidity evaluated in appendix B.2 is thus demonstrated experimentally.

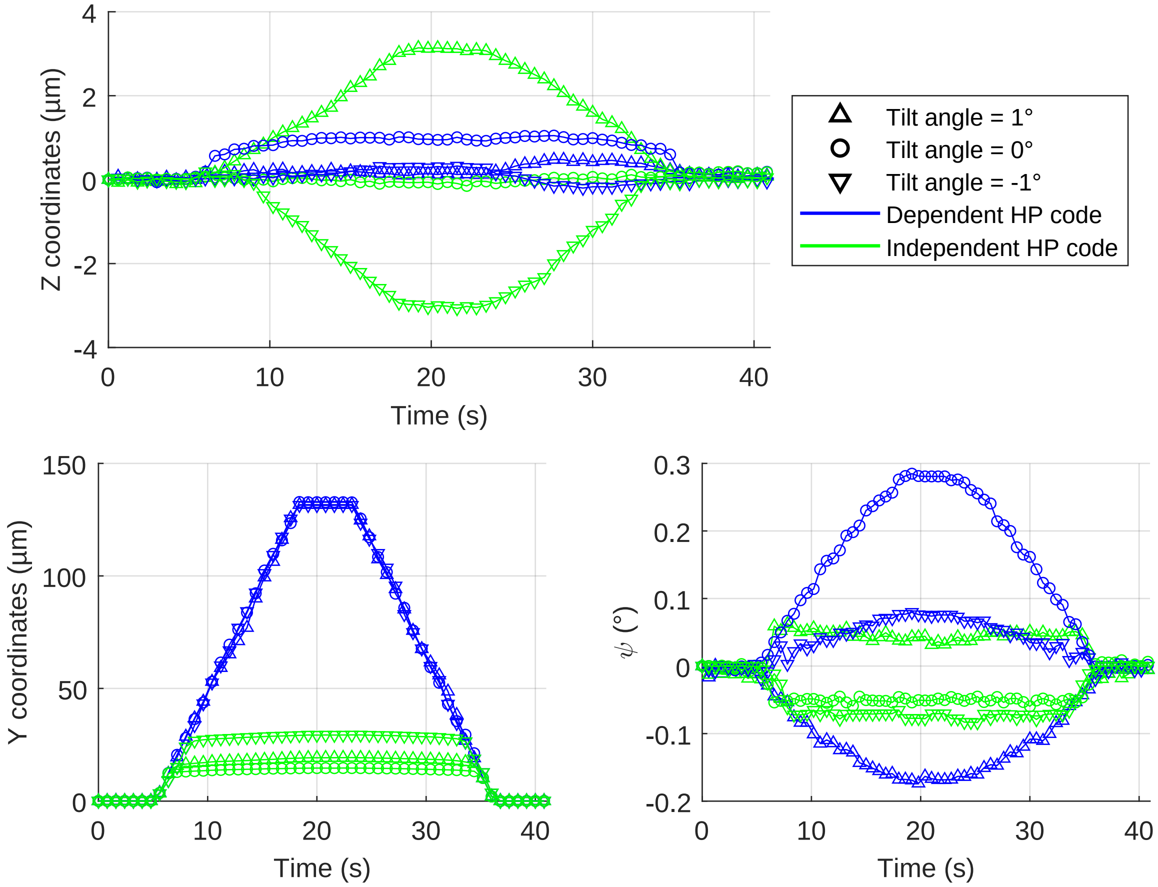

Figure 3.18: HP code coordinates for the compression of a PA11 fiber under different tilt angles. Compression is performed along the y axis.

An unexpected phenomenon occurs however, when looking at the translational movement Z of the HP codes. For a tilt angle of ±1°, the independent HP code experiences a much higher translational movement than the dependent one, in the order of $3\,\mu m$. This sliding motion, which can also be observed in videos of the test, contributes to an increase of the contact surface compared to a purely uniaxial compression, as the one in the finite element simulations. The decrease in force due to the tilt angle is thus not as important, lessening the overall effect of the tilt angle compared to simulation where no such sliding occurs. The exact nature of this sliding motion could not be identified. Given that sensor torsion is unlikely, knowing the sensor's torsional rigidity and lack of HP code rotation, some type of unaccounted system compliance must occur that needs to be further studied. No such sliding can be observed for a parallel configuration, this compliance thus only expresses itself when the sensor performs an off-axis compression.

3.3.5 Conclusions on SFTCT development and validation

In this section, a custom SFTCT experimental setup was presented that focused on addressing a number of previous setup limitations. Improvements were made in terms of vision and relative humidity control. A custom force-displacement sensor was also developed for this application, offering unprecedented capabilities in terms of direct measurements with a disruptive noise to range ratio. The repeatability and linearity of the sensor's behavior were demonstrated leading to repeatable measurements. While applied to the compression of plant fibers, these approaches can offer many advantages in a variety of micro-mechanics or micro-robotics applications.

The question of platen parallelism was also addressed and the influence of the tilt angle in SFTCTs was demonstrated and quantified for the first time. The tilt angle needs to be controlled precisely during single fiber transverse compression tests in order to limit the resulting identification errors on the apparent transverse elastic modulus. For this purpose, an identification protocol was presented, that enables a minimization of the tilt angle with a precision below 0.1°. With this precise control, analytical models can be used to identify the transverse elastic properties of fiber with higher accuracy. The presented parallelism setting protocol could be the basis for tilt angle control for compression at any scale. By adding an additional rotational degree of freedom to the experimental setup, a minimization of the θ angle in the xy plane could also be performed, improving even more measurement accuracy.

An alternative to the tilt angle minimization lies in incorporating it into the analytical model itself. Such a model was developed by *Fabien Amiot* and *Violaine Guicheret-Retel* and work on its validation is being performed in the context of this PhD work, through comparisons with finite element analysis and experimental results.

3.4 Experimental SFTCTs: preparation, protocols and results

With the development, verification and validation of the SFTCT micro-mechatronical setup being performed, testing of plant fibers can be carried out in order to study their transverse behavior. This section first presents the experimental preparations that precede the compression tests and the protocols followed to perform them. The choice of tested fibers will also be discussed. The results of the experimental campaign on three types of plant fibers (nettle, hemp and flax) and a reference synthetic fiber (Kevlar® 29) are presented. Their overall behavior is discussed and material or structural mechanisms are proposed to analyze it. A transverse elastic modulus is identified providing the first such measure on plant fibers. This identified modulus is compared with the values identified through indirect techniques and the anisotropic nature of plant fibers is discussed.

3.4.1 Experimental preparation and morphology measurements

Before performing a SFTCT, a series of preliminary steps must be followed, starting by choosing the fibers to be tested, performing fiber separation and diameter measurements and finally positioning and preloading them on the experimental setup. This section, provides a description of each of these steps.

Choice of fibers

One of the main goals of this PhD thesis is the characterization of plant fiber transverse behavior notably by providing, for the first time, their transverse elastic properties, to improve models and property prediction of bio-based composites. The three bast fibers that can be found in Europe are studied: flax, hemp and nettle. Flax fibers were obtained by *EcoTechnilin* who produces the well separated, unidirectional flax fiber non-woven mats *FlaxTape*^{TM}. Hemp was sourced by the European Union's *SSUCHY* project (2018 roving). Finally, nettles of the Roville variety of the *NETFIB* project were used (120 hours of retting).

Kevlar 29 (K29) fibers, graciously provided by the *École des Mines de Paris - Université PSL*, are used in this study as a reference material. Indeed the properties of this fiber have been measured before in the literature [Phoenix 74, Kawabata 90, Singletary 00a, Wollbrett-Blitz 16]. Furthermore, Kevlar fibers also have diameters that are comparable to those of plant fibers, albeit with geometries that are simpler and more predictable. Extensive comparison of morphological characteristics will be seen in section 3.4.3. As it will also be seen later, Kevlar fibers also present similar material properties to plant fibers, both in the transverse elastic modulus E_T but also the anisotropy ratio E_L/E_T. Overall, these shared characteristics make Kevlar an ideal reference synthetic material for this study.

As extensively discussed in Chapter 2, plant fibers come with a series of challenges in the context of SFTCTs, both morphological and material related. For this reason, a few different fiber types were also used in the context of this PhD, for development and validation purposes. PA11 fibers are used for their uniform geometry during the development of the experimental protocol and to study the influence of the tilt angle on the identification of E_T (see 3.3.4). Horse hairs, provided by the Hochschule Bremen (HSB) were also studied in a wider inter-laboratory exercise on the characterization of natural fibers. In the context of this PhD they were notably used to compare the results of different morphological measurements (see subsection 3.4.1).

Fiber extraction and diameter measurement

Fiber extraction. The first step in any SFTCT lies in isolating a single fiber from its lot. This is relatively easy for synthetic fibers which are well separated from each other. Isolating a single plant fiber however presents some added challenge. Even after being submitted to various extraction processes fibers usually remain, at least to some extent, in a bundle with neighboring fibers. Single fibers must thus be separated from their bundle manually, using tweezers. This procedure adds a survivor bias to experimental measurements. Weaker fibers will break during this manual extraction and will not be tested. Eliminating this bias would require an approach that eliminates manual extraction, in favor of more delicate microrobotic approaches (see subsection 1.4.4).

Fiber morphological characterization. Once a fiber is separated its ends are glued on two separate one-part plastic tabs (Diastron Ltd. Hampshire, UK) using a photo-curing glue (DYMAX, 3099, GmbH, Wiesbaden, Germany). This procedure takes place with the tabs placed inside a sample holder, with a fixed inter-tab distance of $12\,mm$. Fibers are then mounted on a Fiber Dimensional Analysis System (FDAS, Diastron Ltd.). Photos of the system and sample preparation are given in Figure 3.19. Laser shadowgraphy is used to measure the fiber's diameter at a given angle. A laser (Mitutoyo, Japan) hits the fiber and the width of its projected shadow is measured giving an apparent diameter value. The plastic tabs are held pneumatically and can thus be rotated, allowing for 360° measurements. The principle of the measurement is represented in Figure 3.20. The FDAS also uses actuation to move the sample along its longitudinal axis (z axis) allowing for multiple cross section measurement along the fiber's length. Overall, the system allows for fast and easy measurements of a fiber's apparent diameter at various angles and positions along its length. Its has become quite standard in the study of fiber morphology with many works using it for dimensional analysis [Haag 16, Bourmaud 17, Garat 18, Garat 20].

It should be noted however, that the FDAS system cannot provide an accurate reconstruction of a fiber's cross sections. Concave regions for example, cannot be detected. Furthermore, the evolution of an object's apparent diameter in polar coordinates, can generate shapes that are quite different from the real cross section. Elliptical cross sections for example generate a shape that resembles the number "8" as illustrated in Figure 3.20. The narrowest part of this shape represents the minor ellipse radius, r, and the largest one the major radius R.

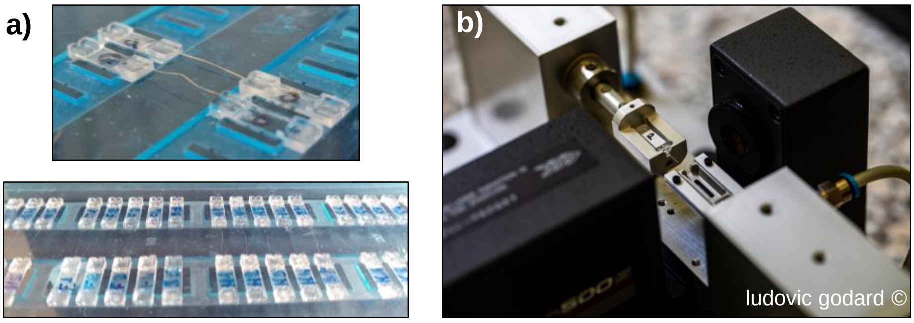

Figure 3.19: a) Single fibers glued on tabs placed inside the sample holder, b) FDAS measurement system, with a larger fiber sample (horse hair) mounted on a single tab placed inside the pneumatic holders. The laser is positioned on the left with diameter measurements taking place with the sensor on the right.

In order to evaluate the ability of the FDAS to assess fiber morphology, a comparison with X-ray micro-tomography is performed. A horse hair is used for this study. Its large elliptical cross section (minor radius of $r \simeq 70\,\mu m$, major radius of $R \simeq 100\,\mu m$) limits

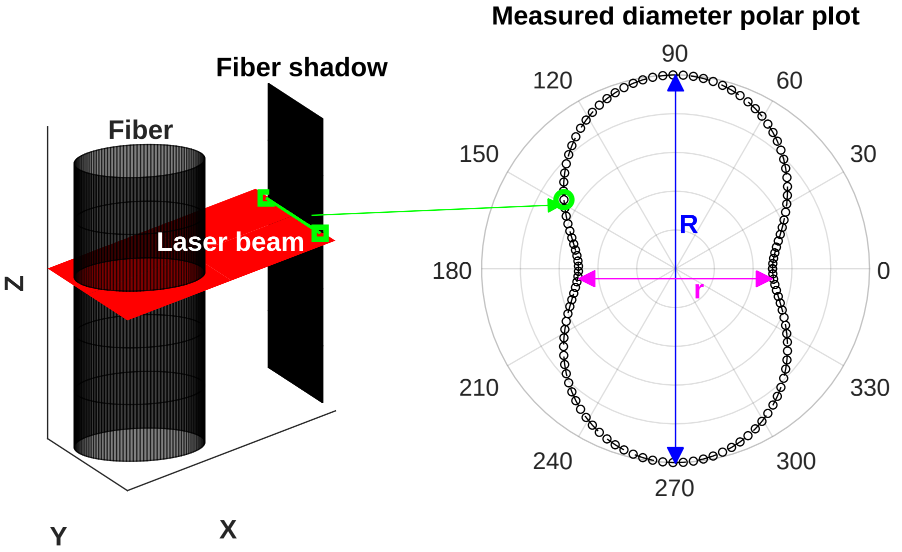

Figure 3.20: Principle of shadowgraphy for elliptical cross section fiber diameter measurements. Maximum and minimum apparent diameters, noted R and r respectively, are measured. For elliptical cross sections, apparent diameter evolution in polar coordinates generates an “8” shape.

measurement noise allowing for an easier comparison. Comparison between the FDAS and tomography measurements are found in Figure 3.21. The FDAS measures the ellitical cross section’s minimum and maximum diameter with very good accuracy. By measuring an apparent diameter through projected object’s projected shadow, it fails however to accurately measure diameter between these two extreme values. For this reason, only maximum and minimum FDAS measured values are used in our analyses.

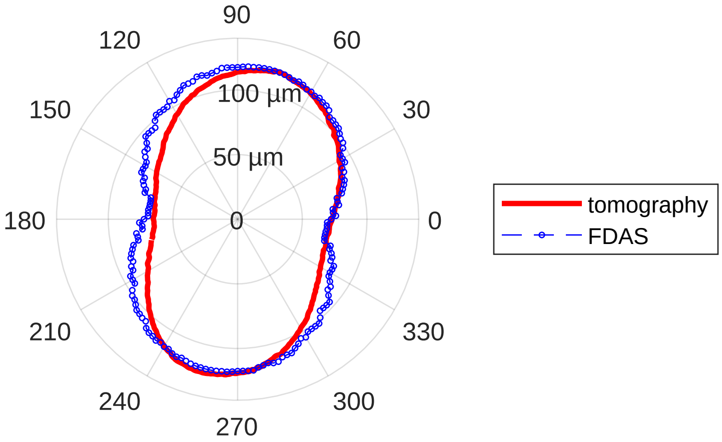

Figure 3.21: Comparison between FDAS and tomography measurements on horse hair.

Fiber cutting. With apparent diameter measurements completed, the next step in fiber preparation consists in cutting the sample in two parts. This provides a fiber in a clamped-free configuration which allows for observations of its transverse cross section during SFTCTs. In order to perform these observations, a regular and straight cross section must be obtained after cutting. For this purpose a custom “guillotine” cutting apparatus was developed, shown in Figure 3.22. A razor blade is mounted on a spring loaded, manually activated sliding mechanism. A steel piece with two machined grooves is positioned under the blade. The first groove, named fiber groove, is used to hold the fiber during cutting. A 3D printed tabs sample holder, mounted on two manual micropositioning tables is used to place the fiber inside this groove. The second groove, named cutting groove, is perpendicular to the fiber one and placed directly under the blade. As the blade moves down it meets the fiber, cutting it and goes through the cutting groove. To optimize cutting quality, the blade is changed after each use. Figure 3.23 presents SEM observations for guillotine-cut synthetic (PA11) and plant (hemp) fibers. Cross sections of good quality quality can be obtained, albeit not very straight.

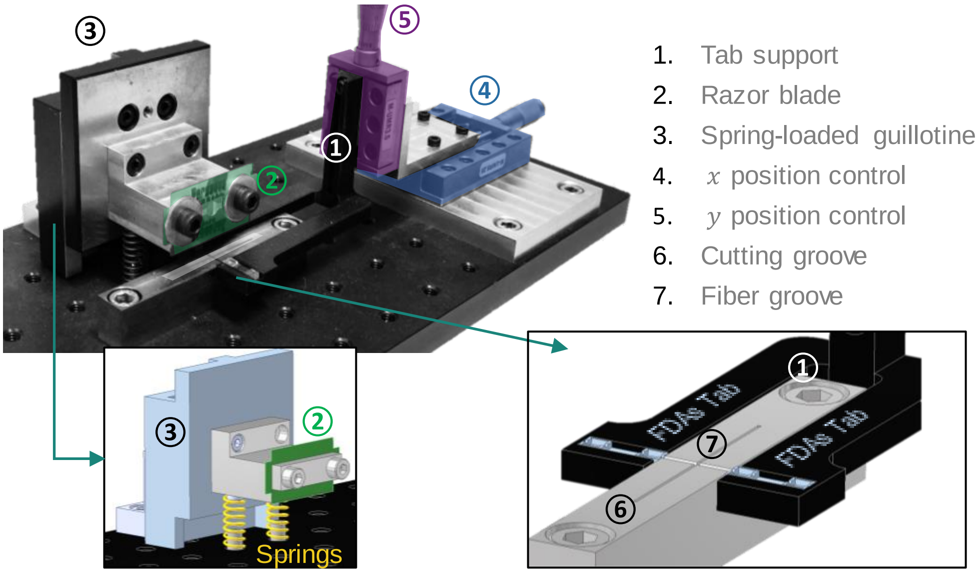

1. Tab support
2. Razor blade
3. Spring-loaded guillotine
4. x position control
5. y position control
6. Cutting groove
7. Fiber groove

Figure 3.22: Custom fiber cutting system (guillotine) with its different components.

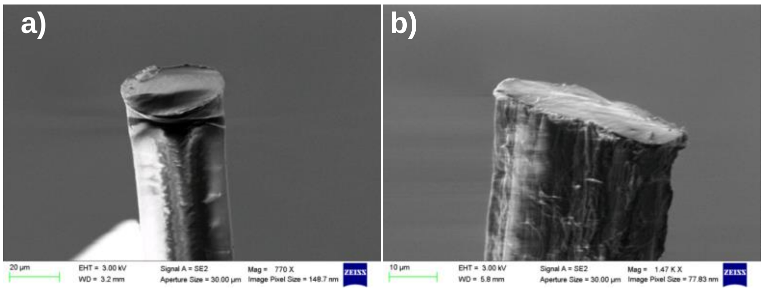

Figure 3.23: Scanning electron microscopy of guillotine cut fibers: a) PA11, b) hemp.

All extraction, measurements and cutting steps are performed in the same room that is controlled in terms of temperature and relative humidity.

3.4.2 Compression protocol

With fiber preparation and measurements completed, transverse compression tests can be performed. The choice of loading protocol is crucial in order for these tests to produce good quality results. In this section, a preloading stage, performed once the fiber is mounted on the experimental setup is described, followed by the compression protocol that is used to study fiber behavior.

Fiber compression phases - preloading control

Once fiber extraction, measurement and cutting is performed, the fiber's plastic tab is mounted on the experimental setup's sample holder and rested on the fixed lower platen with the use of a XYZ manual micropositioner. The fiber is positioned close to the platen edges to facilitate observations with Microscopes 1 and 2. The force displacement sensor is then placed over the fiber using a different manual positioner. The edges of the sensor and the fiber along its length (yz plane) are aligned as much as possible. In that way, the compression of the fiber's end can be observed along its transverse section (xy plane) through Microscope 2. Care is taken to center the fiber's transverse cross section (xy) under the sensor tip. A representation of fiber-sensor positioning as seen by the microscopes was given previously in Figure 3.1.

Once the fiber is positioned on the setup, its end often lifts up and is not in contact with the lower platen due to morphological or internal stress constraints. This is especially true for plant fibers that present more complex morphologies. Furthermore, electrostatic forces can cause the fiber to adhere to the sensor tip once it is placed close to the fiber. Once the sensor is lowered further to perform a compression test, three distinct stages occur:

- Rigid body movement stage. During this stage the fiber moves or slides without deforming. It is most common when the end of the fiber is lifted and not in contact with the fixed platen. Once the fiber gets in contact with the sensor, it follows its movement downwards without deforming. Force measurements fluctuate around a zero value during this stage.

- Partial fiber compression. This stage typically occurs when the fiber first gets in contact with both the fixed platen and the sensor. Sliding and rotation movements occur with the fiber readjusting its position as a result of its restriction between sensor and platen. It is typically in this stage that elliptical fibers rotate with their major axis becoming parallel to the compression platens. During this stage, some fiber deformation takes place therefore the compression force gradually increases non-linearly. The added movement of the fiber however, means that this evolution does not match theoretical SFTCT predictions.

- Full fiber compression. In this stage, the rigid body motion and partial compression has ceased and the fiber is completely constrained between the sensor and the platen. Force increases rapidly during this stage and the fiber deforms in a way that is consistent with theoretical predictions. It is during this step that fiber properties can be identified.

The three described steps, as seen by Microscope 2 are shown in Figure 3.24 in the case of a PA11 fiber compression. In the presented case, the end of the fiber is lifted resulting in a large rigid body motion phase. The partial compression phase is not that important since the geometry of PA11 fibers is quite uniform. The evolution of the force and the sensor's tip displacement[1] during the test are shown in Figure 3.25. No distinct change in

---

[1] as measured by the independent HP code

behavior can be seen between the partial and full compression stage because the transition generally take places gradually and smoothly. For this reason, the end of each phase is determined by visual observation. The partial compression stage is less important during the unloading stage compared to the loading one, less rotations and sliding occur during unloading.

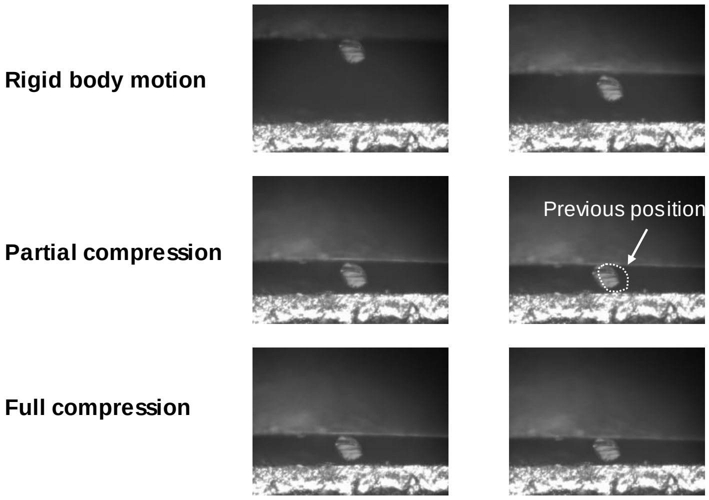

Figure 3.24: PA11 compression stages as seen by Microscope 2.

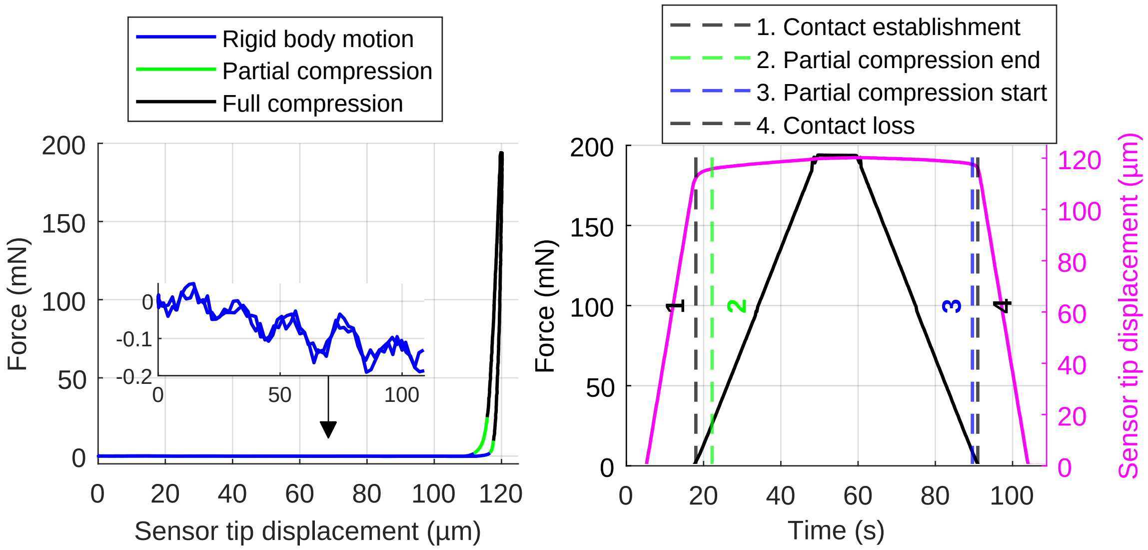

Figure 3.25: Force-displacement of PA11 fiber compression on complete compression cycle. Each compression stage is determined through visual observation.

This multi-step process of compression presents several challenges related to the partial compression stage. Indeed, during this stage the fiber already starts deforming, but the unpredictable nature of the fiber movements makes the use of theoretical models inadequate. Furthermore, identifying the transition between the partial and full compression stages in order to accurately point to the start of full compression is difficult. [Kotani 94] and later [Hillbrick 19] used the least squares method to determine E_T and a distance δ, representing the change in position from the start of contact until the full compression stage. A different approach is used in our case. The fiber gets loaded slowly and incrementally with the operator monitoring its movement. Once the fiber stops showing important rotation movements the platen is stopped. All compressions on Kevlar and plant fibers are performed by returning to this chosen point. The contact between fiber and platen and sensor is thus never lost during testing. Furthermore, 20% of the points at the start of the loading stage or at the end of the unloading stage are discarded systematically in this experimental campaign. This ensures that the remaining data is obtained in a full compression stage and can thus be used for the identification of the fiber's transverse elastic modulus. The influence of the amount of removed points on the identified transverse elastic modulus was shown to be very low through finite element analysis and through experimental data. The details of this study can be found on Appendix B.4.

SFTCT protocol

With a good approximation of the point of pure fiber compression being made, the SFTCT can finally be performed. In order to characterize material properties through mechanical testing, the choice of experimental protocol is crucial. The loading must allow the material to exhibit its behavior in a way that can be measured with the available experimental means and that allows the identification/measurement of its properties. In this study, both the elastic and inelastic behavior of single fibers are investigated.

Loading protocol. Some important constrains guide the choice of loading protocol for the presented experimental campaign. Overall testing time has to be kept short to avoid issues related to thermal drifts in measurement. Furthermore, the protocol has to allow the identification of the fiber's apparent transverse elastic modulus E_T. To do so, a fiber response that is as close to purely elastic as possible is needed at some point of the test. Viscous behavior along with irreversible phenomena such as plasticity, damage and failure must thus be avoided in these zones. On the other hand, the complex transverse behavior of plant fibers, resulting from their unique morphological and material characteristics, is to be demonstrated and studied for the first time. In order to comply to these criteria, the loading protocol presented in Figure 3.26 is chosen.

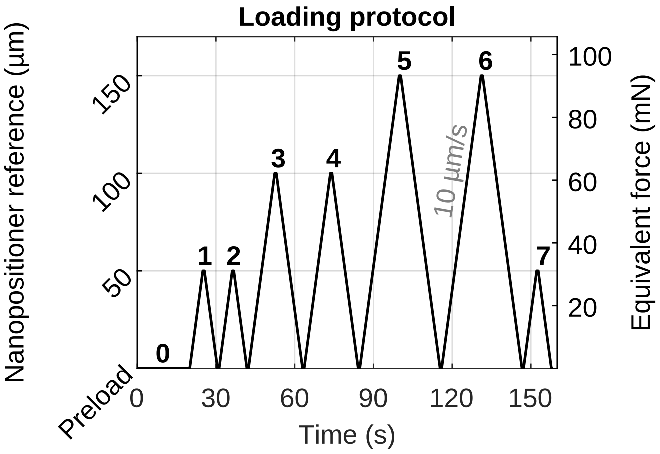

Figure 3.26: Loading protocol for fiber compression, controlled through nanopositioner generated displacement. Equivalent force level is given on the right.

To identify the transverse elastic modulus of the fiber the loading protocol has the following characteristics:

- Every compression load is succeeded by an unloading phase, performed at the same speed. During the loading phase different inelastic phenomena can occur, that can be structural or material in nature. In addition, partial compression is more likely to happen during this phase, even if a preload is applied as discussed in subsection 3.4.2. During the unloading phase however, both inelastic phenomena and fiber movements should be significantly less important. Fiber behavior in this area will thus be closer to purely elastic. For this reason, the identification of fiber transverse elastic modulus is made on the unloading stage.

- The loading speed is set at $10\,\mu m/s$, the maximum available from the used nanopositioner. The same speed is used in the unloading phase. As seen previously in subsection 2.6.1 this should minimize the influence of viscous behavior on the identification of E_T.

- Multiple levels of loading are used. Studying the elastic regime at the fiber scale is a compromise between measurement accuracy and risk of inelastic behavior activation. Performing compression with very low levels of fiber displacement, leads to results that are closer to a purely elastic response, at the expense of a nosier measurement due to low amplitude of force and displacement. Higher loads however can trigger various inelastic mechanisms compromising the measurement of the fiber's elastic parameters. For this reason, multiple amplitude levels (cycle 1,3 and 5) are used to allow an identification of E_T at different deformation ranges.

Inelastic phenomena can be studied through the following protocol attributes:

- In addition, to offering measurements at different deformation ranges, multiple levels of loading allow the study of irreversible behavior as a function of applied load. A large amount of successive tests with numerous incremental increases force level could be used to study this evolution closely. However, this would significantly increase testing time which comes at the risk of thermal drift.

- Repeating a loading cycle at the same amplitude as the first occurrence (cycles 2,4 and 6) allows the study of the material accommodation. Once again the number of repetitions was chosen to be low, to reduce overall testing time.

- Performing a final loading cycle in an identical way to the first loading cycle (cycle 7), offers valuable information on the effect of loading history on material behavior.

Finally, the loading protocol starts with an initial rest of $20\,s$ (phase 0), allowing all the different setup components to load and start registering data properly. Overall testing time is kept under 3 minutes.

Environmental condition regulation. Before each test relative humidity inside the testing chamber is set at $50\,\%$. The time needed for the RH to regulate at 50% is around 45 minutes, as illustrated in Figure 3.27. As the RH stabilizes, the fiber preloading stage can be performed, where the operator determines the transition to full compression. Temperature inside the chamber rises during regulation. During tests however changes in temperature are minor (the chosen loading protocol has a duration of $160\,s$).

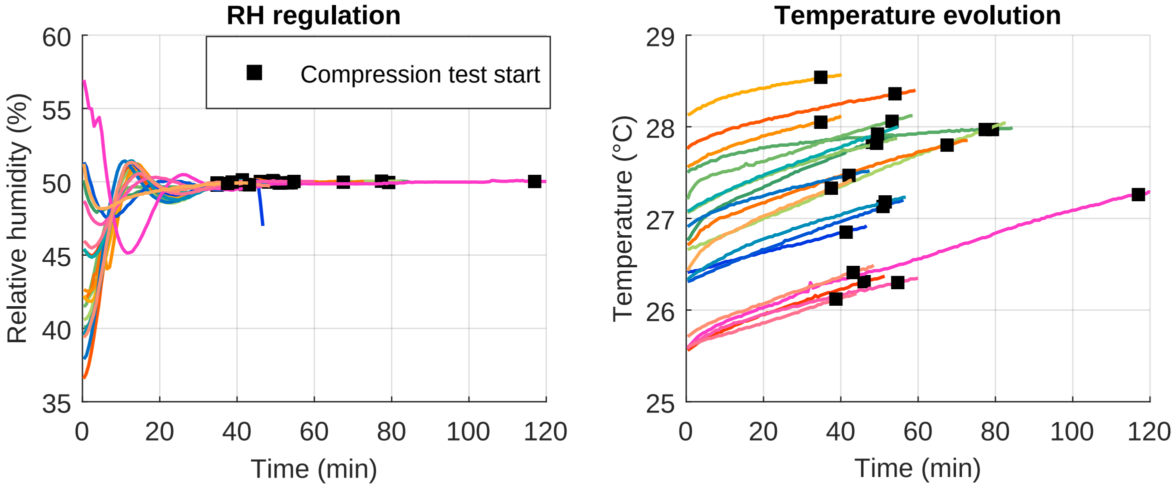

Figure 3.27: Relative humidity regulation and related change in temperature. The start of the compression test is represented with a black square. Each colored line represents a test on a different fiber (Kevlar,flax,hemp or nettle).

3.4.3 SFTCT experimental resullts

This section presents the results obtained through the methods and protocols detailed previously. Morphological measurements are given first with the SFTCT results following the later.

Fiber morphology measurements

Plant fibers were prepared and their diameter was measured with the FDAS as discussed in subsection 3.4.1. Overall, 27 sections were scanned three successive times on a $3\,mm$ segment centered around the center of the fiber. The quick scanning option of the system was used that provides a maximum and a minimum fiber diameter. While the compressed fiber length is of only $300\,\mu m$, given the uncertainty related to fiber positioning and cutting inside the guillotine, a larger fiber segment was measured to ensure that the zone that will be compressed is part of the measurements. Averages values of the minimum d and maximum D apparent fiber diameters across the $3\,mm$ segment of each fiber are given in Table 3.6. The standard deviation (SD) of these measurements is also given. Finally, under an elliptical cross section hypothesis, the ellipse flattening factor f, defined as $f = 1 - d/D$ is calculated.

Flax fibers present the smallest average diameter values and are considerably elliptical with a flattening factor of 0.47. Hemp fibers are slightly larger in size and present a similarly elliptical geometry with flax. Nettle fibers have a minimum diameter that is comparable to hemp but present a much higher maximum diameter, giving them a high flattening factor of 0.65. The standard deviations represent on average across all fibers $14.7\,\%$ of the average minimum diameter and $14.9\,\%$ of the maximum diameter. Deviations in diameter measurements across the $3\,mm$ measurement segments are thus not negligible, but modest considering the morphological variability fibers can exhibit.

For Kevlar, diameter measurements were performed inside a SEM electron microscope, since its light diffracting properties [Roche 85] prevent accurate measurements through

		Fiber n°						
Plant type	**Parameter**	**1**	**2**	**3**	**4**	**5**	**Average**	**Unit**
Nettle	***d***	11.1	13.6	18.6	11.2	12.7	**13.4**	μm
	SD(d)	1.7	2.8	1.2	3.2	1.0	**2.0**	μm
	D	38.3	40.1	49.2	43.7	34.2	**41.1**	μm
	SD(D)	3.1	2.7	3.0	8.4	10.6	**5.6**	μm
	f	0.7	0.7	0.6	0.7	0.6	**0.7**	-
Hemp	***d***	16.1	13.0	18.9	10.2	6.8	**13.0**	μm
	SD(d)	3.3	1.0	1.8	2.6	0.6	**1.8**	μm
	D	29.6	20.6	28.8	17.0	21.0	**23.4**	μm
	SD(D)	3.4	1.0	3.4	4.5	1.9	**2.8**	μm
	f	0.5	0.4	0.3	0.4	0.7	**0.4**	-
Flax	***d***	10.1	15.9	5.34	9.1	8.7	**9.8**	μm
	SD(d)	1.8	0.9	1.1	0.8	2.7	**1.5**	μm
	D	18.6	20.1	20.0	18.6	15.1	**18.5**	μm
	SD(D)	6.1	1.6	6.1	1.9	1.8	**3.5**	μm
	f	0.5	0.2	0.7	0.5	0.4	**0.4**	-

Table 3.6: Plant fibers FDAS measurements: minimum diameter d and maximum diameter D. The average value on a $3mm$ segment is given along with the standard deviation for d(SD(d)) and D (SD(D)). The ellipse flattening ratio $f = 1 - d/D$ is also given.

shadowgraphy. No metallic deposition was used. Its mean diameter across 5 fibers was measured at: $D = 11.06 \pm 0.84\,\mu m$. These measurements are consistent with the ones found in the literature [Phoenix 74, Kawabata 90, Singletary 00a, Wollbrett-Blitz 16].

Single plant fiber behavior under transverse compression

Following the loading protocol detailed in section 3.4.2, Figure 3.28 presents the force-displacement results for the 5 fibers of each tested fiber type. A few key characteristics become immediately apparent when looking at the results:

- Each compression cycle produces an hysteresis loop and results in a residual fiber displacement. It thus clear that inelastic phenomena take place.
- The surface response of plant fibers is much larger than the one of Kevlar because of larger displacements taking place for plant fibers.
- Loading phases present an inverted linearity compared to one predicted by analytical and finite element models (see Chapter 2). It is however similar to the one observed with plastic behavior simulation or extreme cases of viscoelastic behavior (see 2.6). This inversion however, can be seen from the loading phase of the very first cycle, where it is very unlikely for viscoelastic phenomena to have time to express themselves. This behavior thus strongly points to the presence of irreversible mechanisms.
- Fiber behavior during unloading is similar to model predictions, validating the choice to use analytical models to identify the transverse elastic modulus at the unloading stage. This is the case even for the later compression cycles, where 2 to 3 minutes

of testing have occurred. This points to a weak effect of viscoelasticity in the fiber's behavior during the rapid decompression.

- The compression control in terms of force is apparent, with the three distinct force levels being respected for all fibers and loading cycles.

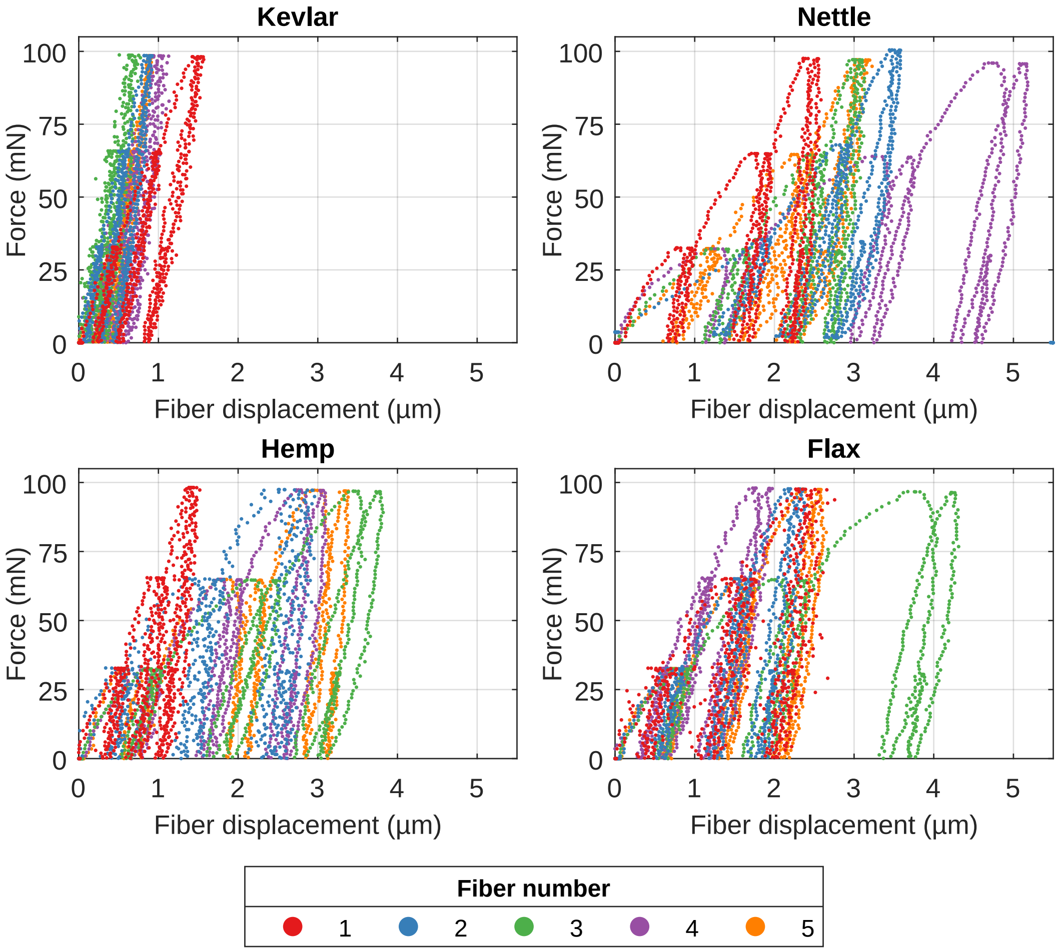

Figure 3.28: Force-displacement experimental results, for the transverse compression of Kevlar and plant fibers.

Overall these results showcase a complex and rich plant fiber behavior that deserves a close investigation. The inelastic nature of fiber displacement will be discussed first, by studying the evolution of fiber residual displacement. A normalized fiber residual displacement U_r, is calculated for each loading cycle as follows;

$$U_r = \frac{U_{ue} - U_{lb}}{R_c} \tag{3.8}$$

where U_{ue} is the fiber position at the end of the unloading phase, U_{lb} is the fiber position at the beginning of this loading cycle and R_c an estimation of the fiber radius that is being compressed (along the y axis). For all plant fibers, observations along the fiber diameter (xy section) point to fibers with their major axis aligned horizontally (x axis) and their minor axis being compressed (y axis). For this reason, their minor radius r was used in the calculation of the normalized residual displacement ($R_c = r$). For Kevlar fibers the average fiber diameter is used.

The evolution of the average residual displacement, across the 5 tested fibers of each type, is given at each loading cycle in Figure 3.29. Plant fibers show a much larger residual displacement than the Kevlar fiber. For Kevlar, this displacement stays under 170 nm or 2 % of the compressed radius. For plant fiber residual displacement is comparable across all fiber types with different fibers showing the highest residual displacement depending on the loading cycle. Its value stays under 1.0 μm or 10 % of the compressed radius. Furthermore, the residual displacement and loading cycle are strongly correlated for all fibers regardless of nature. For the first occurrence of each loading level, residual displacement are significantly more important than for the second one. As expected, higher levels of loading also produce higher levels of residual displacement.

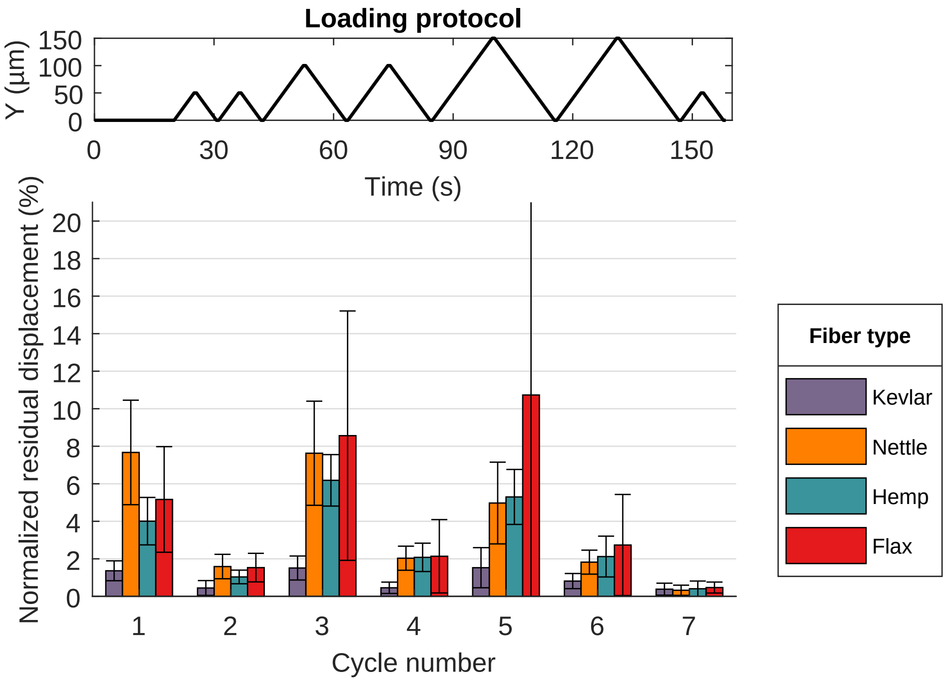

Figure 3.29: Fiber residual displacement normalized by the value of the compressed radius.

An additional way to study the inelastic of fiber behavior lies in an energy study. The energy change related to each hysteresis loop is calculated by the loop's surface area [2] through numerical trapezoidal integration using the *MATLAB* function *trapz*. The evolution of this energy is given in Figure 3.30. Very similar trends with residual displacement results are observed. Energy exchanges are significantly higher for plant fibers. Energy also significantly increases for the first occurrence of a load level before dropping for the second one.

This strong correlation between fiber residual displacement and dissipated energy, offers valuable insights into the inelastic mechanisms that takes place in single plant fiber compression. Typical irreversible material behavior could explain these results. As the fiber gets compressed beyond a certain force level it yields in, or close to the compressed area, storing deformation energy and producing a residual displacement. These quantities increase, as the fiber gets compressed further since the contact width expands and

---

[2] The surface under the unloading curve is subtracted by the surface under the loading curve

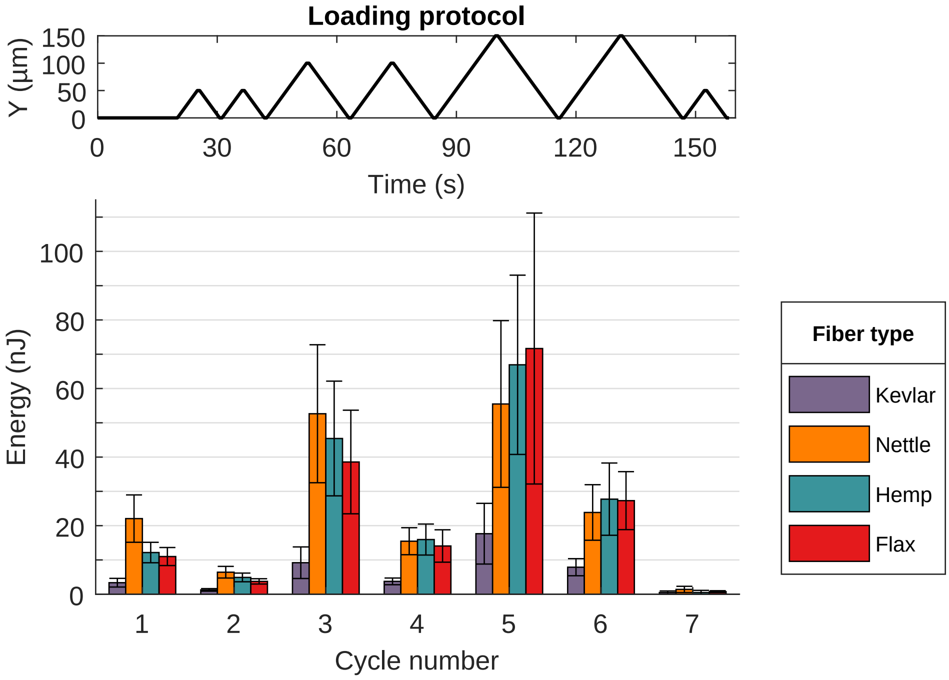

Figure 3.30: Dissipated energy during loading-unloading cycle in single fiber compression.

a larger area of the fiber can yield and deform permanently. However, when the fiber gets compressed again at the same level, less yielding occurs lowering both the residual displacement and stored energy compared to the previous cycle. The observed, open, inelastic hysteresis loop could also be a product of viscoelasticity. Since the used loading protocol does not feature a recovery phase after each compression cycle, viscoelastic deformation does not have the time to decrease. With the current loading protocol, it is not possible to quantify the effect of each of these mechanisms (irreversible or viscoelastic), since an instantaneous residual displacement is studied. As explained previously however, fiber behavior during the loading stages points to a stronger effect of irreversible material behavior compared to viscoelastic.

In addition to these material-related phenomena, the large difference in behavior between Kevlar and plant fibers points to another possible irreversible mechanism. Indeed, structural effects could explain these results. Plant fibers generally possess the large central porosity of their lumen. As extensively previously discussed in subsections 2.5 and 2.6 the lumen adds a structural related displacement to the fiber as it gets compressed. For a given force level however, it could collapse irreversibly producing residual displacements in the fiber's loading history. This permanent deformation also stores energy adding to the surface of the hysteresis loop. When the same force level is repeated, residual displacements are less important since the lumen has already collapsed to some extent. When a higher force level is reached, it collapses further, increasing the residual displacement and stored energy. Kevlar fibers on the other hand, and synthetic fibers in general, can present some porosities [Wollbrett-Blitz 14], they are however much smaller than plant fiber lumens. Therefore, no such structural effects take place and their irreversible behavior is less important.

While the choice of limiting overall testing time was made and thus not many repetitions of each loading level were performed, some conclusions regarding material accommodation can still be made. As explained previously, the nature of the proposed irreversible mechanisms shows that as the same loading level is repeated, less permanent deformation will occur leading to a decrease in the surface area of the hysteresis loop[3]. The presented results, shows this to be true for all fiber types at repeated force levels. Furthermore, loading cycle 7 results in a significant decrease of residual displacement and energy compared to cycles 1 and 2 that are performed at the same force level. While this result is probably affected by the previous loading cycles performed at higher levels it does point to the same conclusion.

Plant fiber transverse elastic modulus identification

While our transverse compression tests revealed a complex fiber behavior, the mechanisms of which were discussed, the unloading phase of each loading cycle produces force-displacement measurements that resemble purely elastic model predictions. The majority of the inelastic phenomena must therefore occur during the loading stage of compression, while the unloading phase is closer to a purely elastic response. As discussed previously, during unloading partial compression problems are also less important. For all these reasons, the transverse elastic modulus of plant fibers is found by inverse identification at the unloading phases of compression. A least squares, trust-region algorithm is used. To obtain a starting point for the identification procedure, that adapts to the given fiber and loading cycle, a linear fit is performed before hand on force per unit length (N/m) and fiber displacement data. The identified slope (in Pa) is used as the starting point of the identification.

For plant fibers, the elliptical geometry approximation (see subsection 2.4.3) is used in the analytical model, with the minor and major ellipse radius being approximated by the minimum and maximum average apparent fiber diameter respectively, as measured by the FDAS. The Kevlar fiber is approximated to a circular section cylinder, with the mean radius measured by SEM images being used in the analytical model. It will be shown next, that all tested fibers are highly anisotropic, the high anisotropy simplification was thus used in the model used ($E_L \gg E_T$, see subsection 2.2.2). The parameters E_L and ν_{LT} are thus not needed for the inverse identification of E_T, while the highly non-influential ν_{TT} (see sensitivity analysis in subsection 2.2.3) is fixed arbitrarily at 0.07.

It is important to note that while closer to purely elastic, fiber behavior will still probably present some inelastic mechanisms during unloading. Fiber morphological complexity is also not represented in the model. For this reason, the term apparent elastic modulus is used to refer to the transverse elastic modulus identified by the analytical model.

An example of analytical model fitting is given for the unloading of cycle 6 in Figure 3.31. While measurements for some fibers (notably hemp fiber 2 and flax fiber 1) are quite noisy, the overall fit matches the experimental results quite well. The average apparent transverse elastic modulus E_T for each fiber type, is given for each compression cycle in Figure 3.32.

The apparent modulus of Kevlar 29 fibers is identified between 1.6 and 2.9 GPa depending on the compression cycle. These values are consistent with the ones found in the literature. [Kawabata 90], [Jones 97] and [Singletary 00a] report values around 2.5 GPa while [Wollbrett-Blitz 16] studies the fiber as a core-skin structure with transverse modulii of 3 and 0.2 GPa respectively. Finally, [Phoenix 74] identifies a modulus at 770 MPa, albeit with less modern experimental means. Our experimental setup is thus able to repro-

---

[3] In a similar way to shakedown and ratchetting behavior [Lemaitre 94].

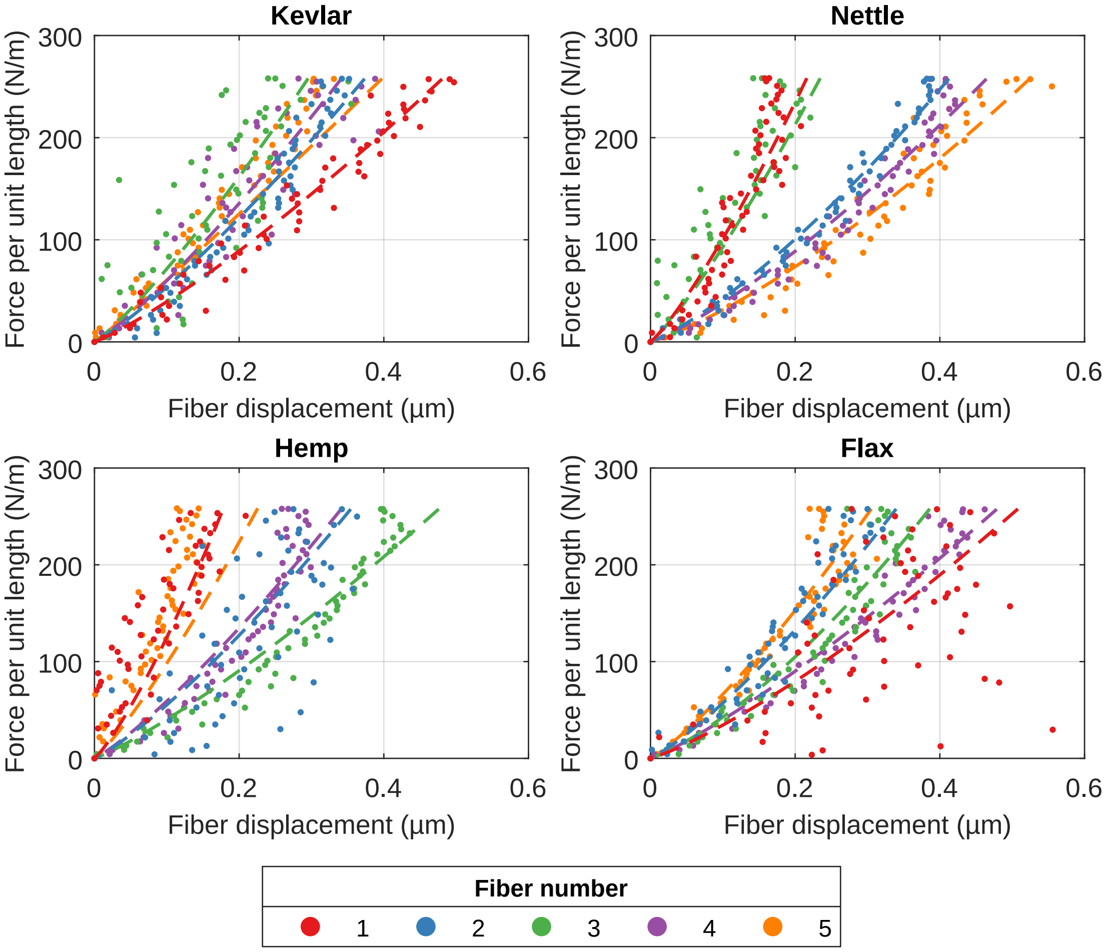

Figure 3.31: Force-displacement experimental results, at the unloading phase of cycle 6, with the fitted analytical model for the transverse compression of kevlar and plant fibers.

duce results found in the literature for synthetic fibers and their relatively uniform nature (atleast compared to plant fibers). Its ability to perform SFTCTs for later identification of the fiber's transverse elastic modulus is thus further validated.

For plant fibers, the apparent transverse elastic modulus is quite similar for all tested plant types, with values between 1 and 3.6 GPa. Interestingly these values are similar to those of Kevlar 29 and can sometimes surpass them, in the case hemp, albeit with high values of standard deviations. Furthermore, as seen in sections 2.4 and 2.5 potential sources of modulus overestimation exist, these results should thus be treated with caution.

When looking at the evolution of the identified transverse modulus with the different compression cycles, a correlation between load level and modulus is quite apparent. This trend in the evolution of fiber apparent modulus is present for all fibers. At a given loading level, no matter if it is the first or second time it is applied, the apparent transverse elastic modulus is identified at a similar value, for a given fiber type. When a higher loading level is applied however, the value of the identified modulus increases and then stabilizes for its repetition. When the load is decreased again for cycle 7, the apparent fiber modulus decreases, without retrieving however the value found for the identical loading level of cycle 1 and 2. It is thus clear, that the inelastic phenomena that take place during compression affect the apparent elastic modulus of the fiber.

Material irreversible mechanisms could explain the increase in identified fiber trans-

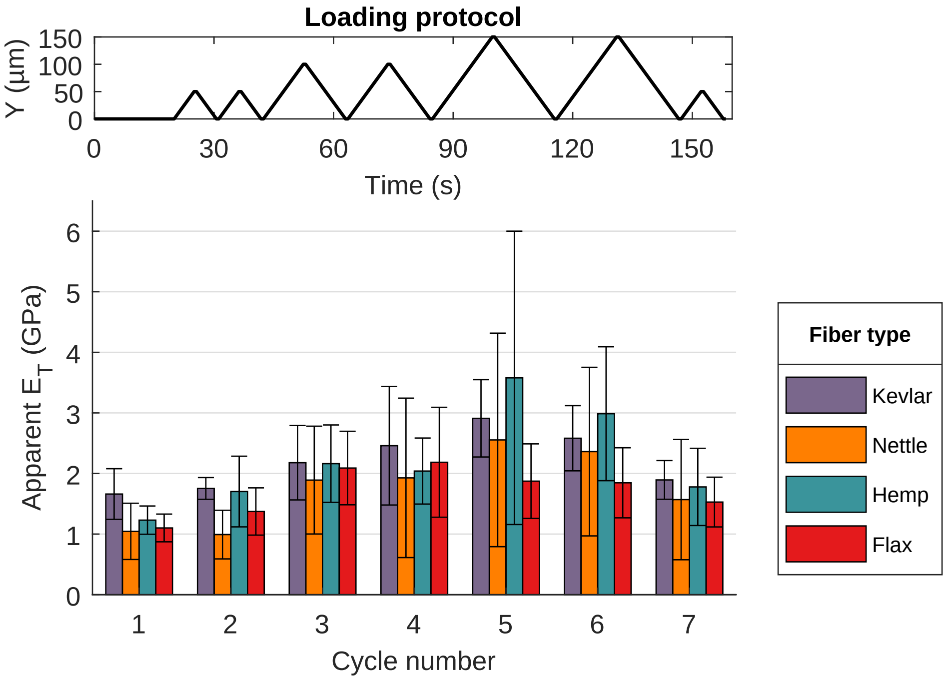

Figure 3.32: Apparent transverse elastic modulus E_T identified by the analytical model at the unloading phase of fiber compression.

verse elastic modulus with the increase in load level. First, a permanent material deformation of the Kevlar fiber or plant fiber cell wall could have a hardening effect, increasing the value of the apparent transverse elastic modulus. For higher levels of force, more permanent deformation and thus more hardening occurs leading to a correlation between load level and identified E_T.

Structural effects could also contribute in an overestimation of E_T leading to higher values of apparent modulus. As a compression cycle is completed, if the fiber deforms permanently, it might adopt a more elliptical geometry or possibly become flatter on the zone that was in contact with the platen as seen in [McDaniel 17]. As identified in sections 2.4.3 and 2.4.4 this can lead to overestimations of the fiber's transverse elastic modulus. Furthermore, in the case of plant fibers, lumens lead to an underestimation of the transverse elastic properties of the fiber, due to the additional structural displacement. Nevertheless, if the lumen collapses irreversibly due to high loads, this underestimating effect is lost. All these mechanisms lead to higher values of identified transverse elastic modulus and are more likely to appear and become influential for higher load levels.

While, both the previously described material and structural mechanisms provide a possible explanation to the correlated increase between loading level and apparent modulus, they fail to explain the reason behind the decrease in the fiber's apparent transverse elastic modulus at cycle 7. After cycle 6 no change in fiber geometry or decrease in permanent deformation should occur, that would lead to a decrease in the apparent elastic modulus at cycle 7. However, fiber damage and fibrillation could explain a decrease in transverse elastic modulus. Material softening has also been reported after a yield point is surpassed. Therefore, if no increase in compression load takes place, (which would lead to an increase in apparent modulus) and if some damage or material softening has occurred during previous cycles, a decrease in apparent modulus could become apparent for cycles performed at lower compression levels.

Given the complexity of the described inelastic and irreversible mechanisms, the apparent modulus at higher load cycles could be overestimated compared to the fiber's pure elastic modulus. The unloading phase of the two first cycles must therefore be the closest to a purely elastic response. It does take place however, within a smaller deformation range, meaning fiber displacement measurements are more effected by noise. Table 3.7 gives the average apparent elastic modulus of each tested fiber type for all cycles and for cycles 1 and 2. Even though the number of tested samples for each fiber type is small (5 fibers), when all loading cycles are considered, the standard deviations in the identified E_T for plant fibers is in the same order of magnitude with the Kevlar fibers, despite their natural origin and consequent diversity. When only the loading cycles 1 and 2 are considered, Kevlar and nettle fibers show significantly lower values of standard deviation compared to flax and hemp.

	Kevlar 29	**Nettle**	**Hemp**	**Flax**
E_T (GPa) all cycles	2.21 ± 0.47	1.76 ± 0.60	2.21 ± 0.81	1.71 ± 0.39
E_T (GPa) cycles 1 & 2	1.71 ± 0.06	1.02 ± 0.04	1.47 ± 0.33	1.24 ± 0.19

Table 3.7: Kevlar 29 and plant fiber apparent transverse elastic modulus for all compression cycles and for cycles 1 and 2. Averages values are given along with standard deviations.

3.4.4 Plant fiber transverse properties: summary and new perspectives

In this section, plant fiber SFTCT were presented for the first time. A specially adapted multi-step experimental protocol was developed for this purpose. Through careful elimination of partial compression effects and rapid loading-unloading cycles, a purely elastic, full compression was isolated as much as possible. This allowed the identification of an apparent transverse elastic modulus for nettle, hemp and flax. The value of this modulus varies as a function of loading cycle, it is roughly situated however between 1 and 2 GPa.

These values are in contrast with the ones obtained by 'back calculation' through tests on composites containing plant fibers. With the use of such methods, [Baley 06] measured a transverse elastic modulus for flax fibers at 8 GPa. Many sources could point to an apparent stiffening of plant fibers when used in composites. Boundary conditions are very different, with the fiber being severely more constrained inside the matrix. During the manufacturing of the composite material, important compression loads are also applied. This could lead to lumen collapse and overall changes in ellipticity and flatness, coupled with material stiffening due to irreversible mechanisms. However, as analyzed by [Shah 16] in the case of tensile properties, numerous sources of uncertainty impact back calculated properties (see subsection 1.3.2). Overall, the direct measurement of the plant fibers transverse properties offer more reliable results that happen to be quite different from the ones that were previously considered.

Finally, the presented direct measurement and resulting values of E_T offer a new perspective on the anisotropic nature of plant fibers. Indeed, the longitudinal elastic modulus of plant fibers is generally in the order of several tens of GPa. Table 3.8 shows this anisotropy ratio (E_L/E_T) for all tested fibers with values of E_L taken from the literature. Our experimental SFTCT results directly show that nettle, hemp and flax fibers are highly anisotropic materials, potentially more so than Kevlar in some cases.

Plant	**Kevlar**	**Nettle**	**Hemp**	**Flax**
$\boldsymbol{E_L\,(GPa)}$	84 [Bencomo-Cisneros 12]	36 -79 [Jeannin 20]	14-44 [Bourmaud 18]	37 - 75 [Bourmaud 18]
$\boldsymbol{E_T\,(GPa)}$	2.21	1.76	2.21	1.71
$\boldsymbol{E_L/E_T}$	38	20-44	6-20	22-44

Table 3.8: Anisotropy ratios E_L/E_T for all tested fiber with longitudinal values taken from the literature. The average E_T across all cycles and tested fibers is given.

3.5 Conclusions and perspectives

In this section an innovative high precision, micro-mechatronic experimental setup, was developed specifically for the purpose of SFTCTs while addressing previous setup limitations. Coupled with a unique multisensing device it allowed for direct measurements of fiber displacement and applied compressive force. The setup's and sensor's measurement ability was validated through repeatability and calibration procedures.

The major influence of platen parallelism on the identification of E_T was demonstrated for the first time and an experimental protocol was developed to address it.

Finally, trough a specially developed, multi-step experimental protocol the transverse behavior of plant fibers was studied for the first time. Their transverse elastic modulus was shown to be similar to the one of Kevlar® 29, between 1 and $2\,GPa$. Inelastic phenomena were also observed and material and structural mechanisms were proposed to explain them. These results also highlighted the highly anisotropic nature of plant fibers and differences between directly measured and 'back calculated' transverse elastic properties.

This work established the groundwork for the study of single plant fiber transverse compression focused on the identification of their transverse elastic properties. In its current configuration, the influence of relative humidity on the fibers transverse behavior could be studied. Compressive failure could also be investigate through the use of higher loads. However, a few improvements could also enable the study of even more fiber behaviors. The most notable, is a fine control of temperature or at least a finer characterization of the temperature's influence on sensor measurements. Such an improvement would allow for loading protocols of larger duration to characterize viscoelasticity or fatigue. Preliminary creep tests were performed and show promising results. More details can be found in Appendix B.5.

The microscopes integrated in the setup could also be put to further use for image-correlation based studies. Such studies were already shown to be possible with this setup on PA11 fibers [Placet 20]. Some studies were also performed on horse hair, since its larger size and macroscopically uniform nature made the analysis easier. For smaller fiber however, like the plant fibers that were tested, a higher magnification and more regular fiber edge would be needed to employ such methods more systematically.

A limitation of the current experimental setup and protocol, lies in its low throughput. Efforts were made to accelerate testing by automating and streamlining software related tasks in the launching and post-treatment of tests. However, samples are still manually extracted, measured and positioned in the setup which is a time-consuming and labor-intensive task. As already discussed, manual extraction also adds biases in the final results. To address these limitations, a new PhD thesis has started, focusing on the development of a micro-robotic platform for the manipulation and testing of plant fibers. In the long term, larger volumes of fibers and statistical approaches could be used to treat the results, offering further knowledge on their properties and characteristics.

In a more general context, this works highlights the development and validation of a custom experimental setup for the study of miro-object transverse behavior. With the added use of a carefully selected experimental protocol complex material and structural behavior can be brought to light. While our work focused on plant fibers other objects of the same scale could be studied.

4

MICRO-MECHATRONIC PEELING TEST - PLANT FIBER INTERFACE ADHESION CHARACTERIZATION

Contents

4.1 Introduction

This chapter treats the characterization of the adhesion between plant fibers, through the use of peeling tests. A custom micromechatronic platform, developed specifically for the purpose of these tests is designed and put to use. Through peeling tests, the force required to separate elementary plant fibers is measured for the first time. Comparison of fiber adhesion between different plant varieties, retting or extraction processes, thus becomes possible. Furthermore, real time observation of the tests offers unprecedented insights into the fracture mechanisms that occur during fiber separation. Macrofibrilar elements bridging and breaking at the peeling interface along with changes in peeling due to kink bands are observed and their influence on the peeling force is quantified.

A major part of this chapter's content is a result of two 6-month internships. First, Thomas Guibaud designed a micromechatronic platform for the purpose of plant fiber peeling. Second, Wajih Akleh performed the first experimental campaign, to measure and compare the interfacial adhesion between different fiber lots. Furthermore, he categorized and studied the fracture mechanisms that occur during peeling in a semi-automated way.

4.2 Characterization method - experimental setup design and validation

4.2.1 Determining fiber interface adhesion - analytical model

Peeling model

As discussed in section 1.4.3 a great number of analytical models has been developed in order to relate measurable quantities to the adhesion between surfaces in a peeling test. Following some earlier works on the subject [Rivlin 44, Spies 53, Gardon 63], a popular peeling model was developed by Kendall [Kendall 75]. His model treats the peeling of an elastic film from a rigid substrate and allows the calculation of a surface energy R. This energy represents the fracture energy required to separate the film from the substrate per unit of area (homogeneous to $J \cdot m^{-2}$ or $N \cdot m^{-1}$). In this work the term adhesion energy will be used to refer to it and the letter γ will be used to note it [1]. The surfaces are considered homogeneous and rectangular, as seen in Figure 4.1.a. The model is written as follows:

$$\gamma = \left(\frac{F}{b}\right)(1 - cos\theta) + \left(\frac{F}{b}\right)^2 \frac{1}{2dE} \tag{4.1}$$

with: F the peeling force, θ the peeling angle, b the surface width, E the film's Young's modulus and d the film's thickness. Kendall showed that for larger peeling angles the films elastic extension term can be neglected (see Figure 4.1.b), simplifying the equation to:

$$\gamma = \left(\frac{F}{b}\right)(1 - cos\theta) \tag{4.2}$$

If the film is thus peeled vertically ($\theta = \pi/2$) the adhesion energy is only a function of the peeling force F and the film width b.

---

[1] this avoids confusion with the fiber radius, often noted R in this work.

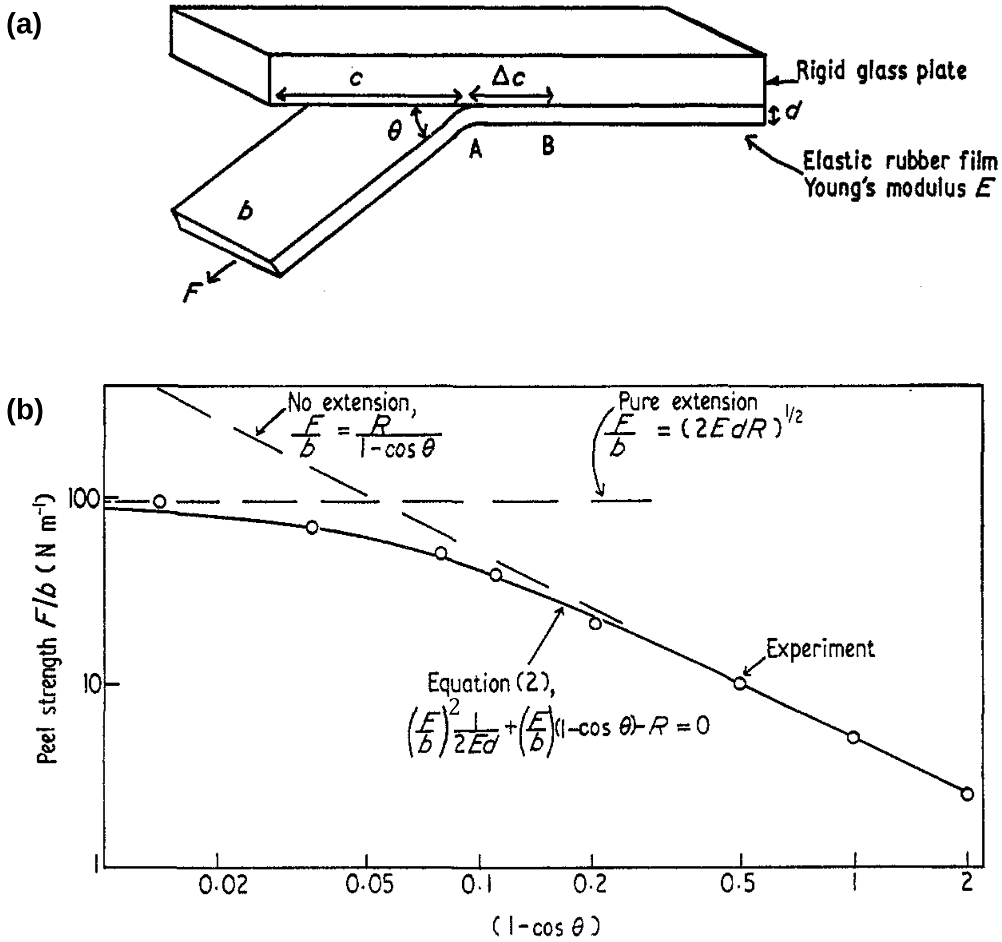

Figure 4.1: (a) Kendall model geometric representation, (b) dependence of surface energy on peeled film extension as a function of peeling angle [Kendall 75]. The adhesion energy R is noted γ in this work.

Pesika et al. showed the existence of two peeling regimes for the peeling of ideal geometries: the constant and variable peel-zone regime [Pesika 07]. Above a critical angle θ_0 the constant peel-zone regime is established, where the peeling force becomes independent of the peeling angle. Below this critical angle, in the variable peel-zone regime, the peeling force increases with an decrease in angle. This critical angle is below 90° ($\theta_0 \leq \pi/2$). This means that as long as peeling angles are maintained close to 90°, the adhesion energy can be calculated only with the peeling force and the film width, without the need to measure the peeling angle.

Model adaptation to plant fiber peeling

To the author's knowledge, the peeling of elementary plant fibers is a test that has not been performed before. For this reason, in this work, existing peeling models will be adapted to fit the needs of the test. However since existing peeling models typically consider ideal geometries, caution is needed in their adaptation to the complex nature of plant fibers.

The peeling model developed by Kendall, presents several advantages and disadvantages for plant fiber peeling tests. First, if the peeling angle is large enough, the longitudinal Young's modulus E_L of the peeled elementary fiber can be omitted. Determining the stiffness of the peeled fiber, or providing an average modulus for the tested plant type (which can show great variability) is hence avoided. On the other hand, Kendall's peeling model considers the peeling substrate to be rigid. In the case of plant fiber peeling, the substrate consists of one or several elementary fibers along with middle lamella that connects them. While this substrate is not rigid, determining its stiffness and integrating it in the model, would represent a significant challenge, considering the complex morphology and composition of plant fiber bundles. Nonetheless, the application of a longitudinal pretension would limit its deflection. For this reason, in this work, the deformation of the peeling substrate are not accounted for and the fiber bundle is considered as rigid.

A significant advantage of the model can also be found in the possible simplifications related to the peeling angle. Given the complexity of plant fibers in terms of morphology, MFA, kink bands and more, it could be expected that the peeling angle varies throughout the test. The fact that this angle can be omitted if it remains close to 90°, eliminates the need to measure the angle during the test, an important simplification.

Finally, in order to use Kendall's model in the context of plant fiber peeling, the contact width b between the peeled fiber and its bundle is needed. This represents a significant challenge. The interface between elementary fibers can have a complex geometry that changes along the fiber's length while also being difficult to access. For this reason in this study, the peeling contact width will be approximated to the fiber's apparent diameter, *i.e.* its width as observed from an overhead microscope. While this approximation is certainly not the most accurate, it introduces an estimation of elementary plant fiber geometric properties into the model, thus allowing the calculation of the adhesion energy and the comparison of adhesive properties between fibers of different sizes.

In conclusion, the adhesion energy at the interface between plant fibers is calculated through:

$$\gamma = \frac{F}{D} \tag{4.3}$$

with F the peeling force and D the apparent fiber diameter. A schematic representation of the plant fiber peeling test, as it is performed in this work, is represented in Figure 4.2.

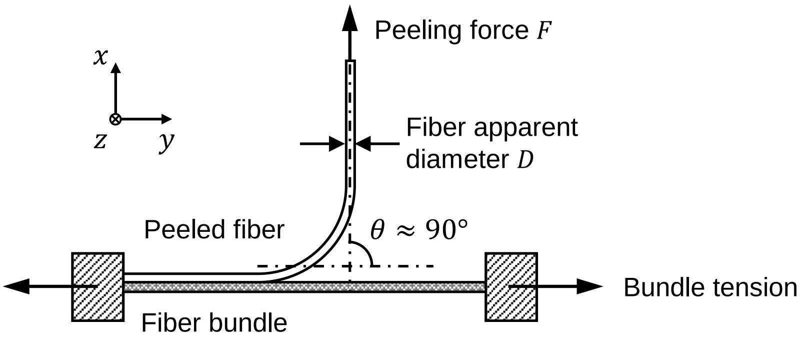

Figure 4.2: Schematic representation of plant fiber peeling.

4.2.2 Experimental setup requirements and design

Peeling test requirements

Since plant fiber peeling has not been performed before, a new experimental setup must be designed. The means necessary to perform accurate characterization in a way that is as simple as possible for the operator, need to be identified accurately. The main requirements to create an experimental setup capable of reliable plant fiber peeling tests are the following.

- An apparatus to hold the elementary fiber that will be peeled. The fiber's orientation should be controlled as much as possible and slipping during peeling should be avoided.
- A support to hold the fiber bundle from which a fiber will be peeled. To minimize movements of the bundle during peeling, in order to help approach the rigid substrate hypothesis of Kendall's model, bundle tension must be controlled. Furthermore, some bundle rotation around its longitudinal axis is crucial, in order for the peeled fiber to face towards the peeling direction. An example of a correct and incorrect peeling configuration is represented in Figure 4.3.
- Actuation, to separate the fiber from its bundle and to maintain a peeling angle close to 90°.
- Force and displacement sensing capabilities, to measure the peeling force and peeled fiber length.
- Observation capabilities, to monitor the peeling test, observe fracture mechanisms and measure the fiber's apparent diameter.
- Positioning capabilities, to keep the fiber grasping and fiber bundle in the same plane.

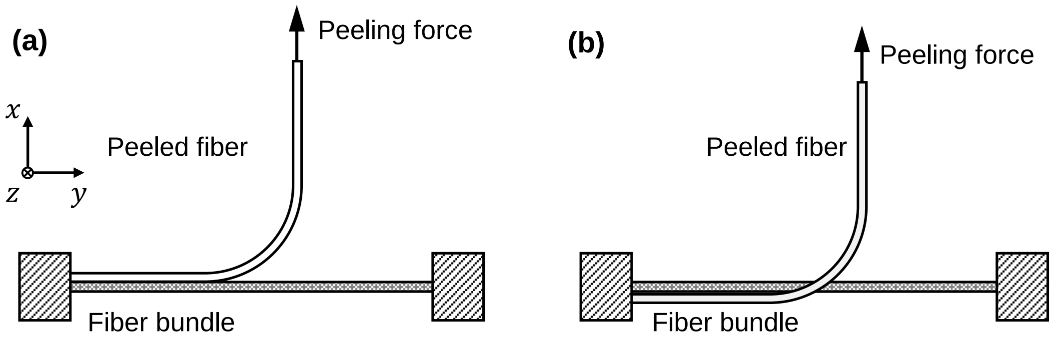

Figure 4.3: Plant fiber peeling correct (a) and incorrect configuration (b). In order to ensure a smooth peeling that matches the geometric representations used in peeling analytical models, the peeled fiber must be facing toward the direction of the peeling force.

Peeling setup design

In order to satisfy the requirements that were deemed necessary to perform plant fiber peeling tests, a custom micromechatronic experimental setup is designed. An overview of its layout and components is given in Figure 4.4. A list of all used components is given in Table 4.1. Further details and explanations are given next.

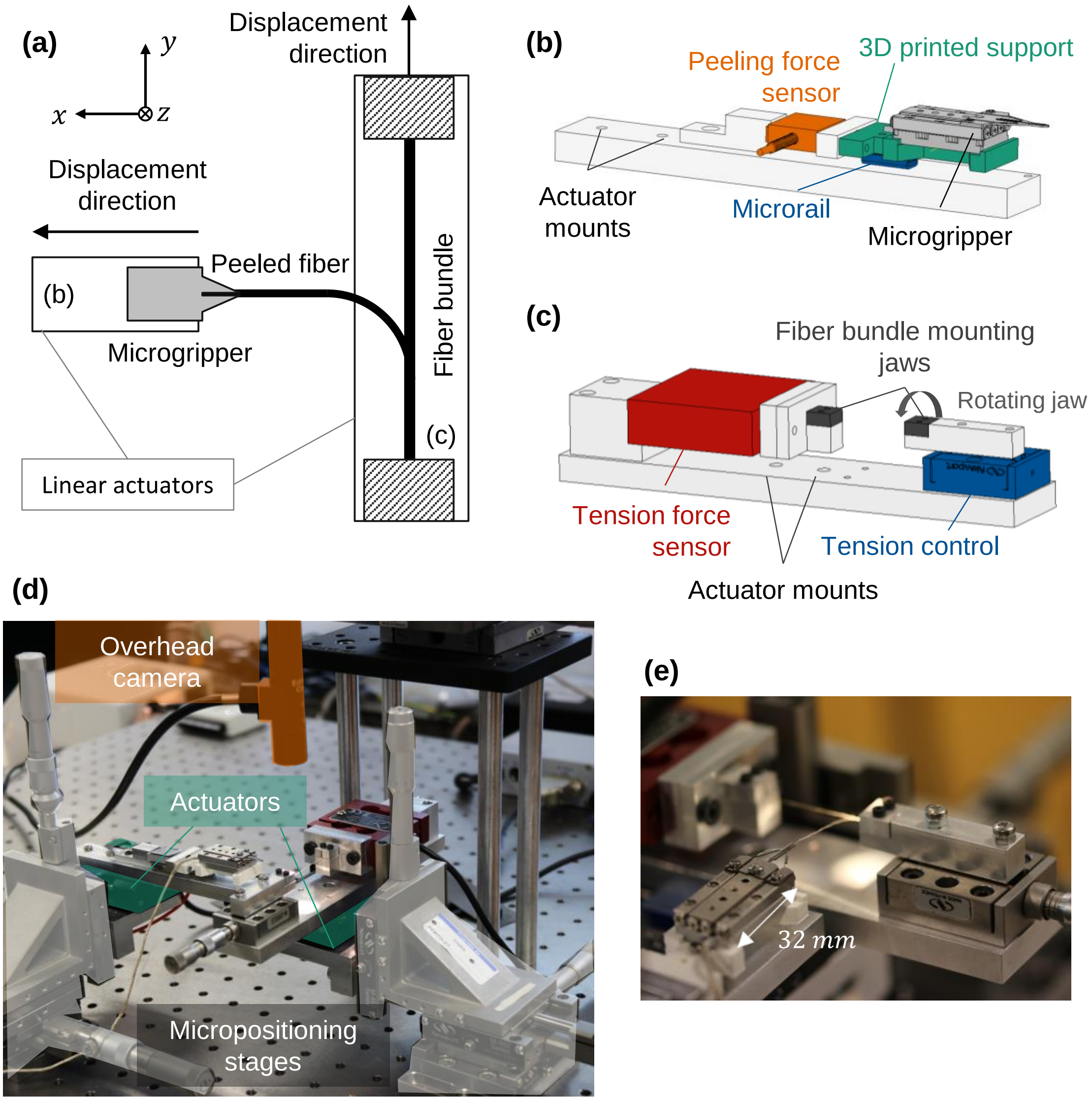

Figure 4.4: Plant fiber peeling micromechatronic setup: (a) illustration of testing main principle, (b) microgripper assembly with force sensing capability (c) fiber bundle support with tension control capability, (d) setup overview, (e) closeup view of plant fiber being pulled from its bundle.

General concept - peeling angle control. The peeling setup is comprised of two main elements: a support for the fiber bundle and a support for a microgripper, which grasps an elementary fiber and separates it from the bundle. In order to perform the peeling, the microgripper and its support structure are mounted on a linear actuator, that moves the gripper away from the bundle. The chosen microgripper's (*SmarAct, SG-1730*) gripping force of 1 *Newton*, allows for minimum fiber slipping during peeling.

To maintain a peeling angle that is close to 90°, the peeling zone must remain in the same axis as the gripper throughout the whole test (at the same y coordinate). To do so, the bundle support is also mounted on a linear actuator moving in the opposite direction to the peeling's propagation. By setting an identical speed for both actuators, the peeling zone stays at the same y coordinate keeping the peeling angle at 90°. An open loop control system is used, no correction of actuator movement is performed to control the peeling angle.

To facilitate the manipulation and mounting of the fiber samples and various setup components, the peeling is performed in the horizontal plane (xy plane). To limit vibrations, the platform is built on an active antivibration table (Newport). A graphical representation is given in Figure 4.4.a. A closeup view of an elementary fiber being pulled from its bundle by the microgripper is given in Figure 4.4.e.

Peeling force measurement. In order to measure the force which is responsible for the peeling of the elementary fiber, force sensing capabilities must be added to the microgripper. A design inspired by the patent of Saketi and Kallio "Micro gripper with force sensor" is produced [Saketi 16]. The design is showed in Figure 4.5. It relies on the use of a micro-rail with a very small friction coefficient. The gripper is fitted into a casing fixed on the moving part of the rail. A small spring links the back of the gripper casing to the fixed part of the rail. This design allows the generation of a relative displacement between the gripper and the fixed part of the rail, compressing or elongating the spring. Through the measurement of these spring deformations the force can be estimated. If the gripper pulls on an object, the reaction force will make slide towards it elongating the spring. If it pushes an object, the reaction force will push it away from it, compressing the spring.

Our experimental setup uses the same gripper-rail configuration, but replaces the spring with a conventional force sensor. Preliminary peeling measurements were performed on a microscale to evaluate the force needed to separate an elementary fiber from its bundle. These preliminary tests showed that the peeling force was in the order of a few mN. For this reason, a sensor with a $100\,mN$ range was chosen. The completed gripper-rail-sensor assembly is shown in Figure 4.4.b. The microrail is fixed onto an aluminum support which is then fixed on a linear acuator. A custom 3D printed casing is made to hold the microgripper.

Fiber bundle support. A custom fiber bundle mounting assembly is also designed (see Figure 4.4.c.). Two screw-closing jaws are used to hold the fiber bundle. One of the bundles can freely rotate around the y axis to help position the elementary fiber, so that it faces towards the microgripper. This mount is fixed on a small manual micropositioning stage allowing a control of bundle tension. A force sensor is placed on the opposite mount to measure the tension force. By eliminating fiber bundle slack, peeling takes place in a smoother since bundle movements become limited. By consequence, this also creates a peeling substrate that is closer to the rigid assumption made by the analytical model.

Test observation. In order to add observation capabilities to the experimental setup, a camera is mounted overhead, above the peeling zone. The synchronous movement of the two actuators to maintain a 90° angle keeps the peeling at roughly the same position throughout the whole test. The camera can thus be stationary but still monitor the

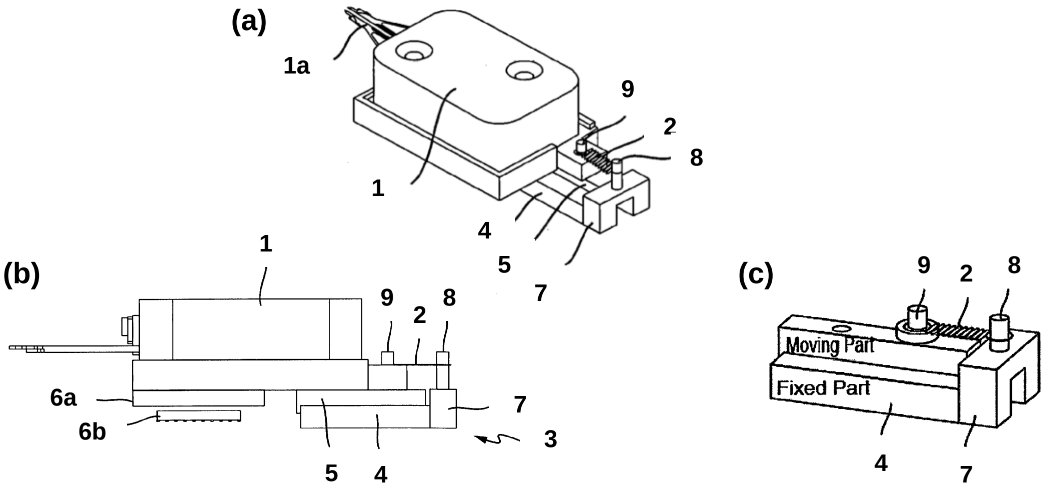

Figure 4.5: (a),(b) view of the gripper (1), rail (4,5) and spring (2) assembly, (c) isolated view of rail and spring. Illustration taken from [Saketi 16]

peeling procedure in its entirety. A telecentric lens is used, for its constant magnification properties and minimized perspective errors, allowing for consistent measurements of fiber apparent diameter. Its larger depth of field also helps keep the peeling zone in focus even if slight off-plane movements occur. An overview of the setup with the overhead camera can be seen in Figure 4.4.d.

Finally, a series of manual micropositionning XYZ stages (*Newport*) allow for a fine adjustment of the position of each setup element. Notably, the gripper and the bundle can be positioned in the same horizontal plane and the peeled fiber can be aligned with the grippers movement axis.

Component	**Company**	**Model**	**Specifications**
Microgripper	SmarAct	SG-1730	gripping force: $1\,N$
Linear actuators	Physik Instrumente	M-111	range: $15\,mm$, repeatability: $0.25\,\mu m$
Peeling force sensor	TEI	FSB	range: $0.1\,N$, non-linearity: $\pm 0.01\%$
Tension force sensor	AEP	TCA	range: $1\,kg$, non-linearity: $\pm 0.03\%$
Camera lens	Edmund optics	67-317	telecentric ,zoom: 8X, field of view: $1.1\,mm \times 0.8\,mm$
Microrail	IKO	-	range: $15\,mm$; friction coefficient: 0.001

Table 4.1: Overview and specifications of components used in the micromechatronic fiber peeling setup.

4.2.3 Experimental setup validation

Before proceeding to the experimental valorization of the created experimental setup, verifying and validating its operation, as well as investigating influential parameters, are important prerequisites. In this section, the influence of peeling speed on adhesion measurements will be discussed along with the influence of microgripper inertia on the measurement of the peeling force.

Influence of peeling speed

In their work on the adhesion between polymer films and flat indenters, Choi et al. showed a dependence of the adhesion's strength to detachment velocity, with higher forces needed for surface separations at higher velocities [Choi 08]. In order to avoid overestimating plant fiber adhesion due to high peeling velocity, its influence was studied experimentally. To eliminate the influence of plant fiber variability on the results, a synthetic, uniform material was considered. Conventional office adhesive tape was chosen for this purpose. Two thin pieces of adhesive were joined together and peeled using the microgripper, as seen in Figure 4.6.a. The same width was used for all tested samples.

The peeling force as a function of the peeled distance for different velocities can be seen in Figure 4.6. Higher velocities lead to significantly higher peeling forces. These results are in accordance with the observations made by [Choi 08]. The peeling force stabilizes under $2\,\mu m/s$. While it cannot be said with certainty that the influence of peeling speed on adhesive tape accurately reflects what happens during plant fiber peeling, it indicates that lower peeling speeds should be preferred to avoid an overestimation of adhesive properties. For this reason, a peeling speed of $1\,\mu m/s$ is chosen for all plant fiber peeling tests.

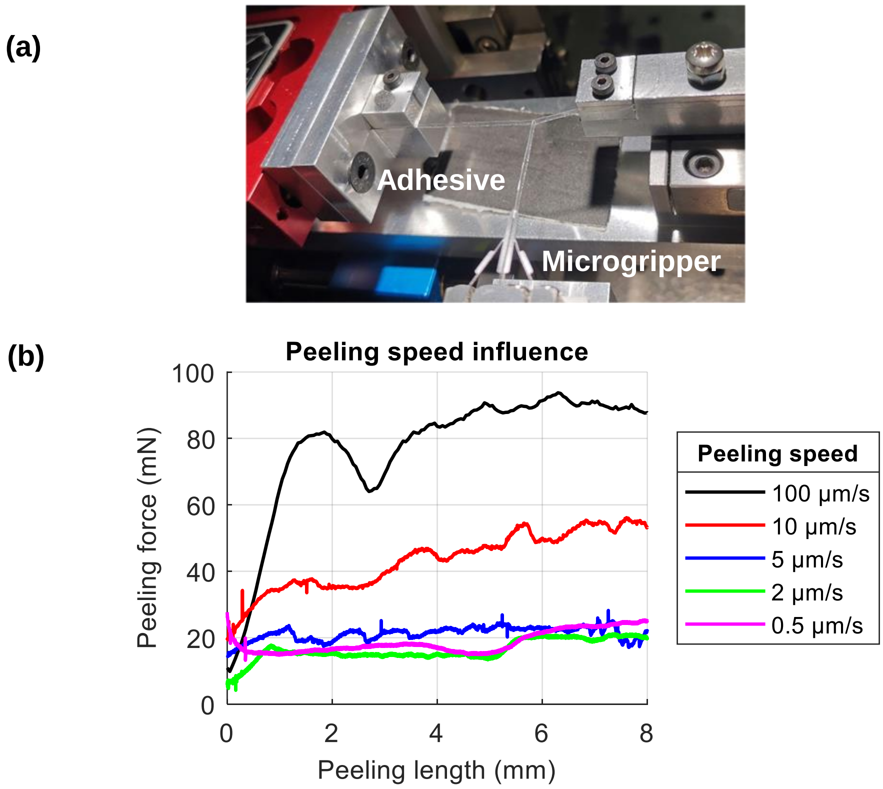

Figure 4.6: Adhesive tape peeling test: (a) experimental configuration, (b) peeling force evolution for different peeling speeds.

System calibration

Since the measurement of the peeling force relies on the relative displacement between the microgripper on one hand and its support structure on the other, the inertia of the gripper will affect force measurements. The cables coming out of the gripper and the sensor can also have an effect, since their size and stiffness is far from being negligible compared to those of the setup's components. To limit it, their position was fixed and enough slack was allowed to avoid cable tension.

To characterize the change in measured force resulting from gripper intertia and cable stresses, a calibration process is proposed. It consists in repeatedly retreating the gripper away from the bundle support without grasping onto a fiber. The speed of 1 $\mu m/s$, used in all future plant fiber peeling tests is used.

The results for 5 retreats are shown in Figure 4.7.a. As the actuator moves, the microgripper, which can freely move on the low friction rail, will tend to resist this movement. The force sensor will thus be in tension, as attested by the increase in force. The change in force measurement is quite repeatable with only one retreat being noticeably different at the start of the test. Figure 4.7.b shows the average result over the five tests, with the shaded area representing the standard deviation. The differences between tests are more important at the beginning of the calibration procedure and progressively reduce. A quadratic polynomial is fitted over the average response with the following expression:

$$F_{calibration} = -0.03x^2 + 0.70x \tag{4.4}$$

with x being the displacement generated by the actuator. During peeling tests the influence of cables and microgripper inertia on force measurements can thus be eliminated through:

$$F_{peeling} = F_{measured} - F_{calibration} \tag{4.5}$$

with $F_{peeling}$ the force separating the fiber from its bundle, $F_{measured}$ the raw force given by the force sensor and $F_{calibration}$ the polynomial identified through the calibration procedure.

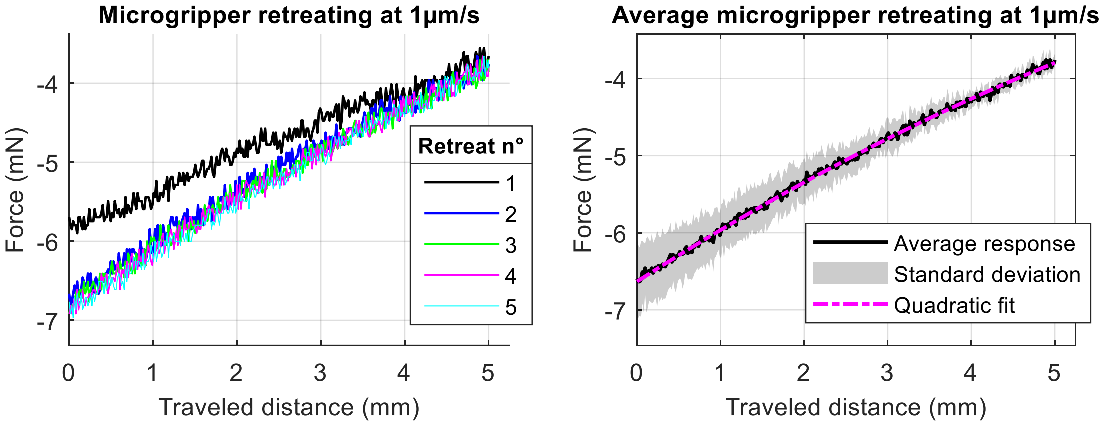

Figure 4.7: Microgripper retreat with no grasped fiber calibration: (a) results of five retreats, (b) average response over 5 tests with fitted quadratic polynomial, the standard deviation is represented as a shaded area.

4.3 Materials and methods

4.3.1 Fiber material

In the context of the *NETFIB* project, different nettle fiber extraction processes were tested by colleagues at the City University of Applied Sciences of Bremen, Germany (Hochschule Bremen (HSB)). Notably, two decortication methods were employed on nettle (L18 clone, grown in Germany) using a Hammer Mill (HM) and a Breaking Unit (BU), which separate fiber bundles from the rest of the plant. A decrease in tensile properties was observed for composites making use of fibers separated with a HM compared to the ones using a BU. Fiber bundle damaging during decortication was identified as a possible explanation for this change in properties. Indeed, the hammer mill is a more agressive process, leading to high fiber individualization at the expense of shorter and sometimes damaged fibers [Bourmaud 18]. The breaking unit is less likely to damage the fibers. The peeling test was chosen to compare the adhesion between fibers issued from these two decortication methods. The ease of fiber separation can then be compared between the two methods and confronted to the risk of damaging the fibers.

Samples from other academic partners have also been received to study the influence of retting level, plant variety and more. These studies are however not finalized at the time of writing of this thesis and will thus not be discussed.

4.3.2 Peeling test preparation

Sample extraction. The first step in the preparation of a peeling test lies in the extraction of fiber bundles from the available material. Fiber material can be found in longer or shorter strands (see Figure 4.8 (a) and (b) respectively). Using, tweezers or his hands, the operator isolates a bundle from its strand. The bundle is inspected under a magnifying lens for any protruding elementary fibers. Once one is spotted, it must often be partially peeled using tweezers until an adequate length is freed to allow an easier grasping by the microgripper (around $10\,mm$). 12 samples of hammer mill and 10 samples of breaking unit decortication were extracted and tested.

Figure 4.8: Examples of processed fibers from which bundles are extracted for peeling tests : (a) long strand, (b) short strand.

Sample mounting. With the fiber sample being prepared, mounting on the experimental setup is next. The bundle is first placed in the mounting jaws. Particular care is taken in the alignment [2] of the bundle and its centering it inside the jaws. The rotating jaw is also used to assure a correct peeling orientation as illustrated in Figure 4.9. Finally, using the tensile control micropositioning stage, tension on the bundle is adjusted to eliminate slack. The tension force is monitored in real time to avoid large stresses that can damage the bundle. While simple in principle it must be noted that the preparation and mounting of a sample for peeling tests, is a delicate process needing particular dexterity and attention from the part of the operator. The elementary fiber can easily be broken off from its bundle during manipulations. Sample preparation can thus take significant time.

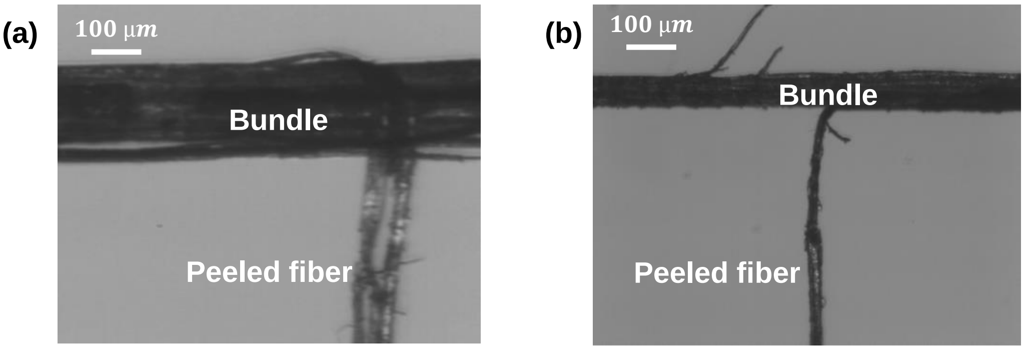

Figure 4.9: (a) Example of incorrect peeling orientation. The peeled fiber (2 fibers in this photo) faces in the opposite direction of the gripper and is being pulled over the bundle. (b) the peeled fiber is facing towards the gripper and can be peeled smoothly.

Force reference point. The next step in the preparation of the peeling test consists in moving the microgripper close to the bundle. The force measured at this empty gripper configuration is saved as a reference of "zero" load F_{ref}. Indeed, some small compressive or tensile force can be detected even when no peeling occurs and when no fiber is gripped. It is a result of the stresses applied during the assembly of the gripper mount, cable stresses, or due to gripper movement on the rail. This force value is subtracted from the force measured by the peeling force sensor. For the sake of consistency, this reference measurement is made at approximately the same position along the peeling axis (x axis).

Position adjustment. With the reference force measurement being made the elementary fiber protruding from the fiber bundle is gripped using the microgripper. The manual micropositioning stages controlling the gripper and bundle supports are used to place the bundle and the gripper in the same horizontal plane. Lateral y positions, of the bundle or gripper, are also adjusted to obtain a 90° angle between the bundle and the elementary fiber as seen in Figure 4.10. Monitoring through the overhead camera makes this process relatively simple. Finally, the gripper is retreated pulling on the elementary fiber and getting it in tension. This movement is stopped, once some peeling starts initiating. During this stage the bundle and the elementary fiber can move quite a lot, moving sometimes, outside of the camera's field of view. It thus important to perform this pretension before launching a test to maximize the chances of observing the fiber peeling in its entirety.

---

[2] along the y axis, see Figure 4.4.a

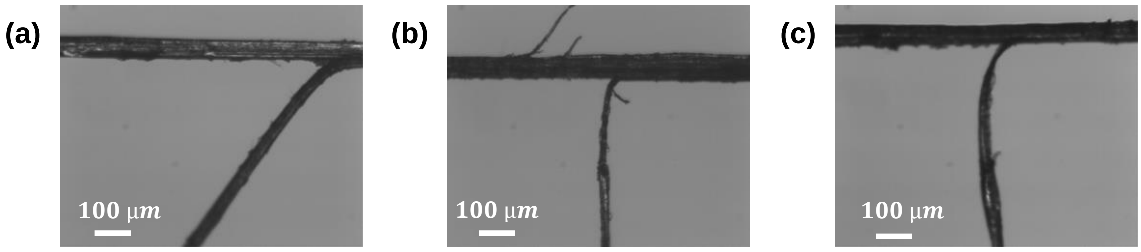

Figure 4.10: Examples of peeling angles: (a) acute, (b) right, (c) obtuse. Micropositioning stages are used to position the peeling zone in front the gripper resulting in a right angle.

4.3.3 Diameter measurement.

In order to calculate the adhesion energy γ at the fiber interface, a diameter measurement is necessary (see section 4.2.1). To do so, an image treatment algorithm is constructed to calculate the fiber's apparent diameter, as seen by the overhead camera. Measurements can be quite challenging, fibers can have many defects or protruding tissues, their orientation can change from photo to photo, while the high magnification of the camera's objective means that the depth of field is quite shallow, leading to often blurry fiber contours. To overcome these challenges, the steps used by the algorithm are the following.

Starting with a raw image of the peeling zone, any major defects which could influence diameter measurements, such as protruding fibrils, are removed using an image processing program. The edited image is then turned into binary, using Otsu's thresholding method [Otsu 96] and the elementary fiber section of the image is cropped. Figure 4.11 illustrates this process. With the image of the elementary fiber being cropped, its average width along the horizontal axis w is calculated. If the fiber is at an angle inside the frame of the image, this width might not be completely representative of the fiber's diameter. For this reason, a linear fit is performed on the median line of the fiber. Through the slope of this linear equation the angle of the fiber inside the camera's frame α is approximated and an apparent fiber diameter D can be calculated:

$$D = cos\alpha \cdot w \tag{4.6}$$

Multiple diameter measurements are typically made for a single peeling test. The followed procedure will be discussed in the following subsection. However the number of measurements stays limited, since the process still needs a manual initial editing of the image and cropping of the elementary fiber. This process could be automated, in order to provide apparent diameter measurements across the whole test.

4.3.4 Data treatment

Data segmentation. During the peeling test, important variations in measured force can occur. These variations can be caused by changes in fiber morphology, the presence of kink bands, the sudden rupture of inter-fiber tissues and more. None peeling phenomena can also occur, such as bundle twisting, intra-bundle rupture and separations and more as illustrated in Figure 4.12. To calculate an adhesion energy that is representative of the actual fiber interface despite these changes in peeling behavior, the results must often be segmented in a number of sections that are treated differently.

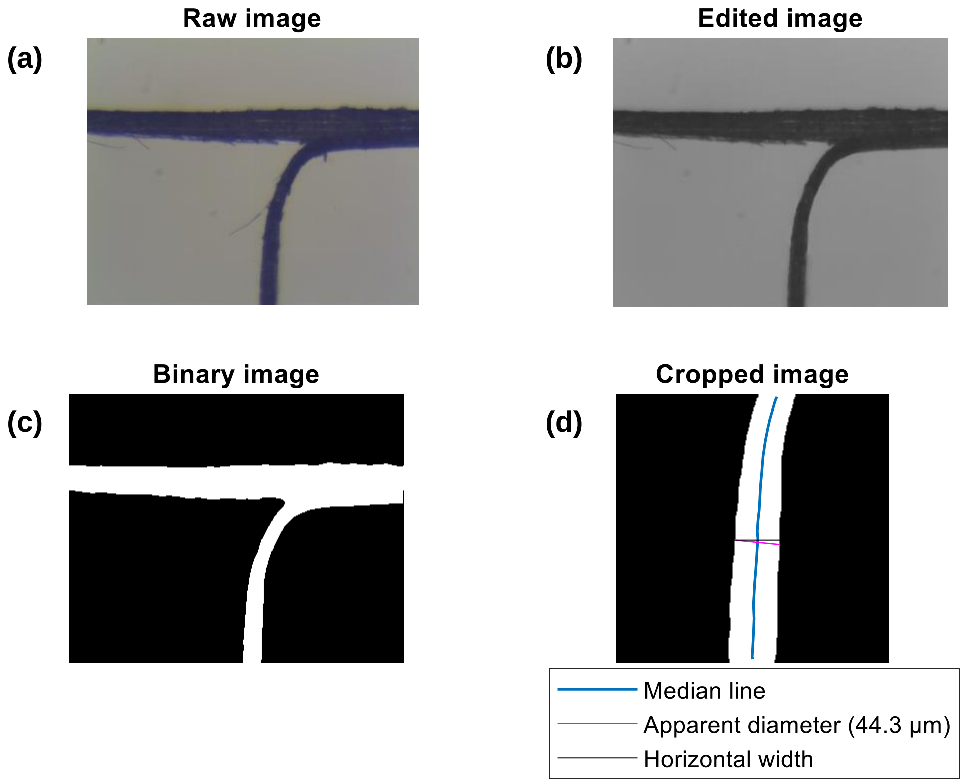

Figure 4.11: Elementary fiber apparent diameter measurement: (a) raw image, (b) edited image, (c) image binarization, (d) elementary fiber apparent diameter measurement.

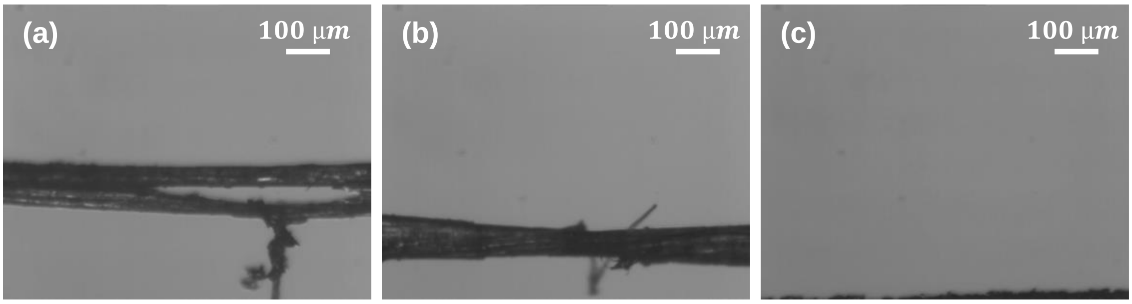

Figure 4.12: Examples of unusable segments of peeling tests: (a) fiber bundle splitting, (b) fiber bundle twisting around its longitudinal axis, (c) peeling zone moving out of frame.

Figure 4.13.a illustrates a case where peeling behavior is distinctly different between three stages of the test. In stage 1, at the beginning of the test shows an increase in force as the fibers still gets in tension, therefore this stage does not correspond to peeling. Two distinct peeling regimes are then seen (stages 2 and 3). When such cases occur the video recorded by the overhead camera is examined to understand the nature of the change between peeling regimes. In the present case, the diameter of the peeled fiber decreased significantly in stage 3, inducing a decrease in peeling force (see Figure 4.13.c and c). In this case, to accurately estimate adhesion energy, stage 1 is not used in its calculation and two separate diameters measurements are made for stage 2 and 3 each.

This approach is adopted for all peeling tests. If a certain test stage does not correspond to a smooth peeling behavior, such as those illustrated in Figure 4.12, it is not used in the adhesion energy calculations. If a change in peeling behavior is a result of a change in diameter, separate diameter measurements are performed for each stage.

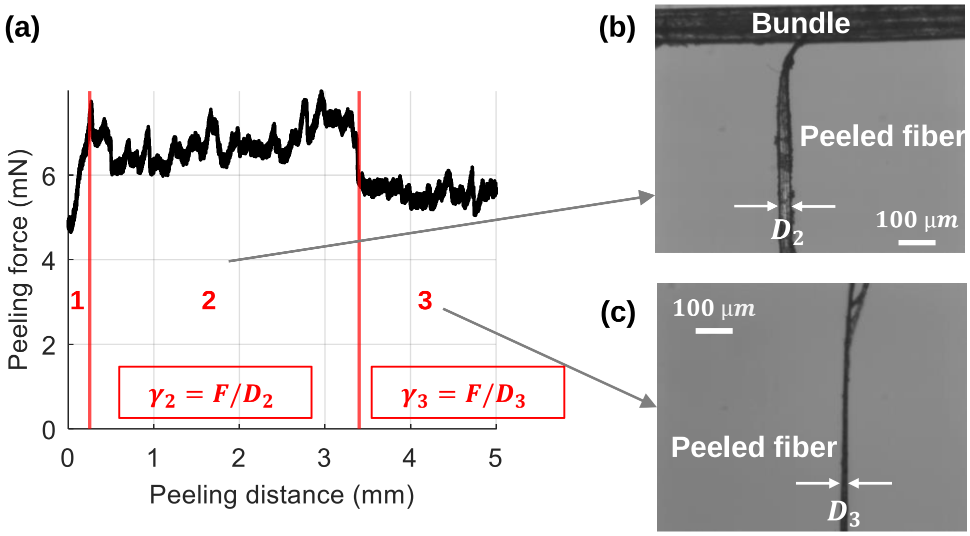

Figure 4.13: (a) Peeling test results with three distinct stages, (b) image of peeled fiber in stage 2, (c) image of peeled fiber in stage 3. The adhesion energy of stage 2 and 3 (γ_2, γ_3 are calculated with the according apparent diameter D_2, D_3).

Outlier detection. The detection and categorization of the phenomena that cause abrupt changes in peeling behavior can be very time consuming. For this reason, a semi-automated simple algorithm is constructed. First, the derivative of the peeling force with respect to the peeling length is calculated. For most of the peeling tests this value remains relatively stable with most variations being caused by the force measurement noise (see Figure 4.15). When sudden changes in peeling force occur however, peaks in the derivative value are produced. To detect these outliers in the value of the derivative, the InterQuartile Range (IQR) is used [Dekking 05]. The IQR represents the difference between the 25th (Q1) and the 75th (Q3) percentile of a given dataset. A lower (LF) and upper fence (UF) can then be defined (they represent -2.698σ and 2.698σ respectively):

$$LF = Q1 - 1.5 \times IQR, \quad (4.7)$$

$$UF = Q3 + 1.5 \times IQR \quad (4.8)$$

Any value in peeling force derivative that is smaller than LF or higher than HF is considered a statistical outlier. For each detected outlier in a given test, the according snippet of the test's video is shown to the user. The user can then choose between a series of categories to define the source behind the change in force. The change in peeling force ΔF related to this abrupt change in peeling behavior is also calculated. Figure 4.15 shows an example of a peeling test with the derivative value and its outliers.

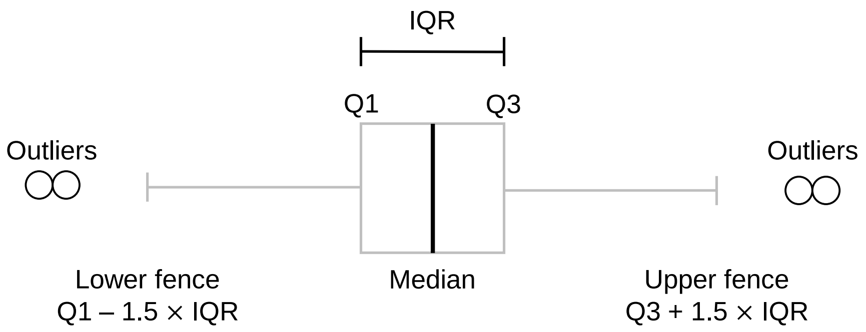

Figure 4.14: InterQuartile Range (IQR), lower and upper fence and outlier representation

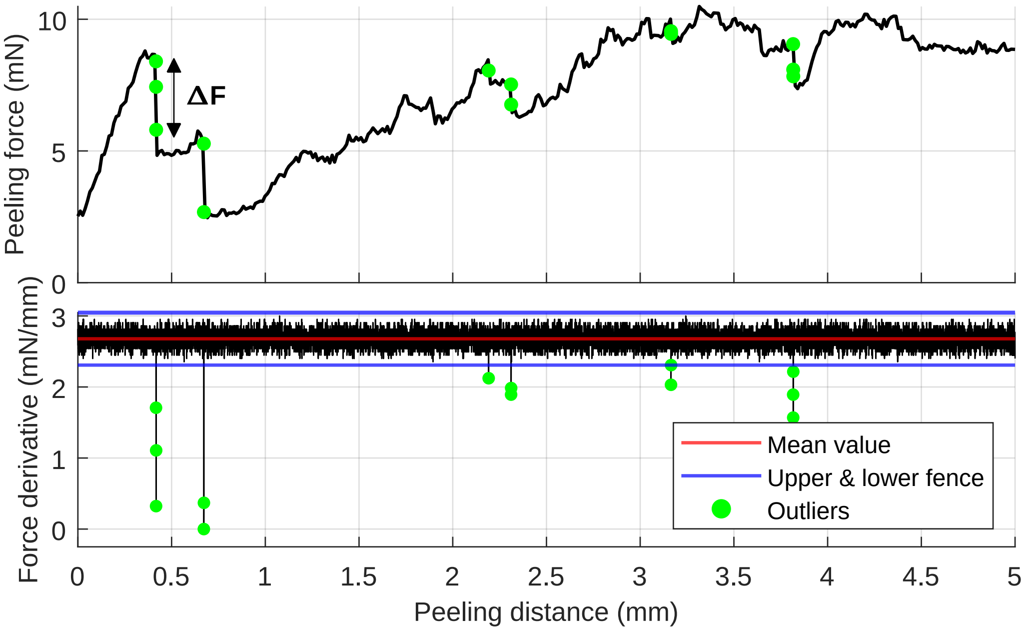

Figure 4.15: Peeling force and its derivative as a function of peeling length, with detected outliers.

4.3.5 Sample saving

Once the peeling test is completed, the fiber bundle along with the protruding peeled fiber are taken off their experimental setup. To allow for future studies on the sample, such as microscopic observations of the peeling zone or Raman spectroscopy, the fiber samples must be saved. For this purpose, custom cardboard frames for the bundle and the peeled fiber are fabricated by laser cutting (see Figure 4.16.a and b respectively). Millimetric graduations are engraved to help with position referencing.

The process of sample saving is performed as follows. The fiber bundle is positioned on a paper frame with the peeled fiber facing vertically upwards as seen in Figure 4.16.c and d. The peeled bundle surface is thus oriented towards the upper face of the cardboard frame, making future observations easier. The peeling zone's end is positioned at around a millimeter away from the lower frame border, offering a consistent reference position for the end of the peeling zone. The ends of the bundle are glued onto the cardboard frame. The elementary fiber is then removed and placed in its own frame. While care is taken to orient the peeled surface toward the upper face of the frame, it is much more difficult than in the case of the fiber. Indeed, the small size and cylindrical nature of the elementary fiber does not offer the operator many points of reference. If the fiber is rotated slightly during manipulation, finding the peeling zone again is close to impossible without powerful microscopy tools.

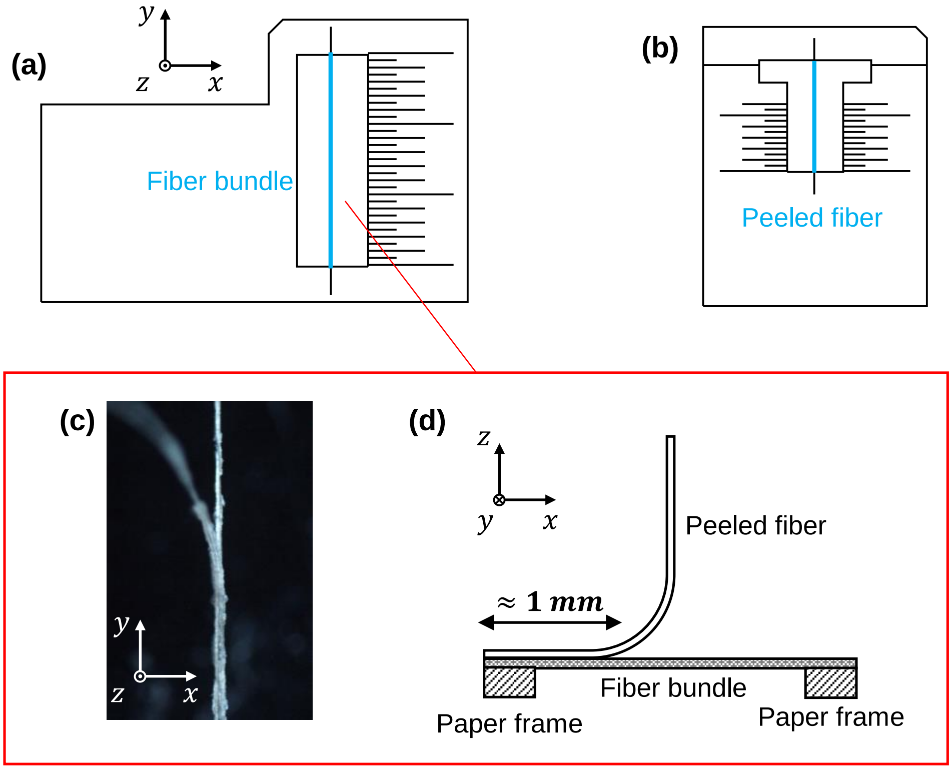

Figure 4.16: (a) fiber bundle and (b) peeled fiber, cardboard supports. Bundles are positioned with the peeled fiber facing upwards as seen (c) and (d). The peeled fiber is then removed and positioned on its dedicated frame.

4.4 Fiber peeling results and discussions

4.4.1 Peeling results - adhesion energy

Typical peeling behavior

Typical elementary fiber peeling behavior is shown in Figure 4.17.a. These results can be compared to those at the stem scale as observed by Réquilé et al. for hemp [Réquilé 18] (see Figure 4.17.b). In the initial peeling stage (stage 1) the force increases as the peeled object gets in tension and deforms elastically. For tests on our experimental setup, the application of a pretension to the elementary fiber before the test starts, to help keep the peeling zone in the field of view of the camera (see section 2.3), means that some of stage 1 occurs during test preparation. As peeling continues, the force increases and a crack between the peeled object and substrate start propagating (stage 2). For plant stems a drop in force (or energy) can be seen at that stage, as the peeled object elastically unloads. This is generally not observed at the elementary fiber scale. Finally, in stage 3, variations in force can be seen as morphological or compositional differences in the interface of peeled object and the substrate cause changes in peeling behavior. These difference are much more pronounced at the fiber scale.

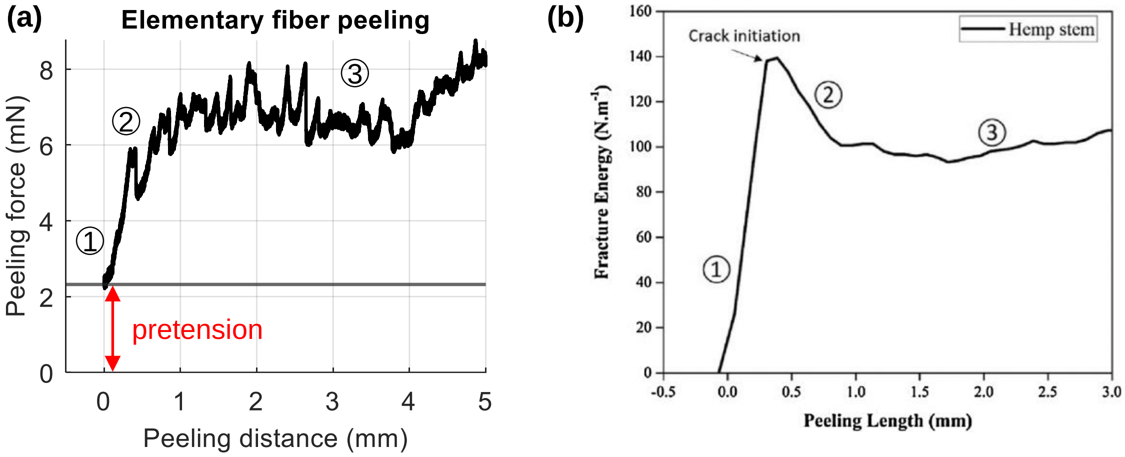

Figure 4.17: Typical peeling behavior at: (a) the elementary fiber scale, (b) the stem scale [Réquilé 18].

Experimental campaign results

The results of all peeling tests for hammer mill and breaking unit separated nettle are presented in Figure 4.18. The peeling force as a function of the peeled distance is represented. All fibers were tested with a speed of $1\,\mu m/s$ over $5\,mm$. The peeled fiber broke in four separate occasions, for fibers separated by HM, before reaching this distance. No rupture was observed for BU fibers.

In most cases the peeling force does not exceed $10\,mN$. The force data is characterized by gradually increases in force, with sudden drop offs. These increases are related to points along the fiber interface that are more difficult to peel. The exact nature of these variations will be discussed in the next subsection (4.4.2). As the peeling reaches these "hard points", peeling can momentarily stop, or stutter until the fiber separates from the bundle and a smoother peeling resumes. During these stops, the peeling zone can momentarily get out of the camera's field of view. Observation of the peeling zone can be lost in more extreme cases.

The average adhesion energy γ across all tests and for each decortication method, along with the average peeling force and apparent diameter measurements is given in Table 4.2. The average adhesion energy between fibers that have been decorticated by the breaking unit ($0.27\,mN$) is higher compared to those where a hammer mill was used ($0.22\,mN$). HM fibers thus seem easier to separate, attesting to a higher degree of elementary fiber individualization within the bundle or potentially some fiber bundle damaging. Indeed fiber rupture only occurred for HM fibers, pointing to larger damage in the fibers compared to the BU method.

Nevertheless, the overall difference in adhesion energy between the two methods is minor, especially when the standard deviation values are considered. Therefore, BU fibers are almost as easy to separate as HM fibers. Using the breaking unit for fiber decortication

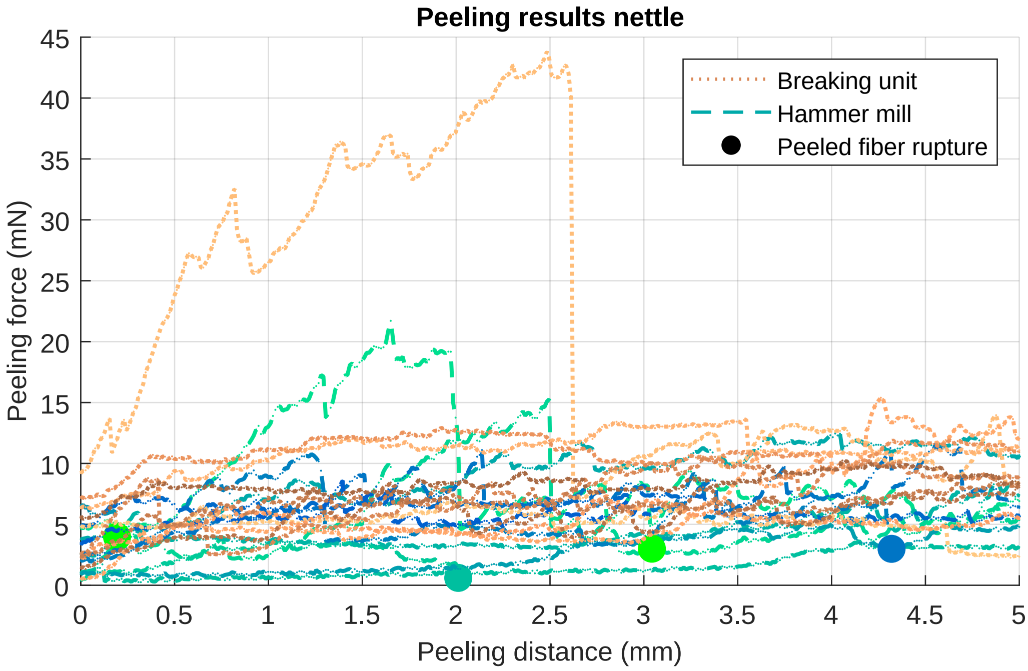

Figure 4.18: Results of peeling test campaign on hammer mill and breaking unit decorticated nettle fibers.

can thus produce a quasi-equivalent level of elementary fiber individualization compared to the hammer mill while using a less aggressive approach, limiting the risk of fiber damage. In any case these measurements, represent to authors knowledge, the first direct measurement of plant fiber interfacial adhesion properties.

Decortication process	Adhesion energy γ $(mN/\mu m)$	Peeling force F (mN)	Apparent diameter D (μm)
Breaking unit	0.27 ± 0.14	7.80 ± 0.97	34.28 ± 8.92
Hammer unit	0.22 ± 0.10	6.37 ± 0.99	29.10 ± 7.50

Table 4.2: Average value and standard deviation of peeling force, diameter and adhesion energy for each decortication method. 12 samples were tested for the hammer mill and 10 for the breaking unit.

4.4.2 Fracture mechanisms classification

Through the outlier detection algorithm, two main rupture mechanisms that cause large changes in peeling force are detected: peeling over kink bands and macrofibril breaking at the interface between the peeled fiber and its bundle. Examples are shown in Figure 4.3.

Kink bands are local defects along the fiber length, often accompanied by changes in MicroFibrilar Angle (MFA) (see subsection 1.2.3). While, their observation can be challenging with the lens used in the current peeling setup, kink bands can be seen however as spots along the peeled fiber, that are larger and darker compared to the rest of the fiber (see Figure 4.19.a). During the test, a noticeable stutter can be seen when the peeling reaches these spots, with decohesion momentarily stopping and the peeling force increasing, before the peeled fiber suddenly separates again and peeling resumes.

To the authors knowledge, the macrofibril breaking mechanism has never been observed before. These objects, with diameters in the order of 1 to 5 μm, are seen bridging the interface between the peeled fiber and its bundle (see Figure 4.19.b). As the fiber keeps getting pulled by the microgripper, they elongate increasing the value of the peeling force. The exact nature of these macrofibrils is difficult to determine. Cellulose mesofribrils are characterized by diameters of a few hundred nanometers [Güven 16] (see subsection 1.2.3). Observed macrofibrils could thus potentially be an assembly of cellulose mesofibrils. Fine layers of the middle lamella or the compound middle lamella (middle lamella + primary cell wall) could also explain the nature of these objects.

In any case, macrofibril apparition during the test, begs the question: which is the interface that gets separated during plant fiber peeling ? If the observed macrofibrils are pieces of the middle lamella then separation occurs at the elementary fiber interface, with eventually some cell wall layers getting separated from their fiber as well. Let us now consider the case wherethe macrofibrils are cellulosic. Than, the observed peeling phenomena are very unique. As discussed in Chapter 1 a noticeable change in MFA can be seen between the cell wall layers of the fibers, with some fibrils possibly creating bridges between layers [Roland 95]. Peeling might thus occur between the primary and secondary cell wall of the fiber or between layers of the secondary cell wall (S1, S2, S3). If this is not the case, then fibrils must be bridging the gap between elementary fibers across the middle lamella.

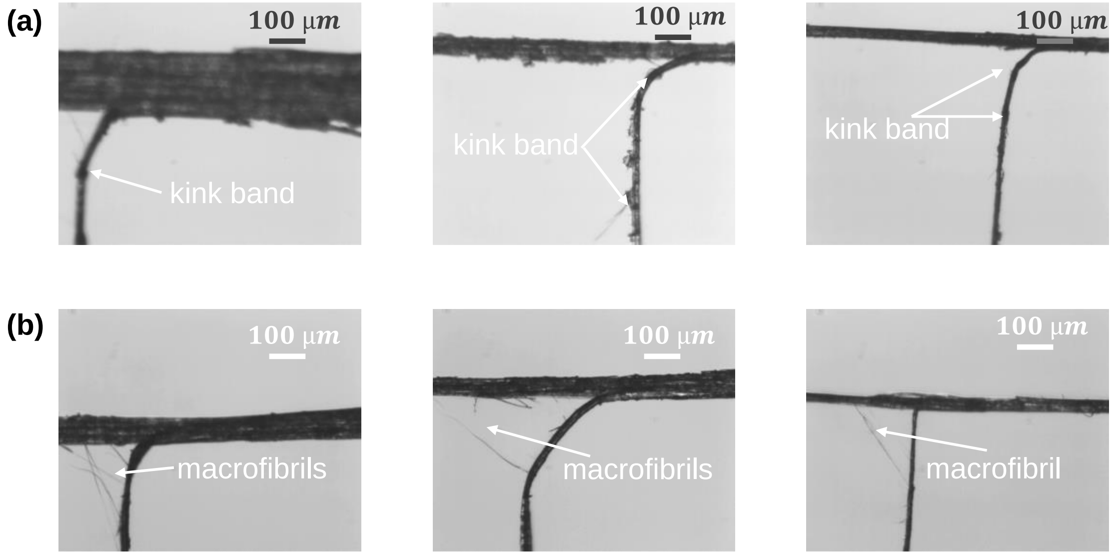

Figure 4.19: Example of common plant fiber rupture mechanisms causing abrupt variation in peeling force: (a)rupture over kink bands seen as larger and darker small spots on the peeled fiber, (b) cellullose macrofibril bridging and braking in the interface between the peeled fiber and its bundle.

Across all tested fibers and drops in peeling force that were statistical outliers, 24 force changes were classified as kink band related (11 for BU and 13 for HM fibers) and 10 as macrofibril related (5 each for BU and HM fibers). Table 4.3 shows the drop in force (ΔF)

resulting from these phenomena. On average the ΔF for kink bands is in the order of $1\,mN$ while for the cellulose macrofibrils it is around half that value at $0.52\,mN$. ΔF can be interpreted as the force that must be added to the baseline force that causes the peeling of the interfiber surface, in order to break the macrofibrils or overcome the adhesion at the kink bands. To the author's knowledge no other such measurement can be found in the literature. Diving ΔF by the according surface area of these objects would result in a measurement of their strength. While an estimation of kink band strength is difficult, knowing that the observed macrofibril diameters are around 1 to $5\,\mu m$ (see Figure 1.6), by considering them as cylinders of circular cross section, their ultimate strength can be estimated at 25 to $650\,MPa$.

	Force drop after breaking ΔF (mN)	
Decortication method	Kink bands	Fibril bridging
Breaking unit (BU)	0.42 ± 0.32	0.25 ± 0.08
Hammer mill (HM)	1.51 ± 3.02	0.78 ± 0.86
Global average	1.01 ± 2.26	0.52 ± 0.64

Table 4.3: Peak force and force drop related to peeling over kink bands and cellulose fibril breaking for different decortication methods of nettle.

When comparing the values of ΔF between the two decortication methods, values are significantly higher and more variable for HM fibers compared to the BU ones. The reasons behind this are still unclear.

Of course, many other instances of kink band and macrofibril breaking might have occurred during peeling tests, however they must have produced smaller changes in force, which were not statistical outliers. Such cases are more probable for macrofibril bridging, where only the breaking of largest ones might be easily detectable, in terms of visual observation or force measurements. Finer macrofibrils, or mesofibrils, must have a lower impact on the peeling force, making semi-automated detection difficult.

Overall, the presence of kink bands and macrofibril bridging causes a significant increase in the force needed to separate the plant fiber surfaces. Furhter investigation and understanding of these mechanisms could provide the basis for biomimetic approaches, to reproduce such natural adhesion mechanisms in engineered materials.

4.4.3 Microscopic observations - additional characterization perspectives

In order to better understand the mechanisms that take place during plant fiber peeling, SEM observations were performed at the INRAE BIA facilities in Nantes, France. A single bundle-peeled fiber sample was observed, resulting from a series of preliminary peeling tests. Observations were performed separately on the bundle and the peeled fiber, seen in Figure 4.20.

When observing the fiber bundles an apparent track which could have been left behind by the extraction of the peeled fiber is observed (see Figure 4.20.a). Signs of macrofibrils on the peeled surface can also be seen (see Figure 4.20.a). Observation on the peeled

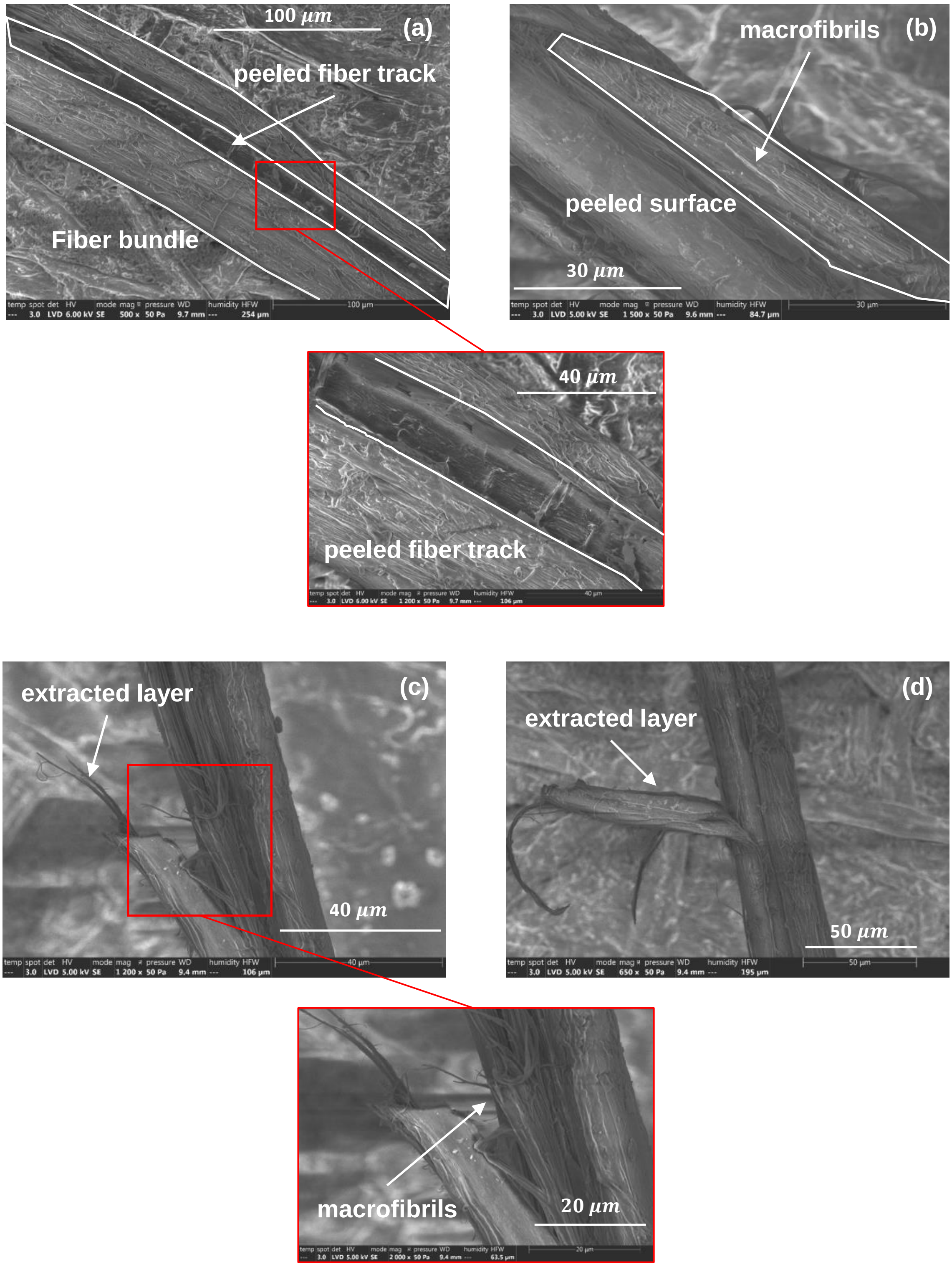

Figure 4.20: SEM observations of nettle fiber bundle peeled zones: (a) apparent track left by the extraction of the peeled fiber, (b) signs of fibrils on the peeled surface. Observations on the peeled fiber: fiber layer separation (c and d) and fibrils (d) can be seen.

fiber reveal an extracted layer that is still attached to the fiber in some places (see Figure 4.20.c and d). Signs of macrofibrils are also seen (see Figure 4.20.c).

X-ray tomography was also performed in the FEMTO-ST institute (*MYPHISTO*) in

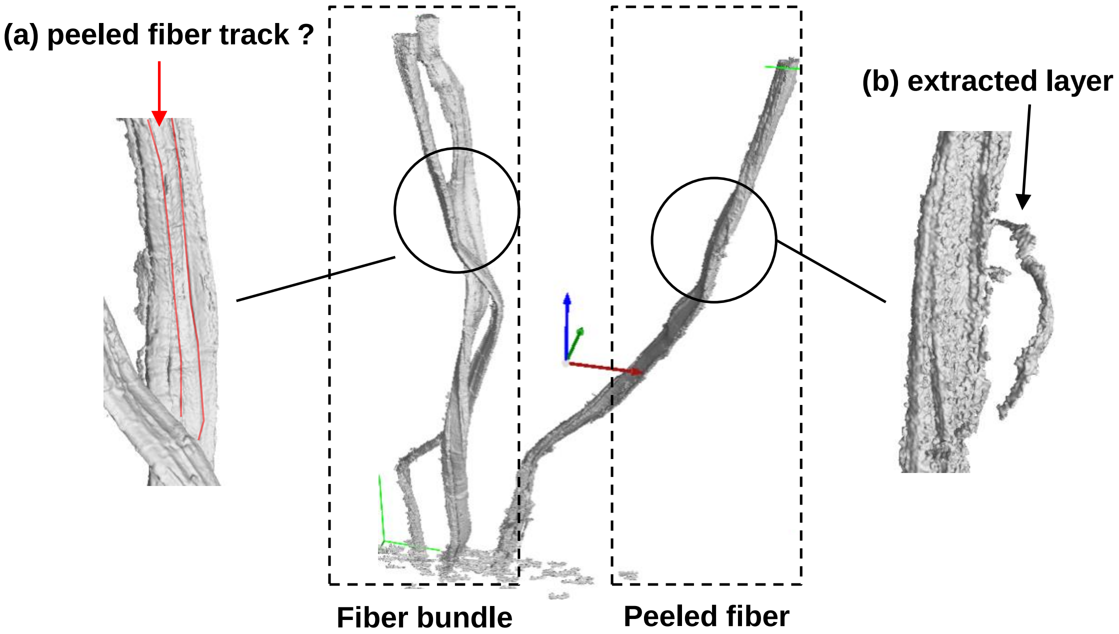

Figure 4.21: X-ray microtomography of fiber bundle and peeled fiber. The fiber bundle separated during tomography preparations. (a) Potential track left behind by peeled fiber, (b) semi-detached fiber layer.

Besançon ,France, on a different peeled sample. Similar features were observed in the reconstructed geometry with potential peeling tracks observed on the bundle (see Figure 4.21.a) and traces of semi-detached layers on the peeled fiber(see Figure 4.21.b).

To discover the exact nature of the bridging macrofibrils and which are the fiber layers that get separated during, Raman spectroscopy can be used [Gardiner 89]. Through this technique, the molecules present in the tested sample can be detected, allowing the determination of its structural fingerprint. By using Raman spectroscopy on the peeled surface of the bundle and elementary fiber the presence of cellulose, hemicellulose, lignin or phenolic compounds could be identified. According to the detected biochemical composition, the nature of the studied object could be determined.

4.5 Conclusions and perspectives

In this chapter, the adhesion properties of the interface between plant fibers was studied experimentally with the use of a newly designed micromechatronic setup. This setup allows the peeling of an elementary fiber from its bundle and the measurement of the associated force, while maintaining the peeling angle close to 90° and offering an observation of the decohesion zone throughout the test. A series of peeling tests on nettles fibers produced the following main results:

- the adhesion energy of the fiber interface was determined for the first time. These measurements allowed the comparison of two different decortication methods.
- fiber separation over kink bands and macrofibril bridging and breaking at the fiber interface were observed for the first time. These mechanisms were shown to increase

the strength of the fiber interface. The resulting increase in peeling force to overcome them was quantified.

- SEM imagery and X-ray microtomography were used to observe the peeled surfaces, showing visible separated layers and fibrils.

The samples were saved in a way that allows further investigations, new mechanisms of natural adhesion and fiber separation in bast fibers could thus be discovered. The experimental setup and protocol will also allow the study of the influence of many other parameters on interfiber adhesion such as retting, plant variety, extraction processes, MFA and more. These peeling tests can thus actively contribute in the development of fiber production chains that offer high quality plant fiber, composite reinforcements, by helping the optimization of fiber separating procedures through direct adhesion measurements.

Many improvements can also be made to significantly increase the accuracy of the adhesion measurements:

- the measurement of contact width between the separating surfaces during peeling can be significantly improved. The current apparent diameter measurement is a first approximation allowing the calculation of adhesion energy, however an additional camera observing directly into the peeling zone would improve contact width measurements greatly. First attempts were made during this thesis work, however the dynamic nature of the peeling tests makes observations very difficult. Observations of the peeling zone after the test, could also be used to perform these measurements. Finally, performing the peeling test in-situ would provide great morphological characterization abilities however, the setup would need to be miniaturised to achieve them.

- the peeling model used to calculate adhesion energy could be enriched to account for more of the various parameters that could impact interfiber adhesion. Models found in the literature for ideal objects could be adapted for plant fibers to account for parameters such as of the properties of the peeling substrate [Lamblet 07], peeling velocity [Choi 08], viscoelasticity [Kim 88, Chen 13], preload [Chen 09], friction [Tian 06] or microfibrillar angle. Finite element analysis could also be used to simulate the peeling of complex geometries or to account for plastic deformations [Crocombe 82, Hadavinia 06].

- similarly to the single fiber compression setup presented in Chapter 3, a custom chamber could be built for the peeling setup to allow for an active relative humidity control during peeling tests.

- the influence of fiber bundle tension on the measured adhesion properties could be studied.

GENERAL CONCLUSIONS AND PERSPECTIVES

General conclusions and contributions

This doctoral thesis is positioned in the context of the growing need and demand for sustainable and environmentally friendly materials. Plant Fiber Composites (PFC) have become a major driving force towards the adoption of such materials. The main goal of this PhD work, consisted in characterizing previously unknown plant fiber mechanical properties, to actively contribute in the design and development of new high performance PFCs. Through a literature review, a plethora of plant fiber tensile properties characterization was evidenced in contrast to a complete lack of transverse properties. The importance of fiber separation for composite performance has also been identified as a major indicator of PFC performance, however the complex process of fiber extraction still relies on subjective and organoleptic criteria to evaluate interfiber adhesion.

This thesis presented for the first time, a study of plant fiber transverse behavior and interfiber adhesion through tests at the elementary fiber and bundle scale, using innovative micromechatronic setups, developed especially for this application.

Single fiber transverse properties

Plant fiber transverse behavior was studied through the Single Fiber Transverse Compression Test (SFTCT). A critical review of existing experimental platforms was performed identifying several key limitations. A new micromechatronic setup was developed offering major advances in terms of measurement accuracy, system compliance, relative humidity control and observation capabilities. The major influence of platen parallelism on compressive property characterization, was also quantified for the first time (error over 30% on E_T for 1° angle) and a new method to control it was proposed (sub 0.1° accuracy). This unique setup allowed the study of plant fiber compressive behavior. The transverse elastic modulus of plant fibers was characterized through direct fiber testing for the first time, showing a highly anisotropic fiber nature, with a stiffness that is comparable to synthetic fibers $(1 - 2\,GPa\ )$. The intricate nature of plant fiber compressive behavior was also approached with Finite Element Analysis (FEA). The influence of fiber morphology and material behavior was studied and the limitations of SFTCT analytical models were identified. Hybrid approaches employing microscopic observations, finite element analysis and neural networks were shown to have significant potential in the mechanical characterization of complex objects such as plant fibers. Overall, this newly found knowledge, on plant fiber transverse properties should significantly improve the design and modeling of plant fiber composites.

Interfiber adhesion properties

Interfiber adhesion was studied through peeling of an elementary fiber from its bundle. A new micromechatronic experimental setup was developed for this purpose. The energy needed for the separation of the elementary fiber was calculated for the first time. Previously unknown fracture mechanisms were also observed, offering a new perspective on natural adhesion mechanisms and new insights into the fiber layer separation that takes place during extraction. Indeed, kink bands and macrofibrils were shown to increase the strength of adhesion between fibers and the force needed to break them was quantified. Finally, microscopic observations offered a close look at the structurally rich and complex peeled interface. A sample saving protocol was proposed to make such observations easier and more reliable in the future. Overall, the characterization of plant fiber adhesion properties should help the optimization of fiber extraction processes by providing an accurate way to compare fiber separation as a function of plant variety, retting level, decortication process and more. Well separated fibers will thus be easier to obtain, increasing the mechanical performance of the composites they will reinforce.

Experimental platform development and maturation

This thesis work contributed in the creation and the maturation of innovative experimental platforms. Work on a microcompression experimental setup had began a few years before the start of this thesis. The Technological Readiness Level (TRL) of this setup could be characterized by a level 3 [Mankins 09], since it represented an experimental proof of concept, with a small number of performed tests and little to none validation procedures. Throughout this thesis significant time, material and labor investments were made to facilitate the use of the platform, develop experimental protocols and finally, quantify and validate its performance. It was also used to perform a first experimental campaign, placing it at the end of this thesis at a TRL of 4 to 5, as a platform validated in lab environment and used in its relevant setting. The setup was also recently made part of the micro and nanorobotics center (*μROBOTEX*) of the *FEMTO-ST* institute, part of the wider French *ROBOTEX* network, offering compression characterization to the industry. A new PhD thesis plans to push the setup's TRL even further focusing on the automation and eventual commercialization of the setup. Finally, a new experimental micro-peeling setup was also designed, fabricated and used in a lab environment during this thesis. Its proof of concept has been demonstrated, and a few additional validation procedures would place it at a TRL of 4.

Perspectives

The presented work can constitute the foundations of many future developments, in the field of compression and peeling but also in the wider scale of plant fiber characterization. Some of these perspectives and future works are discussed below.

Single fiber transverse compression

The current SFTCT setup would allow for the study of the influence of Relative Humidity (RH) on the transverse properties of plant fibers. A fine control of temperature would also minimize small measurement deviations, unlocking the ability to characterize the viscoelastic behavior of plant fiber through creep tests. The compressive failure, or the fatigue of plant fibers can also be studied. Compression of fiber bundles or other microscale objects would also be possible, expanding the characterization of transverse properties to new fiber scales or research domains. An alternative to tilt angle control, by accounting it in analytical models is also possible, making accurate transverse compression more accessible. Finally, Finite Element Analysis (FEA) can greatly expand transverse property characterization. Complex 3D geometries and behavior laws, structural defects, starting fiber position and more could all be modeled and studied expanding our knowledge and understanding on the subject.

Plant fiber peeling

Similarly to compression experiments, the influence of RH on fiber adhesion properties could be studied, provided a testing chamber with active RH is made for the peeling setup. Analytical peeling models accounting for more parameters (substrate properties, pretension, peeling speed and more) could be adapted to plant fiber peeling, improving adhesion calculation precision and opening the way to new characterizations. Morphology, microstructure and material behavior could also be modeled and studied, notable through FEA. Microscopy and spectroscopy studies should also improve our understanding on the separation of bundles into elementary fibers. Observed natural adhesion mechanisms could form the basis for new bio-inspired adhesives.

Wider outlook on plant fiber characterization

While this thesis focused on plant fiber transverse and adhesion properties, other characterization efforts can also be made. Notably, plant fiber damping properties can be characterized through modal analysis or dynamic loading. When looking at a wider scale however, four major challenges in plant fiber characterization remain:

1. **The number of tested samples.** Given the natural variability of plant fiber properties, a large number of fibers should be tested to reduce the uncertainty on their mechanical properties. This can only be realistically achieved through the automation of the testing process. Major contributions from the fields of automation, control and microrobotics are needed to achieve this.

2. **Fiber manipulation.** The manual handling of plant fibers during the testing preparation stages can introduce defects and damage the fibers, causing a subsequent underestimation of their mechanical properties. On the other hand, a measurement bias can also be introduced, as weaker fiber who tend to break during preparation will not be tested. For this reason, advances in fiber manipulation should be made to prepare fibers in a way that is delicate and precise while also being more repeatable, eliminating operator influence on the preparation procedure.

3. **Fiber morphological characterization.** Accurate knowledge of fiber morphology greatly increases the understanding of its mechanical behavior, while also improving accuracy in the characterization process. Scanning electron microscopy or X-ray tomography offer great characterization accuracy, albeit with a limited space to place samples. This makes *in situ* testing with conventional experimental setups impossible, while moving the fiber between testing and microscopy devices increase the risk of damaging them. Therefore, the miniaturization of mechanical testing apparati, should be explored, allowing for parallel observation and testing of the fiber *in situ*.

4. **Plant fiber behavior modeling.** The complex morphology, structural organization and biochemical composition of plant fibers, makes the modeling of their behaviors extremely complex. Analytical models of increased complexity can be developed to model these parameters, their complex interactions however can cause

> major modeling difficulties. FEA can be used to remedy this to some extent. Mechanical testing of fibers with complex geometries and material behavior can be simulated, as complexity increases however, so does the computation time and cost. Phenomenological approaches can be used, they require however a great number of experimental testing to create robust models. Data-driven approaches can breach the gap between analytical, numerical and phenomenological modeling. Experimental datasets can be created with a few well-chosen experiments and expanded on through FEA, while analytical approaches can be used to construct indicators. The combination of all these data can feed machine learning algorithms, providing models of plant fiber behavior that should be unmatched in terms of richness and complexity at the expense of some transparency due to their "black box" nature.

Overall, plant fiber characterization is a complex subject requiring the synergy of many scientific fields to explore nature's finely optimized structural reinforcements. Their environmental and mechanical potential however, are worth the efforts of the scientific community, as they can form the basis of what a modern, state of the art material should be: high performance and environmentally friendly.

A

ADDITIONAL SFTCT MODELING ELEMENTS

A.1 Analytical-finite element model comparison

In this section the ability of SFTCT analytical models to identify the transverse elastic modulus E_T of a fiber is evaluated through finite element analysis data. The 2D quarter fiber finite element model presented in section 2.3 is used. The model identification accuracy is evaluated by the relative difference between the transverse elastic modulus defined in the Finite Element Model (FEM) and the one identified by the analytical model based on FEA results, named ΔE_T. The least square residual of the identification is also considered. More details on this process are given in 2.3.1. Results are presented in Table A.1.

Model	$\boldsymbol{\Delta E_T}$**(%)**	**Residual (nm)**
Cheng	-9.32	0.98
Cheng $b \ll R$	-7.32	0.87
Morris	-7.88	0.87
Lundberg	-0.17	0.45
Phoenix	-0.13	0.44
Phoenix $b \ll R$	1.28	0.42
Jawad	$-3 \cdot 10^{-4}$	0.43
Jawad $b \ll R$	$-6 \cdot 10^{-5}$	0.44
Foppl	5.48	0.48
Sherif	12.13	0.45
Anazodo (small strain)	-12.10	-
Anazodo (large strain)	38.06	-

Table A.1: Results of inverse identification on finite element simulation data for different SFTCT analytical models.

It can be seen that regardless of simplifying hypotheses, Jawad's model leads to the lowest value of ΔE_T, followed by Phoenix's and Lundberg's models. The rest of the models lead to larger ΔE_T values, their predictions are thus different from the one of the simulation. An underestimation of E_T ($\Delta E_T < 0$) occurs with models with a stiffer response (Cheng, Morris) and an overestimation with models with a less stiff response (Foppl, Sherif) (see Figure 2.3). The values of the least-squares residual are comparable between all models except for Cheng and Morris who produce higher values. Their ability to reproduce the simulated behavior is thus worse.

For the Anazodo models the contact arc length s is calculated from U/R data. Then a value of E_T is calculated directly for every force and displacement data point. These

E_T values are then averaged to give a single prediction, which is used to calculate ΔE_T. Since no inverse identification takes place, no residual is calculated.

The SFTCT model chosen for all studies in this work is Jawad's since it produces a result that is very close to the simulations.

A.2 Domain of validity of analytical model simplifying hypotheses

The goal of this section consists in providing a framework to determine if a simplifying hypothesis can be used on the analytical model, given the studied fiber type. To do so the difference between the displacement calculated with the original ($U_{original}$) or simplified Jawad model ($U_{simplified}$) is calculated, for different combinations of input parameters. This difference is then expressed as a percentage of the fiber radius R to assess if it is significant or not. The resulting parameter will be named ΔU .

$$\Delta U = \frac{|U_{original} - U_{simplified}|}{R} \tag{A.1}$$

A.2.1 Contact width simplification

As seen in equation 2.6 the contact half width b is a function of the force per unit length F_L, the fiber radius R and the material properties E_T, E_L, ν_{LT}. The sensitivity analysis performed by [Wollbrett-Blitz 16] showed that the parameters E_L and ν_{LT} have a minimal influence on the fiber's transverse displacement. There is no reason to assume this is not the case for b. For this reason, in the study of contact width simplification these parameters are fixed at $E_L = 50\,GPa$ and $\nu_{LT} = 0.4$. The applied force will have a major impact on the contact width during transverse compression. However all models are derived with a purely elastic and small strain assumption. Studying the contact width under very high levels of force, which would lead to large strains and inelastic phenomena, is thus not justified. For this reason F_L will be fixed at $350\,mN$, the maximum level of force attainable with our experimental setup (see Chapter 3). Therefore, ΔU is evaluated as a function of R, with values between $1\mu m$ and $100\mu m$, and E_T with values between $100\,MPa$ and $10\,GPa$.

Isovalues of ΔU as a function of R and E_T are given in Figure A.1. Larger and stiffer fibers results in very low values of ΔU, the outputs of the original and simplified model are thus very close. For smaller and less stiff fibers however, the difference can go over 1%. Given the difficulty to obtain accurate measurements at the fiber scale, a difference of this scale resulting only from modeling choices is not negligible.

In conlusion, for fibers such as carbon where $E_T > 2\,GPa$ [Naito 07] the hypothesis could be used without any major impact even for small radii. Caution should be used however for polymer fibers where $E_T < 1\,GPa$ [Stamoulis 07] or even aramid fibers where $E_T \approx 2\,GPa$. This work, will show that the value of E_T for plant fibers is similar to aramid fibers, for this reason the contact width simplification is not used.

A.2.2 High anisotropy simplification

The simplifying hypothesis used in cases of high anisotropy is given in equations 2.25 and 2.26. This simplification is performed on terms that depend only on the fiber's material

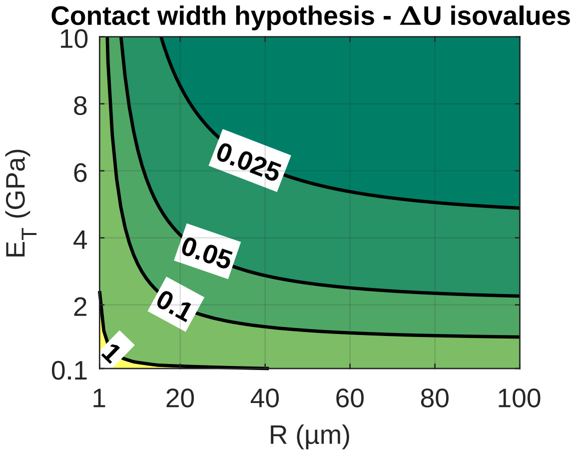

Figure A.1: Isovalues of ΔU (as a percentage) for different combinations of fiber radius R and transverse elastic modulus E_T. A maximum value of 2.8% is obtained for $R = 1\mu m$ and $E_T = 100\,MPa$. A minimum value of 0.01% is obtained for $R = 100\mu m$ and $E_T = 10\,GPa$.

properties. For this reason, in this study of ΔU, the maximum experimentally obtainable force of $350\,mN$ is used along with a radius R of $16\,\mu m$. The sensitivity of the fiber's radial displacement to the ν_{TT} Poisson ratio has been shown to be very weak [Wollbrett-Blitz 16], for this reason it is set at 0.07. ΔU is evaluated as a function of the ν_{LT} Poisson ratio, with values between 0.05 and 0.5, and the anisotropy ratio E_L/E_T, with values between 1 and 50.

Isovalues of ΔU as a function of ν_{LT} and E_L/E_T are given in Figure A.2. Values remain small for the majority of the parameter space. The simplification can be performed without any major differences for anisotropic fibers such as carbon and aramid. However, for fibers with lower anisotropy ratios and higher values of ν_{LT}, such as polymer fibers [Placet 20], caution should be employed in the use of this simplification. In the case of plant fibers, this work will show that anisotropy ratios are high, in the range of 30, the high anisotropy simplification can thus be used.

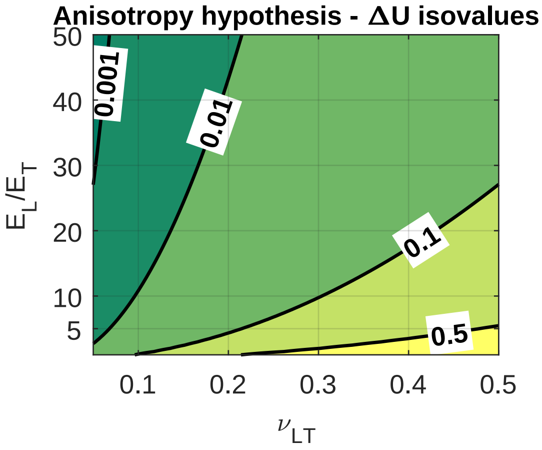

Figure A.2: Isovalues of ΔU (as a percentage) for different combinations of Poisson ratio ν_{LT} and anisotropy ratio E_L/E_T. A maximum value of 12.5% is obtained for $E_L/E_T = 1$ and $\nu_{LT} = 0.5$. A minimum value of $5 \cdot 10^{-4}$% is obtained for$E_L/E_T = 50$ and $\nu_{LT} = 0.05$.

A.3 Comparing σ_{yy} and T_{n_y} integrations

In analytical SFTCT models, the force per unit length is typically obtained by integrating the vertical stress component along the contact width as follows:

$$F_L = \int_{-b}^{b} \sigma_{yy} dx \tag{A.2}$$

Through finite element analysis however, the contact half width b cannot be known precisely in advance. For this reason a potential contact zone of width $2Rcos(\pi/3)$ was defined in the finite element model. In the finite element model the integration performed is thus :

$$F_L = \int_{-Rcos(\pi/3)}^{Rcos(\pi/3)} \sigma_{yy} dx \tag{A.3}$$

If vertical stresses occur outside of the actual contact half-width they will also be integrated causing an error in the estimation of the contact force per unit length. While these errors are small for a circular geometry, for more complex geometries the errors can be larger. Integrating the vertical component of the contact pressure T_{n_y} offers an alternative to this issue. Figure A.3 shows the distribution of σ_{yy} and pressure T_{n_y} over the defined contact zone for $0 \leq x \leq Rcos(\pi/3)$ (the 2D quarter fiber finite element model presented in section 2.3 is used.). T_{n_y} is calculated only within the contact half width, resulting in positive values with zero values outside of it. σ_{yy} has both positive and negative values, as well as non-zero values in zones where T_{n_y} is zero. Its positive values are also higher overall compared to T_{n_y}. These differences are reflected in ΔE_T and the residual as seen in Table A.2. Both are higher when the force per unit length, that is given to the analytical model for inverse identification, is a result of an integration of σ_{yy}. Values for a force integrated from T_{n_y} are very small, attesting to a very close result with analytical predictions. For this reason T_{n_y} is used in all presented studies. The following statement can be made:

$$F_L = \int_{-b}^{b} \sigma_{yy} dx \cong \int_{-Rcos(\pi/3)}^{Rcos(\pi/3)} T_{n_y} dx \tag{A.4}$$

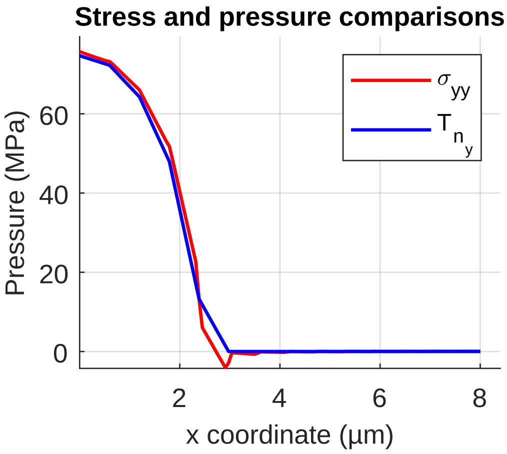

Figure A.3: Vertical stress σ_{yy} and vertical component of contact pressure T_{n_y} over the defined contact zone.

Integrated parameter	$\Delta E_T (\%)$	Residual (nm)
σ_{yy}	0.92	0.62
T_{n_y}	$-3 \cdot 10^{-4}$	0.43

Table A.2: Comparison of σ_{yy} and T_{n_y} integrations.

A.4 Mesh element quality and accuracy

To choose the best suited element type for SFTCTs four different meshes are compared. A mesh with triangular elements, free and mapped quadrilaterals and finally a mix of mapped quadrilaterals and triangular elements are compared. The element size is set at $R/26$ for all elements.

The values of ΔE_T and of the least-squares residual are given in Table A.3 for each element time, along with the number of degrees of freedom and the computation time. Triangular elements lead clearly to the lowest value of ΔE_T, with the rest of the meshes yielding similar results. In terms of residual, structured quadrilaterals lead to the lowest value with others being very similar. A small gain in computation times is gained with quadrilateral elements since they result in a lower number of degrees of freedom. While the amount of saved time is small in these 2D studies they could become more important for 3D models.

Element type	Degrees of freedom	CPU time (s)	$\Delta E_T (\%)$	Residual (nm)
Free triangular	6549	13	$-3 \cdot 10^{-4}$	0.43
Free quadrilateral	4431	11	-0.059	0.3963
Structured quadrilateral	4933	11	-0.037	0.0381
Mixed	5989	12	-0.074	0.3815

Table A.3: Element type comparison.

Mesh quality is evaluated by *COMSOL* with a skewness criterion (the closest to 1 the better). Figure A.4 illustrates this mesh quality assessment for the different studied meshes. Triangular elements and the mixed mesh lead to the best results. Quadrilateral elements result in a lower average quality. Mapped quadrilateral elements especially lead to zones of low quality, since the cannot easily adjust to the circular geometry.

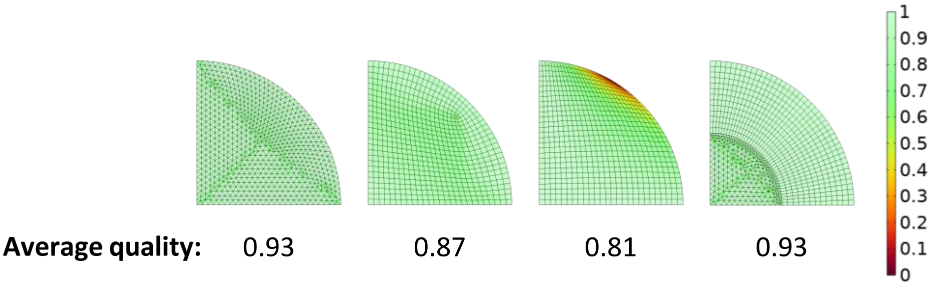

Figure A.4: Skewness mesh quality for triangular, free quadrilateral, mapped quadrilateral and mixed elements.

Overall the differences between different element types remain small for all compared criteria. However some choices can still be made. The mixed element mesh offers no improvement in terms of accuracy or quality, but requires a time consuming manual adjustment of the mesh for each fiber geometry. It will thus not be used. The mapped quadrilateral elements did results in the lowest residual, however, they produce some low quality mesh zones and average ΔE_T values. For this reason they will also be excluded. Free quadrilateral offer a gain in computation time in the expense of some mesh quality and identification accuracy. Triangular elements are thus the best choice. They easily adapt to all geometries producing high quality meshes while also remaining accurate.

A.5 Choice of viscoelastic model

In their simplest form stress relaxation and creep behavior can be represented by the changes illustrated in Figure A.5. Under a constant strain (or displacement) stresses gradually relax with an exponential decrease. With a constant stress (or force) strains increase at a decreasing rate, approaching an asymptotically steady state. To represent this material behavior viscoelastic models can be used. These models are represented by a combination of springs, of elastic constant E, and dampers characterized by a viscosity constant η ($Pa \cdot s$). The simplest viscoelastic models are result of a combination of one of each of these elements either in series, known as the Maxwell model, or in parallel, known as the Kelvin-Voigt model, as seen in Figure A.6. Their governing constitutive relations are derived from the laws of mechanical elements in series or in parallel and can be written as follows, considering a solid isotopic material:

$$\text{Maxwell model}: \frac{\dot{\sigma}}{E} + \frac{\sigma}{\eta} = \dot{\varepsilon} \tag{A.5}$$

$$\text{Kelvin-Voigt model}: \sigma = E\varepsilon + \eta\dot{\varepsilon} \tag{A.6}$$

By solving the differential equations it is possible to study the material response as a function of time. For the Maxwell model:

$$\sigma = \sigma_0 e^{-\frac{t}{\tau}} + \eta\dot{\varepsilon}(1 - e^{-\frac{t}{\tau}}) \tag{A.7}$$

$$\varepsilon = \varepsilon_0 + (\frac{\dot{\sigma}}{E} + \frac{\sigma}{\eta})t \tag{A.8}$$

For the Kelvin-Voigt model :

$$\sigma = E\varepsilon + \eta\dot{\varepsilon} \tag{A.9}$$

$$\varepsilon = \varepsilon_0 e^{-\frac{t}{\tau}} + \frac{\sigma}{E}(1 - e^{-\frac{t}{\tau}}) \tag{A.10}$$

with $\tau = \eta/E$ the relaxation time (for stress relaxation tests) or retardation time (for creep tests).

Each of these models is better suited for one type of quasi-static test. The Maxwell model predicts an exponential decrease (relaxation) of the stress when subjected to a constant strain (cf. equation A.7). Under a constant stress however the strain keeps increasing linearly as a function of time, which does not represent realistic material behavior under these conditions (cf. equation A.8). For this reason the Maxwell model is

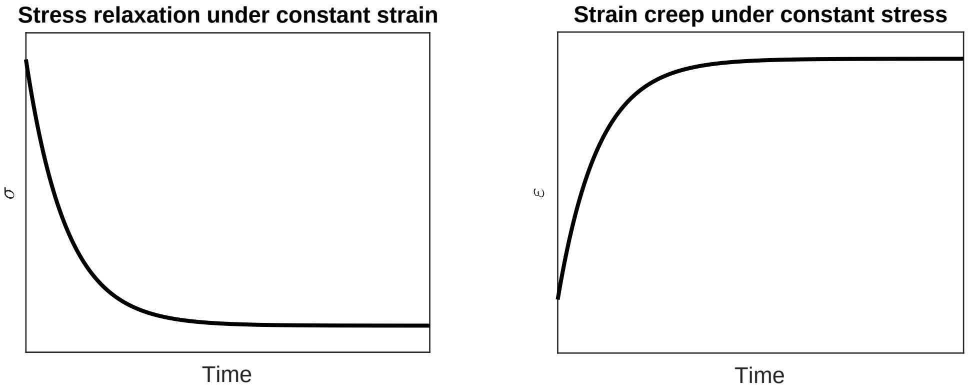

Figure A.5: Simplest stress relaxation and creep behavior.

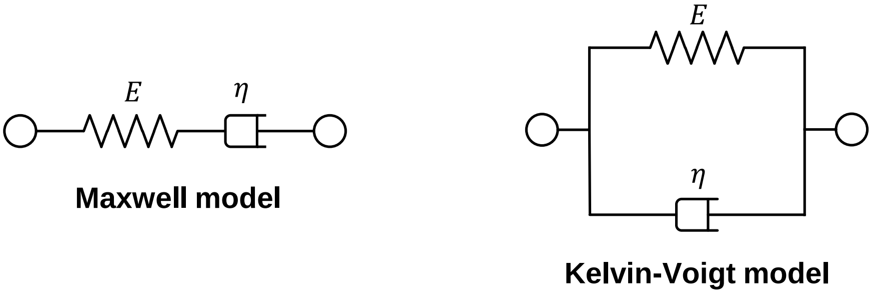

Figure A.6: Schematic representation of simple viscoelastic models.

well suited to stress relaxation tests but not creep tests. In the case of the Kelvin-Voigt model, under a constant stress, strains gradually tend towards the value of a purely elastic strain σ/E with a decelerating rate (cf. equation A.10). At a constant strain however, stresses increase linearly in pure elastic manner (cf. equation A.9). For this reason the Kelvin-Voigt model is adapted to the prediction of creep behavior.

Often material viscoelastic behavior can be much more complex than the simple cases illustrated in Figure A.5. This is the case for plant fibers, knowledge however on the underlying mechanisms is still poor. Additional springs and dampers can be added in series or in parallel to the models in order to describe these complex phenomena. The association between elements and the properties of each spring or damper might be very different between plant species and fiber micro-structure. For this reason a more general approach will be used in the context of this study. A simple viscoelastic model will be used with a single spring and a single damper. This viscous constant will be varied along a large range of values. The impact of fiber viscosity on the material response of a fiber under transverse compression will thus be studied along a wide range of possible viscoelastic behaviors.

The used finite element model imposes the upper platen displacement in order to compress the fiber. For this reason we will use the Maxwell model. A simple analogy can be made to justify this choice. We saw that the Maxwell model is best suited for relaxation tests, where strain is imposed. In terms of loading conditions imposed displacement and imposed strain are analogous. The constitutive relations can also be used to understand this choice. Under a constant strain increase rate, for the Kelvin-Voigt model, the resulting stress would be the result of the addition between the elastic part and the viscous part of the model as seen in equation A.10. The overall stress would thus be higher than a pure elastic material and change linearly. For the Maxwell model however, a non-linear response with lower stress levels than a purely elastic response are obtained. The comparison between the two viscoelastic models and a purely elastic one for a strain increasing at a constant rate can be seen in Figure A.7. For the loading conditions that are used in this study, the Kelvin-Voigt response is clearly not a realistic material response contrary to the Maxwell model.

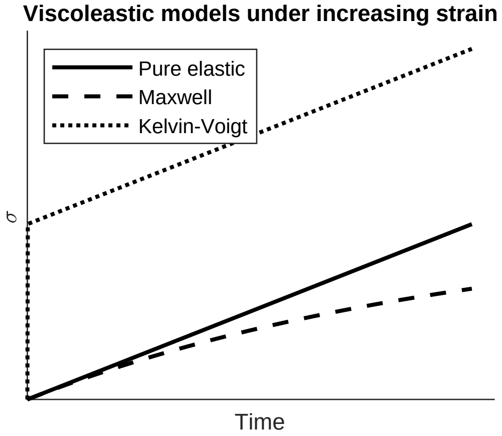

Figure A.7: Comparison of simple viscoelastic and purely elastic models under an constant strain increase rate.

B

ADDITIONAL ELEMENTS ON SFTCT EXPERIMENTAL DEVELOPMENT, VALIDATION AND RESULTS

B.1 Contact detection

As long as the sensor is not in contact with an object the vertical coordinate of the dependent and independent HP code must be roughly the same (given some noise and angle within the camera frame). The relative displacement between the two is thus close to zero, $\Delta Y \simeq 0$. As soon as contact occurs the sensor's beams start deforming and a relative displacement appears between the two parts of the sensor $\Delta Y > 0$. To detect the point at which contact occurs a robust method that is not sensitive to sensor noise is necessary.

In an ideal case, ΔY can be represented by a section with two linear parts: one that is constant and equal to zero as long as no contact occurs and one that is increasing with a constant slope when compression takes place. The function can be written as:

$$f(t) = max(0, ct + a) \tag{B.1}$$

with: t the time, c the slope and a the point where the function intercepts the x axis. Through a least squares regression, the coefficients c and a are identified and the function f is fitted to experimental ΔY data. By calculating the second derivative of f a Dirac function is obtained with its maximum at the point of contact. An example of experimental data, fitted function and detected point is given in Figure B.1. This fitting and deriving procedure thus enables to detect the contact in a robust way without being influenced by noise or moments of bad HP code detection.

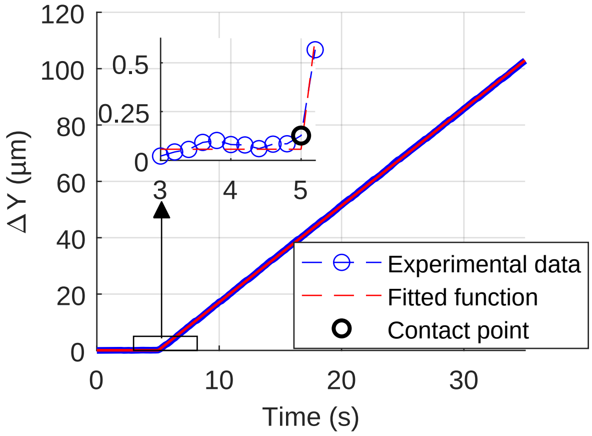

Figure B.1: . Contact detection through linear segment fitting and derivation.

B.2 Stiffness determination with finite element analysis - detailed model

In this section, finite element analysis is used to determine the compressive and torsional stiffness of the FU sensor.

To do so, the CAD model of the sensor is loaded into *COMSOL Multiphysics*® (see Figure B.2). Since the sensor thickness ($500\,\mu m$) is small compared to its dimension along the y and z axis ($16.8\,mm$ and $15.1\,mm$), a 2D plane stress model can be used. The sensor material is modeled as linearly elastic with a Young's modulus of $E = 169\,GPa$ based on values given by Hopcroft et al. [Hopcroft 10]. The displacement of the sensor around its 2 mounting holes, located on the uppermost part, is blocked. To simulate sensor compression a vertical load, F_{comp}, is applied to the sensor tip along the $-y$ direction. An amplitude of $350\,mN$ is chosen, since it results in a quasi-total deformation of the sensor, with the HP codes almost reaching the end of their $500\,\mu m$ clearance. To simulate sensor torsion an horizontal load, F_{tors}, is applied to the sensor tip along the x direction. The same amplitude as compression tests is used. The load is applied with 20 increments to provide multiple data points. The boundary conditions of the simulation along with the sensor deformed shape at $F_{comp} = 350\,mN$ are given in Figure B.2.

To evaluate compressional stiffness the relative displacement of the two HP codes needs to be known. The vertical coordinates of two points located at the center of the HP code regions are used. Knowing these coordinates throughout the test, the relative displacement between the two, ΔY, can be calculated. A linear fit of ΔY and F_{comp} results in a compressional stiffness of $k = 773.5\,N/m$ (see subsection 3.3.2) with a coefficient of determination of $R^2 = 1$. The calculated stiffness value is very close to one calculated analytically, the small difference can be attributed to structural effects of small geometric beam features such as rounded edges, that are not accounted for analytically.

To evaluate torsional stiffness the overall reaction moment τ is evaluated along the out of plane x axis. The rotation of the sensor's tip γ is also evaluated. A linear fit of γ and τ results in a torsional stiffness of $k_t = 0.06\,N \cdot m/°$ with a coefficient of determination of $R^2 = 1$. Considering the sensor as a beam of length $13.8\,mm$ (distance between sensor tip and fixation hole) an horizontal force of $4.48\,N$ would be required to turn the sensor tip by 1 degree. Such values are completely unrealistic in the context of our SFTCTs.

In conclusion, finite element simulations were used in order to quantify the sensors stiffness in compression and torsion. Torsional rigidity is found to be very high, limiting off-axis movements and attesting to the good design of CT joints. Compressional stiffness on the other hand is found to be low enough, to allow for a linear sensor compression along its vertical axis.

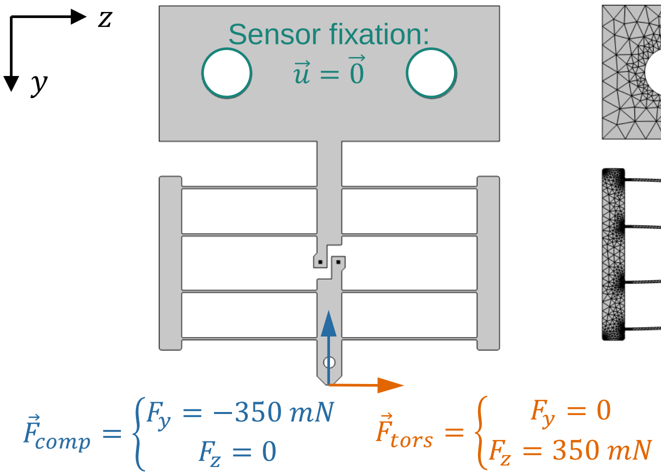

Figure B.2: Left: Boundary conditions of sensor behavior finite element analysis. The black dots replacing the HP codes are where the Y_u and Y_l data are calculated. Right: meshed and deformed geometry after applying a vertical compressive force of $350\,mN$.

B.3 Micro-fabricated assembly for compact SFTCT experimental setups

In an attempt to create a SFTCT that is significantly more compact than the one presented in 3.3.1 a new force-displacement sensor was designed and fabricated. The following design choices were made:

- A two part structure is made on $390\,\mu m$ thick silicon wafers. The upper part is a force displacement sensor similar to the one presented in 3.3.2. The lower part plays the role of the fixed platen. Two breakable joints link the two parts to ensure parallelism between them. Once the sensor-platen assembly is solidly mounted the joints can be broken.
- HP codes are positioned on the sensor tip and on the platen. Fiber displacement can be measured though the sensor's HP code, while the platen one is used to correct potential movements of the platen due to system compliance. Both HP codes can be tracked with a single camera.
- No dependent HP code is printed since it would not be possible to fit it along the independent HP code inside the same camera's field of view. The position generated by the actuator would be used to calculate relative displacement between the two parts of the sensor. While less robust, this approach was shown to produce satisfactory results.

This sensor and SFTCT configuration have not been tested or characterized yet. The reduced footprint and relative simplicity of the setup could serve as a basis for test automation or in-situ measurements in environments such as scanning electron microscopes or topographers, where space is limited.

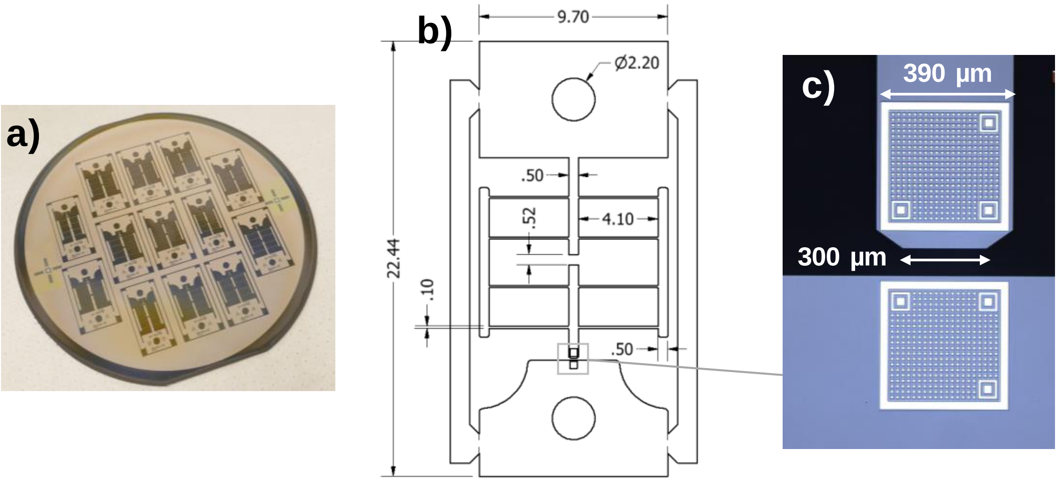

Figure B.3: Micro-fabricated assembly for compact SFTCT setup: a) view of silicon wafer with microfabricated assemblies, b) single sensor platen assembly (sensor on top, platen on bottom) with breakable connecting joints, c) zoom on sensor and platen HP codes.

B.4 Influence of removed data points on E_T identification and residual

When SFTCTs are performed, determining the point for which the fiber is in state of full compression is difficult. A possible approach is to eliminate a certain amount of compression data (at the start of the loading or at the end of the unloading stage) for which it is estimated that partial compression occurs. Thus a new zero point in force and displacement is fixed and analytical models can be used for the identification of E_T. However a question can be asked: what is the error made on the identified modulus if too many points are removed and the new zero point represents a state where the fiber is already deformed. In this section finite element analysis will be used to answer this question. Furthermore, the adequate number of removed points for the experimental fiber compression tests presented in section 3.4.3 will be discussed, through the study of the evolution of the least squares residual, in the identification of E_T.

For finite element analysis the 2D quarter fiber model presented in section 2.3 is used. Finite element analysis has the advantage of offering a true “zero” point representing the start of a full compression. Points, starting from 0, are gradually removed from the force-displacement data. Each time a point is removed the next one is set as to zero. The analytical model’s ability to identify the transverse elastic modulus of the fiber and describe its behavior is studied through ΔE_T and the least squares residual (as presented in subsection 2.3.1). A maximum fiber displacement of $1\,\mu m$ was simulated with this model.

The results of this study are shown in Figure B.4. As the number of removed points grows, both ΔE_T and the residual increase. The transverse elastic modulus gets overestimated ($\Delta E_T > 0$) because the removed points are at the start of compression where the slope is the lowest. However, both the values of ΔE_T and of the residual remain low for all studied configurations. Even when 70 % of the force-displacement points are removed the error on the identification of E_T remains under 1 %. Removing a large amount of points from the SFTCT force-displacement simulation curve has no significant influence on the identification of E_T. and the analytical model's ability to describe fiber behavior.

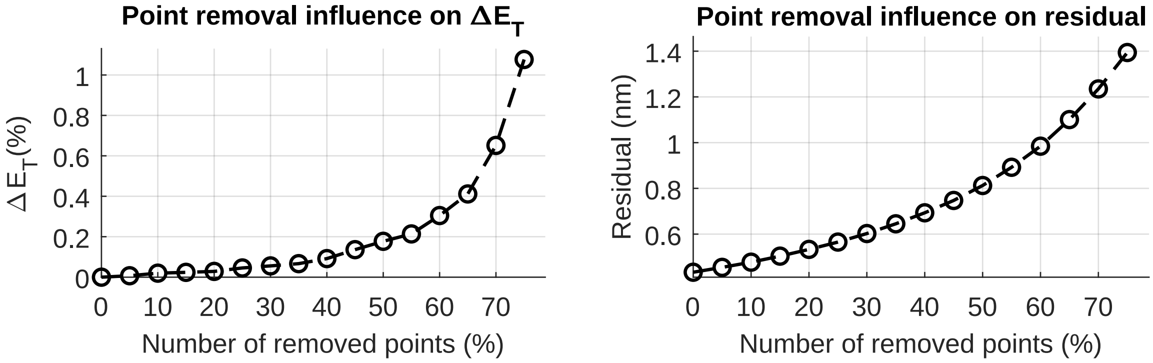

Figure B.4: Influence of force-displacement simulation data removal on ΔE_T and least-squares residual.

Contrary to finite element analysis, the true "zero" point where full compression begins cannot be determined accurately experimentally, in order to perform the same type of study on ΔE_T. However the influence of the number of removed points on the least-squares residual can still be evaluated. While the value of the residual will be majorly impacted by measurement noise its correlation with the number of removed points can be studied.

The following procedure is followed to perform this study. The initial zero in the experimental point corresponds to the point where the operator determined that the end of the partial compression of the fiber occurred, by visual monitoring. Identification of E_T is performed at the unloading stage of the compression tests presented in section 3.4, with 0 % to 70 % of the final points (close to the loss of contact) being removed. Fiber displacement values are comparable to the ones of the previous finite element study with values under $1\,\mu m$. The residual of the least-squares identification is then averaged across all tested fibers (5 fibers of Kevlar, nettle, hemp and flax) for each unloading phase of identical level (protocol details can be found in subsection 3.4). Figure B.5 presents this average value as a function of the number of removed points. The standard deviation is represented by the shaded area around each curve. For the average residual of cycles 1, 2 and 7 the value of the residual steadily increases with the number of removed points. Measurement noise at these low amplitude levels is however quite high, as attested by the larger average values and the large standard deviation of the residual. For the higher amplitude levels, 3 and 4 or 5 and 6 both the average residual value and its its standard deviation is lower, thanks to a reduced amount of noise and higher overall amount of points. Furthermore, residual values remain stable until 30 to 40 % of the total points are removed, where they starts rising. Overall, removing some points from the end of the unloading phase has thus no significant impact on the analytical model's ability to fit the experimental data, especially for compressions with higher amplitude levels.

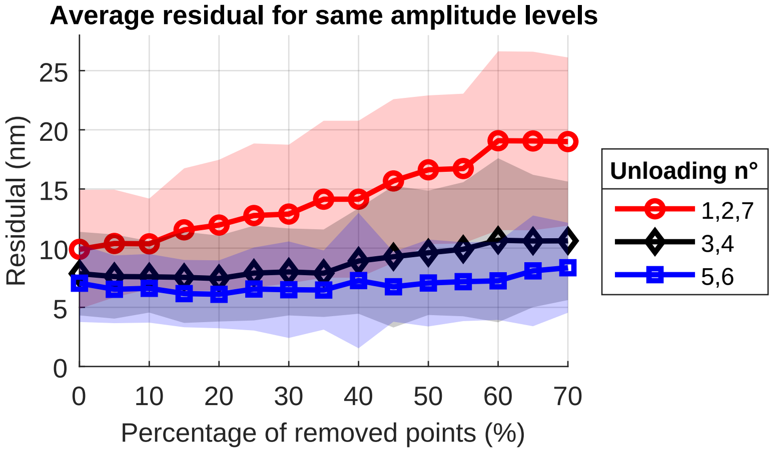

Figure B.5: Influence of experimental force-displacement data removal on least-squares residual. The mean values of the residual are represented by the continuous line with the shaded representing the standard deviation.

In conclusion, the minor impact of data removal from the start of the loading phase and the end of unloading phase was shown through finite element and experimental analysis. For fiber displacements at the order of the micrometer, up to 30 % or 40 % of these points can be removed without any major impact on the identification of E_T. This removal can help to ensure that a full compression regime is studied and no rotation or sliding motion occur (which should cause a significantly larger error).

B.5 On the identification of viscoelastic properties through creep tests

As discussed in subsection 3.3.3, performing SFTCTs over long periods of time, might come with temperature related drifts in HP code measurements. For this reason, systematic investigation of fiber behavior over longer time scales were not performed. However, some creep tests were performed to evaluate the possibility of performing them in the future, if the temperature related effects are minimized.

A typical creep loading protocol is used. After a rapid loading performed at maximum nanopositioner speed ($10\,\mu m/s$) a steady nanopositioner position is held for 10 minutes. As already explained in subsection 3.3.2 this results in a steady force level applied on the fiber, due to the compliant nature of the used force-displacement sensor. During this stage the fiber can thus exhibit its viscoelastic behavior. Once the 10 minutes have passed, the fiber is rapidly decompressed at the same speed as the loading. A 10 minute recovery phase then takes place. Relative humidity is regulated at 50 % during this test.

The results of the creep test on a nettle fiber are shown on Figure B.6 through the evolution of the applied compressive force and fiber displacement as a function of time. The regulation of the force is apparent with only a small relaxation of $0.2\,mN$ taking place during the creep phase and $0.4 mN$ during recovery, for a force amplityde of around $64\,mN$. Fiber displacement, follows a typical creep behavior with a non-linear decelerating increase in displacement during the steady load phase, and gradual non-linear decrease during the recovery phase. Changes in the displacement are in the order of 100 nm. It is unclear how much of this change is related to temperature related measurement drifts. Fiber visco-elastic generated displacement could thus be even smaller which would bring them to the limits of the current sensor design measurement ability of around 40 nm.

In conclusion, these preliminary tests show that fibers might exhibit typical creep behavior that could be used to identify their viscous mechanical properties. Temperature regulation is however important to guarantee the validity of these measurements. Changes in sensor design to allow detection of even smaller movements could also be beneficial.

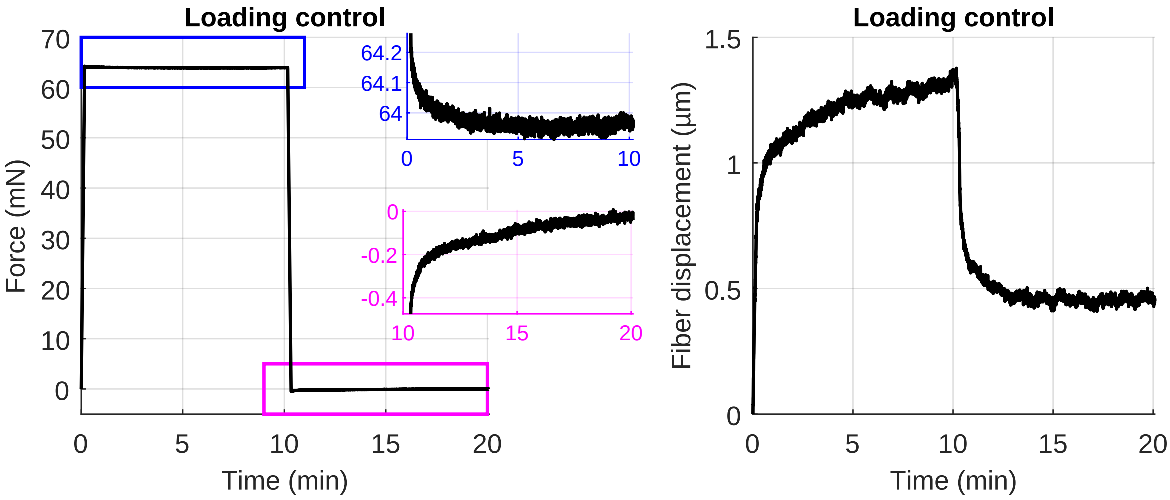

Figure B.6: Creep test imposed force and fiber response. Fiber creep behavior is in the same magnitude as thermal drifts.

Bibliography

[Adekomaya 20] O. Adekomaya. *Adaption of green composite in automotive part replacements: discussions on material modification and future patronage.* Environmental Science and Pollution Research, vol. 27, no. 8, pages 8807–8813, 2020.

[Akin 01] D. E. Akin, J. A. Foulk, R. B. Dodd & D. D. McAlister. *Enzyme-retting of flax and characterization of processed fibers.* Journal of Biotechnology, vol. 89, no. 2-3, pages 193–203, 2001.

[Ali Zernadji 22] S. Ali Zernadji, M. Rokbi, M. Benhamida & D. Hammiche. *Estimation of fiber/polymer bond strength from maximum load values recorded in the micro-bond tests.* Materials Today: Proceedings, vol. 53, pages 247–252, 2022.

[Alix 12] S. Alix, L. Lebrun, S. Marais, E. Philippe, A. Bourmaud, C. Baley & C. Morvan. *Pectinase treatments on technical fibres of flax: Effects on water sorption and mechanical properties.* Carbohydrate Polymers, vol. 87, no. 1, pages 177–185, 2012.

[Alves 10] C. Alves, P. M. Ferrão, A. J. Silva, L. G. Reis, M. Freitas, L. B. Rodrigues & D. E. Alves. *Ecodesign of automotive components making use of natural jute fiber composites.* Journal of Cleaner Production, vol. 18, no. 4, pages 313–327, 2010.

[Anazodo 81] U. G. Anazodo & E. R. Norris. *Effects of genetic and cultural practices on the mechanical properties of corn cobs.* Journal of Agricultural Engineering Research, vol. 26, no. 2, pages 97–107, 1981.

[Anazodo 83] U. Anazodo & S. Chikwendu. *Poisson ' s Ratio and Elastic Modulus of Radially Small Deformation Approximation.* Transactions of the ASAE, vol. 26, pages 923–929, 1983.

[Andersons 05] J. Andersons, E. Sparniņš, R. Joffe & L. Wallström. *Strength distribution of elementary flax fibres.* Composites Science and Technology, vol. 65, no. 3-4, pages 693–702, 2005.

[Andre 20] A. N. Andre, P. Sandoz, B. Mauze, M. Jacquot & G. J. Laurent. *Sensing One Nanometer over Ten Centimeters: A Microencoded Target for Visual In-Plane Position Measurement.* IEEE/ASME Transactions on Mechatronics, vol. 25, no. 3, pages 1193–1201, 2020.

[Andre 21] A. N. Andre, P. Sandoz, B. Mauze, M. Jacquot & G. J. Laurent. *Robust Phase-Based Decoding for Absolute (X, Y, Θ) Positioning by Vision.* IEEE Transactions on Instrumentation and Measurement, vol. 70, 2021.

[André 22a] A. N. André, P. Sandoz, M. Jacquot & G. J. Laurent. *Pose Measurement at Small Scale by Spectral Analysis of Periodic Patterns.* International Journal of Computer Vision, vol. 130, no. 6, pages 1566–1582, 2022.

[Andre 22b] A. N. Andre, O. Lehmann, J. Govilas, G. J. Laurent, H. Saadana, P. Sandoz, V. Gauthier, A. Lefevre, A. Bolopion, J. Agnus, V. Placet & C. Clevy. *Automating Robotic Micro-Assembly of Fluidic Chips and Single Fiber Compression Tests Based-on $XY\Theta$ Visual Measurement With High-Precision Fiducial Markers.* IEEE Transactions on Automation Science and Engineering, pages 1–14, 2022.

[Andreev 91] G. E. Andreev. *A review of the Brazilian test for rock tensile strength determination. Part I: calculation formula.* Mining Science and Technology, vol. 13, no. 3, pages 445–456, 1991.

[Aslan 11] M. Aslan, G. Chinga-Carrasco, B. F. Sørensen & B. Madsen. *Strength variability of single flax fibres.* Journal of Materials Science, vol. 46, no. 19, pages 6344–6354, 2011.

[Asmatulu 14] E. Asmatulu, J. Twomey & M. Overcash. *Recycling of fiber-reinforced composites and direct structural composite recycling concept.* Journal of Composite Materials, vol. 48, pages 593–608, 2014.

[Awalekar 18] Y. J. Awalekar, A. S. Takalkar & S. S. Shinde. *Investigation of Peel Resistance of Adhesives Materials: A Review.* Proceedings of Engineering and Technology Innovation, vol. 10, no. January, pages 19–28, 2018.

[Azakawa 43] T. Azakawa. *New test method for evaluating internal stress due to compression of concrete (the splitting tension test)(part 1).* J Jpn Soc Civ Eng, vol. 29, pages 777–787, 1943.

[Bacci 11] L. Bacci, S. Di Lonardo, L. Albanese, G. Mastromei & B. Perito. *Effect of different extraction methods on fiber quality of nettle (Urtica dioica L.).* Textile Research Journal, vol. 81, no. 8, pages 827–837, 2011.

[Bachtiar 10] D. Bachtiar, S. M. Sapuan, E. S. Zainudin, A. Khalina & K. Z. M. Dahlan. *The tensile properties of single sugar palm (Arenga pinnata) fibre .* IOP Conference Series: Materials Science and Engineering, vol. 11, page 012012, 2010.

[Baley 02] C. Baley. *Analysis of the flax fibres tensile behaviour and analysis of the tensile stiffness increase.* Composites Part A: Applied Science and Manufacturing, vol. 33, no. 7, pages 939–948, jul 2002.

[Baley 06] C. Baley, Y. Perrot, F. Busnel, H. Guezenoc & P. Davies. *Transverse tensile behaviour of unidirectional plies reinforced with flax fibres.* Materials Letters, vol. 60, no. 24, pages 2984–2987, 2006.

[Baley 14] C. Baley & A. Bourmaud. *Average tensile properties of French elementary flax fibers.* Materials Letters, vol. 122, pages 159–161, 2014.

[Baley 21] C. Baley, A. Bourmaud & P. Davies. *Eighty years of composites reinforced by flax fibres: A historical review.* Composites Part A: Applied Science and Manufacturing, vol. 144, page 106333, 2021.

[Barbulée 14] A. Barbulée, J. P. Jernot, J. Bréard & M. Gomina. *Damage to flax fibre slivers under monotonic uniaxial tensile loading.* Composites Part A: Applied Science and Manufacturing, vol. 64, pages 107–114, 2014.

[Beakou 13] A. Beakou & K. Charlet. *Mechanical properties of interfaces within a flax bundle - Part II: Numerical analysis.* International Journal of Adhesion and Adhesives, vol. 43, pages 54–59, 2013.

[Beaugrand 15] J. Beaugrand & S. Guessasma. *Scenarios of crack propagation in bast fibers: Combining experimental and finite element approaches.* Composite Structures, vol. 133, pages 667–678, 2015.

[Beaugrand 17] J. Beaugrand, S. Guessasma & J. E. Maigret. *Damage mechanisms in defected natural fibers.* Scientific Reports, vol. 7, no. 1, pages 1–7, 2017.

[Beese 13] A. M. Beese, D. Papkov, S. Li, Y. Dzenis & H. D. Espinosa. *In situ transmission electron microscope tensile testing reveals structure-property relationships in carbon nanofibers.* Carbon, vol. 60, pages 246–253, 2013.

[Bencomo-Cisneros 12] J. A. Bencomo-Cisneros, A. Tejeda-Ochoa, J. A. García-Estrada, C. A. Herrera-Ramírez, A. Hurtado-Macías, R. Martínez-Sánchez & J. M. Herrera-Ramírez. *Characterization of Kevlar-29 fibers by tensile tests and nanoindentation.* Journal of Alloys and Compounds, vol. 536, no. SUPPL.1, pages S456–S459, 2012.

[Bensadoun 16] F. Bensadoun, B. Vanderfeesten, I. Verpoest, A. W. Van Vuure & K. Van Acker. *Environmental impact assessment of end of life options for flax-MAPP composites.* Industrial Crops and Products, vol. 94, pages 327–341, 2016.

[Bergman 97] A. Bergman & E. Mcewen. *Sinew-Reinforced and Composite.* In H. Knecht, editeur, Projectile Technology, pages 143—-160. Springer US, 1997.

[Bettahar 22] H. Bettahar, O. Lehmann, C. Clevy, N. Courjal & P. Lutz. *6-DoF Full Robotic Calibration Based on 1-D Interferometric Measurements for Microscale and Nanoscale Applications.* IEEE Transactions on Automation Science and Engineering, vol. 19, no. 1, pages 348–359, 2022.

[Bhushan 11] B. Bhushan & Y. C. Jung. *Natural and biomimetic artificial surfaces for superhydrophobicity, self-cleaning, low adhesion, and drag reduction.* Progress in Materials Science, vol. 56, no. 1, pages 1–108, 2011.

[Bieniawski 78] Z. T. Bieniawski & I. Hawkes. *Suggested Methods for Determining Tensile Strength of Rock Materials - 1. Suggested Method for Determining Direct Tensile Strength.* International Journal of Rock Mechanics and Mining Sciences, vol. 15, no. 3, pages 99–103, 1978.

[Bleuze 18] L. Bleuze, G. Lashermes, G. Alavoine, S. Recous & B. Chabbert. *Tracking the dynamics of hemp dew retting under controlled environmental conditions.* Industrial Crops and Products, vol. 123, no. June, pages 55–63, 2018.

[Bockelmann 02] U. Bockelmann, B. Essevaz-Roulet, P. Thomen & F. Heslot. *Mechanical opening of DNA by micro manipulation and force measurements.* Comptes Rendus Physique, vol. 3, no. 5, pages 585–594, 2002.

[Bodros 08] E. Bodros & C. Baley. *Study of the tensile properties of stinging nettle fibres (Urtica dioica).* Materials Letters, vol. 62, no. 14, pages 2143–2145, may 2008.

[Bos 02] H. Bos, M. Van Den Oever & O. Peters. *Tensile and compressive properties of flax fibres for natural fibre reinforced composites.* Journal of Materials Science, vol. 37, pages 1683–1692, 2002.

[Bourmaud 09] A. Bourmaud & C. Baley. *Rigidity analysis of polypropylene/vegetal fibre composites after recycling.* Polymer Degradation and Stability, vol. 94, no. 3, pages 297–305, 2009.

[Bourmaud 12] A. Bourmaud & C. Baley. *Nanoindentation contribution to mechanical characterization of vegetal fibers.* Composites Part B: Engineering, vol. 43, no. 7, pages 2861–2866, 2012.

[Bourmaud 13a] A. Bourmaud, G. Ausias, G. Lebrun, M. L. Tachon & C. Baley. *Observation of the structure of a composite polypropylene/flax and damage mechanisms under stress.* Industrial Crops and Products, vol. 43, no. 1, pages 225–236, 2013.

[Bourmaud 13b] A. Bourmaud, C. Morvan, A. Bouali, V. Placet, P. Perré & C. Baley. *Relationships between micro-fibrillar angle, mechanical properties and biochemical composition of flax fibers.* Industrial Crops and Products, vol. 44, pages 343–351, 2013.

[Bourmaud 15] A. Bourmaud, M. Gibaud, A. Lefeuvre, C. Morvan & C. Baley. *Influence of the morphology characters of the stem on the lodging resistance of Marylin flax.* Industrial Crops and Products, vol. 66, no. 1, pages 27–37, 2015.

[Bourmaud 16a] A. Bourmaud, M. Gibaud & C. Baley. *Impact of the seeding rate on flax stem stability and the mechanical properties of elementary fibres.* Industrial Crops and Products, vol. 80, pages 17–25, 2016.

[Bourmaud 16b] A. Bourmaud, A. Le Duigou, C. Gourier & C. Baley. *Influence of processing temperature on mechanical performance of unidirectional polyamide 11-flax fibre composites.* Industrial Crops and Products, vol. 84, pages 151–165, 2016.

[Bourmaud 17] A. Bourmaud, H. Dhakal, A. Habrant, J. Padovani, D. Siniscalco, M. H. Ramage, J. Beaugrand & D. U. Shah. *Exploring the potential of waste leaf sheath date palm fibres for composite reinforcement through a structural and mechanical analysis.* Composites Part A: Applied Science and Manufacturing, vol. 103, pages 292–303, dec 2017.

[Bourmaud 18] A. Bourmaud, J. Beaugrand, D. U. Shah, V. Placet & C. Baley. *Towards the design of high-performance plant fibre composites.* Progress in Materials Science, vol. 97, no. May, pages 347–408, 2018.

[Bourmaud 19] A. Bourmaud, D. Siniscalco, L. Foucat, C. Goudenhooft, X. Falourd, B. Pontoire, O. Arnould, J. Beaugrand & C. Baley. *Evolution of flax cell wall ultrastructure and mechanical properties during the retting step.* Carbohydrate Polymers, vol. 206, no. May 2018, pages 48–56, 2019.

[Brandt 13] A. Brandt, J. Gräsvik, J. P. Hallett & T. Welton. *Deconstruction of lignocellulosic biomass with ionic liquids.* Green Chemistry, vol. 15, no. 3, pages 550–583, 2013.

[Burgert 03] I. Burgert, K. Frühmann, J. Keckes, P. Fratzl & S. E. Stanzl-Tschegg. *Microtensile Testing of Wood Fibers Combined with Video Extensometry for Efficient Strain Detection.* Holzforschung, vol. 57, no. 6, pages 661–664, 2003.

[Burgert 06] I. Burgert. *Exploring the micromechanical design of plant cell walls.* American Journal of Botany, vol. 93, no. 10, pages 1391–1401, 2006.

[Burri 19] J. T. Burri, H. Vogler, G. Munglani, N. F. Laubli, U. Grossniklaus & B. J. Nelson. *A Microrobotic System for Simultaneous Measurement of Turgor Pressure and Cell-Wall Elasticity of Individual Growing Plant Cells.* IEEE Robotics and Automation Letters, vol. 4, no. 2, pages 641–646, 2019.

[Carlsbecker 05] A. Carlsbecker & Y. Helariutta. *Phloem and xylem specification: Pieces of the puzzle emerge.* Current Opinion in Plant Biology, vol. 8, no. 5, pages 512–517, 2005.

[Carneiro 43] F. Carneiro. *A new method to determine the tensile strength of concrete.* Paper presented at the 5th meeting of the Brazilian Association for Technical Rules, 1943.

[Cavarretta 12] I. Cavarretta & C. O'Sullivan. *The mechanics of rigid irregular particles subject to uniaxial compression.* Geotechnique, vol. 62, no. 8, pages 681–692, 2012.

[Chaillet 13] N. Chaillet, M. Hafez & P. Lambert. *Actuators for Microrobotics.* In Microrobotics for Micromanipulation, pages 99–178. John Wiley & Sons, Inc., Hoboken, NJ, USA, mar 2013.

[Charlet 07] K. Charlet, C. Baley, C. Morvan, J. P. Jernot, M. Gomina & J. Bréard. *Characteristics of Hermès flax fibres as a function of their location in the stem and properties of the derived unidirectional composites.* Composites Part A: Applied Science and Manufacturing, vol. 38, no. 8, pages 1912–1921, 2007.

[Charlet 08]	K. Charlet. *Contribution à l ' étude de composites unidirectionnels renforcés par des fibres de lin : relation entre la microstructure de la fibre et ses propriétés mécaniques To cite this version : HAL Id : tel-01133091 Contribution à l ' étude de composites unidire.* Thèse de doctorat, Université de Caen, 2008.
[Charlet 09]	K. Charlet, S. Eve, J. P. Jernot, M. Gomina & J. Breard. *Tensile deformation of a flax fiber.* Procedia Engineering, vol. 1, no. 1, pages 233–236, 2009.
[Charlet 10a]	K. Charlet, J. P. Jernot, S. Eve, M. Gomina & J. Bréard. *Multi-scale morphological characterisation of flax: From the stem to the fibrils.* Carbohydrate Polymers, vol. 82, no. 1, pages 54–61, 2010.
[Charlet 10b]	K. Charlet, J. P. Jernot, J. Breard & M. Gomina. *Scattering of morphological and mechanical properties of flax fibres.* Industrial Crops and Products, vol. 32, no. 3, pages 220–224, 2010.
[Charlet 10c]	K. Charlet, J. P. Jernot, M. Gomina, L. Bizet & J. Bréard. *Mechanical properties of flax fibers and of the derived unidirectional composites.* Journal of Composite Materials, vol. 44, no. 24, pages 2887–2896, 2010.
[Charlet 11a]	K. Charlet & A. Béakou. *Mechanical properties of interfaces within a flax bundle Part I: Experimental analysis.* International Journal of Adhesion and Adhesives, vol. 31, no. 8, pages 875–881, 2011.
[Charlet 11b]	K. Charlet & A. Béakou. *Mechanical properties of interfaces within a flax bundle Part I: Experimental analysis.* International Journal of Adhesion and Adhesives, vol. 31, no. 8, pages 875–881, 2011.
[Chaudhary 20]	V. Chaudhary & F. Ahmad. *A review on plant fiber reinforced thermoset polymers for structural and frictional composites.* Polymer Testing, vol. 91, no. July, page 106792, 2020.
[Chen 09]	B. Chen, P. Wu & H. Gao. *Pre-tension generates strongly reversible adhesion of a spatula pad on substrate.* Journal of the Royal Society Interface, vol. 6, no. 35, pages 529–537, 2009.
[Chen 13]	H. Chen, X. Feng, Y. Huang, Y. Huang & J. A. Rogers. *Experiments and viscoelastic analysis of peel test with patterned strips for applications to transfer printing.* Journal of the Mechanics and Physics of Solids, vol. 61, no. 8, pages 1737–1752, 2013.
[Cheng 04]	M. Cheng, W. Chen & T. Weerasooriya. *Experimental investigation of the transverse mechanical properties of a single Kevlar® KM2 fiber.* International Journal of Solids and Structures, vol. 41, no. 22-23, pages 6215–6232, 2004.
[Cheng 05]	M. Cheng, W. Chen & T. Weerasooriya. *Mechanical Properties of Kevlar ® KM2 Single Fiber.* Journal of Engineering Materials and Technology, vol. 127, no. April, pages 197–203, 2005.
[Chikwendu 84]	S. C. Chikwendu & U. G. Anazodo. *Poisson'S Ratio and Elastic Modulus of Radially Compressed Biomaterials: Ii. Large Deformation Approximation.* Transactions of the American Society of Agricultural Engineers, vol. 27, no. 5, pages 1563–1572, 1984.
[Choi 08]	S. T. Choi, S. R. Lee & Y. Y. Earmme. *Measurement of time-dependent adhesion between a polymer film and a flat indenter tip.* Journal of Physics D: Applied Physics, vol. 41, no. 7, 2008.
[Cisse 15]	O. Cisse, V. Placet, V. Guicheret-Retel, F. Trivaudey & M. L. Boubakar. *Creep behaviour of single hemp fibres. Part I: viscoelastic properties and their scattering under constant climate.* Journal of Materials Science, vol. 50, no. 4, pages 1996–2006, 2015.

[Clair 03] B. Clair, R. Arinero, G. Lévèque, M. Ramonda & B. Thibaut. *Imaging the mechanical properties of wood cell wall layers by atomic force modulation microscopy.* IAWA Journal, vol. 24, no. 3, pages 223–230, 2003.

[Clévy 11] C. Clévy, M. Rakotondrabe & N. Chaillet. Signal measurement and estimation techniques for micro and nanotechnology. Springer Science & Business Media, 2011.

[Collotta 16] M. Collotta, L. Solazzi, S. Pandini, G. Tomasoni, M. Alberti & G. Donzella. *Design and realization a skiff racing boat hull made of natural fibers reinforced composite.* AIP Conference Proceedings, vol. 1736, 2016.

[Crocombe 82] A. D. Crocombe & R. D. Adams. *An Elasto-Plastic Investigation of the Peel Test.* The Journal of Adhesion, vol. 13, no. 3-4, pages 241–267, 1982.

[CW Nguong S Debnath 13] S. N. B. L. CW Nguong S Debnath. *A review on natural fibre reinforced polymer composites.* World Acad Sci Eng Technol, vol. 7, no. 1, pages 1123–1130, 2013.

[Czibula 19] C. Czibula, C. Ganser, T. Seidlhofer, C. Teichert & U. Hirn. *Transverse viscoelastic properties of pulp fibers investigated with an atomic force microscopy method.* Journal of Materials Science, vol. 54, no. 17, pages 11448–11461, 2019.

[Dan Foresee 97] F. Dan Foresee & M. T. Hagan. *Gauss-Newton approximation to bayesian learning.* IEEE International Conference on Neural Networks - Conference Proceedings, vol. 3, pages 1930–1935, 1997.

[Darvell 90] B. W. Darvell. *Uniaxial compression tests and the validity of indirect tensile strength.* Journal of Material Science, vol. 25, pages 757–780, 1990.

[Davies 98] G. Davies & D. Bruce. *Effect of Environmental Relative Humidity and Damage on the Tensile Properties of Flax and Nettle Fibers.* Textile Research Journal, vol. 68, no. 9, pages 623–629, sep 1998.

[Defoirdt 10] N. Defoirdt, S. Biswas, L. D. Vriese, L. Q. N. Tran, J. V. Acker, Q. Ahsan, L. Gorbatikh, A. V. Vuure & I. Verpoest. *Assessment of the tensile properties of coir, bamboo and jute fibre.* Composites Part A: Applied Science and Manufacturing, vol. 41, no. 5, pages 588–595, 2010.

[Dekking 05] F. M. Dekking, C. Kraaikamp, H. P. Lopuhaä & L. E. Meester. A Modern Introduction to Probability and Statistics. Springer Texts in Statistics. Springer London, London, 2005.

[Del Masto 17] A. Del Masto, F. Trivaudey, V. Guicheret-Retel, V. Placet & L. Boubakar. *Nonlinear tensile behaviour of elementary hemp fibres: a numerical investigation of the relationships between 3D geometry and tensile behaviour.* Journal of Materials Science, vol. 52, no. 11, pages 6591–6610, 2017.

[Del Masto 18] A. Del Masto. *Transition d'échelle entre fibre végétale et composite UD : propagation de la variabilité et des non-linéarités.* Thèse de doctorat, Université Bourgogne Franche-Comté, 2018.

[Del Masto 19] A. Del Masto, F. Trivaudey, V. Guicheret-Retel, V. Placet & L. Boubakar. *Investigation of the possible origins of the differences in mechanical properties of hemp and flax fibres: A numerical study based on sensitivity analysis.* Composites Part A: Applied Science and Manufacturing, vol. 124, no. June, page 105488, 2019.

[Dittenber 12] D. B. Dittenber & H. V. Gangarao. *Critical review of recent publications on use of natural composites in infrastructure.* Composites Part A: Applied Science and Manufacturing, vol. 43, no. 8, pages 1419–1429, 2012.

[Duch 99] W. Duch & N. Jankowski. *Survey of neural transfer functions.* Neural Computing Surveys, vol. 2, pages 163–212, 1999.

[Duval 11] A. Duval, A. Bourmaud, L. Augier & C. Baley. *Influence of the sampling area of the stem on the mechanical properties of hemp fibers.* Materials Letters, vol. 65, no. 4, pages 797–800, 2011.

[Eder 13] M. Eder, O. Arnould, J. W. Dunlop, J. Hornatowska & L. Salmén. *Experimental micromechanical characterisation of wood cell walls.* Wood Science and Technology, vol. 47, no. 1, pages 163–182, 2013.

[El-hady 12] A. El-hady & A. E. Hafez. *PHYSIO-CHEMICAL AND MECHANICAL DETERIORATION OF MONUMENTAL MUD BRICK IN EGYPT.* Egyptian Journal of Archaeological and Restoration Studies, vol. 2, no. 2, pages 103–107, 2012.

[Elsayad 20] K. Elsayad, G. Urstöger, C. Czibula, C. Teichert, J. Gumulec, J. Balvan, M. Pohlt & U. Hirn. *Mechanical Properties of cellulose fibers measured by Brillouin spectroscopy.* Cellulose, vol. 27, no. 8, pages 4209–4220, 2020.

[Espinosa 12] H. D. Espinosa, R. A. Bernal & T. Filleter. *In situ TEM electromechanical testing of nanowires and nanotubes.* Small, vol. 8, no. 21, pages 3233–3252, 2012.

[Faruk 12] O. Faruk, A. K. Bledzki, H. P. Fink & M. Sain. *Biocomposites reinforced with natural fibers: 2000-2010.* Progress in Polymer Science, vol. 37, no. 11, pages 1552–1596, 2012.

[Faruk 14] O. Faruk, A. K. Bledzki, H. P. Fink & M. Sain. *Progress report on natural fiber reinforced composites.* Macromolecular Materials and Engineering, vol. 299, no. 1, pages 9–26, 2014.

[Foppl 07] A. Foppl. *Die wichtigsten lehren der hoheren elastizitat- stheorie,.* Vorlesungen uber Technische Mechanik. B. G. Teub- ner, pages 311–372, 1907.

[Frei 13] W. Frei. *Meshing Your Geometry: When to Use the Various Element Types*, 2013.

[Fuentes 19] C. A. Fuentes, J. Witters, J. Petit, L. M. Trindade & A. W. van Vuure. *Microstructure and mechanical properties of hemp elementary fibres for composite applications by micro-computed tomography and digital image correlation.* ICCM International Conferences on Composite Materials, vol. 2019-Augus, no. June, pages 26–30, 2019.

[Gabrion 22] X. Gabrion, G. Koolen, M. Grégoire, S. Musio, M. Bar, D. Botturi, G. Rondi, E. de Luycker, S. Amaducci, P. Ouagne, A. Van Vuure & V. Placet. *Influence of industrial processing parameters on the effective properties of long aligned European hemp fibres in composite materials.* Composites Part A: Applied Science and Manufacturing, vol. 157, 2022.

[Gal 22] O. Gal. *fit _ ellipse*, 2022.

[Garat 18] W. Garat, S. Corn, N. Le Moigne, J. Beaugrand & A. Bergeret. *Analysis of the morphometric variations in natural fibres by automated laser scanning: Towards an efficient and reliable assessment of the cross-sectional area.* Composites Part A: Applied Science and Manufacturing, vol. 108, no. February, pages 114–123, 2018.

[Garat 20] W. Garat, N. Le Moigne, S. Corn, J. Beaugrand & A. Bergeret. *Swelling of natural fibre bundles under hygro- and hydrothermal conditions: Determination of hydric expansion coefficients by automated laser scanning.* Composites Part A: Applied Science and Manufacturing, vol. 131, no. December 2019, page 105803, 2020.

[Gardiner 89] D. J. Gardiner & P. R. Graves, editeurs. Practical Raman Spectroscopy. Springer Berlin Heidelberg, Berlin, Heidelberg, 1989.

[Gardon 63] J. L. Gardon. *Peel adhesion. I. Some phenomenological aspects of the test.* Journal of Applied Polymer Science, vol. 7, no. 2, pages 625–641, 1963.

[Gassan 01] J. Gassan, A. Chate & A. K. Bledzki. *Calculation of elastic properties of natural fibers.* Journal of Materials Science, vol. 36, no. 15, pages 3715–3720, 2001.

[Gholampour 20] A. Gholampour & T. Ozbakkaloglu. A review of natural fiber composites: properties, modification and processing techniques, characterization, applications, volume 55. Springer US, 2020.

[Gibaud 15] M. Gibaud, A. Bourmaud & C. Baley. *Understanding the lodging stability of green flax stems; The importance of morphology and fibre stiffness.* Biosystems Engineering, vol. 137, pages 9–21, 2015.

[Gindl 04] W. Gindl, H. S. Gupta, T. Schöberl, H. C. Lichtenegger & P. Fratzl. *Mechanical properties of spruce wood cell walls by nanoindentation.* Applied Physics A: Materials Science and Processing, vol. 79, no. 8, pages 2069–2073, 2004.

[Gindl 08] W. Gindl, M. Reifferscheid, R. B. Adusumalli, H. Weber, T. Röder, H. Sixta & T. Schöberl. *Anisotropy of the modulus of elasticity in regenerated cellulose fibres related to molecular orientation.* Polymer, vol. 49, no. 3, pages 792–799, 2008.

[Gogoli 21] K. Gogoli, F. Gehring, C. Poilâne & M. Morales. *Analysis of morphological variations of flax fibre bundles by Fraunhofer diffraction.* Industrial Crops and Products, vol. 171, no. April, 2021.

[Gogoli 22] K. Gogoli. *Contribution à l ' étude des faisceaux de fibres de lin : analyse des relations morphologie-comportement mécanique-ultrastructure.* Thèse de doctorat, Normandie Université, 2022.

[Govilas 22] J. Govilas, V. Guicheret-Retel, F. Amiot, J. Beaugrand, V. Placet & C. Clévy. *Platen parallelism significance and control in single fiber transverse compression tests.* Composites Part A: Applied Science and Manufacturing, vol. 159, no. May, 2022.

[Grandgeorge 21] P. Grandgeorge, C. Baek, H. Singh, P. Johanns, T. G. Sano, A. Flynn, J. H. Maddocks & P. M. Reis. *Mechanics of two filaments in tight orthogonal contact.* Proceedings of the National Academy of Sciences of the United States of America, vol. 118, no. 15, pages 1–8, 2021.

[Graupner 14] N. Graupner, J. Rößler, G. Ziegmann & J. Müssig. *Fibre/matrix adhesion of cellulose fibres in PLA, PP and MAPP: A critical review of pull-out test, microbond test and single fibre fragmentation test results.* Composites Part A: Applied Science and Manufacturing, vol. 63, pages 133–148, 2014.

[Grégoire 21] M. Grégoire, M. Bar, E. De Luycker, S. Musio, S. Amaducci, X. Gabrion, V. Placet & P. Ouagne. *Comparing flax and hemp fibres yield and mechanical properties after scutching/hackling processing.* Industrial Crops and Products, vol. 172, 2021.

[Grigoray 15] O. Grigoray, H. Wondraczek, S. Daus, K. Kühnöl, S. K. Latifi, P. Saketi, P. Fardim, P. Kallio & T. Heinze. *Photocontrol of mechanical properties of pulp fibers and fiber-to-fiber bonds via self-assembled polysaccharide derivatives.* Macromolecular Materials and Engineering, vol. 300, no. 3, pages 277–282, 2015.

[Gu 16] Z. Gu, S. Li, F. Zhang & S. Wang. *Understanding surface adhesion in nature: A peeling model.* Advanced Science, vol. 3, no. 7, pages 1–13, 2016.

[Guelpa 16] V. Guelpa, P. Sandoz, M. A. Vergara, C. Clévy, N. Le Fort-Piat & L. G. J. Laurent. *2D visual micro-position measurement based on intertwined twin-scale patterns.* Sensors and Actuators, A: Physical, vol. 248, pages 272–280, 2016.

[Guessasma 19] S. Guessasma & J. Beaugrand. *Damage kinetics at the sub-micrometric scale in bast fibers using finite element simulation and high-resolution X-ray micro-tomography.* Frontiers in Plant Science, vol. 10, no. February, pages 1–11, 2019.

[Guicheret-Retel 15] V. Guicheret-Retel, O. Cisse, V. Placet, J. Beaugrand, M. Pernes & M. L. Boubakar. *Creep behaviour of single hemp fibres. Part II: Influence of loading level, moisture content and moisture variation.* Journal of Materials Science, vol. 50, no. 5, pages 2061–2072, 2015.

[Guo 16] Z. Guo, D. Casem, M. Hudspeth, X. Nie, J. Sun & W. Chen. *Transverse compression of two high-performance ballistic fibers.* Textile Research Journal, vol. 86, no. 5, pages 502–511, 2016.

[Gurunathan 15] T. Gurunathan, S. Mohanty & S. K. Nayak. *A review of the recent developments in biocomposites based on natural fibres and their application perspectives.* Composites Part A: Applied Science and Manufacturing, vol. 77, pages 1–25, 2015.

[Güven 16] O. Güven, S. N. Monteiro, E. A. Moura & J. W. Drelich. *Re-Emerging Field of Lignocellulosic Fiber – Polymer Composites and Ionizing Radiation Technology in their Formulation.* Polymer Reviews, vol. 56, no. 4, pages 702–736, 2016.

[Haag 16] K. Haag & J. Müssig. *Scatter in tensile properties of flax fibre bundles: influence of determination and calculation of the cross-sectional area.* Journal of Materials Science, vol. 51, no. 17, pages 7907–7917, 2016.

[Hadavinia 06] H. Hadavinia, L. Kawashita, A. J. Kinloch, D. R. Moore & J. G. Williams. *A numerical analysis of the elastic-plastic peel test.* Engineering Fracture Mechanics, vol. 73, no. 16, pages 2324–2335, 2006.

[Hadley 65] D. Hadley, I. Ward & J. Ward. *The transverse compression of anisotropic fibre monofilaments.* Proceedings of the Royal Society of London. Series A. Mathematical and Physical Sciences, vol. 285, no. 1401, pages 275–286, 1965.

[Hamad 17] S. F. Hamad, N. Stehling, C. Holland, J. P. Foreman & C. Rodenburg. *Low-Voltage SEM of Natural Plant Fibers: Microstructure Properties (Surface and Cross-Section) and their Link to the Tensile Properties.* Procedia Engineering, vol. 200, pages 295–302, 2017.

[Harashima 96] F. Harashima, M. Tomizuka & T. Fukuda. *Mechatronics - "What Is It, Why, and How?" An editorial.* IEEE/ASME Transactions on Mechatronics, vol. 1, no. 1, pages 1–4, mar 1996.

[Heinze 15] T. Heinze. *Cellulose: Structure and properties.* Advances in Polymer Science, vol. 271, pages 1–52, 2015.

[Hertz 96] H. Hertz, D. Jones & G. Schott. *On the contact of rigid elastic solids and on hardness.* In Miscellaneous Papers, chapitre VI, pages 163–183. Macmillan, 1896.

[Hillbrick 19] L. K. Hillbrick, J. Kaiser, M. G. Huson, G. R. Naylor, E. S. Wise, A. D. Miller & S. Lucas. *Determination of the transverse modulus of cylindrical samples by compression between two parallel flat plates.* SN Applied Sciences, vol. 1, no. 7, pages 1–11, 2019.

[Hirvonen 11] J. Hirvonen, P. Saketi & P. Kallio. *Automatic image-based detection of paper fiber ends.* Third International Conference on Digital Image Processing (ICDIP 2011), vol. 8009, no. April, page 80092N, 2011.

[Hirvonen 14a] J. Hirvonen, A. Hanninen & P. Kallio. *Design and implementation of an illumination system for microrobotic paper fiber studies.* Proceedings - IEEE International Conference on Robotics and Automation, no. September 2015, pages 5854–5859, 2014.

[Hirvonen 14b] J. Hirvonen, S. K. Latifi, P. Kallio & K. Palovuori. *Semi-automatic measurement of microfibril angle on a microrobotic platform.* 2014 International Conference on Manipulation, Manufacturing and Measurement on the Nanoscale, 3M-NANO 2014 - Conference Proceedings, no. October, pages 326–329, 2014.

[Hirvonen 15a] J. Hirvonen & P. Kallio. *Automatic image-based detection and inspection of paper fibres for grasping.* IET Computer Vision, vol. 9, no. 4, pages 588–594, 2015.

[Hirvonen 15b] J. Hirvonen, M. Von Essen & P. Kallio. *Automated microrobotic manipulation of paper fiber bonds.* IEEE International Conference on Intelligent Robots and Systems, vol. 2015-Decem, no. January 2016, pages 784–789, 2015.

[Hirvonen 16] J. Hirvonen, M. Myllys & P. Kallio. *Method for 3D fibre reconstruction on a microrobotic platform.* Journal of Microscopy, vol. 263, no. 1, pages 20–33, 2016.

[Hirvonen 17] J. Hirvonen, Y. Lai, P. Kallio, G. Cunha & O. Rojas. *Automated estimation of contact angle on hydrophobic fibers using a microrobotic platform.* IEEE 3M-NANO 2016 - 6th IEEE International Conference on Manipulation, Manufacturing and Measurement on the Nanoscale, no. 310332, pages 130–135, 2017.

[Hopcroft 10] M. A. Hopcroft, W. D. Nix & T. W. Kenny. *What is the Young's modulus of silicon?* Journal of Microelectromechanical Systems, vol. 19, no. 2, pages 229–238, 2010.

[Hu 10] W. Hu, M.-T. Ton-That, F. Perrin-Sarazin & J. Denault. *An improved method for single fiber tensile test of natural fibers.* Polymer Engineering & Science, vol. 50, no. 4, pages 819–825, apr 2010.

[Hull 99] R. Hull. Properties of crystalline silicon. IET, 1999.

[Ilczyszyn 12] F. Ilczyszyn, A. Cherouat & G. Montay. *Mechanical modeling of hemp fibres behaviour using digital imaging treatment.* Advanced Materials Research, vol. 423, pages 143–153, 2012.

[Islam 08] M. S. Islam. *The Influence of Fibre Processing and Treatments on Hemp Fibre/Epoxy and Hemp Fibre/PLA Composites.* Thèse de doctorat, The University of Waikato, Hamilton, New Zealand, 2008.

[Islam 10] M. S. Islam, K. L. Pickering & N. J. Foreman. *Influence of alkali treatment on the interfacial and physico-mechanical properties of industrial hemp fibre reinforced polylactic acid composites.* Composites Part A: Applied Science and Manufacturing, vol. 41, no. 5, pages 596–603, 2010.

[Jaouen 07] G. Jaouen, T. Alméras, C. Coutand & M. Fournier. *How to determine sapling buckling risk with only a few measurements.* American Journal of Botany, vol. 94, no. 10, pages 1583–1593, 2007.

[Jawad 78] S. A. Jawad & I. M. Ward. *The transverse compression of oriented nylon and polyethylene extrudates.* Journal of Materials Science, vol. 13, no. 7, pages 1381–1387, jul 1978.

[Jawaid 11] M. Jawaid & H. P. Abdul Khalil. *Cellulosic/synthetic fibre reinforced polymer hybrid composites: A review.* Carbohydrate Polymers, vol. 86, no. 1, pages 1–18, 2011.

[Jeannin 20] T. Jeannin, L. Yung, P. Evon, L. Labonne, P. Ouagne, M. Lecourt, D. Cazaux, M. Chalot & V. Placet. *Native stinging nettle (Urtica dioica L.) growing spontaneously under short rotation coppice for phytomanagement of trace element contaminated soils: Fibre yield, processability and quality.* Industrial Crops and Products, vol. 145, no. July 2019, page 111997, 2020.

[Joannès 20] S. Joannès, F. Islam & L. Laiarinandrasana. *Uncertainty in Fibre Strength Characterisation Due to Uncertainty in Measurement and Sampling Randomness.* Applied Composite Materials, vol. 27, no. 3, pages 165–184, 2020.

[Jones 97] M. C. Jones, E. Lara-Curzio, A. Kopper & D. C. Martin. *The lateral deformation of cross-linkable PPXTA fibres.* Journal of Materials Science, vol. 32, no. 11, pages 2855–2871, 1997.

[Josse 04] G. Josse, P. Sergot, C. Criton & M. Dorget. Measuring interfacial adhesion between a soft viscoelastic layer and a rigid surface using a probe method, volume 80. 2004.

[Kamst 99] G. F. Kamst, J. Vasseur, C. Bonazzi & J. J. Bimbenet. *New method for the measurement of the tensile strength of rice grains by using the diametral compression test.* Journal of Food Engineering, vol. 40, no. 4, pages 227–232, 1999.

[Kandemir 20] A. Kandemir, T. R. Pozegic, I. Hamerton, S. J. Eichhorn & M. L. Longana. *Characterisation of natural fibres for sustainable discontinuous fibre composite materials.* Materials, vol. 13, no. 9, 2020.

[Kawabata 90] S. Kawabata. *Measurement of the transverse mechanical properties of high-performance fibres.* Journal of the Textile Institute, vol. 81, no. 4, pages 432–447, 1990.

[Keckes 03] J. Keckes, I. Burgert, K. Frühmann, M. Müller, K. Kölln, M. Hamilton, M. Burghammer, S. V. Roth, S. Stanzl-Tschegg & P. Fratzl. *Cell-wall recovery after irreversible deformation of wood.* Nature Materials, vol. 2, no. 12, pages 810–814, 2003.

[Keller 01] A. Keller, M. Leupin, V. Mediavilla & E. Wintermantel. *Influence of the growth stage of industrial hemp on chemical and physical properties of the fibres.* Industrial Crops and Products, vol. 13, no. 1, pages 35–48, 2001.

[Kendall 75] K. Kendall. *Thin-film peeling-the elastic term.* Journal of Physics D: Applied Physics, vol. 8, no. 13, pages 1449–1452, 1975.

[Kersavage 73] P. C. Kersavage. *Moisture content effect on tensile properties of individual Douglas-fir latewood tracheids.* Wood and Fiber, vol. 5, no. 2, pages 105–117, 1973.

[Kessler 98] R. Kessler, U. Becker, R. Kohler & B. Goth. *Steam explosion of flax — a superior technique for upgrading fibre value.* Biomass and Bioenergy, vol. 14, no. 3, pages 237–249, mar 1998.

[Khaldi 16] M. Khaldi, A. Vivet, A. Bourmaud, Z. Sereir & B. Kada. *Damage analysis of composites reinforced with Alfa fibers: Viscoelastic behavior and debonding at the fiber/matrix interface.* Journal of Applied Polymer Science, vol. 133, no. 31, pages 1–11, 2016.

[Kim 88] K. S. Kim & N. Aravas. *Elastoplastic analysis of the peel test.* International Journal of Solids and Structures, vol. 24, no. 4, pages 417–435, 1988.

[Komati 16] B. Komati, C. Clevy & P. Lutz. *High bandwidth microgripper with integrated force sensors and position estimation for the grasp of multistiffness micro-components.* IEEE/ASME Transactions on Mechatronics, vol. 21, no. 4, pages 2039–2049, 2016.

[Komuraiah 14] A. Komuraiah, N. S. Kumar & B. D. Prasad. *Chemical Composition of Natural Fibers and its Influence on their Mechanical Properties.* Mechanics of Composite Materials, vol. 50, no. 3, pages 359–376, 2014.

[Koronis 13] G. Koronis, A. Silva & M. Fontul. *Green composites: A review of adequate materials for automotive applications.* Composites Part B: Engineering, vol. 44, no. 1, pages 120–127, 2013.

[Kotani 94] T. Kotani, J. Sweeney & I. M. Ward. *The measurement of transverse mechanical properties of polymer fibres.* Journal of Materials Science, vol. 29, no. 21, pages 5551–5558, 1994.

[Kozhar 15] S. Kozhar, M. Dosta, S. Antonyuk, S. Heinrich & U. Bröckel. *DEM simulations of amorphous irregular shaped micrometer-sized titania agglomerates at compression.* Advanced Powder Technology, vol. 26, no. 3, pages 767–777, 2015.

[Ku 11] H. Ku, H. Wang, N. Pattarachaiyakoop & M. Trada. *A review on the tensile properties of natural fiber reinforced polymer composites.* Composites Part B: Engineering, vol. 42, no. 4, pages 856–873, 2011.

[Kvavadze 09] E. Kvavadze, O. Bar-Yosef, A. Belfer-Cohen, E. Boaretto, N. Jakeli, Z. Matskevich & T. Meshveliani. *30,000-Year-Old Wild Flax Fibers.* Science, vol. 325, no. 5946, page 1359, 2009.

[Ladner 19] I. S. Ladner, M. A. Cullinan & S. K. Saha. *Tensile properties of polymer nanowires fabricated: Via two-photon lithography.* RSC Advances, vol. 9, no. 49, pages 28803–28813, 2019.

[Laermer 20] F. Laermer, S. Franssila, L. Sainiemi & K. Kolari. Deep reactive ion etching. INC, 2020.

[Lamblet 07] M. Lamblet, E. Verneuil, T. Vilmin, A. Buguin, P. Silberzan & L. Léger. *Adhesion enhancement through micropatterning at polydimethylsiloxane-acrylic adhesive interfaces.* Langmuir, vol. 23, no. 13, pages 6966–6974, 2007.

[Lanzilao 16] G. Lanzilao, P. Goswami & R. S. Blackburn. *Study of the morphological characteristics and physical properties of Himalayan giant nettle (Girardinia diversifolia L.) fibre in comparison with European nettle (Urtica dioica L.) fibre.* Materials Letters, vol. 181, pages 200–203, oct 2016.

[Latifi 15] S. K. Latifi, P. Saketi & P. Kallio. *Microrobotic system for multi-rate measurement of bio-based fibres Z-directional bond strength.* Journal of Micro-Bio Robotics, vol. 10, no. 1-4, pages 13–26, 2015.

[Läubli 21] N. F. Läubli, J. T. Burri, J. Marquard, H. Vogler, G. Mosca, N. Vertti-Quintero, N. Shamsudhin, A. DeMello, U. Grossniklaus, D. Ahmed & B. J. Nelson. *3D mechanical characterization of single cells and small organisms using acoustic manipulation and force microscopy.* Nature Communications, vol. 12, no. 1, pages 1–11, 2021.

[Laurikainen 20] P. Laurikainen, M. Kakkonen, M. von Essen, O. Tanhuanpää, P. Kallio & E. Sarlin. *Identification and compensation of error sources in the microbond test utilising a reliable high-throughput device.* Composites Part A: Applied Science and Manufacturing, vol. 137, no. June, page 105988, 2020.

[le Duigou 17] A. le Duigou, J. Merotte, A. Bourmaud, P. Davies, K. Belhouli & C. Baley. *Hygroscopic expansion: A key point to describe natural fibre/polymer matrix interface bond strength.* Composites Science and Technology, vol. 151, pages 228–233, 2017.

[Lee 03] S. G. Lee, S. S. Choi, W. H. Park & D. Cho. *Characterization of surface modified flax fibers and their biocomposites with PHB.* Macromolecular Symposia, vol. 197, pages 089–100, 2003.

[Lee 14] H. V. Lee, S. B. A. Hamid & S. K. Zain. *Conversion of Lignocellulosic Biomass to Nanocellulose: Structure and Chemical Process.* The Scientific World Journal, vol. 2014, pages 1–20, 2014.

[Lefeuvre 14a] A. Lefeuvre, A. Bourmaud, C. Morvan & C. Baley. *Elementary flax fibre tensile properties: Correlation between stress-strain behaviour and fibre composition.* Industrial Crops and Products, vol. 52, pages 762–769, 2014.

[Lefeuvre 14b] A. Lefeuvre, A. Bourmaud, C. Morvan & C. Baley. *Tensile properties of elementary fibres of flax and glass: Analysis of reproducibility and scattering.* Materials Letters, vol. 130, pages 289–291, 2014.

[Legland 13] D. Legland & J. Beaugrand. *Automated clustering of lignocellulosic fibres based on morphometric features and using clustering of variables.* Industrial Crops and Products, vol. 45, pages 253–261, 2013.

[Lemaitre 94] J. Lemaitre & J.-L. Chaboche. Mechanics of Solid Materials. Cambridge University Press, 1994.

[Li 13] D. Li & L. N. Y. Wong. *The brazilian disc test for rock mechanics applications: Review and new insights.* Rock Mechanics and Rock Engineering, vol. 46, no. 2, pages 269–287, 2013.

[Li 17] Q. Li, Y. Li & L. Zhou. *A micromechanical model of interfacial debonding and elementary fiber pull-out for sisal fiber-reinforced composites.* Composites Science and Technology, vol. 153, pages 84–94, 2017.

[Liang 14] Q. Liang, D. Zhang, G. Coppola, Y. Wang, S. Wei & Y. Ge. *Multi-dimensional MEMS/micro sensor for force and moment sensing: A review.* IEEE Sensors Journal, vol. 14, no. 8, pages 2643–2657, 2014.

[Lim 10] J. Lim, J. Q. Zheng, K. Masters & W. W. Chen. *Mechanical behavior of A265 single fibers.* Journal of Materials Science, vol. 45, no. 3, pages 652–661, 2010.

[Little 05] E. G. Little, D. Tocher, D. Colgan & P. O'Donnell. *An analysis of the factors influencing the data derived from a plug type three-dimensional strain rosette under compression and torsion.* Strain, vol. 41, no. 4, pages 193–202, 2005.

[Liu 10] H. Liu. *On the Levenberg-Marquardt training method for feed-forward neural networks.* Proceedings - 2010 6th International Conference on Natural Computation, ICNC 2010, vol. 1, no. Icnc, pages 456–460, 2010.

[Liu 21] T. Liu, P. Butaud, V. Placet & M. Ouisse. *Damping behavior of plant fiber composites: A review.* Composite Structures, vol. 275, no. August 2020, page 114392, 2021.

[Liu 22] T. Liu, Y. Gaillard, P. Butaud, V. Placet & M. Ouisse. *In situ damping identification of plant fiber composites using dynamic grid nanoindentation.* Composites Part A: Applied Science and Manufacturing, vol. 163, no. January, page 107158, 2022.

[Loo 58] T.-T. Loo. *Effect of Curvature on the Hertz Theory for Two Circular Cylinders in Contact.* Journal of Applied Mechanics, vol. 25, no. 1, pages 122–124, 1958.

[Lundberg 49] G. Lundberg & E. Yhland. Cylinder compressed between two plane bodies. SKF, 1949.

[MacKay 92] D. J. C. MacKay. *Bayesian Interpolation.* Neural Computation, vol. 4, no. 3, pages 415–447, 1992.

[MacLeod 21] M. MacLeod, H. P. H. Arp, M. B. Tekman & A. Jahnke. *The global threat from plastic pollution.* Science, vol. 373, no. 6550, pages 61–65, 2021.

[Madsen 09] B. Madsen, A. Thygesen & H. Lilholt. *Plant fibre composites - porosity and stiffness.* Composites Science and Technology, vol. 69, no. 7-8, pages 1057–1069, 2009.

[Mahmud 21] S. Mahmud, K. M. Hasan, M. A. Jahid, K. Mohiuddin, R. Zhang & J. Zhu. Comprehensive review on plant fiber-reinforced polymeric biocomposites, volume 56. Springer US, 2021.

[Mankins 09] J. C. Mankins. *Technology readiness assessments : A retrospective.* Acta Astronautica, vol. 65, no. 9-10, pages 1216–1223, 2009.

[Mansor 19] M. R. Mansor, M. T. Mastura, S. M. Sapuan & A. Z. Zainudin. *11 - The environmental impact of natural fiber composites through life cycle assessment analysis.* In Durability and Life Prediction in Biocomposites, Fibre-Reinforced Composites and Hybrid Composites, pages 257–285. Woodhead Publishing, 2019.

[Markarian 07] J. Markarian. *Long fibre reinforced thermoplastics continue growth in automotive.* Plastics, Additives and Compounding, vol. 9, no. 2, pages 20–23, 2007.

[Markides 18] C. F. Markides, E. D. Pasiou & S. K. Kourkoulis. *A preliminary study on the potentialities of the Circular Semi-Ring test.* Procedia Structural Integrity, vol. 9, pages 108–115, 2018.

[Marrot 13] L. Marrot, A. Lefeuvre, B. Pontoire, A. Bourmaud & C. Baley. *Analysis of the hemp fiber mechanical properties and their scattering (Fedora 17).* Industrial Crops and Products, vol. 51, pages 317–327, 2013.

[Mattrand 14] C. Mattrand, A. Béakou & K. Charlet. *Numerical modeling of the flax fiber morphology variability.* Composites Part A: Applied Science and Manufacturing, vol. 63, pages 10–20, 2014.

[Mauze 20] B. Mauze, R. Dahmouche, C. Clevy, P. Sandoz, F. Hennebelle & G. J. Laurent. *Visual Measurements at Small Scales: Guidelines to Reduce Uncertainties down to a Few Nanometers.* In Proceedings of MARSS 2020: International Conference on Manipulation, Automation, and Robotics at Small Scales, numéro Section III, 2020.

[McCallion 82] H. McCallion & N. Truong. *The deformation of rough cylinders compressed between smooth flat surfaces of hard blocks.* Wear, vol. 79, no. 3, pages 347–361, 1982.

[McCulloch 43] W. S. McCulloch & W. Pitts. *A logical calculus of the ideas immanent in nervous activity.* The Bulletin of Mathematical Biophysics, vol. 5, no. 4, pages 115–133, 1943.

[McDaniel 17] P. B. McDaniel, S. Sockalingam, J. M. Deitzel, J. W. Gillespie, M. Keefe, T. A. Bogetti, D. T. Casem & T. Weerasooriya. *The effect of fiber meso/nanostructure on the transverse compression response of ballistic fibers.* Composites Part A: Applied Science and Manufacturing, vol. 94, pages 133–145, 2017.

[Mead 18] J. L. Mead, H. Xie, S. Wang & H. Huang. *Enhanced adhesion of ZnO nanowires during: In situ scanning electron microscope peeling.* Nanoscale, vol. 10, no. 7, pages 3410–3420, 2018.

[Mead 20]	J. L. Mead, S. Wang, S. Zimmermann & H. Huang. *Interfacial adhesion of ZnO nanowires on a Si substrate in air.* Nanoscale, vol. 12, no. 15, pages 8237–8247, 2020.
[Melelli 20a]	A. Melelli, O. Arnould, J. Beaugrand & A. Bourmaud. *The middle lamella of plant fibers used as composite reinforcement: Investigation by atomic force microscopy.* Molecules, vol. 25, no. 3, 2020.
[Melelli 20b]	A. Melelli, F. Jamme, D. Legland, J. Beaugrand & A. Bourmaud. *Microfibril angle of elementary flax fibres investigated with polarised second harmonic generation microscopy.* Industrial Crops and Products, vol. 156, no. July, page 112847, 2020.
[Melelli 21a]	A. Melelli. *Evolution of the ultrastructure , parietal composition and mechanical properties of flax fibres over time.* Thèse de doctorat, Université de Bretagne Sud, 2021.
[Melelli 21b]	A. Melelli, S. Durand, O. Arnould, E. Richely, S. Guessasma, F. Jamme, J. Beaugrand & A. Bourmaud. *Extensive investigation of the ultrastructure of kink-bands in flax fibres.* Industrial Crops and Products, vol. 164, no. August 2020, 2021.
[Melelli 22]	A. Melelli, S. Durand, C. Alvarado, A. Kervoëlen, L. Foucat, M. Grégoire, O. Arnould, X. Falourd, F. Callebert, P. Ouagne, A. Geairon, S. Daniel, F. Jamme, C. Mauve, B. Gakière, A. Bourmaud & J. Beaugrand. *Anticipating global warming effects: A comprehensive study of drought impact of both flax plants and fibres.* Industrial Crops and Products, vol. 184, no. May, 2022.
[Mesquita 21]	F. Mesquita, S. Bucknell, Y. Leray, S. V. Lomov & Y. Swolfs. *Single carbon and glass fibre properties characterised using large data sets obtained through automated single fibre tensile testing.* Composites Part A: Applied Science and Manufacturing, vol. 145, no. March, page 106389, 2021.
[M'Ewen 49]	E. M'Ewen. *XLI. Stresses in elastic cylinders in contact along a generatrix (including the effect of tangential friction).* The London, Edinburgh, and Dublin Philosophical Magazine and Journal of Science, vol. 40, no. 303, pages 454–459, 1949.
[Mikczinski 13]	M. Mikczinski & H. X. Nguyen. *Assessing Transverse Fibre Properties : Fibre Compression and Artificial Hornification By Periodic Compression.* Advances in Pulp and Paper Research, Transactions of the XVth Fundamental Research Symposium, Cambridge, no. September 2013, pages 803–820, 2013.
[Mohammed 15]	L. Mohammed, M. N. Ansari, G. Pua, M. Jawaid & M. S. Islam. *A Review on Natural Fiber Reinforced Polymer Composite and Its Applications.* International Journal of Polymer Science, vol. 2015, 2015.
[Mook 07]	W. M. Mook, J. D. Nowak, C. R. Perrey, C. B. Carter, R. Mukherjee, S. L. Girshick, P. H. McMurry & W. W. Gerberich. *Compressive stress effects on nanoparticle modulus and fracture.* Physical Review B - Condensed Matter and Materials Physics, vol. 75, no. 21, pages 1–10, 2007.
[Morris 68]	S. Morris. *39—The Determination of the Lateral-Compression Modulus of Fibres.* Journal of the Textile Institute, vol. 59, no. 11, pages 536–547, 1968.
[Mounier 14]	D. Mounier, C. Poilâne, H. Khelfa & P. Picart. *Sub-gigahertz laser resonant ultrasound spectroscopy for the evaluation of elastic properties of micrometric fibers.* Ultrasonics, vol. 54, no. 1, pages 259–267, 2014.
[Muskhelishvili 77]	N. Muskhelishvili. Some Basic Problems of the Mathematical Theory of Elasticity. Springer Dordrecht, 1 edition, 1977.

[Müssig 10] J. Müssig, editeur. Industrial Applications of Natural Fibres. Wiley, apr 2010.

[Müssig 15] J. Müssig & K. Haag. The use of flax fibres as reinforcements in composites. Elsevier, 2015.

[Nagavally 17] R. R. Nagavally. *Composite Materials - History, Types, Fabrication Techniques, Advantages, and Applications.* International Journal of Mechanical And Production Engineering, vol. 5, no. 9, pages 82–87, 2017.

[Nair 14] G. R. Nair, J. Kurian, V. Yaylayan, D. Rho, D. Lyew & G. S. Raghavan. *Microwave-assisted retting and optimization of the process through chemical composition analysis of the matrix.* Industrial Crops and Products, vol. 52, pages 85–94, 2014.

[Naito 07] K. Naito, Y. Tanaka, J.-m. Yang & Y. Kagawa. *Tensile properties of ultrahigh strength PAN-based , ultrahigh modulus pitch-based and high ductility pitch-based carbon fibers.* Carbon, vol. 6, pages 4–10, 2007.

[Naito 17] K. Naito, Y. Tanaka & J. M. Yang. *Transverse compressive properties of polyacrylonitrile (PAN)-based and pitch-based single carbon fibers.* Carbon, vol. 118, pages 168–183, 2017.

[Nilsson 07] T. Nilsson & P. J. Gustafsson. *Influence of dislocations and plasticity on the tensile behaviour of flax and hemp fibres.* Composites Part A: Applied Science and Manufacturing, vol. 38, no. 7, pages 1722–1728, 2007.

[Nitta 13] Y. Nitta, K. Goda, J. Noda & W. I. Lee. *Cross-sectional area evaluation and tensile properties of alkali-treated kenaf fibres.* Composites Part A: Applied Science and Manufacturing, vol. 49, pages 132–138, 2013.

[Nuez 22] L. Nuez, E. Richely, J. Perez, S. Guessasma, J. Beaugrand, P. D'Arras, A. Bourmaud & C. Baley. *Exploring the effect of relative humidity on dynamic evolution of flax fibre's microfibril angle through in situ tensile tests under synchrotron X-ray diffraction.* Industrial Crops and Products, vol. 188, no. September, 2022.

[Nyambuu 14] U. Nyambuu & W. Semmler. *Trends in the extraction of non-renewable resources : The case of fossil energy.* Economic Modelling, vol. 37, pages 271–279, 2014.

[Nyholm 01] K. Nyholm, P. Ander, S. Bardage & G. Daniel. *Dislocations in pulp fibres - Their origin, characteristics and importance - A review.* Nordic Pulp and Paper Research Journal, vol. 16, no. 4, pages 376–384, 2001.

[Oksman 02] K. Oksman, L. Wallström, L. A. Berglund & R. D. Toledo Filho. *Morphology and mechanical properties of unidirectional sisal-epoxy composites.* Journal of Applied Polymer Science, vol. 84, no. 13, pages 2358–2365, 2002.

[Olesiak 75] H. Olesiak & A. P. Wilczynski. Mechanika teoretyczna i stosowana. Panstowe Wydawnictwo Naukowe, 1975.

[Otsu 96] Otsu & N. *A threshold selection method from gray-level histograms.* IEEE Trans. on Systems, Man and Cybernetics, vol. 9, no. 1, pages 62–66, 1996.

[Ouyang 08] P. R. Ouyang, T. C., W. J. Zhang & G. S. Yang. *Micro-motion devices technology : The state of arts review.* The International Journal of Advanced Manufacturing Technology volume, vol. 38, pages 463–478, 2008.

[Page 71] D. H. Page, F. El-Hosseiny & K. Winkler. *Behaviour of Single Wood Fibres under Axial Tensile Strain.* Nature, vol. 229, no. 5282, pages 252–253, jan 1971.

[Pearson 96] K. Pearson. *Mathematical Contributions to the Theovy of Evolution.—III. Heredity, and Panmixia.* Philosophical Transactions of the Royal Society of London., vol. 187, no. Series A, Containing Papers of a Mathematical or Physical Character, pages 253–318, 1896.

[Pereira 14] C. M. Pereira & M. S. Martins. Flame Retardancy of Fiber-Reinforced Polymer Composites Based on Nanoclays and Carbon Nanotubes. Elsevier B.V., 2014.

[Perrin 07] D. Perrin, M. Alteirac, S. Corn & M. E. Shanahan. *A novel method for the measurement of elastic moduli of fibres.* Composites Part A: Applied Science and Manufacturing, vol. 38, no. 1, pages 71–79, 2007.

[Pesika 07] N. Pesika, Y. Tian, B. Zhao, K. Rosenberg, H. Zeng, P. McGuiggan, K. Autumn & J. N. Israelachvili. *Peel-zone model of tape peeling based on the gecko adhesive system.* Journal of Adhesion, vol. 83, no. 4, pages 383–401, 2007.

[Phoenix 74] S. Phoenix & J. Skelton. *Transverse Compressive Moduli and Yield Behavior of Some Orthotropic, High-Modulus Filaments.* Textile Research Journal, pages 934–940, 1974.

[Pickering 07] K. L. Pickering, G. W. Beckermann, S. N. Alam & N. J. Foreman. *Optimising industrial hemp fibre for composites.* Composites Part A: Applied Science and Manufacturing, vol. 38, no. 2, pages 461–468, 2007.

[Pickering 16] K. L. Pickering, M. G. Efendy & T. M. Le. *A review of recent developments in natural fibre composites and their mechanical performance.* Composites Part A: Applied Science and Manufacturing, vol. 83, pages 98–112, 2016.

[Pinnock 66] P. R. Pinnock, I. M. Ward & J. M. Wolfe. *The compression of anisotropic fibre monofilaments. II.* Proceedings of the Royal Society of London. Series A. Mathematical and Physical Sciences, vol. 291, no. 1425, pages 267–278, 1966.

[Pisupati 19] A. Pisupati, A. Ayadi, M. Deléglise-Lagardère & C. H. Park. *Influence of resin curing cycle on the characterization of the tensile properties of flax fibers by impregnated fiber bundle test.* Composites Part A: Applied Science and Manufacturing, vol. 126, no. August, page 105572, 2019.

[Placet 12a] V. Placet, O. Cisse & M. L. Boubakar. *Influence of environmental relative humidity on the tensile and rotational behaviour of hemp fibres.* Journal of Materials Science, vol. 47, no. 7, pages 3435–3446, 2012.

[Placet 12b] V. Placet, F. Trivaudey, O. Cisse, V. Gucheret-Retel & M. L. Boubakar. *Diameter dependence of the apparent tensile modulus of hemp fibres: A morphological, structural or ultrastructural effect?* Composites Part A: Applied Science and Manufacturing, vol. 43, no. 2, pages 275–287, 2012.

[Placet 14] V. Placet, O. Cissé & M. Lamine Boubakar. *Nonlinear tensile behaviour of elementary hemp fibres. Part I: Investigation of the possible origins using repeated progressive loading with in situ microscopic observations.* Composites Part A: Applied Science and Manufacturing, vol. 56, pages 319–327, 2014.

[Placet 17] V. Placet, A. Day & J. Beaugrand. *The influence of unintended field retting on the physicochemical and mechanical properties of industrial hemp bast fibres.* Journal of Materials Science, vol. 52, no. 10, pages 5759–5777, 2017.

[Placet 20] V. Placet, M. Blot, T. Weemaes, H. Bernollin, G. Laurent, F. Amiot, C. Clévy & J. Beaugrand. *Transverse compressive properties of natural fibers determined using micro mechatronic systems and 2D full-field measurements.* Materials Today: Proceedings, vol. 31, pages 303–308, 2020.

[Poritsky 50] H. Poritsky. *Stresses and Deflections of Cylindrical Bodies in Contact With Application to Contact of Gears and of Locomotive Wheels.* Journal of Applied Mechanics, vol. 17, pages 191–201, 1950.

[Pourchet 19] S. Pourchet, R. Sonnier, M. Ben-Abdelkader, Y. Gaillard, Q. Ruiz, V. Placet, L. Plasseraud & G. Boni. *New Reactive Isoeugenol Based Phosphate Flame Retardant: Toward Green Epoxy Resins.* ACS Sustainable Chemistry and Engineering, vol. 7, no. 16, pages 14074–14088, 2019.

[Prapavesis 20] A. Prapavesis, V. Tojaga, S. Östlund & A. Willem van Vuure. *Back calculated compressive properties of flax fibers utilizing the Impregnated Fiber Bundle Test (IFBT).* Composites Part A: Applied Science and Manufacturing, vol. 135, no. May, page 105930, 2020.

[Prasad 83] S. V. Prasad, C. Pavithran & P. K. Rohatgi. *Alkali treatment of coir fibres for coir-polyester composites.* Journal of Materials Science, vol. 18, no. 5, pages 1443–1454, 1983.

[Rabe 96] U. Rabe, K. Janser & W. Arnold. *Vibrations of free and surface-coupled atomic force microscope cantilevers: Theory and experiment.* Review of Scientific Instruments, vol. 67, no. 9, pages 3281–3293, 1996.

[Rabelo 01] G. F. Rabelo, I. M. Dal Fabbro & A. W. Linares. *Contact stress area measurement of spherical fruit.* Acta Horticulturae, vol. 562, pages 195–200, 2001.

[Ramachandramoorthy 18] R. Ramachandramoorthy, A. Beese & H. Espinosa. *In situ electron microscopy tensile testing of constrained carbon nanofibers.* International Journal of Mechanical Sciences, vol. 149, no. April 2017, pages 452–458, 2018.

[Ramesh 17] M. Ramesh, K. Palanikumar & K. H. Reddy. *Plant fibre based biocomposites: Sustainable and renewable green materials.* Renewable and Sustainable Energy Reviews, vol. 79, no. May, pages 558–584, 2017.

[Reiterer 01] A. Reiterer, H. Lichtenegger, P. Fratzl & S. E. Stanzl-Tschegg. *Deformation and energy absorption of wood cell walls with different nanostructure under tensile loading.* Journal of Materials Science, vol. 36, no. 19, pages 4681–4686, 2001.

[Ren 14] D. Ren, Z. Yu, W. Li, H. Wang & Y. Yu. *The effect of ages on the tensile mechanical properties of elementary fibers extracted from two sympodial bamboo species.* Industrial Crops and Products, vol. 62, pages 94–99, 2014.

[Ren 15] D. Ren, H. Wang, Z. Yu, H. Wang & Y. Yu. *Mechanical imaging of bamboo fiber cell walls and their composites by means of peakforce quantitative nanomechanics (PQNM) technique.* Holzforschung, vol. 69, no. 8, pages 975–984, 2015.

[Réquilé 18] S. Réquilé, A. Le Duigou, A. Bourmaud & C. Baley. *Peeling experiments for hemp retting characterization targeting biocomposites.* Industrial Crops and Products, vol. 123, no. July, pages 573–580, 2018.

[Rice 14] B. Rice, J. Quinzi, L. Lund, J. Ulreich & M. Shoup. *Measurement of Young's modulus and damping of fibers at cryogenic temperatures.* Cryogenics, vol. 63, pages 43–48, 2014.

[Richely 21a] E. Richely. *Combined experimental and numerical approaches to understand the structure-mechanical property relationship of flax fibres and bundles.* Thèse de doctorat, Université de Nantes, 2021.

[Richely 21b] E. Richely, S. Durand, A. Melelli, A. Kao, A. Magueresse, H. Dhakal, T. Gorshkova, F. Callebert, A. Bourmaud, J. Beaugrand & S. Guessasma. *Novel insight into the intricate shape of flax fibre lumen.* Fibers, vol. 9, no. 4, 2021.

[Richely 22a] E. Richely, A. Bourmaud, H. Dhakal, Z. Zhang, J. Beaugrand & S. Guessasma. *Exploring the morphology of flax fibres by X-ray microtomography and the related mechanical response by numerical modelling.* Composites Part A: Applied Science and Manufacturing, vol. 160, no. February, page 107052, 2022.

[Richely 22b] E. Richely, L. Nuez, J. Pérez, C. Rivard, C. Baley, A. Bourmaud, S. Guessasma & J. Beaugrand. *Influence of defects on the tensile behaviour of flax fibres: Cellulose microfibrils evolution by synchrotron X-ray diffraction and finite element modelling.* Composites Part C: Open Access, vol. 9, no. July, 2022.

[Richely 22c] E. Richely, A. Bourmaud, V. Placet, S. Guessasma & J. Beaugrand. *A critical review of the ultrastructure, mechanics and modelling of flax fibres and their defects.* Progress in Materials Science, vol. 124, no. July 2020, page 100851, 2022.

[Rivlin 44] R. S. Rivlin. *The effective work of adhesion.* vol. IX, no. 106, page 109, 1944.

[Robertson 15] D. J. Robertson, S. L. Smith & D. D. Cook. *On measuring the bending strength of septate grass stems.* American Journal of Botany, vol. 102, no. 1, pages 5–11, 2015.

[Roche 85] E. J. Roche, M. S. Wolfe, A. Suna & P. Avakian. *Light Diffraction Effects from Kevlar Aramid Fibers.* Journal of Macromolecular Science, Part B, vol. 24, no. 1-4, pages 141–157, 1985.

[Roland 95] J. C. Roland, M. Mosiniak & D. Roland. *Dynamique du positionnement de la cellulose dans les parois des fibres textiles du lin (Linum usitatissimum).* Acta Botanica Gallica, vol. 142, no. 5, pages 463–484, 1995.

[Romhány 03] G. Romhány, J. Karger-Kocsis & T. Czigány. *Tensile Fracture and Failure Behavior of Technical Flax Fibers.* Journal of Applied Polymer Science, vol. 90, no. 13, pages 3638–3645, 2003.

[Rosemberg 65] J. A. Rosemberg. *Bacteria responsible for the retting of Brazilian flax.* Applied microbiology, vol. 13, no. 6, pages 991–992, 1965.

[Roudier 12] A. Roudier. *Analyse multi-échelle du comportement.* Thèse de doctorat, Université Blaise Pascal - Clermont-Ferrand II, 2012.

[Ruiz 20] Q. Ruiz, S. Pourchet, V. Placet, L. Plasseraud & G. Boni. *New eco-friendly synthesized thermosets from isoeugenol-based epoxy resins.* Polymers, vol. 12, no. 1, pages 1–15, 2020.

[Sadrmanesh 19] V. Sadrmanesh & Y. Chen. *Bast fibres: structure, processing, properties, and applications.* International Materials Reviews, vol. 64, no. 7, pages 381–406, 2019.

[Saketi 12] P. Saketi, M. Von Essen, M. Mikczinski, S. Heinemann, S. Fatikow & P. Kallio. *A flexible microrobotic platform for handling microscale specimens of fibrous materials for microscopic studies.* Journal of Microscopy, vol. 248, no. 2, pages 163–171, 2012.

[Saketi 14a] P. Saketi, J. Hirvonen, Y. Lai, C. Ganser, C. Teichert, J. Järnström, P. Fardim & P. Kallio. *Automated Drop-on-Fiber contact angle measurement using a microrobotic platform using a microrobotic platform.* Nordic Pulp and Paper Research Journal, vol. 29, no. 2, pages 225–231, 2014.

[Saketi 14b] P. Saketi, S. K. Latifi & K. Pasi. *Microrobotic Platform for the Measurement of Fiber-Fiber Friction.* In Progress in Paper Physics, numéro September, pages 1–4, 2014.

[Saketi 16] P. Saketi & P. Kallio. *Micro gripper with force sensor*, 2016.

[Sakuma 19] S. Sakuma, K. Nakahara & F. Arai. *Continuous Mechanical Indexing of Single-Cell Spheroids.* IEEE Robotics and Automation Letters, vol. 4, no. 3, pages 2973–2980, 2019.

[Sala 22] B. Sala, P. Watjanatepin, H. Zarafshani, V. Guicheret-Retel, F. Trivaudey, F. Scarpa, K. Van Acker & V. Placet. *Creep behaviour of eco-friendly sandwich composite materials under hygrothermal conditions.* Composites Part B: Engineering, vol. 247, no. July, page 110291, 2022.

[Sanjay 18] M. R. Sanjay, P. Madhu, M. Jawaid, P. Senthamaraikannan, S. Senthil & S. Pradeep. *Characterization and properties of natural fiber polymer composites: A comprehensive review.* Journal of Cleaner Production, vol. 172, pages 566–581, 2018.

[Sawpan 10] M. A. Sawpan. *Mechanical Performance of Industrial Hemp Fibre Reinforced Polylactide and Unsaturated Polyester Composites.* Thèse de doctorat, The University of Waikato, Hamilton, New Zealand., 2010.

[Schulgasser 92] K. Schulgasser & A. Witztum. *On the strength, stiffness and stability of tubular plant stems and leaves.* Journal of Theoretical Biology, vol. 155, no. 4, pages 497–515, 1992.

[Shah 12] D. U. Shah, P. J. Schubel, P. Licence & M. J. Clifford. *Determining the minimum, critical and maximum fibre content for twisted yarn reinforced plant fibre composites.* Composites Science and Technology, vol. 72, no. 15, pages 1909–1917, 2012.

[Shah 13] D. U. Shah. *Developing plant fibre composites for structural applications by optimising composite parameters: A critical review.* Journal of Materials Science, vol. 48, no. 18, pages 6083–6107, 2013.

[Shah 16] D. U. Shah, R. K. Nag & M. J. Clifford. *Why do we observe significant differences between measured and 'back-calculated' properties of natural fibres?* Cellulose, vol. 23, no. 3, pages 1481–1490, 2016.

[Shahzad 12] A. Shahzad. *Hemp fiber and its composites - A review.* Journal of Composite Materials, vol. 46, no. 8, pages 973–986, 2012.

[Sharma 88] H. S. Sharma. *Chemical retting of flax using chelating compounds.* Annals of Applied Biology, vol. 113, no. 1, pages 159–165, 1988.

[Sharma 99] H. S. Sharma, G. Fauchey & G. Lyons. *Comparison of physical, chemical, and thermal characteristics of water-, dew-, and enzyme-retted flax fibers.* Journal of Applied Polymer Science, vol. 74, no. 1, pages 139–143, 1999.

[Shen 20] M. Shen, W. Huang, M. Chen, B. Song, G. Zeng & Y. Zhang. *(Micro) plastic crisis : Un-ignorable contribution to global greenhouse gas emissions and climate change.* Journal of Cleaner Production, vol. 254, pages 120–138, 2020.

[Sherif 76] S. Sherif, L. Segerlind & J. Frame. *An equation for the modulus of elasticity of a radially compressed cylinder.* Transactions of the ASAE., 1976.

[Shetty 86] D. K. Shetty, A. R. Rosenfiled & W. H. Duckworth. *Mixed-Mode Fracture of Ceramics in Diametral Compression.* Journal of the American Ceramic Society, vol. 69, no. 6, pages 437–443, 1986.

[Singletary 00a] J. Singletary, H. Davis, Y. Song, M. K. Ramasubramanian & W. Knoff. *Transverse compression of PPTA fibers. Part I. Fiber transverse structure.* Journal of Materials Science, vol. 35, no. 3, pages 583–592, 2000.

[Singletary 00b] J. Singletary, H. Davis, Y. Song, M. K. Ramasubramanian & W. Knoff. *Transverse compression of PPTA fibers. Part II. Fiber transverse structure.* Journal of Materials Science, vol. 35, no. 3, pages 583–592, 2000.

[Smits 16]	J. Smits. *Fiber-Reinforced Polymer Bridge Design in the Netherlands: Architectural Challenges toward Innovative, Sustainable, and Durable Bridges.* Engineering, vol. 2, no. 4, pages 518–527, 2016.
[Sobol 01]	I. Sobol. *Global sensitivity indices for nonlinear mathematical models and their Monte Carlo estimates.* Mathematics and Computers in Simulation, vol. 55, no. 1-3, pages 271–280, 2001.
[Sockalingam 12]	S. Sockalingam & G. Nilakantan. *Fiber-matrix interface characterization through the microbond test: A review.* International Journal of Aeronautical and Space Sciences, vol. 13, no. 3, pages 282–295, 2012.
[Sockalingam 14]	S. Sockalingam, J. W. Gillespie & M. Keefe. *On the transverse compression response of Kevlar KM2 using fiber-level finite element model.* International Journal of Solids and Structures, vol. 51, no. 13, pages 2504–2517, jun 2014.
[Sockalingam 16]	S. Sockalingam, R. Bremble, J. W. Gillespie & M. Keefe. *Transverse compression behavior of Kevlar KM2 single fiber.* Composites Part A: Applied Science and Manufacturing, vol. 81, pages 271–281, 2016.
[Solomon 02]	W. K. Solomon & V. K. Jindal. *Comparison of mechanical tests for evaluating textural changes in potatoes during thermal softening.* Journal of Texture Studies, vol. 33, no. 6, pages 529–542, 2002.
[Spies 53]	G. Spies. *The Peeling Test on Redux-bonded Joints.* Aircraft Engineering and Aerospace Technology, vol. 25, no. 3, pages 64–70, 1953.
[Stamboulis 99]	A. Stamboulis, C. Baillie & E. Schulz. *Interfacial characterisation of flax fibre-thermoplastic polymer composites by the pull-out test.* Angewandte Makromolekulare Chemie, vol. 272, no. 4759, pages 117–120, 1999.
[Stamboulis 01]	A. Stamboulis, C. A. Baillie & T. Peijs. *Effects of environmental conditions on mechanical and physical properties of flax fibers.* Composites - Part A: Applied Science and Manufacturing, vol. 32, no. 8, pages 1105–1115, 2001.
[Stamoulis 05]	G. Stamoulis, C. Wagner-Kocher & M. Renner. *An experimental technique to study the transverse mechanical behaviour of polymer monofilaments.* Experimental techniques, vol. 29, no. August, pages 26–31, 2005.
[Stamoulis 07]	G. Stamoulis, C. Wagner-Kocher & M. Renner. *Experimental study of the transverse mechanical properties of polyamide 6.6 monofilaments.* Journal of Materials Science, vol. 42, no. 12, pages 4441–4450, 2007.
[Suri 96]	M. Suri. *Analytical and computational assessment of locking in the hp finite element method.* Computer Methods in Applied Mechanics and Engineering, vol. 133, no. 3-4, pages 347–371, 1996.
[Tan 13]	N. Tan, C. Clevy & N. Chaillet. *Calibration of single-axis nanopositioning cell subjected to thermal disturbance.* Proceedings - IEEE International Conference on Robotics and Automation, pages 3660–3665, 2013.
[Tan 15a]	N. Tan, C. Clévy & N. Chaillet. *Calibration of nanopositioning stages.* Micromachines, vol. 6, no. 12, pages 1856–1875, 2015.
[Tan 15b]	N. Tan, C. Clévy, G. J. Laurent, P. Sandoz & N. Chaillet. *Accuracy quantification and improvement of serial micropositioning robots for in plane motions.* IEEE Transactions on robotics, vol. 31, no. 6, 2015.
[Teklal 18]	F. Teklal, A. Djebbar, S. Allaoui, G. Hivet, Y. Joliff & B. Kacimi. *A review of analytical models to describe pull-out behavior – Fiber/matrix adhesion.* Composite Structures, vol. 201, no. October 2017, pages 791–815, 2018.
[Thomason 11]	J. L. Thomason, J. Carruthers, J. Kelly & G. Johnson. *Fibre cross-section determination and variability in sisal and flax and its effects on fibre performance characterisation.* Composites Science and Technology, vol. 71, no. 7, pages 1008–1015, 2011.

[Thuault 14] A. Thuault, J. Bazin, S. Eve, J. Bréard & M. Gomina. *Numerical study of the influence of structural and mechanical parameters on the tensile mechanical behaviour of flax fibres.* Journal of Industrial Textiles, vol. 44, no. 1, pages 22–39, 2014.

[Tian 06] Y. Tian, N. Pesika, H. Zeng, K. Rosenberg, B. Zhao, P. McGuiggan, K. Autumn & J. Israelachvili. *Adhesion and friction in gecko toe attachment and detachment.* Proceedings of the National Academy of Sciences of the United States of America, vol. 103, no. 51, pages 19320–19325, 2006.

[Timoshenko 70] S. Timoshenko & J. Goodier. Theory of Elasticity. McGraw-Hill, 1970.

[Tiwari 21] B. Tiwari, M. Blot, G. J. Laurent, J. Agnus, P. Sandoz, P. Lutz & C. Clevy. *A High Range-to-Resolution Multiaxis muForce and Torque Sensing Platform.* IEEE/ASME Transactions on Mechatronics, vol. 26, no. 4, pages 1837–1845, 2021.

[Trease 05] B. P. Trease, Y. M. Moon & S. Kota. *Design of large-displacement compliant joints.* Journal of Mechanical Design, Transactions of the ASME, vol. 127, no. 4, pages 788–798, 2005.

[Trivaudey 15] F. Trivaudey, V. Placet, V. Guicheret-Retel & M. L. Boubakar. *Nonlinear tensile behaviour of elementary hemp fibres. Part II: Modelling using an anisotropic viscoelastic constitutive law in a material rotating frame.* Composites Part A: Applied Science and Manufacturing, vol. 68, pages 346–355, 2015.

[Viotti 22] C. Viotti, K. Albrecht, S. Amaducci, P. Bardos, C. Bertheau, D. Blaudez, L. Bothe, D. Cazaux, A. Ferrarini, J. Govilas, H.-j. Gusovius, T. Jeannin, C. Lühr, J. Müssig, M. Pilla, V. Placet, M. Puschenreiter, A. Tognacchini, L. Yung & M. Chalot. *Nettle , a Long-Known Fiber Plant with New Perspectives.* Materials, vol. 15, page 4288, 2022.

[Virk 12] A. S. Virk, W. Hall & J. Summerscales. *Modulus and strength prediction for natural fibre composites.* Materials Science and Technology (United Kingdom), vol. 28, no. 7, pages 864–871, 2012.

[von Essen 14] M. von Essen, J. Hirvonen, S. Kuikka & P. Kallio. *Robotic software frameworks and software component models in the development of automated handling of individual natural fibers.* Journal of Micro-Bio Robotics, vol. 9, no. 1-2, pages 29–45, 2014.

[Wanasingha 21] N. Wanasingha, N. K. Dutta & N. R. Choudhury. *Emerging bioadhesives: from traditional bioactive and bioinert to a new biomimetic protein-based approach.* Advances in Colloid and Interface Science, vol. 296, page 102521, 2021.

[Wang 11] G. Wang, S. Q. Shi, J. Wang, Y. Yu, S. Cao & H. Cheng. *Tensile properties of four types of individual cellulosic fibers.* Wood and Fiber Science, vol. 43, no. 4, pages 353–364, 2011.

[Wei 15] Y. Wei & Q. Xu. *An overview of micro-force sensing techniques.* Sensors and Actuators, A: Physical, vol. 234, pages 359–374, 2015.

[Wiecek 14] T. Wiecek. *A new method for the measurement of static and dynamic Young's moduli of long fibres.* Composites Part A: Applied Science and Manufacturing, vol. 60, pages 1–7, 2014.

[Witik 13] R. A. Witik, R. Teuscher, V. Michaud, C. Ludwig & J. A. E. Månson. *Carbon fibre reinforced composite waste: An environmental assessment of recycling, energy recovery and landfilling.* Composites Part A: Applied Science and Manufacturing, vol. 49, pages 89–99, 2013.

[Wollblad 18a] C. Wollblad. *How to Set Up a Mesh in COMSOL Multiphysics® for CFD Analyses*, 2018.

[Wollblad 18b] C. Wollblad. *Your Guide to Meshing Techniques for Efficient CFD Modeling*, 2018.

[Wollbrett-Blitz 14] J. Wollbrett-Blitz. *Comportement mécanique longitudinal et transverse, micro-mécanismes de déformation et effet de la température sur la fibre Kevlar® 29.* Thèse de doctorat, Ecole nationale supérieure des mines de Paris, 2014.

[Wollbrett-Blitz 16] J. Wollbrett-Blitz, S. Joannès, R. Bruant, C. Le Clerc, M. R. De La Osa, A. Bunsell & A. Marcellan. *Multiaxial mechanical behavior of aramid fibers and identification of skin/core structure from single fiber transverse compression testing.* Journal of Polymer Science, Part B: Polymer Physics, vol. 54, no. 3, pages 374–384, 2016.

[Womack 08] W. J. Womack, B. G. Santoni & C. M. Puttlitz. *Diametral compression of non-circular diaphyseal bone sections.* Journal of Biomechanics, vol. 41, no. 1, pages 194–199, 2008.

[Wong 07] S. Wong, R. A. Shanks & A. Hodzic. *Effect of additives on the interfacial strength of poly(l-lactic acid) and poly(3-hydroxy butyric acid)-flax fibre composites.* Composites Science and Technology, vol. 67, no. 11-12, pages 2478–2484, 2007.

[Wythoff 93] B. J. Wythoff. *Backpropagation neural networks. A tutorial.* Chemometrics and Intelligent Laboratory Systems, vol. 18, no. 2, pages 115–155, 1993.

[Xue 09] Y. Xue, Y. Du, S. Elder, K. Wang & J. Zhang. *Temperature and loading rate effects on tensile properties of kenaf bast fiber bundles and composites.* Composites Part B: Engineering, vol. 40, no. 3, pages 189–196, 2009.

[Xue 21] Z. Xue, G. Chen, C. Wang & R. Huang. *Peeling and sliding of graphene nanoribbons with periodic van der Waals interactions.* Journal of the Mechanics and Physics of Solids, vol. 158, no. May 2021, page 104698, 2021.

[Yamanaka 96] K. Yamanaka & S. Nakano. *Ultrasonic atomic force microscope with overtone excitation of cantilever.* Japanese Journal of Applied Physics, Part 1: Regular Papers and Short Notes and Review Papers, vol. 35, no. 6 SUPPL. B, pages 3787–3792, 1996.

[Yang 12] Y. Yang, R. Boom, B. Irion, D.-j. V. Heerden, P. Kuiper & H. D. Wit. *Chemical Engineering and Processing : Process Intensification Recycling of composite materials.* Chemical Engineering and Processing: Process Intensification, vol. 51, pages 53–68, 2012.

[Yang 22] Y. Yang, M. Zhao, H. Yinguo, H. Zhang, N. Guo & Y. Zheng. *Micro-force sensing techniques and traceable reference forces: a review.* Measurement Science and Technology, vol. 33, no. 11, page 114010, nov 2022.

[Yi 18] X. S. Yi, X. Zhang, F. Ding & J. Tong. *Development of bio-sourced epoxies for bio-composites.* Aerospace, vol. 5, no. 2, pages 1–9, 2018.

[Yoshida 05] M. Yoshida, H. Ogiso, S. Nakano & J. Akedo. *Compression test system for a single submicrometer particle.* Review of Scientific Instruments, vol. 76, no. 9, 2005.

[Yu 11] Y. Yu, Z. Jiang, B. Fei, G. Wang & H. Wang. *An improved microtensile technique for mechanical characterization of short plant fibers: A case study on bamboo fibers.* Journal of Materials Science, vol. 46, no. 3, pages 739–746, 2011.

[Zamil 14] M. S. Zamil, H. Yi & V. M. Puri. *Mechanical characterization of outer epidermal middle lamella of onion under tensile loading.* American Journal of Botany, vol. 101, no. 5, pages 778–787, 2014.

[Zeng 15] X. Zeng, S. J. Mooney & C. J. Sturrock. *Assessing the effect of fibre extraction processes on the strength of flax fibre reinforcement.* Composites Part A: Applied Science and Manufacturing, vol. 70, pages 1–7, 2015.

[Zhang 13] S. Y. Zhang, B. H. Fei, Y. Yu, H. T. Cheng & C. G. Wang. *Effect of the amount of lignin on tensile properties of single wood fibers.* Forest Science and Practice, vol. 15, no. 1, pages 56–60, 2013.

[Zhang 19] Z. Zhang, W. Xian, J. Liu, C. Dai & Y. Sun. *Robotic Micromanipulation: Fundamentals and Applications.* Annual Review of Control, Robotics, and Autonomous Systems, vol. 2, pages 181–203, 2019.

[Zimniewska 11] M. Zimniewska, M. Wladyka-przybylak & J. Mankowski. *Cellulose Fibers: Bio- and Nano-Polymer Composites.* Cellulose Fibers: Bio- and Nano-Polymer Composites, 2011.

[Zou 09] L. Zou, H. Jin, W. Y. Lu & X. Li. *Nanoscale structural and mechanical characterization of the cell wall of bamboo fibers.* Materials Science and Engineering C, vol. 29, no. 4, pages 1375–1379, 2009.

LIST OF FIGURES

LIST OF TABLES

Titre : Caractérisation mécanique des fibres végétales à l'aide de moyens micro-mécatroniques de haute précision : étude du comportement transversal de fibres élémentaires et de l'adhésion inter-fibres

Mots-clés : fibres végétales, micromecanique, micromechatronique, compression transverse, pelage, analyse éléments finis

Abstract

Les fibres utilisées couramment dans les matériaux compositesLeurs renforts fibreux sont cependant issus de ressources non renouvelables ou nécessitent des procédés de fabrication gourmands en énergie. le développement de nouveaux matériaux composites micrométriqueLe remplacement de ces fibres (verre, carbone, Kevlar) par des fibres végétales (lin, chanvre, ortie) représente une alternative écologique de plus en plus populaire. En effet, ces fibres sont à la fois renouvelables et biodégradables, néanmoins, la connaissance de leurs propriétés mécaniques est encore limitée. Pourtant, la caractérisation de ces propriétés est essentielle pour le développement de nouveaux composites respectueux de l'environnement. Néanmoins, la petite taille et la morphologie complexe des fibres végétales constituent des défis majeurs pour leur caractérisation.

Dans cette thèse de doctorat, deux approches différentes sont utilisées pour surmonter ces défis. Premièrement, des plateformes expérimentales micro-mécatroniques de haute précision sont développées pour effectuer des mesures à l'échelle des fibres. aleDeuxièmement, l'influence de différents paramètres morphologiques et matériels sur le comportement des fibres est évaluée et quantifiée par analyse d’éléments finis. Grâce à ces approches, le comportement transversal des fibres végétales et l'adhésion inter-fibres sont étudiés et caractérisés pour la première fois, à travers des essais de compression transverse et de pelage.

La compression transversale d'une fibre élémentaire est un essai complexe. L’augmentation de la surface de contact pendant la compression induit une réponse non-linéaire, même pour des matériaux purement élastiques. Pour cette raison, des modèles analytiques, faisant des simplifications majeures dans la représentation de la géométrie et du comportement matériau de la fibre, sont utilisés pour identifier ses propriétés élastiques. En simulant la compression de fibres à géométrie complexe, ainsi que différents comportements matériau, le domaine de validité de ces modèles est évalué pour la première fois. L’influence majeure de l’alignement des plateaux de compression sur les résultats est démontrée par des expériences et des simulations. Un nouveau protocole visant à minimiser les désalignements entre plateaux est proposé. Enfin, une plateforme expérimentale micro-mécatronique innovante est développée pour la compression de fibres. Le développement de nouveaux capteurs, le contrôle du parallélisme et de l'humidité relative mais aussi l'actionnement précis et les multiples observations microscopiques en temps réel, offrent des capacités sans précédent en termes de précision et de répétabilité des mesures. Grâce à cette plateforme, le comportement en compression transversale de fibres végétales est étudié pour la première fois et leurs propriétés élastiques transverses sont identifiées.

Les essais de pelage sont une approche typique pour mesurer l'adhésion entre surfaces. Une nouvelle plateforme micro-mécatronique est développée pour effectuer du pelage sur des fibres végétales. Une micro-pince actionnée, permet de saisir une seule fibre et de la séparer de son faisceau. Grâce à un capteur de force intégré, l'adhésion inter-fibre est directement mesurée. Ces mesures offrent des informations nouvelles et précieuses pour les processus d'extraction des fibres végétales, qui reposent actuellement sur des observations subjectives et des critères organoleptiques. En outre, des mécanismes de fracture complexes entre les fibres et leurs composants sont observés, indiquant une existence de mécanismes d'adhésion naturelle à l'échelle du micron.

Globalement, nombreuses propriétés mécaniques des fibres végétales à haut potentiel industriel est caractérisée pour la première fois. Les méthodes et les protocoles développés peuvent également être appliqués à la caractérisation de divers autres objets à n'importe quelle échelle.

Université Bourgogne Franche-Comté
32, avenue de l’ Observatoire
25000 Besançon

Title: Plant fiber mechanical characterization with high precision micro-mechatronic means: investigation of single fiber transverse behavior and inter-fiber adhesion

Keywords: plant fibers, micromechanics, micromechatronics, transverse compression, peeling, finite element analysis

Abstract

The fibers that are commonly used in composite materials (glass, carbon, Kevlar), are generally issued from non-renewable resources or require energy intensive manufacturing processes. Replacing such fibers with plant fibers, like flax, hemp or nettle, represents an environmentally friendly alternative, that is growing in popularity. Indeed, these fibers are both renewable and biodegradable, while also being lightweight and presenting good engineering properties. With the exception of longitudinal properties however, knowledge of their mechanical properties is still limited. Yet, characterizing these properties is essential to the development of new environmentally friendly composites. Nevertheless, the micrometric size and complex morphology of plant fibers constitute major challenges in their characterization.

In this doctoral thesis two different approaches are employed to overcome these challenges. First, high precision, micro-mechatronic experimental platforms are developed to perform measurements at the fiber-scale. Using these platforms, plant fiber transverse behavior and inter-fiber adhesion are studied and characterized for the first time ever, through single fiber transverse compression and peeling tests, respectively. Second, finite element analysis is used to evaluate the influence of different morphological and material parameters on fiber compressive behavior.

Single fiber transverse compression represents a challenging test. The change in contact area during compression leads to a non-linear response, even for purely elastic materials. For this reason, analytical models, making major simplifications in the representation of fiber geometry and material behavior, are used to identify elastic properties. By simulating the compression of complex plant fiber geometries and different material behaviors, the area of validity of these models is evaluated. The major influence of the compression platen parallelism on the results, is shown and quantified by experiments and simulations. A new protocol to minimize platen misalignments is also proposed. Finally, an innovative micro-mechatronic experimental platform is developed for fiber compression. The use of custom multi-sensing devices, parallelism and relative humidity control but also precise actuation and multiple real-time microscopic observations, offer unprecedent capabilities in terms of measurement accuracy and repeatability. Using this platform, the transverse compressive behavior of plant fibers is studied and their transverse elastic properties are identified.

Peeling tests represent a typical approach to measure the adhesion between surfaces. A new micro-mechatronic platform to perform peeling tests on plant fibers is developed. An actuated micro-gripper, allows the gripping of a single fiber and its separation from its neighbors Through an integrated force sensor, the adhesion between fibers is directly measured. These measurements offer new, valuable insights and data to the extraction processes that are employed for plant fiber separation, which rely on subjective observations and organoleptic criteria. Furthermore, complex fracture mechanisms between fibers and their constituent components are also observed, pointing to the existence of natural adhesion mechanisms at the micron scale.

Overall, numerous mechanical properties of plant fibers with high industrial potential, are characterized for the first time. The tools and methods that are developed can also be applied in the characterization of various other objects at any scale.

Université Bourgogne Franche-Comté
32, avenue de l’ Observatoire
25000 Besançon